Politecnico di Milano

School of Industrial and Information Engineering

Department of Electronics, Information and Bioengineering

A thesis submitted in fulfillment of the requirements for the degree of Master of Science in Biomedical Engineering

4D flow MRI-based non-invasive hemodynamic assessment and diagnosis in aortic coarctations

Author:

Simone Saitta

ID: 852133

Supervisors:

Prof. Alberto Redaelli

Prof. Xiao Yun Xu

Co-supervisors:

Selene Pirola

Dr. Filippo Piatti

Academic year: 2016-2017

Contents

List of Figures

List of Tables

Sommario

Introduzione

La coartazione dell'aorta (CoA) è una malattia cardiaca congenita (CHD) caratterizzata da un restringimento dell'aorta. La parete aortica ristretta rappresenta un'impedenza anomala al flusso, forzando così il ventricolo sinistro a generare una pressione più elevata per fornire sufficiente flusso di sangue attraverso l'aorta. Di conseguenza, le caratteristiche patologiche includono ipertrofia cardiaca, alterazioni degenerative dell'aorta prossimale e aumento della pressione sanguigna nel parte superiore del corpo [1].

Il fattore diagnostico più distintivo per determinare la gravità funzionale della CoA è la differenza di pressione picco-picco trans-coartazione [4, 5]. Sebbene l'uso di catetere sia considerato il modo più accurato per valutare in maniera invasiva le differenze di pressione a cavallo di una coartazione, tale tecnica comporta l'introduzione di un trasduttore di pressione attraverso un catetere ed è spesso sconsigliata. Pertanto, una stima rapida, non invasiva ed accurata della caduta di pressione trans-coartazione migliorerebbe significativamente la diagnosi e il trattamento anticipato della CoA.

Ad oggi, gli studi di fluidodinamica computazionale (CFD) e interazione fluido-struttura (FSI) sono stati ampiamente utilizzati per analizzare in modo non invasivo il flusso sanguigno e valutare le cadute di pressione associate a coartazioni [6, 7]. Nonostante le simulazioni numeriche forniscano livelli di dettaglio spaziale e temporale abitrariamente elevati, esse sono computazionalmente costose e la loro accuratezza dipende fortemente dalle ipotesi alla base del modello. Con i recenti progressi nelle sequenze di acquisizione,

la risonanza magnetica a contrasto di fase 4D (nota anche come *4D flow MRI* o *4D flow*) fornisce sia informazioni morfologiche sui tessuti che misure di velocità tridimensionali, temporali e tridirezionali. Questa tecnica gode dei vantaggi della risonanza magnetica, come l'uso di radiazioni non ionizzanti, e sfrutta le proprietà magnetiche degli ioni idrogeno per indurre uno sfasamento sui loro *spins* magnetici proporzionale alla loro velocità. In base alla direzione dei gradienti di campo magnetico imposti dall'esterno, è possibile misurare le velocità del flusso sanguigno lungo la direzione specificata. La tecnica *4D flow* è stata già utilizzata per estrarre parametri emodinamici di interesse come portate, sforzo di taglio sulla parete (WSS) e pressione [8]. In particolare, le differenze di pressione *in vivo* possono essere stimate dalle immagini di *4D flow* risolvendo l'equazione di Poisson della pressione (PPE) derivata dalle equazioni di Navier-Stokes:

$$-\Delta p = \nabla \cdot \left[\rho \left(\frac{\partial \boldsymbol{v}}{\partial t} + \boldsymbol{v} \cdot \nabla \boldsymbol{v} - g \right) - \mu \Delta \boldsymbol{v} \right], \tag{1}$$

dove la pressione p può essere calcolata dal campo di velocità $\boldsymbol{v}$ con le sue derivate, con ρ e μ uguali a densità e viscosità del sangue. Nel contesto della CoA, l'obiettivo principale del presente lavoro è di valutare la fattibilità e l'affidabilità della stima di pressione da *4D flow MRI*. A tale scopo, in questo lavoro un algoritmo denominato 4DF-FEPPE è stato sviluppato in MATLAB per risolvere la PPE da dati di *4D flow* sfruttando il metodo degli elementi finiti. Per prima cosa è stata eseguita una simulazione CFD su una geometria aortica idealizzata e i suoi risultati sono stati usati per generare un *dataset 4D flow* sintetico con il quale sono stati confrontati e validati i risultati di 4DF-FEPPE. Successivamente le pressioni ottenute da immagini *4D flow* di un paziente con CoA sono state validate con modelli *in silico* e *in vitro*. Le simulazioni numeriche effettuate in questa tesi includono lo spostamento della parete dei vasi secondo un *coupled momentum method* per l'interazione fluido-struttura (CMM-FSI) recentemente formulato in [9]. L'apparato sperimentale sviluppato comprendeva un modello stampato in 3D dell'aorta in questione collegato a una pompa centrifuga e trasduttori di pressione lungo l'aorta discendente.

Materiali e metodi

4D stima della pressione basata sul flusso

Per risolvere la PPE dai dati di *4D flow MRI*, il metodo di risoluzione agli elementi finiti è stato implementato in MATLAB. Una regione di interesse (ROI) è stata segmentata dalle immagini di *4D flow* utilizzando uno strumento MATLAB sviluppato in precedenza, e una superficie 3D estratta da immagini di risonanza magnetica angiografica (MRA) è stata co-registrata sui dati di *4D flow*. Successivamente una mesh di esaedri a otto nodi è stata costruita in corrispondenza della ROI (Figura 1). Adottando una formulazione isoparametrica sono state definite le funzioni di forma di Lagrange con le loro derivate, e attraverso un'integrazione numerica di Gauss a 2 punti sono state calcolate le matrici dei coefficienti per ogni elemento e successivamente assemblate quelle globali.

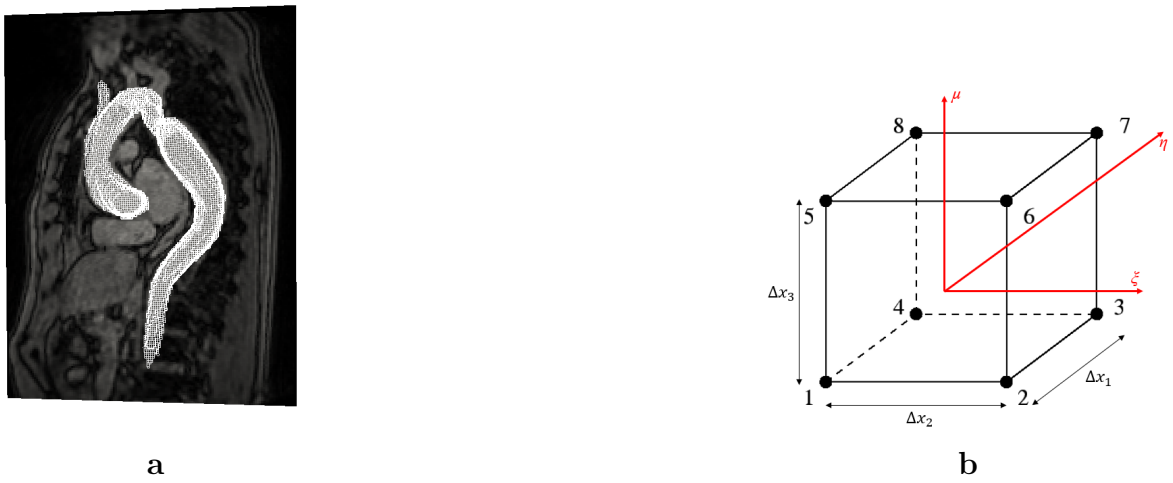

a **b**

Figura 1: Mesh di elementi finiti su una immagine del volume acquisito (a), e rappresentazione di un elemento esaedrico a otti nodi con le sue coordinate naturali (b). Δx_1, Δx_2 e Δx_3 rappresentano le dimensioni dei pixels assiociati alle immagini.

Le derivate prime e seconde nello spazio sono state calcolate dalle velocità misurate da *4D flow* utilizzando varie combinazioni di differenze finite. Le derivate prime sono state approssimate con schemi del quarto e terzo ordine di accuratezza, mentre le derivate seconde usando schemi del quarto, terzo e secondo ordine. La diminuzione in ordine di accuratezza è forzata dalla dipendenza dai nodi vicini degli schemi di ordine superiore. Le derivate nel tempo sono state calcolate usando schemi del secondo e primo ordrine.

La soluzione agli elementi finiti della PPE (Equazione 1) (FE-PPE) richiede condizioni al contorno da imporre su uno o più nodi nel dominio. In 4DF-FEPPE viene imposta una pressione uguale a zero nel punto più basso dell'aorta discendente per tutti gli istanti temporali: le differenze di pressione sono state quindi calcolate rispetto a questo punto di riferimento. Al fine di validare 4DF-FEPPE, un set di dati sintetici è stato ottenuto da una simulazione CFD eseguita con Fluent in cui una curva di velocità è stata imposta all'inlet e una pressione uguale a zero è stata imposta su tutti gli outlet (Figura 2).

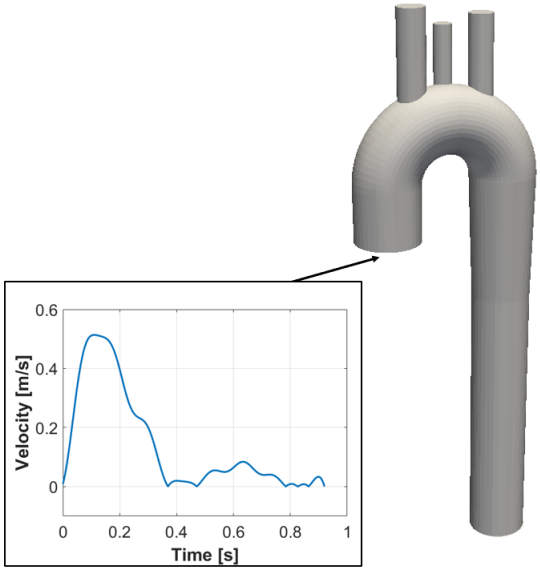

Figura 2: Modello 3D idealizzato di aorta sana usato per la simulazione CFD e i cui risultati sono stati utilizzati per generare dati sintentici. La velocità media imposta all'inlet è mostrata nel grafico come linea blu.

I dataset artificiali di dati *4D flow* sono stati ottenuti seguendo la metodologia descritta in [10] utilizzando codice precedentemente scritto. Le velocità e le coordinate cartesiane dei nodi della mesh CFD sono state esportate dai risultati della simulazione e i campi di velocità sono stati sottocampionati spazialmente e temporalmente per simulare le tipiche risoluzioni del *4D flow*; in particolare, sono stati esportati sei istanti temporali dai risultati della simulazione CFD. Per riprodurre il rumore osservato nelle immagini di *4D flow*, del rumore con distribuzione gaussiana è stato aggiunto ai campi di velocità sottocampionati (Figura 3).

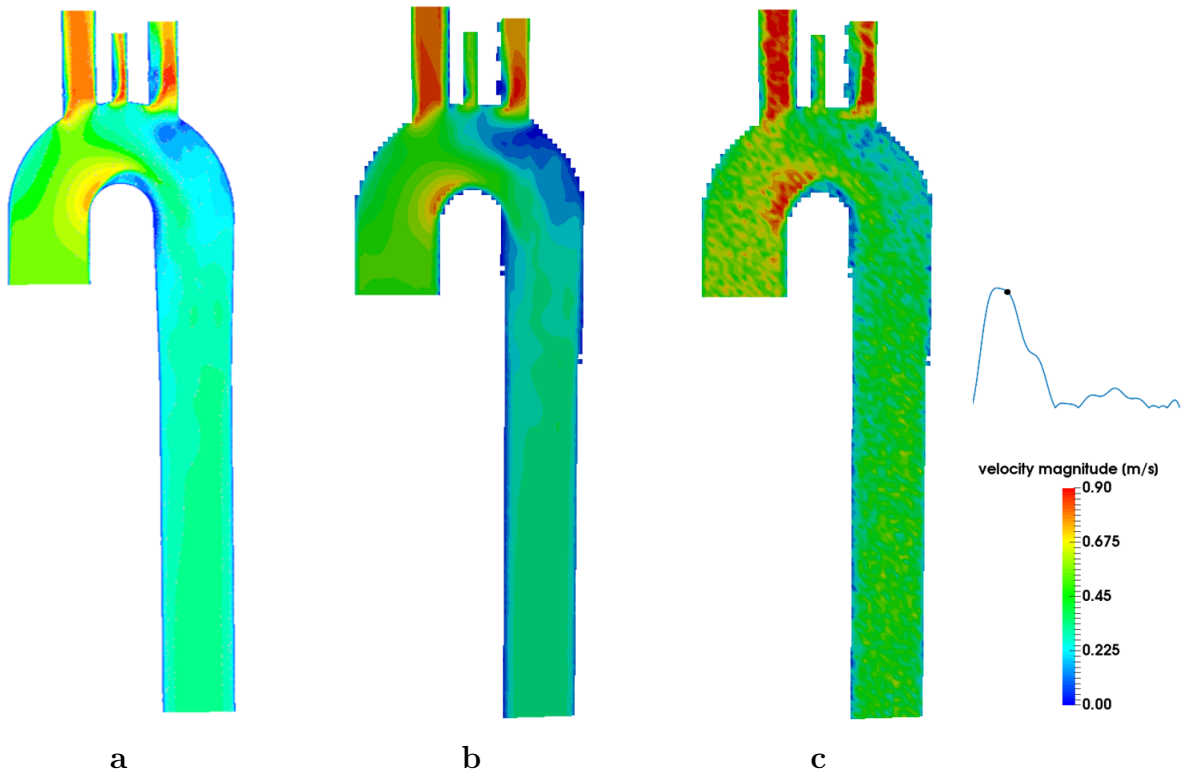

Figura 3: Effetto del sottocampionamento (b) e dell'aggiunta di rumore (c) sul campo di velocità originale ottenuto da Fluent (a).

Inoltre sono stati valutati gli effetti di un filtro *divergence-free wavelet* (DFW) presentato in [11] in termini di campi di velocità e distribuzioni di pressione. Tale filtro consente di separare un campo di velocità in componenti con divergenza nulla e con divergenza non nulla, riducendo i contributi delle due componenti in modo da ottenere un campo di velocità che sia più vicino a un campo solenoidale. 4DF-FEPPE è stato quindi testato utilizzando tre diversi tipi di velocità come dato di partenza: velocità sottocampionate, velocità con rumore e velocità processate con DFW. I risultati e le prestazioni di 4DF-FEPPE sono stati poi confrontati con un codice simile precedentemente sviluppato.
Infine 4DF-FEPPE è stato applicato ad un dataset di *4D flow* di un paziente con CoA composto da 21 frame, e i risultati sono stati validati con due simulazioni numeriche e un banco prova sperimentale.

Simulazioni numeriche

Due simulazioni numeriche sono state eseguite sulla stessa geometria paziente-specifica

utilizzando il software *open source* CRIMSON. In tali modelli sono state incluse sia l'emodinamica che la meccanica strutturale della parete. La portata paziente-specifica estratta da $4Dflow$ è stata imposta all'inlet, mentre per tenere conto dell'effetto della vascolatura distale e ottenere curve fisiologiche di portata e pressione, dei modelli Windkessel a tre elementi (3-WK) sono stati imposti agli outlet (Figura 4). In entrambe le simulazioni, le proprietà meccaniche delle pareti arteriose sono state rappresentate come elastiche lineari, con un modulo di Young di 878000 Pa, uno spessore di 1 mm e un rapporto di Poisson di 0.5 [12]. Il sangue è stato rappresentato come fluido newtoniano con viscosità dinamica di 4 cP e densità di 1060 kg/m^3.

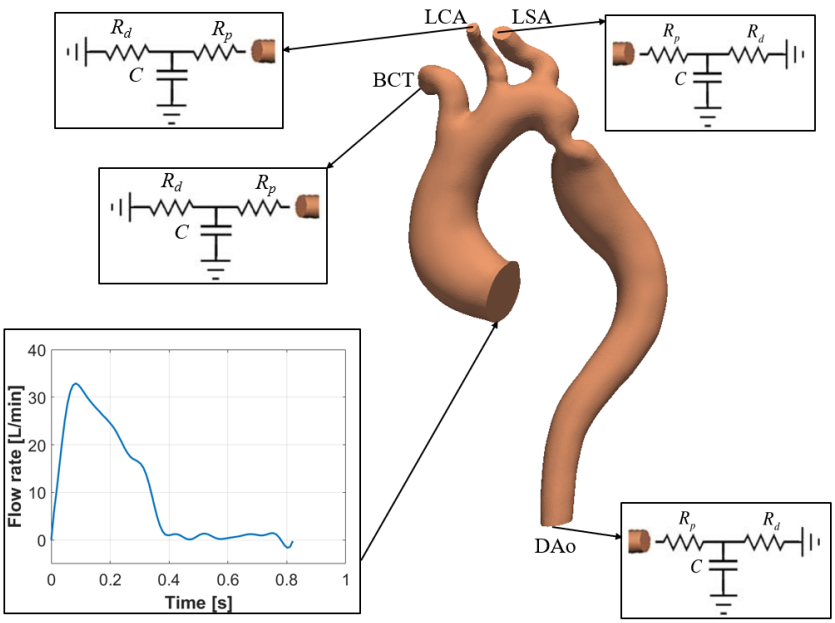

Figura 4: Descrizione delle condizioni al contorno del modello usato per le simulazioni numeriche; la portata paziente-specifica è imposta in ingresso, mentre modelli 3-WK sono imposti alle uscite per tronco brachiocefalico (BCT), arteria carotide sinistra (LCA), arteria succlavia sinistra (LSA) e aorta discendente (DAo).

La geometria 3D di partenza per le simulazioni è stata estratta da immagini di MRA tramite il software *open source* ITK-SNAP. La superficie esportata è stata poi processata con Autodesk Meshmixer e importata in CRIMSON per essere discretizzata. La mesh consisteva di ∼4m di elementi tetraedrici con un boundary layer (Figura 5).

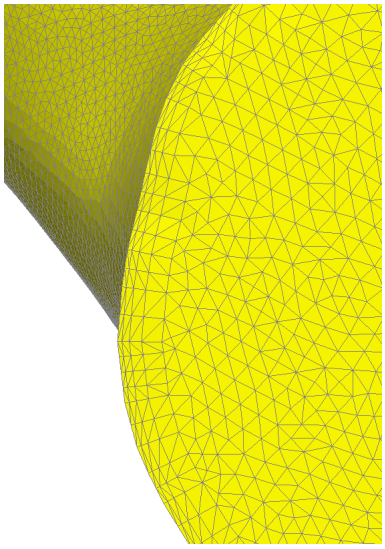

Figura 5: Visualizzazione dei dettagli della mesh in corrispondenza dell'inlet.

Per le condizioni al contorno sugli outlet i parametri dei 3-WK sono stati calcolati secondo [15]. Una pressione media nel ciclo cardiaco ($\overline{P}$) è stata ipotizzata per ogni outlet e le relative portate mediate nel tempo sono state estratte da *4D flow*. Sono stati quindi calcolate le resistente prossimali (R_p) e distali (R_d) insieme alle compliance C per ogni outlet usando relazioni introdotte in [16], [17] e [18].

Le due simulazioni condotte in questo lavoro differiscono nei valori dei parametri dei 3-WK ai rami sovra-aortici. In Simulation-1 una pressione media $\overline{P} = 80$ mmHg è stata usata per impostare i 3-WK sia dell'aorta discendente che dei sovra-aortici. In Simulation-2 la pressione media usata per impostare i 3-WK ai tre vasi sovra-aortici è stata aumentata di 18 mmHg rispetto a quella usata in Simulation-1, mentre una pressione media di 80 mmHg è stata usata per i 3-WK dell'aorta discendente. L'aumento di 18 mmHg sui sovra-aortici corrisponde ad una stima della massima differenza di pressione trans-coartazione calcolata da Simulation-1. Simulation-2 è stata condotta con lo scopo di valutare la sensitività della differenza di pressione trans-coartazione alla pressione media utilizzata nell'impostare i 3-WK agli outlet dei vasi sovra-aortici. I parametri dei 3-WK usati nelle due simulazioni sono riportati in Tabella 1. Entrambe le simulazioni sono state validate con i dati grezzi di *4D flow* in termini di portate attraverso gli outlet, mappe a colori di velocità e streamlines in aorta discendente. Dopo che l'accuratezza di entrambe

le simulazione è stata confermata tramite il confronto con il dato grezzo di *4D flow*, i risultati delle simulazioni sono stati confrontati con quelli di 4DF-FEPPE in termini di differenze di pressione trans-coartazione, con lo scopo di validare l'algortimo sviluppato per la stima della pressione da *4D flow*.

		R_p	C	R_d
BCT	Simulation-1	0.0294	12.1872	0.1281
	Simulation-2	0.0294	9.2751	0.1635
LCA	Simulation-1	0.0872	1.2950	1.3955
	Simulation-2	0.0872	0.9855	1.7291
LSA	Simulation-1	0.0418	3.7653	0.4682
	Simulation-2	0.0418	10.0218	0.1583
DAo	Simulation-1	0.0203	10.0218	0.1583
	Simulation-2	0.0203	10.0218	0.1583

Tabella 1: Valori dei parametri dei Windkessel usati in Simulation-1 e Simulation-2: resistenze prossimali R_p, compliance C and resistenze distali R_d per il tronco brachiocefalico (BCT), arteria carotide sinistra (LCA), arteria succlavia sinistra (LSA) e aorta discendente (DAo). Le resistenze sono espresse in g/(mm^4·s), mentre la compliances in mm^4·s^2/g.

Analisi *in vitro*

Per validare ulteriormente le stime di pressione *in vivo* basate sul *4D flow*, è stato messo a punto un banco prova idraulico. I tre vasi sovra-aortici sono stati rimossi dalla geometria 3D e cinque porte (*ports*) sono state create lungo l'aorta per poter connettere dei trasduttori di pressione (Figure 6).

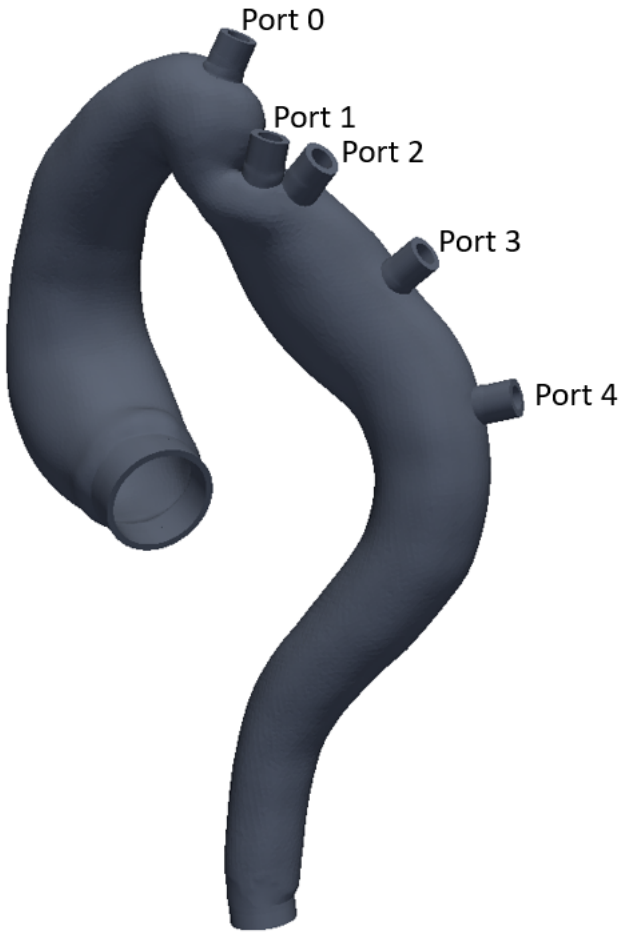

Figura 6: Modello 3D modificato con ingressi per trasduttori di pressione.

Il modello in Figura 6 stampato in 3D è stato collegato ad una pompa centrifuga, a un reservoir a pressione atmosferica e a dei trasduttori di pressione piezoelettrici (Figure 7). Sono stati eseguiti tre test in condizioni di flusso stazionario: uno in cui la portata imposta corrispondeva alla portata di picco in aorta discendente misurata da *4D flow* (denominata Q), e gli altri due utilizzando $0.9Q$ e $1.1Q$.

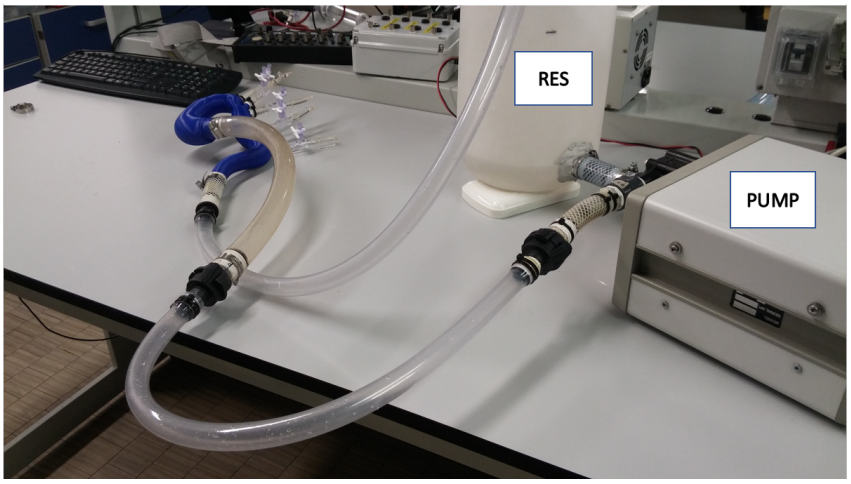

Figura 7: Configurazione della piattaforma con reservoir a pressione atmosferica (RES) e pompa centrifuga (PUMP).

Risultati

Stima di pressione da *4D flow*

Per valutare l'effetto del sottocampionamento del campo di velocità e l'aggiunta del rumore sulla stima della pressione, 4DF-FEPPE è stato testato utilizzando tre campi di velocità diversi come input. Le distribuzioni di pressione sono state inizialmente calcolate utilizzando le velocità estratte dalla soluzione CFD sottocampionate e senza rumore aggiunto. Successivamente l'effetto del rumore gaussiano sulla stima delle pressioni è stato valutato utilizzando le velocità sottocampionate con rumore come input per il codice 4DF-FEPPE. In fine i campi di pressione sono stati calcolati utilizzando i campi di velocità con rumore pre-processati con il filtro DFW. L'effetto del sottocampionamento, dell'aggiunta di rumore e del filtro DFW per un istante temporale sistolico è mostrato in Figura 8, mentre le mappe di differenze di pressione sono mostrate in Figura 9. Nei risultati di 4DF-FEPPE tutti i valori di pressione sono differenze di pressione rispetto al punto più in basso dell'aorta discendente, dove è stata imposta una pressione nulla per tutti gli istanti temporali.

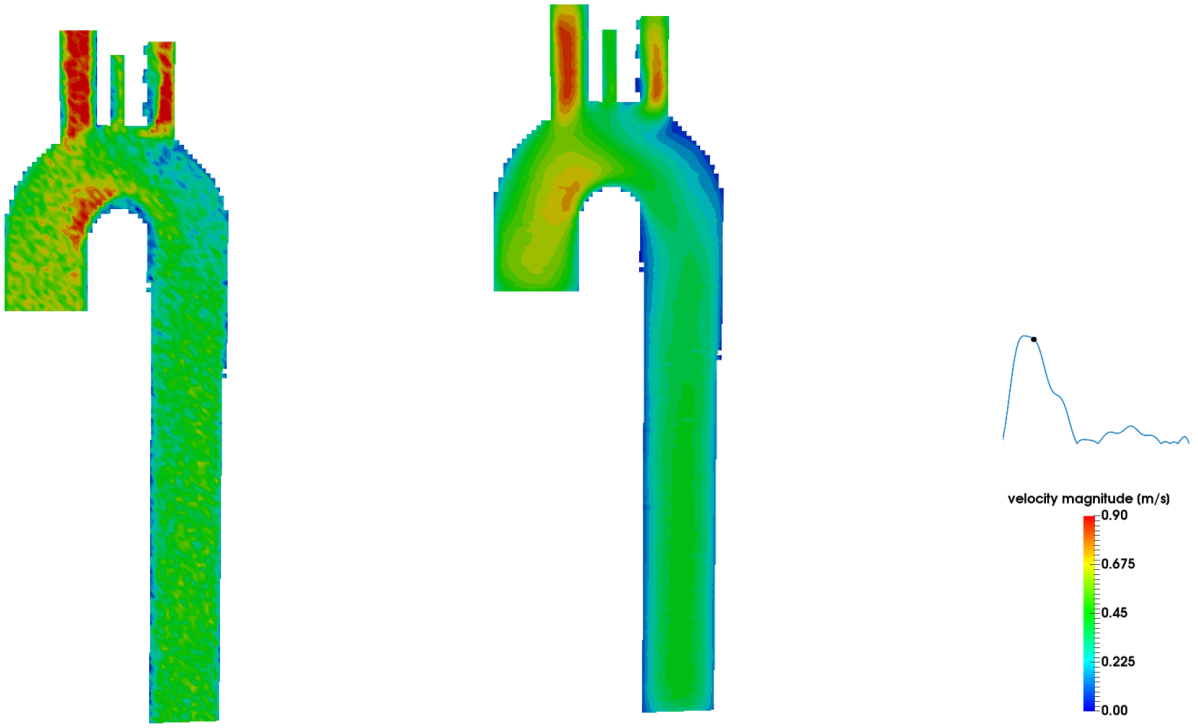

Figura 8: Effetto del filtro DFW sul campo di velocità con rumore aggiunto artificialmente; prima (a) e dopo (b) il filtraggio.

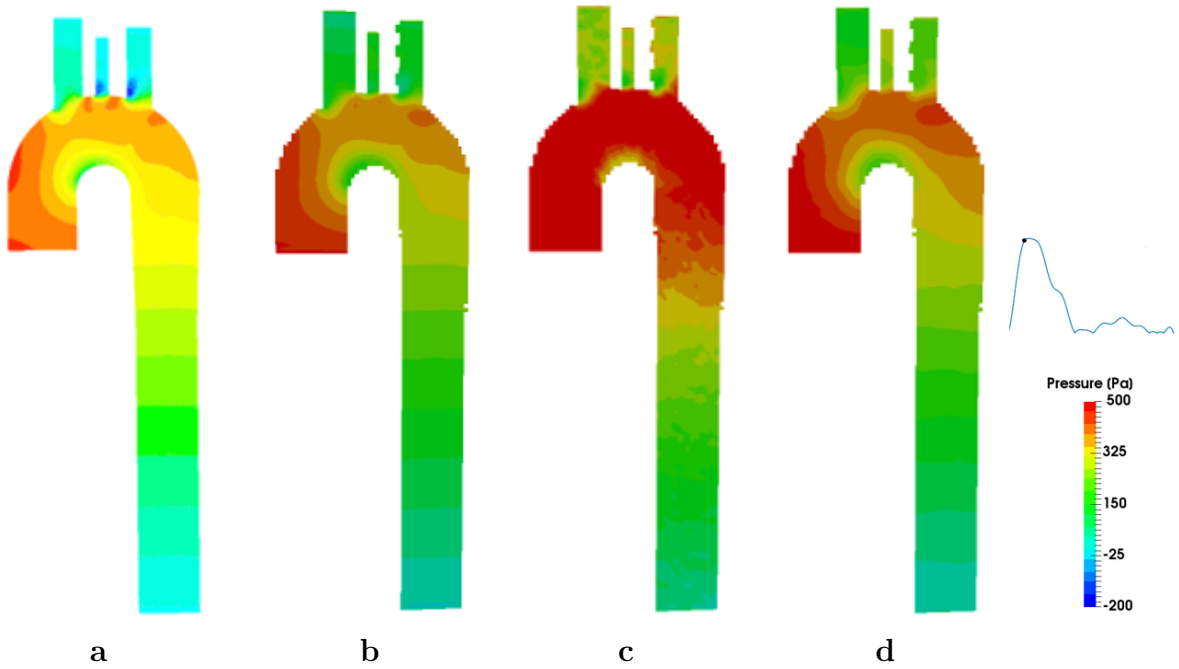

Figura 9: Confronto tra mappe di pressioni calcolate con Fluent (a) e 4DF-FEPPE usando come input: velocità sottocampionate(b), velocità sottocampionate con rumore aggiunto (c) e velocità sottocampionate con rumore processate con DFW (d).

Utilizzando i campi di velocità sottocampionati come input, i risultati di 4DF-FEPPE sono stati trovati in buon accordo con le distribuzioni di pressione calcolate da CFD, con valori di pressione media diversi di 197 Pa al massimo. Utilizzando i campi di velocità sottocampionati con rumore come input per 4DF-FEPPE, è stata osservata una maggiore discrepanza tra le distribuzioni di pressione calcolate con 4DF-FEPPE e con Fluent, con valori di pressione medi diversi fino a 278 Pa. Con i campi di velocità processati tramite DFW come input, le distribuzioni di pressione sono state trovate in migliore accordo con i dati CFD, discostandosi dalla soluzione calcolata da Fluent di 137 Pa al massimo in termini di pressione media nel dominio. I valori di pressione media nello spazio con deviazioni standard sono mostrati in Figura 10.

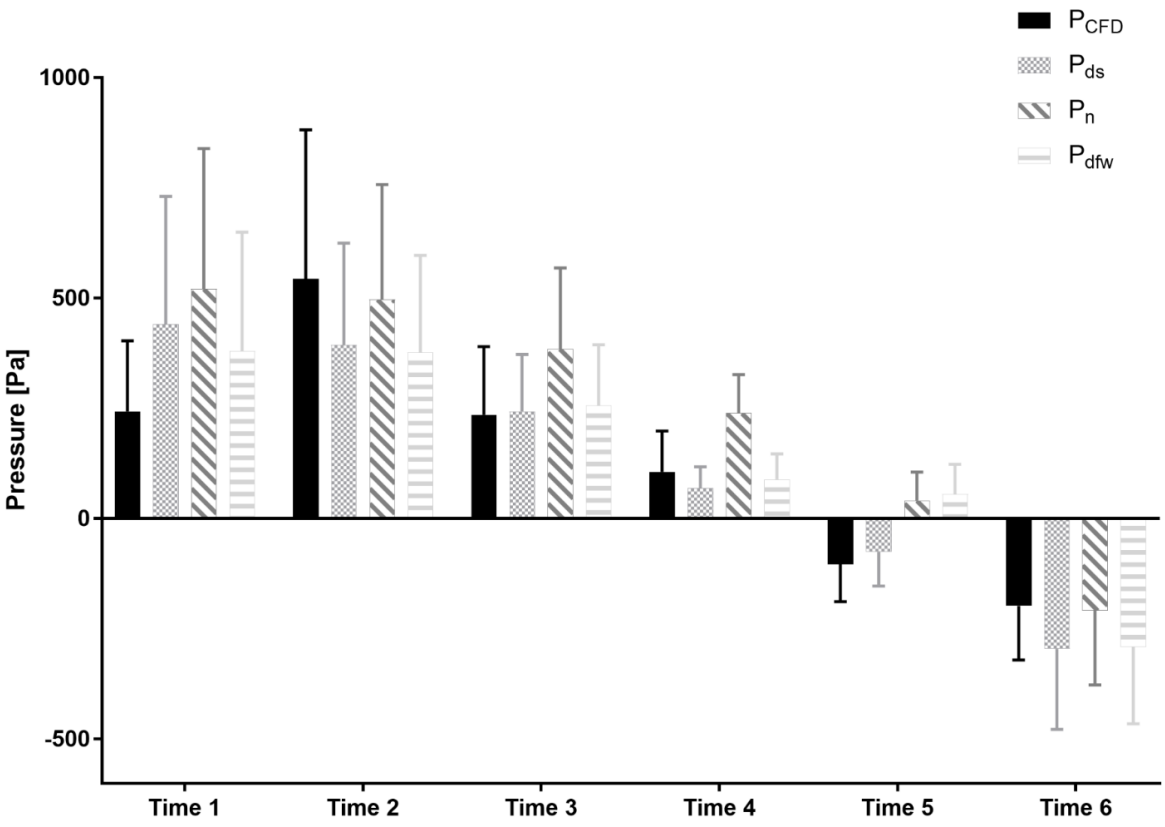

Figura 10: Valori medi di pressione con deviazione standard ottenuti dalla simulazione CFD (P_{CFD}) e daa 4DF-FEPPE usando veloicità sottocampionate (P_{ds}), veloicità sottocampionate con rumore (P_n) e veloicità sottocampionate con rumore processate con DFW (P_{dfw}).

L'aggiunta di rumore con distribuzione gaussiana ha portato ad una sovrastima delle velocità rispetto al caso sottocampionato. In particolare i valori medi del modulo della velocità dopo l'aggiunta del rumore sono stati aumentati del 199% per l'istante Time 1, e

almeno del 30% per tutti gli altri istanti temporali. D'alto canto l'applicazione del filtro DFW ha portato ad una diminuzione dei valori medi di velocità con rumore per tutti gli istanti temporali, risultando in velocità medie più alte rispetto al caso sottocampionato almeno del 15% per tutti gli istanti temporali eccetto Time 1.

Nel caso paziente-specifico di CoA, 4DF-FEPPE ha prodotto risultati che rispecchiano le distribuzioni di pressione tipicamente osservate in pazienti con CoA, con una netta differenza di pressione tra le regioni a monte e a valle del restringimento durante la sistole (Figure 12). Una differenza di pressione trans-coartazione picco-picco (Δp_{pp}) di 17.6 mmHg è stata ottenuta, mentre il massimo valore di differenza di pressione (Δp_m) è stato trovato uguale a 21.09 mmHg (Figura 11).

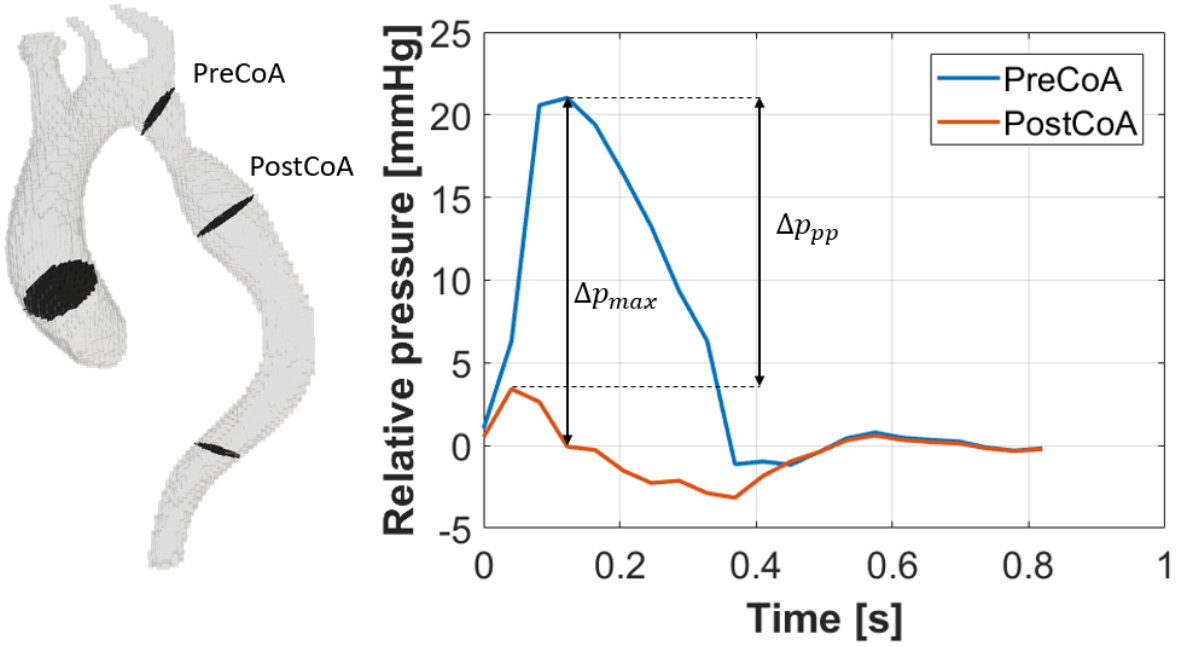

Figura 11: Differenze di pressione mediate in sezione a monte (PreCoA) e a valle (PostCoA) della coartazione.

L'applicazione del filtro DFW ha portato ad una riduzione del rumore dei dati *4D flow* grezzi, ma è risultata in una riduzione sistematica delle velocità, con un errore percentuale del -21.3% in media, calcolato come:

$$error = \frac{\overline{v}_{dfw} - \overline{v}_{raw}}{\overline{v}_{raw}} \cdot 100, \tag{2}$$

dove $\overline{v}_{dfw}$ è la media del modulo della velocità nello spazio filtrata e $\overline{v}_{raw}$ è la media del modulo della velocità nello spazio non processata da *4D flow*. Di conseguenza il Δp_{pp} trans-coartazione dopo l'applicazione del DFW è stato ridotto a 12.9 mmHg.

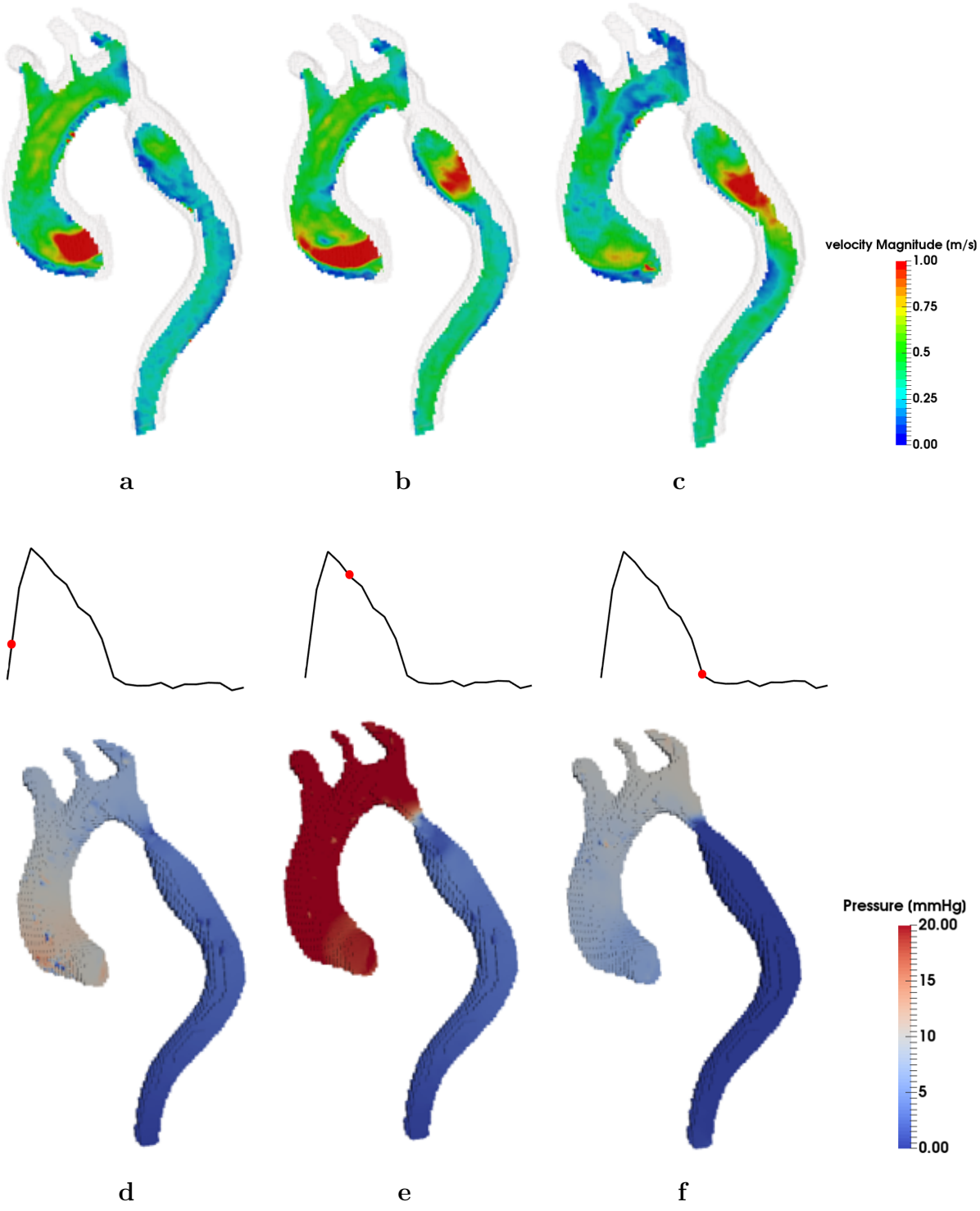

Figura 12: Mappe a colori del modulo della velocità estratte da *4D flow* (a-c) e mappe di differenze di pressione calcolate con 4DF-FEPPE (d-f).

Simulazioni numeriche

Le due simulazioni numeriche svolte in questo lavoro sono state validate quantitativamente e qualitativamente con i dati grezzi di *4D flow* in termini di mappe a colori di velocità e distribuzioni di portata (Figura 13). Le portate medie attraverso gli outlet sono riportate in Tabella 2. Entrambe le simulazioni hanno dato risultati che sono stati trovati in accordo con i dati grezzi *4D flow*, con soltanto una modesta sottostima del picco di portata e una sovrastima della portata diastolica attraverso l'outlet di aorta discendente. In particolare i picchi di portata attraverso questo outlet calcolati dalle simulazioni Simulation-1 e Simulation-2 sono stati di 1.43 L/min and 0.83 L/min rispettivamente più bassi confrontati con quelli del *4D flow*.

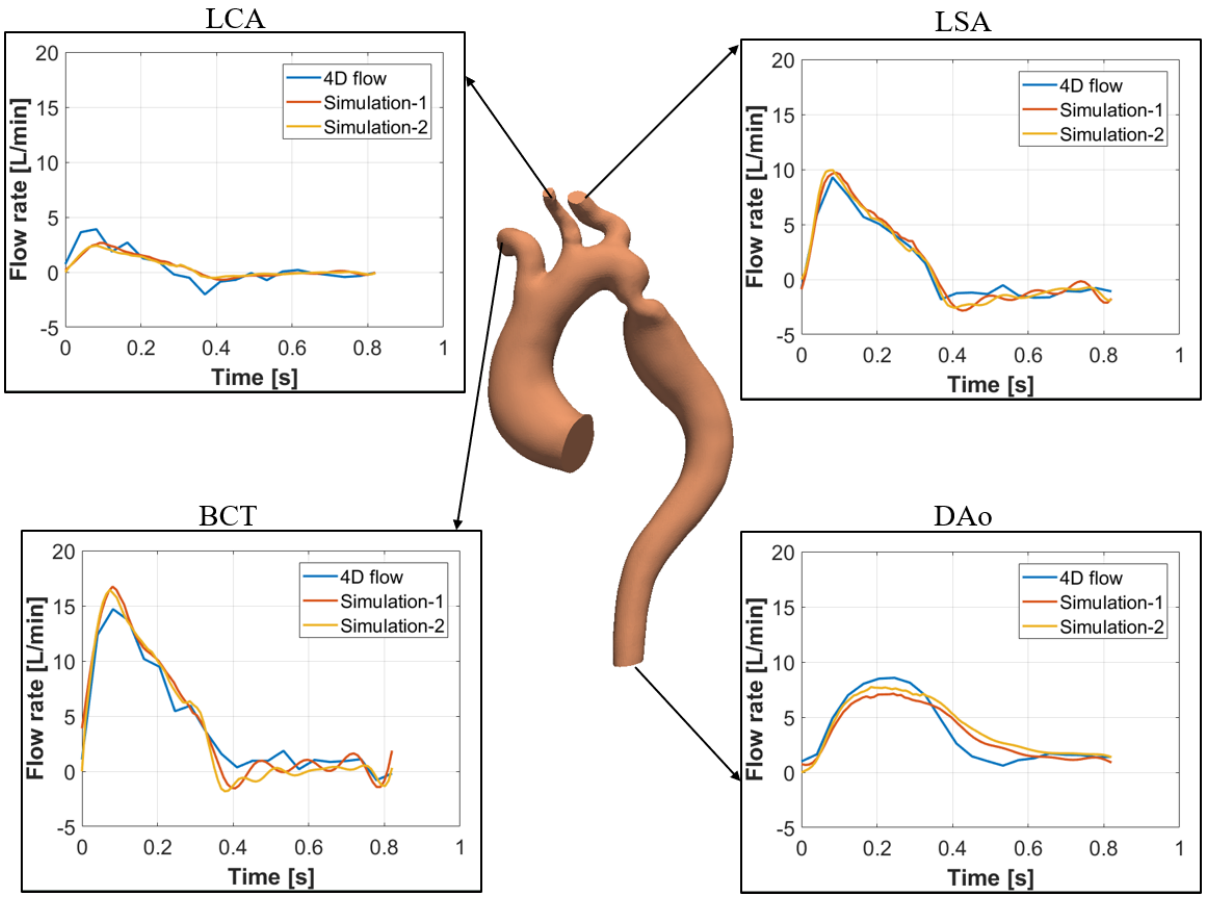

Figura 13: Portate nel tempo confrontate tra dati *4D flow* e risultati di Simulation-1 e Simulation-2.

Outlet	$\overline{Q}_{4Dflow}$	$\overline{Q}_{Simulation-1}$	$\overline{Q}_{Simulation-2}$
BCT	4.06	4.22	3.93
LCA	0.43	0.48	0.44
LSA	1.26	1.52	1.35
DAo	3.58	3.55	4.05

Tabella 2: Medie nel tempo delle portate. Confronto tra dati *4D flow* e risultati di Simulation-1 e Simulation-2 relativi a: tronco brachiocefalico (BCT), arteria carotide sinistra (LCA), arteria succlavia sinistra (LSA) e aorta discendente (DAo). Tutti i valori sono in L/min.

Dopo essere stai validati, i risultati delle simulazioni sono stati confrontati con le pressioni calcolate da *4D flow* con 4DF-FEPPE. Questo confronto è stato fatto per validare i risultati dell'algoritmo sviluppato. Un Δp_{pp} trans-coartazione uguale a 16.86 mmHg e un Δp_m di 22.43 mmHg sono stati ottenuti da Simulation-1. Da Simulation-2 sono stati ottenuti un Δp_{pp} di 18.56 mmHg e un Δp_m di 23.89 mmHg.

Complessivamente le differenze di pressione trans-coartazione calcolate da *4D flow* sono state trovate in buon accordo con i risultati delle simulazioni numeriche, con solo una lieve sottostima della caduta di pressione calcolata da 4DF-FEPPE. Le differenze di pressione trans-coartazione ottenute con Simulation-1 e 4DF-FEPPE sono mostrate in Figura 14 insieme all'errore relativo calcolato come: $error = \left|\frac{\Delta p_{simulation} - \Delta p_{4Dflow}}{\Delta p_{simulation}}\right|$. Analogamente, le differenze di pressione calcolate con Simulation-2 e 4DF-FEPPE sono mostrate in Figura 15.

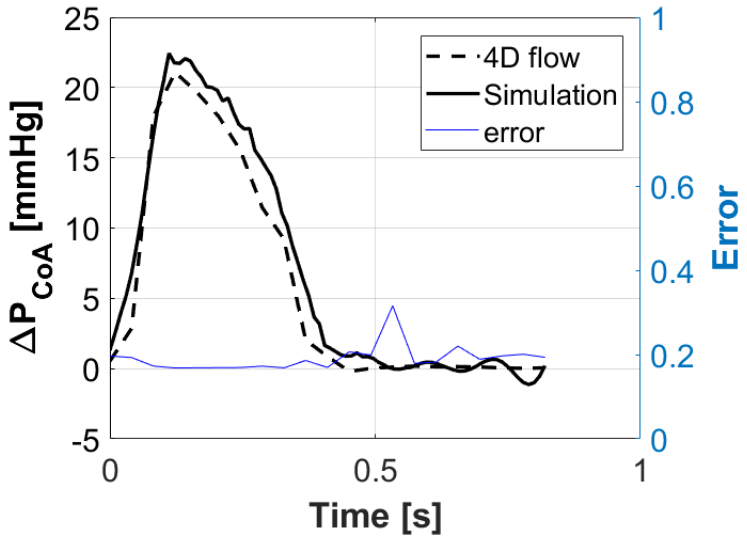

Figura 14: Differenze di pressione a cavallo della coartazione: risultati di 4DF-FEPPE e di Simulation-1. L'errore relativo è rappresentato in blu.

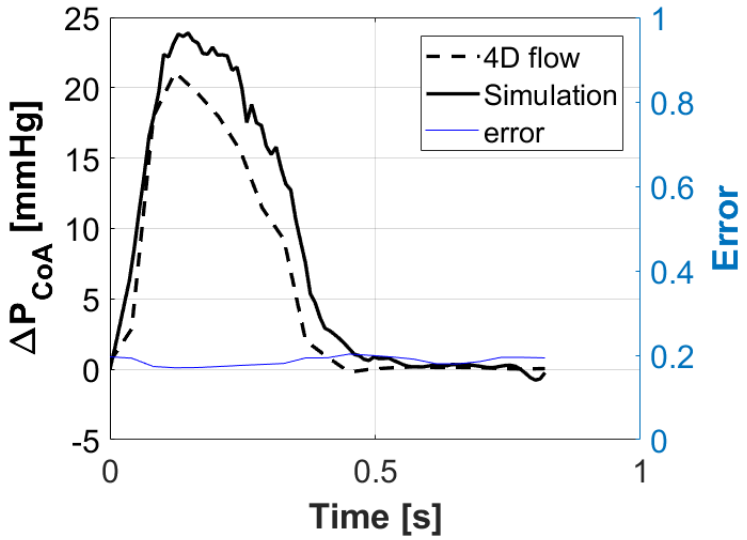

Figura 15: Differenze di pressione a cavallo della coartazione: risultati di 4DF-FEPPE e di Simulation-2. L'errore relativo è rappresentato in blu.

Analisi *in vitro*

Le misure di pressione prese nel modello *in vitro* tramite trasduttori di pressione sono state confrontate con le massime differenze di pressione ottenute dalle simulazioni numeriche e da 4DF-FEPPE su sezioni lungo l'aorta corrispondenti alle posizioni dei trasduttori (Figura 16). Tutti i valori di Δp in Tabella 3 sono stati calcolati come differenze rispetto alla pressione misurata in Port 1 (nel caso *in vitro*) e rispetto alla pressione misurata in

sezione PRE (nel caso *in silico*) (Figura 16). I risultati sono riportati per le tre prove effettuate con tre portate stazionarie: $Q_{low} = 0.9Q$,$Q = 8.56$L/min e $Q_{high} = 1.1Q$ (Tabelle 3). I valori di Δp_1, Δp_2, Δp_3 e Δp_4 calcolati con 4DF-FEPPE sono risultati diversi rispetto alle misure sul banco prova usando Q di 1 mmHg, 0.37 mmHg, 4.5 mmHg e 2.8 mmHg rispettivamente; mentre i risultati di Simulation-1 si sono rivelate superiori rispetto alle misure *in vitro*, con differenze da 1 a 4.3 mmHg e da Simulation-2 sono state ottenute differenze di pressione più alte fino a 6.4 mmHg.

a **b**

Figura 16: Modello 3D usato per la piattaforma *in vitro* con le porte create per i trasduttori di pressione (a) e le corrispondenti sezioni nel dominio computazionale(b) (denominate S1-S4).

	Δp_1 [mmHg]	Δp_2 [mmHg]	Δp_3 [mmHg]	Δp_4 [mmHg]
in vitro (Q_{low})	14.6	13.7	13.6	14.5
in vitro (Q)	19.4	20.73	16.6	16.8
in vitro (Q_{high})	23.6	23.2	23.5	21.6
Simulation-1	21.5	21.8	20.9	19.7
Simulation-2	22.7	23.1	23	21
4DF-FEPPE	20.4	21.1	21.1	19.6

Tabella 3: Differenze di pressione misurate *in vitro* e calcolate in Simulation-1, Simulation-2 e 4DF-FEPPE. Tutti i Δp sono calcolati come differenze di pressione tra Port 1 (o sezione PRE) e un Port (o sezione) specificato dal pedice.

Discussione and conclusioni

In questa tesi sono state valutate la fattibilità e l'affidabilità della stima di differenze di pressione da *4D flow*. A questo scopo è stato sviluppato l'algoritmo 4DF-FEPPE e i suoi risultati sono stati validati mettendo a punto due simulazioni numeriche e un banco prova idraulico. L'algoritmo sviluppato si è dimostrato estremamente efficiente rispetto ad un simile codice precedentemente scritto, riuscendo a calcolare le pressioni in meno di cinque minuti per un dataset *4D flow* da 21 frames.

Stima di pressione basata su *4D flow*

Il confronto sulla pressione calcolata da 4DF-FEPPE e dalla simulazione CFD ha permesso di validate e testare l'approccio sviluppato confrontandone i risultati con quelli di CFD considerati soluzione esatta. Complessivamente 4DF-FEPPE si è dimostrato in grado di rappresentare le corrette distribuzioni di pressione con un buon livello di accuratezza, discostandosi dai risultati CFD di non più di 3 mmHg in termini di pressioni mediate nello spazio utilizzando campi di velocità con rumore come dato di partenza. Inoltre la metodologia implementata in questo lavoro permette di calcolare le pressioni da *4D flow* in pochi minuti: mantenere i tempi computazionali più bassi possibili è di importanza fondamentale per poter applicare tale algoritmo nella diagnosi clinica.

Per quanto riguarda il modello idealizzato usato per validare 4DF-FEPPE, l'aggiunta di rumore con distribuzione gaussiana ha portato a campi di velocità con valori più alti rispetti alle velocità semplicemente sottocampionate. In questo caso l'applicazione del filtro DFW ha comportato una riduzione, in media, del 48% rispetto al caso con rumore. Dunque la tendenza del processo di aggiunta di rumore ad aumentare i valori di velocità, insieme alla riduzione delle velocità causata dal DFW ha portato a distribuzioni di pressione più simili ai dati CFD (Figure 9 e 10).

Nel caso paziente-specifico riportato l'uso del filtro DFW ha permesso di rimuovere il rumore dai dati grezzi di *4D flow*, mantenendo le strutture fluide osservate. Tuttavia i valori del modulo di velocità mediati nello spazio sono risultati, per ogni istante tem-

porale, ridotti fino al 30% rispetto ai dati non processati, che, in corrispondenza della coartazione ha portato ad una riduzione della velocità del getto, a suo volta associata ad un Δp_{pp} più basso di 5 mmHg. La tendenza del filtro DFW ad abbassare i valori di velocità è stata osservata in maniera simile nel dataset generato artificialmente. Nonostante ciò, come predentemente discusso, l'aggiunta di rumore ha portato a campi di velocità con valori significativamente più alti rispetto al caso semplicemente sottocampionato, mentre il reale rumore osservato nelle immagini *4D flow* non ha questo effetto sui campi di velocità misurati.

Simulazioni numeriche

Le due simulazioni numeriche riportate in questo lavoro sono diverse nei valori dei parametri 3-WK imposti agli outlet dei vasi sovra-aortici. In particolare mentre in Simulation-1 è stata usata la stessa pressione media (80 mmHg) per impostare i 3-WK di tutti gli outlet, in Simulation-2 la pressione media usata per i sovra-aortici è stata aumentata di un valore corrispondente ad una stima della massima differenza di pressione trans-coartazione osservata dai risultati di Simulation-1. Poichè non era disponibile nessuna informazione sulla pressione del paziente, la stessa pressione media per impostare i 3-WK è stata ipotizzata in Simulation-1. Tuttavia, nel contesto patologico della CoA, tale supposizione potrebbe essere considerata poco realistica e Simulation-2 è stata effettuata allo scopo di valutare l'effetto di questa specifica del modello sul calo di pressione trans-coartazione.
In entrambe le simulazioni le pareti dei vasi sono state approssimate con un modello lineare elastico omogeneo su tutto il dominio solido. Sono stati scelti i valori di modulo elastico e spessore da [12] dopo una serie di prove effettuate con diverse combinazioni di moduli elastici e spessori, che hanno però dato risultati peggiori in termini di confronto con il *4D flow*.
La stessa pressione media usata per impostare i 3-WK in Simulation-1 ha portato a risultati di distribuzione di portata in buon accordo con i dati *4D flow*, con una differenza massima di portata media nei sovra-aortici di 0.26 L/min nell'arteria succlavia sinistra, che corrisponde al 21% della portata misurata da *4D flow*. L'aumento di 18 mmHg nella

pressione media usata per impostare i 3-WK nei sovra-aortici in Simulation-2 ha portato ad avere una portata maggiore attraverso l'aorta discendente rispetto a Simulation-1, mentre dal punto di vista qualitativo di mappe a colori di velocità e streamlines, i risultati delle due simulazioni si sono rivelati molto simili.

Complessivamente entrambe le soluzioni hanno portato a risultati che sono stati trovati in buon accordo con i dati grezzi *4D flow*, e nonostante l'aumento di 18 mmHg nella pressione media imposta agli outlet sovra-aortici in Simulation-2, solo una minima differenza è stata osservata tra le differenze di pressione trans-coartazione calcolate dalle due simulazioni.

Validazione dei risultati di 4DF-FEPPE

Nel caso paziente-specifico in questione, da Simulation-1 sono stati ottenuti un Δp_m di 22.43 mmHg e un Δp_{pp} di 16.85 mmHg, mentre un Δp_m di 23.89 mmHg e un Δp_{pp} di 18.56 mmHg sono stati ottenuti da Simulation-2. Le differenze di pressione calcolate con 4DF-FEPPE utilizzando i dati grezzi di *4D flow* hanno portato a valori picco-picco e massimi più bassi di 1 mmHg e 2.8 mmHg rispetto ai risultati di Simulation-2. Rispetto ai risultati di Simulation-1 le differenze di pressione picco-picco e massima si sono rivelate più bassa di 1.34 mmHg e più alta di 0.75 mmHg rispettivamente. In questo caso l'applicazione del filtro DFW sui campi di velocità misurati da *4D flow* ha portato a risultati significativamente peggiori in termini di confronto con i risultati delle simulazioni. In particolare le velocità processate con il DFW hanno portato a differenze di pressione trans-coartazione più basse di più di 5 mmHg. Dunque, nonostante il DFW abbia permesso una riduzione del rumore, è risultato inefficace nel migliorare la stima di differenza di pressione trans-coartazione. Per quanto riguarda il dataset sintentico precedentemente discusso, l'aggiunta di rumore artificiale ha portato a velocità complessivamente più alte, che sono state smussate e ridotte dal filtro DFW, risultando in un confronto migliore col dato di partenza. L'aumento nei valori di velocità dovuto all'aggiunta del rumore si è rivelato poco accurato nel replicare il rumore realmente osservato nelle immagini di velocità *4D flow*.

La messa a punto della piattaforma idraulica ha permesso di validare ulteriormente i risultati di 4DF-FEPPE e di confermarne l'accuratezza. Nonostante le misure di Δp prese dai trasduttori di pressione siano diverse dai risultati di 4DF-FEPPE di valori da 0.37 mmHg a 4.5 mmHg, tali misure sono state effettuate su un modello rigido con flusso stazionario. Queste semplificazioni portano inevitabilmente a delle incertezze sulle differenze di pressione misurate. Da un lato la rigidezza delle pareti dovrebbe condurre a differenze di pressione più alte, come è ben noto nelle applicazioni vascolari [9, 19]; d'altro canto l'imposizione di una portata stazionaria nel tempo porta a trascurare il contributo degli effetti transienti sul Δp totale [114].

Conclusioni

In conclusione il lavoro svolto in questa tesi ha permesso di dimostrare come un approccio basato sul *4D flow MRI*, validato con metodologie *in silico* e *in vitro* è stato in grado di fornire una valutazione non invasiva e accurata della severità di coartazioni dell'aorta e dell'emodinamica coinvolta. Lo strumento sviluppato permette anche agli operatori insesperti di ottenere, in pochi minuti, le distribuzioni di pressione 4D da immagini di *4D flow* in qualsiasi regione di interesse. Questo algoritmo è stato progettato con lo scopo di supportare i clinici nella diagnosi non invasiva e precoce della CoA, una patologia in cui la differenza di pressione a cavallo del restringimento è un fattore diagnostico di fondamentale importanza.

Abstract

Clinical background

Coarctation of the aorta (CoA) is a congenital heart disease (CHD) characterized by a narrowing of the aorta. The narrowed aortic wall represents an abnormal impedance to flow, thus forcing the left ventricle to generate a higher pressure to provide sufficient blood flow through the aorta. Consequently, pathologic features include cardiac hypertrophy, degenerative changes in the proximal aorta and increased blood pressure in the upper part of the body [1].

The most distinguishing diagnostic factor to determine the functional severity of CoA is the trans-coarctation peak-to-peak pressure drop [4, 5]. While cardiac catheterization is considered the gold standard to invasively assess pressure differences across a coarctation, such technique involves the introduction of a pressure transducer through a catheter and is often advised against. Therefore, an early non-invasive and accurate estimation of the trans-coarctation pressure drop would significantly improve CoA diagnosis and treatment pre-planning.

To date, computational fluid dynamics (CFD) and fluid-structure interaction (FSI) studies have been widely used to analyze blood flow and evaluate pressure drops associated with a coarctation non-invasively [6, 7]. Despite providing arbitrarily high levels of spatial and temporal detail, numerical simulations are computationally expensive, time consuming and their accuracy hinges on modeling assumptions.

With recent advancements in acquisition sequences, 4D phase-contrast magnetic reso-

nance imaging (also referred to as 4D flow MRI or 4D flow) provides both tissue morphological information and volumetric, temporal and 3-directional velocity measurements. This technique enjoys the advantages of MRI, such as the use of non-ionizing radiations, and takes advantage of the magnetic properties of hydrogen ions to induce a phase-shift on their magnetic spins which is proportional to their velocity. According to the direction of external imposed magnetic field gradients, blood flow velocities along a specified direction can be measured. 4D flow MRI has been used to extract hemodynamic parameters of interest such as flow rates, wall shear stress (WSS) and pressure [8]. In particular, pressure differences *in vivo* can be estimated from 4D flow images by solving the Poisson pressure equation (PPE) derived from the Navier-Stokes equations:

$$-\Delta p = \nabla \cdot \left[\rho \left(\frac{\partial \boldsymbol{v}}{\partial t} + \boldsymbol{v} \cdot \nabla \boldsymbol{v} - g \right) - \mu \Delta \boldsymbol{v} \right],$$

where pressure (p) is derived explicitly as a function of the velocity field ($\boldsymbol{v}$) and its derivatives, with ρ and μ being blood density and viscosity.

In the context of CoA, the main goal of the present work was to assess the feasibility and reliability of pressure estimation based on 4D flow MRI. In this work, an algorithm referred to as 4DF-FEPPE was developed in MATLAB to solve the PPE from 4D flow data taking advantage of the finite element method. First, a CFD simulation on an idealized aortic geometry was carried out; its results were used to generate a synthetic 4D flow dataset against which 4DF-FEPPE performance was benchmarked and its results validated. Then, 4D flow-based pressure calculated from 4D flow images of a CoA patient were validated against both *in silico* and *in vitro* methodologies. The numerical simulations carried out in this thesis accounted for vessel wall displacement using a coupled momentum method for fluid-solid interaction (CMM-FSI) recently formulated in [9]. The developed experimental apparatus comprised a 3D printed model of the aorta at issue connected to a centrifugal pump and pressure transducers.

Materials and Methods

4D flow-based pressure estimation

In order to solve the PPE from 4D flow MRI data, a finite element framework was implemented in MATLAB. A region of interest (ROI) was segmented from 4D flow images using a previously developed MATLAB tool, and a 3D surface extracted from magnetic resonance angiographic (MRA) images was co-registered to 4D flow data. Then, a finite element voxel-based mesh was built within the ROI (Figure 17). Mesh cells were 8-node hexahedral elements, whose dimensions corresponded to the acquired voxel spacings. Adopting an isoparametric formulation, element Lagrangian shape functions and their derivatives were defined, and through a 2-point Gauss integration element matrices were calculated and assembled.

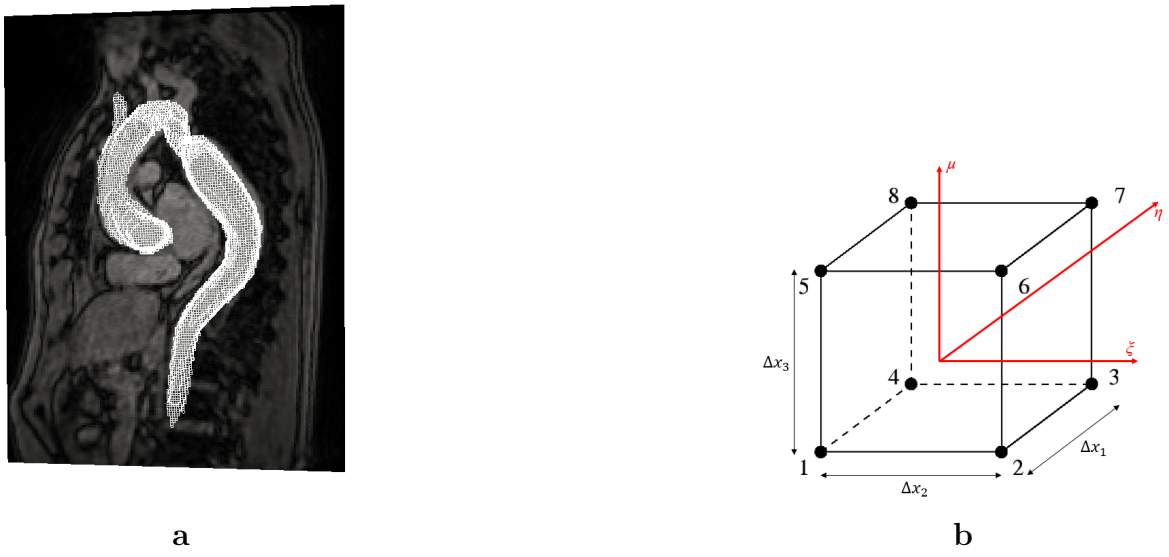

Figure 17: Finite element mesh over a slice of the acquired image volume (a), and representation of the 8-node hexahedron with its natural coordinates (b).Δx_1 Δx_2 Δx_3 represent the pixel spacings associated with the images.

To solve the PPE, first and second spatial velocity derivatives were calculated from 4D flow velocities using various combinations of finite difference schemes. First order derivatives were approximated by 4^{th} and 3^{rd} order schemes, while second order derivatives were approximated using 4^{th}, 3^{rd} and 2^{nd} order schemes. The decrease in order of accuracy was forced by the dependency on neighboring nodes of higher order schemes. Time derivative

were computed using 2nd or 1st order finite differences.

The finite element solution of the PPE (FE-PPE) required boundary conditions to be imposed on one or more nodes in the domain. In 4DF-FEPPE, zero pressure was imposed on the lowest point in the descending aorta for all time steps: 4D pressure differences were hence calculated with respect to this reference point.

In order to validate and benchmark 4DF-FEPPE, a synthetic dataset was obtained from a CFD simulation run with Fluent using a transient velocity inlet boundary condition (Figure 18). In this simulation, zero-pressure was imposed on all outlets.

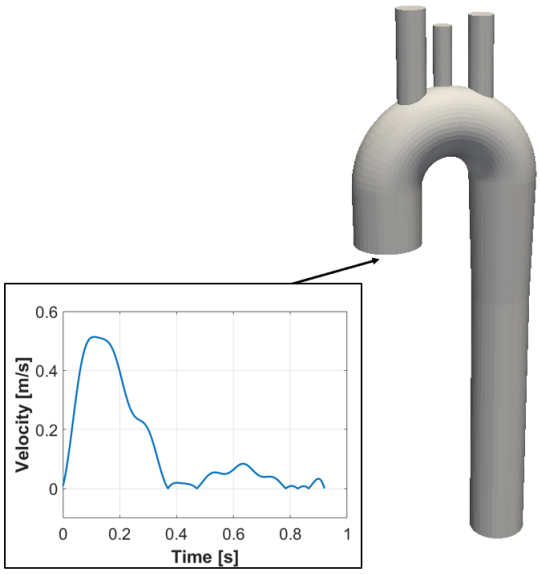

Figure 18: Idealized 3D model of healthy aorta used for a CFD simulation whose results were exported to generated a synthetic dataset. The average velocity imposed at the inlet is shown in as a blue waveform.

Artificial 4D flow datasets were obtained following the methodology described in [10] using in-house software. Velocities and Cartesian coordinates were exported from the simulation results and velocity fields were spatially and temporally downsampled to mimic typical 4D flow resolutions; in particular, six time points were exported from the CFD simulation results. In order to reproduce noise observed in 4D flow images, Gaussian noise exceeding the maximum velocity in the domain by 5% was added to the downsampled velocity fields (Figure 19).

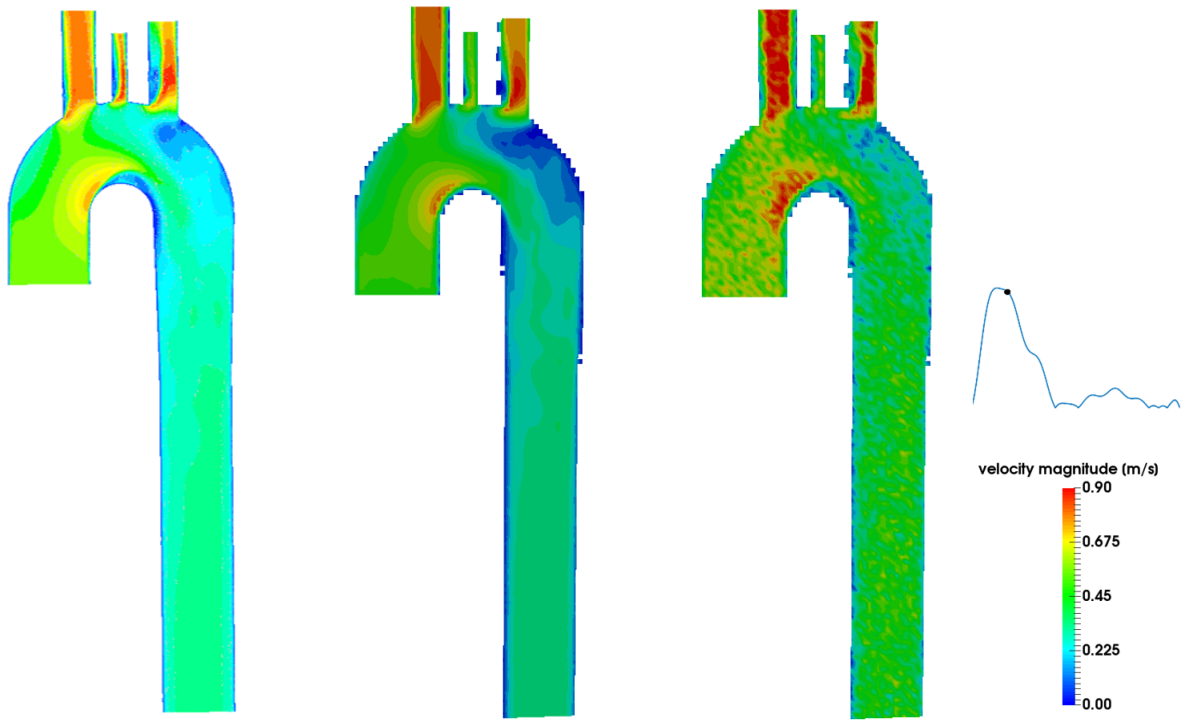

Figure 19: Effect of downsampling (b) and noise addition (c) on the original velocity field obtained from Fluent (a).

Moreover, the effects of a divergence-free wavelet (DFW) filter presented in [11] were evaluated in terms of velocity fields and pressure distributions. Such filter allows to separate a velocity field in divergence-free and non-divergence-free components, reducing the two components contributions to enforce a soft divergence-free condition on the original velocity fields. Therefore, 4DF-FEPPE was tested using three different kinds of velocity inputs: downsampled velocities, noisy downsampled velocities and DFW-processed velocities. 4DF-FEPPE results and performance were then compared to a similar previously developed code.

Finally, 4DF-FEPPE was applied to a 4D flow dataset of a CoA patient consisting of 21 frames and its results were validated against two numerical simulations and an experimental test bench.

Numerical simulations

Two numerical simulations were run on the same patient-specific geometry using the

open-source software CRIMSON. These simulations accounted for both hemodynamics and linearized wall mechanics. The patient-specific flow rate extracted from 4D flow was imposed at the inlet, while to account for the effect of distal vasculature and obtain physiological flow rate and pressure curves, outlet boundary conditions were represented by 3-element Windkessel models (3-WK) (Figure 20). In both simulations, arterial wall mechanical properties were modeled as linear elastic, with a Young's modulus of 878000 Pa, thickness of 1 mm and Poisson's ratio of 0.5 [12]. Blood was modeled as a Newtonian fluid with dynamic viscosity of 4 cP and density of 1060 kg/m^3.

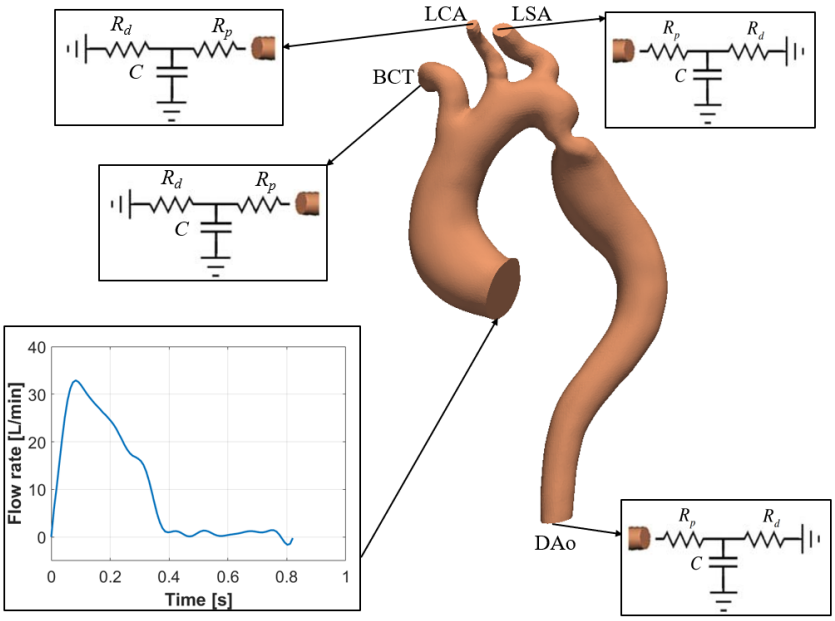

Figure 20: Description of the model boundary conditions used in the numerical simulations; the patient-specific transient flow rate was imposed at the inlet, while 3-WK were set as outlet boundary conditions for the brachiocephalic trunk (BCT), left carotid artery (LCA), left subclavian artery (LSA) and descending aorta (DAo).

The 3D geometry was extracted from MRA images using the open-source software ITK-SNAP. The exported surface was then pre-processed using Autodesk Meshmixer and imported in CRIMSON to be meshed. The mesh consisted of ∼4m elements and was made of tetrahedral elements with a boundary layer (Figure 21).

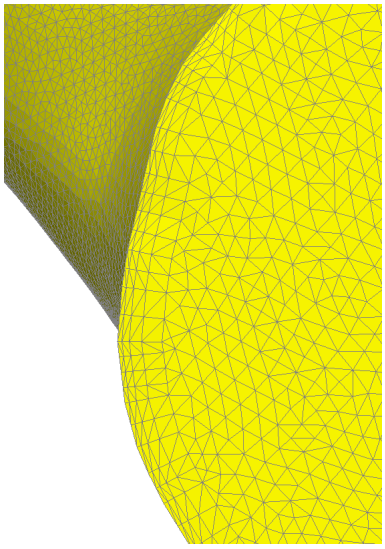

Figure 21: Visualization of mesh details in a zoomed in screenshot of the aortic inlet.

3-WK parameters for outlet boundary conditions were calculated according to [15]. Briefly, for each outlet an average pressure over the cardiac cycle $\overline{P}$ was assumed and flow rate curves were extracted from 4D flow data. Then, the proximal (R_p) and distal (R_d) resistances were calculated together with the compliance (C) using the relationships introduced in [16], [17] and [18].

The two simulations carried out in this study differed by 3-WK parameters at the supra-aortic branches. In Simulation-1 a mean pressure $\overline{P} = 80$ mmHg was used to tune 3-WK for the descending aorta outlet (DAo) and the three supra-aortic branches. In Simulation-2 the mean pressure used to tune 3-WK in the three supra-aortic branches was increased by 18 mmHg, while a mean pressure of 80 mmHg was used to tune 3-WK at the DAo. The 18 mmHg increase at the aortic branches corresponded to an estimation of the maximum trans-coarctation pressure drop obtained from Simulation-1 results. Simulation-2 was carried out to evaluate the sensitivity of the trans-coarctation pressure drop to the mean pressure used to tune outlet 3-WK models at the supra-aortic outlets. 3-WK parameter values for the two simulations are reported in Table 4. Both simulations were validated against raw 4D flow data in terms of flow rate curves through the outlets, velocity magnitude contours and streamlines along the descending aorta. Once the accuracy of both simulations was confirmed by comparison with raw 4D flow data, both

simulations results were compared to 4DF-FEPPE results in terms of trans-coarctation pressure drops for the purpose of validating the developed algorithm for 4D flow-based pressure estimation.

		R_p	C	R_d
BCT	Simulation-1	0.0294	12.1872	0.1281
	Simulation-2	0.0294	9.2751	0.1635
LCA	Simulation-1	0.0872	1.2950	1.3955
	Simulation-2	0.0872	0.9855	1.7291
LSA	Simulation-1	0.0418	3.7653	0.4682
	Simulation-2	0.0418	10.0218	0.1583
DAo	Simulation-1	0.0203	10.0218	0.1583
	Simulation-2	0.0203	10.0218	0.1583

Table 4: Windkessel parameter values used in Simulation-1 and Simulation-2: proximal resistance R_p, compliance C and distal resistance R_d for the brachiocephalic trunk (BCT), left carotid artery (LCA), left sublavian artery (LSA) and descending aorta (DAo). Resistances are expressed in g/(mm^4·s), while compliances are expressed in mm^4·s^2/g.

In vitro analysis

To further validate *in vivo* 4D flow-derived pressure estimations, a hydraulic test bench was set up. The three supra-aortic vessels were removed from the 3D geometry and five ports were created along the aorta to allow for pressure transducers to be connected (Figure 22).

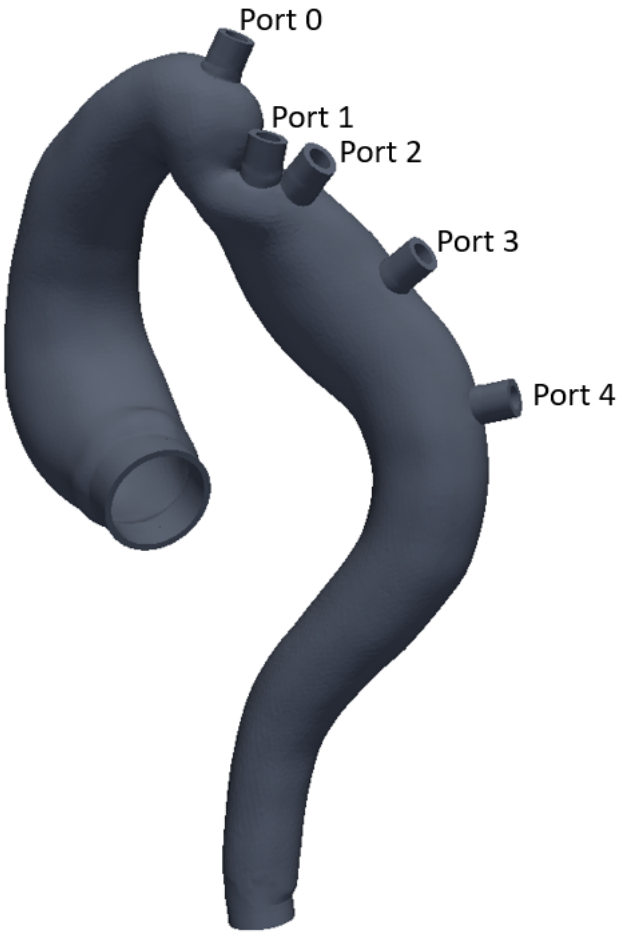

Figure 22: Modified 3D model with ports.

The model in Figure 22 was printed in 3D and connected to a centrifugal pump, an atmospheric pressure reservoir and piezoelectric pressure transducers (Figure 23). Three steady flow tests were conducted, one where a flow rate corresponding to the 4D flow-derived peak flow rate through the DAo (referred to as Q) was imposed by the pump, and the other two with $0.9Q$ and $1.1Q$.

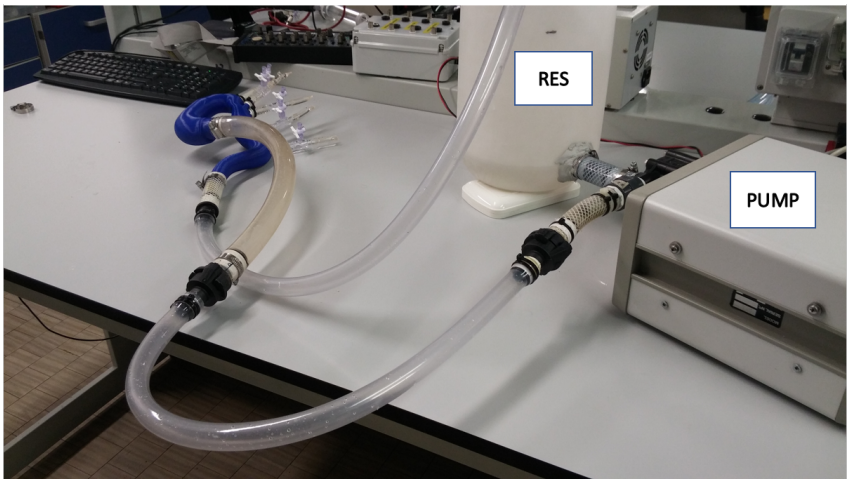

Figure 23: Platform configuration with the atmospheric pressure reservoir (RES) and centrifugal pump (PUMP).

Results

4D flow-based pressure estimation

In order to evaluate the effects of velocity downsampling and noise addition on pressure estimation, 4DF-FEPPE was tested using three kinds of velocity fields as input. First, pressure distributions were calculated using CFD-derived downsampled velocities without noise. Then the effect of Gaussian noise addition on pressure estimation was evaluated by using noisy downsampled velocity fields as input for the 4DF-FEPPE. Finally, pressure fields were calculated using noisy velocity fields preprocessed with the DFW filter. The effect of downsampling, noise addition and DFW processing for one systolic time point is shown in Figure 24, while pressure difference fields are shown in Figure 25. In 4DF-FEPPE results all pressure values are differences with respect to the lowest point in the descending aorta, where pressure is set to zero at all time points.

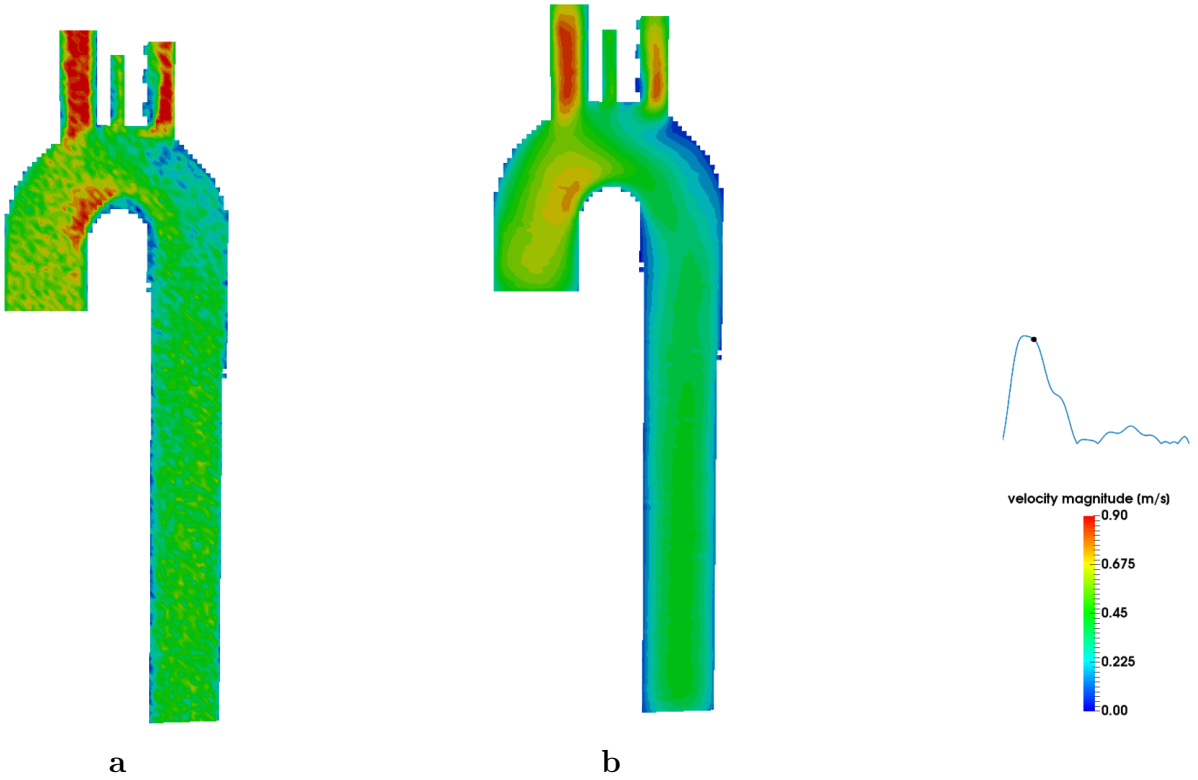

Figure 24: Effect of DFW filter on a synthetically generated noisy velocity field; before (a) and after (b) filtering.

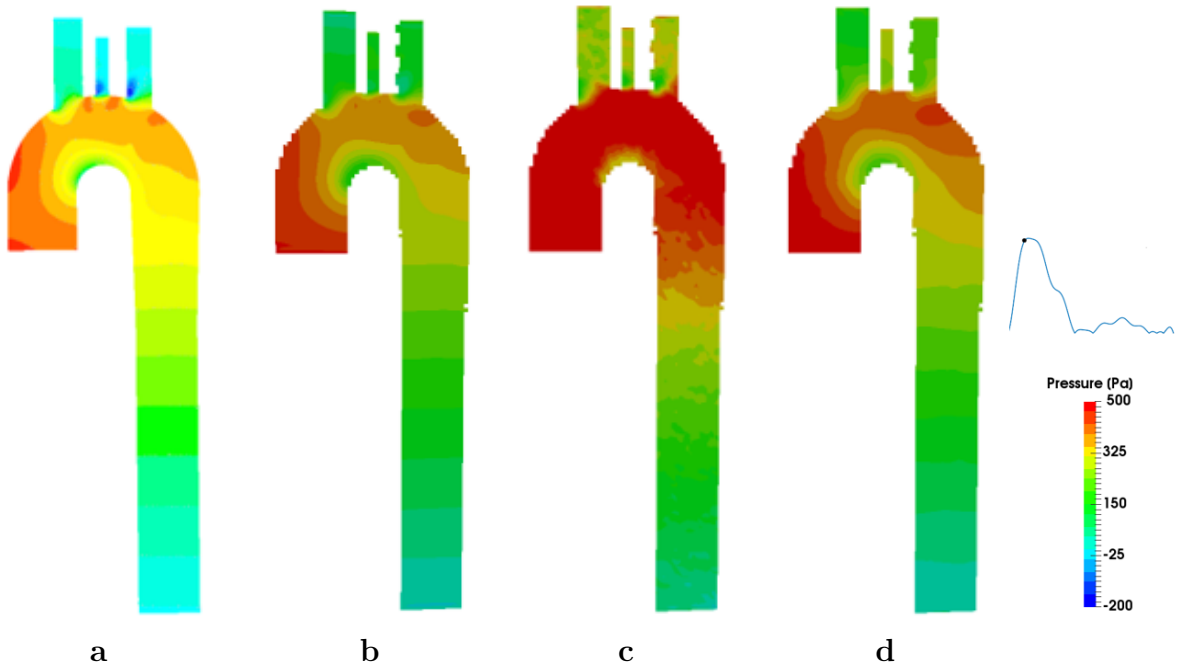

Figure 25: Pressure comparison between Fluent results (a) and FE-PPE solution using as input: downsampled velocities (b), downsampled velocities with added Gaussian noise (c) and downsampled velocities with noise preprocessed with a DFW filter (d).

4DF-FEPPE results were in good agreement with CFD-based pressure fields when downsampled velocity fields were used as input, with space-averaged pressures differing by 197 Pa at most. When noisy velocity fields were used as input for 4DF-FEPPE, pressure distributions did not resemble the CFD solution as well as in the previous case, with space-averaged pressures differing by up to 278 Pa. When DFW-processed velocity fields were used as 4DF-FEPPE input, pressure distributions were in better agreement with CFD data, with average pressure values differing by 137 Pa at most. Space-averaged pressure values with standard deviations are shown in Figure 26.

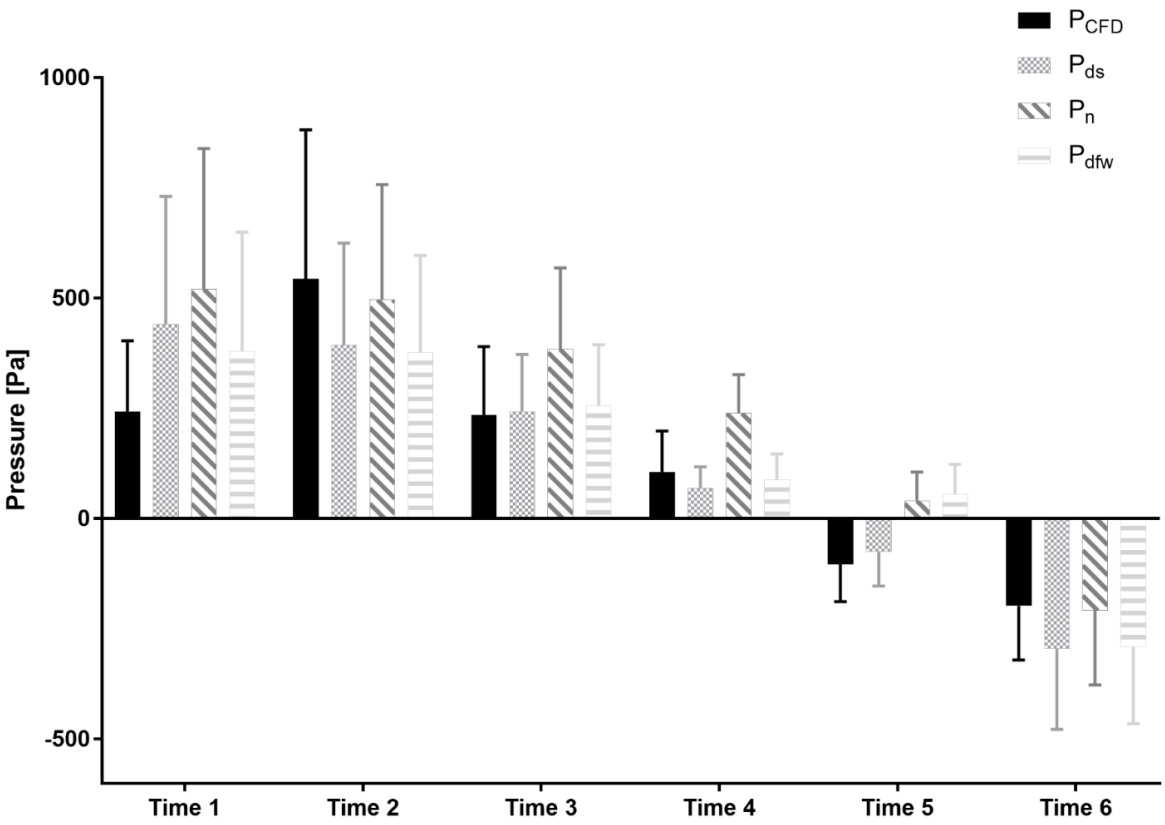

Figure 26: Mean pressure values with standard deviation obtained with the CFD simulation (P_{CFD}) and mean pressure differences with respect to the lowest point in the descending aorta with standard deviation obtained with 4DF-FEPPE using downsampled velocities (P_{ds}), downsampled velocities with Gaussian noise (P_n) and downsampled velocities with Gaussian noise preprocessed with a DWF filter (P_{dfw}).

The addition of Gaussian noise resulted in an overestimation of velocities with respect to the downsampled case. In particular, average velocity magnitudes after noise addition were higher than downsampled values by 199% for Time 1, and by at least 30% for all

other time points. On the other hand, application of the DFW filter decreased average noisy velocity fields at all time points, resulting in space-averaged velocity magnitudes that were higher than downsampled velocities by less than 15% for all time points except for Time 1.

In the patient-specific case of CoA, 4DF-FEPPE produced results that resembled pressure distributions typically observed in CoA patients, with a clear pressure difference between regions proximal and distal to the narrowing (Figure 27).

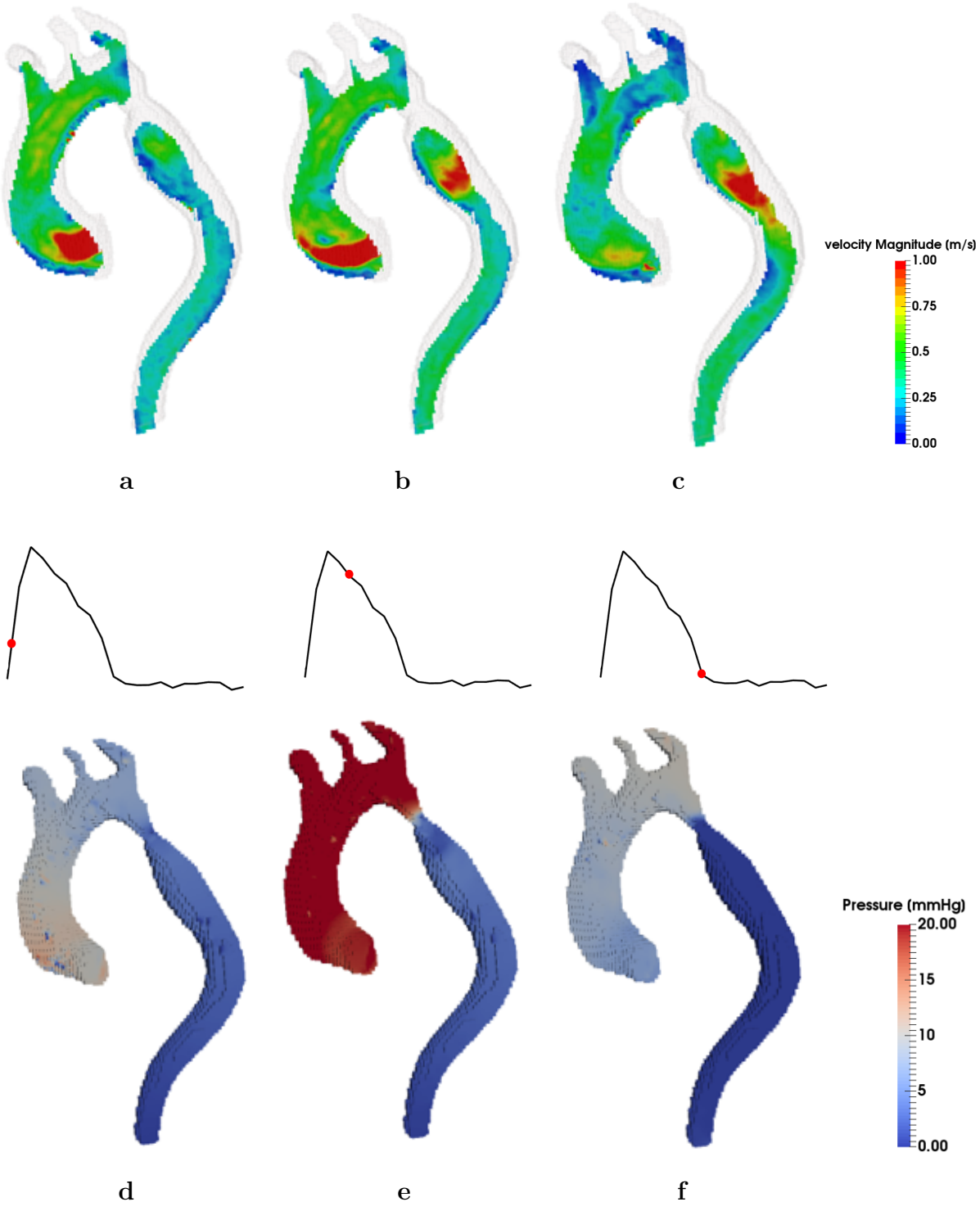

Figure 27: Velocity contours extracted from 4D flow MR images (a-c) and pressure difference maps calculated using 4DF-FEPPE (d-f).

A peak-to-peak trans-coarctation pressure drop (Δp_{pp}) of 17.6 mmHg was obtained, while the maximum pressure drop (Δp_m) was found equal to 21.09 mmHg (Figure 28).

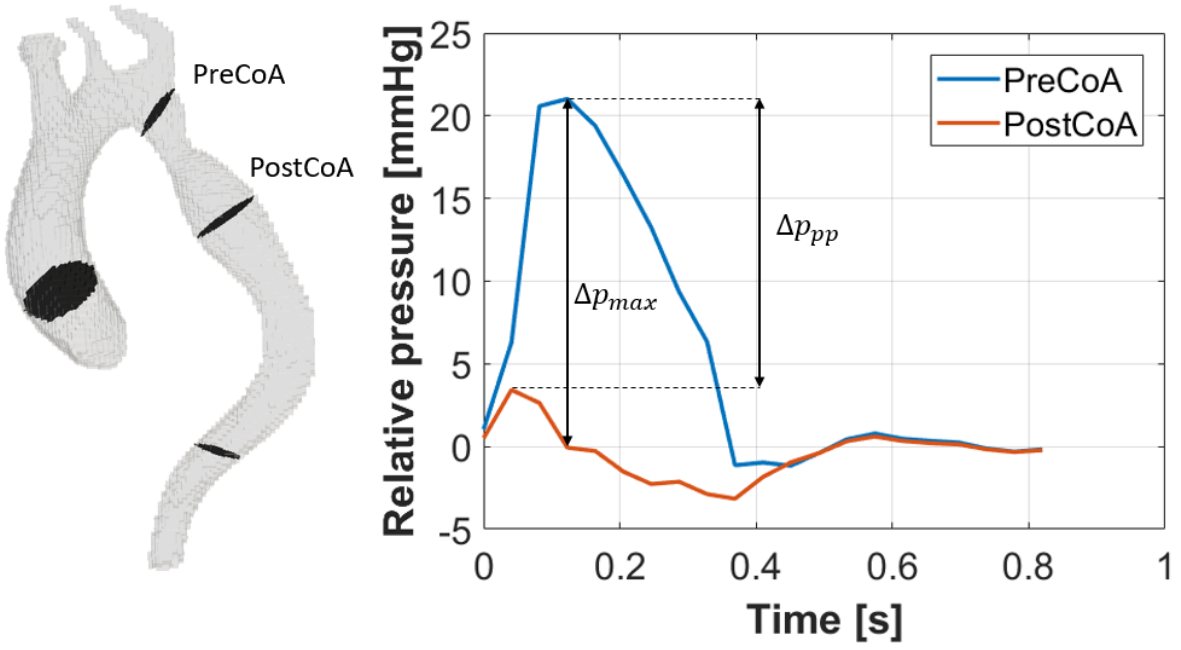

Figure 28: Cross-section averaged pressure differences over time on planes proximal (PreCoA) and distal (PostCoA) to the coarctation.

Application of the DFW filter allowed for efficient denoising of raw 4D flow velocity fields, but resulted in a systematic velocity reduction, with a percent error of -21.3% on average, calculated as:

$$error = \frac{\overline{v}_{dfw} - \overline{v}_{raw}}{\overline{v}_{raw}} \cdot 100,$$

where $\overline{v}_{dfw}$ is the DFW-processed space-averaged velocity and $\overline{v}_{raw}$ the unprocessed 4D flow average velocity. Consequently, the trans-coarctation Δp_{pp} was reduced to 12.9 mmHg after DFW application.

Numerical simulations

The two numerical simulations herein reported were validated both quantitatively and qualitatively against raw 4D flow data, in terms of velocity contour comparison and flow rate distributions (Figure 29). Average flow rates through the outlets are reported in Table 5. Both simulations results were in good agreement with raw 4D flow data, with only a slight underestimation of the flow rate peak and a greater diastolic flow rate in

DAo. More specifically, peak flow rate through the DAo were 1.43 L/min and 0.83 L/min lower than 4D flow data for Simulation-1 and Simulation-2 respectively.

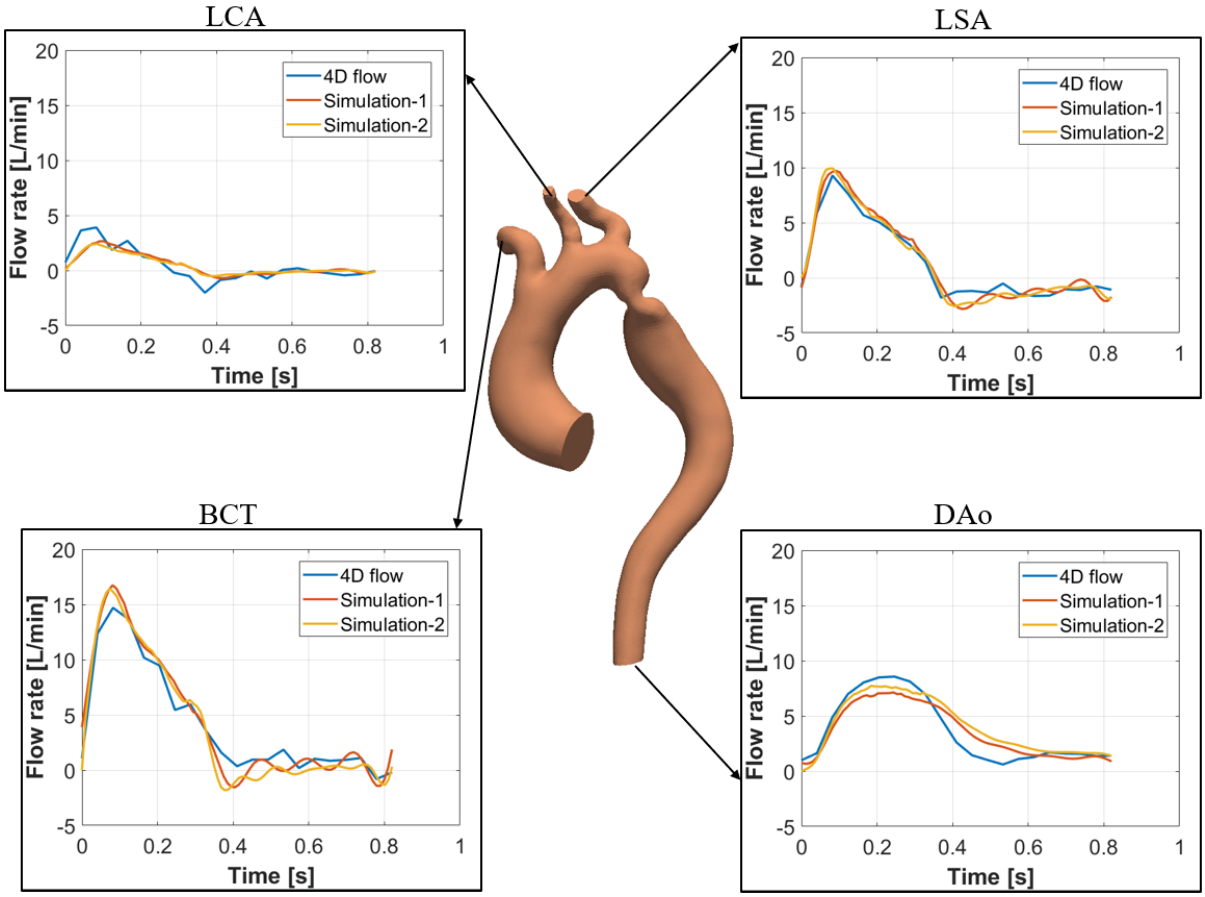

Figure 29: Flow rates over time compared between 4D flow data, Simulation-1 and Simulation-2 results.

Outlet	$\overline{Q}_{4Dflow}$	$\overline{Q}_{Simulation-1}$	$\overline{Q}_{Simulation-2}$
BCT	4.06	4.22	3.93
LCA	0.43	0.48	0.44
LSA	1.26	1.52	1.35
DAo	3.58	3.55	4.05

Table 5: Time averaged flow rates comparison between 4D flow data, Simulation-1 and Simulation-2 for the brachiocephalic trunk (BCT), left carotid artery (LCA), left subclavian artery (LSA) and descending aorta (DAo). All values are expressed in L/min.

Once the simulations were validated, their pressure results were compared to 4D flow-derived pressures obtained with 4DF-FEPPE. This comparison was performed to validate the results of the developed algorithm. Trans-coarctation Δp_{pp} obtained from Simulation-1 was equal to 16.86 mmHg, while a Δp_m of 22.43 mmHg was found. In Simulation-2

trans-coarctation Δp_{pp} was equal to 18.56 mmHg, while a Δp_m of 23.89 mmHg was found.

Overall, 4D flow-derived pressure differences were in good agreement with numerical simulations results, showing only a slight underestimation of pressure drops by 4DF-FEPPE. In Figure 30 trans-coarctation pressure drops obtained with Simulation-1 and 4DF-FEPPE are shown together with the relative error calculated as: $error = \left|\frac{\Delta p_{simulation} - \Delta p_{4Dflow}}{\Delta p_{simulation}}\right|$. Similarly, Figure 31 shows pressure drops obtained with Simulation-2 and 4DF-FEPPE with the relative error.

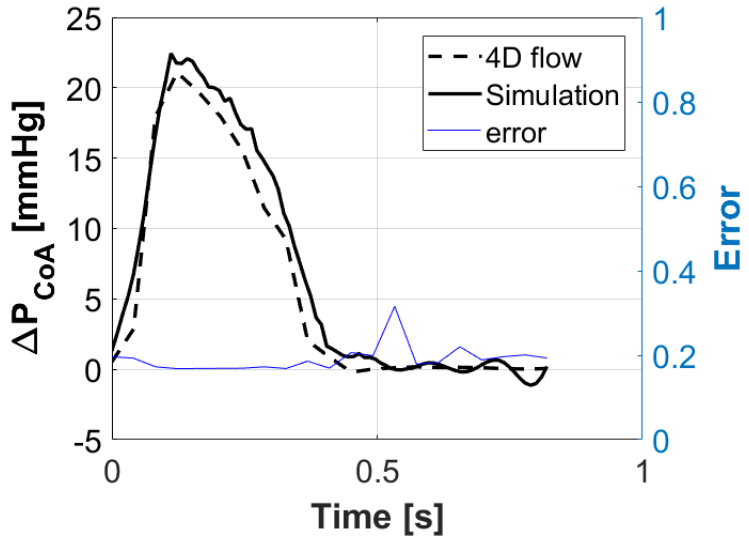

Figure 30: Plane averaged pressure difference across the coarctation: 4D flow-based curve calculated with 4DF-FEPPE vs. Simulation-1 results. Relative error is plotted as a blue line.

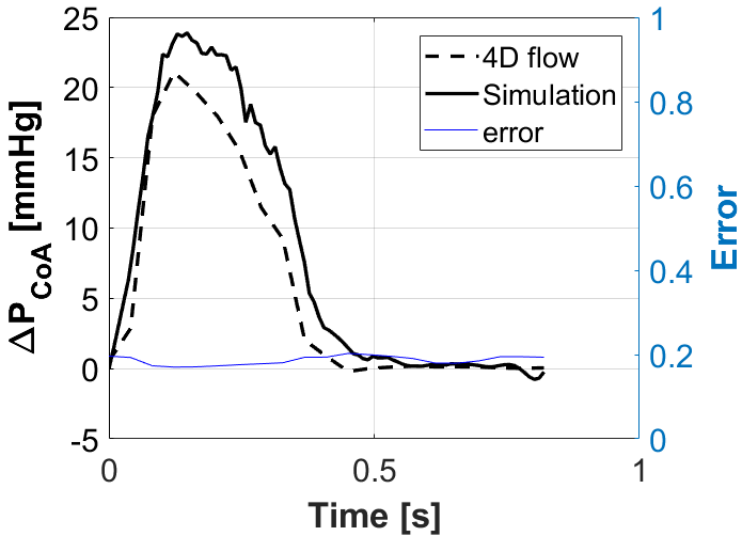

Figure 31: Plane averaged pressure difference across the coarctation: 4D flow-based curve vs. Simulation-2. Relative error is plotted as a blue line.

In vitro analysis

Pressure measurements taken *in vitro* by pressure transducers were compared to maximum pressure drops obtained with both numerical simulations and 4DF-FEPPE results on corresponding cross-sections (Figure 32). All Δp values in Table 6 were calculated as differences with respect to pressure at Port 1 in the *in vitro* case, and with respect to section PRE in the *in silico* case (Figure 32). Results are reported for the three steady flow rates tested: $Q_{low} = 0.9Q$,$Q = 8.56$L/min and $Q_{high} = 1.1Q$ (Table 6). Δp_1, Δp_2, Δp_3 and Δp_4 calculated with 4DF-FEPPE differed from test bench measurements using Q by 1 mmHg, 0.37 mmHg, 4.5 mmHg and 2.8 mmHg respectively; while Simulation-1 produced results that overestimated *in vitro* measurements by 1 to 4.3 mmHg and Simulation-2 pressure differences were higher than measurements by up to 6.4 mmHg.

a **b**

Figure 32: 3D model used in the *in vitro* setup with ports for pressure transducers (a) and corresponding cross-sections in the computational domain (b) (referred to as S1-S4).

	Δp_1 [mmHg]	Δp_2 [mmHg]	Δp_3 [mmHg]	Δp_4 [mmHg]
in vitro (Q_{low})	14.6	13.7	13.6	14.5
in vitro (Q)	19.4	20.73	16.6	16.8
in vitro (Q_{high})	23.6	23.2	23.5	21.6
Simulation-1	21.5	21.8	20.9	19.7
Simulation-2	22.7	23.1	23	21
4DF-FEPPE	20.4	21.1	21.1	19.6

Table 6: Pressure differences measured *in vitro* and calculated with Simulations 1 and 2 and 4DF-FEPPE. All Δp values are pressure differences between Port 1 (or section PRE) and a certain Port (or section) identified by the subscript.

Discussion and Conclusions

In this thesis, the feasibility and reliability of 4D flow-based pressure difference estimation was assessed. For this purpose, the algorithm 4DF-FEPPE was developed and its results were validated against both numerical simulations and a hydraulic *in vitro* model. The developed algorithm proved to be extremely efficient compared to a previously developed code, allowing to calculate pressures in less than five minutes for a 21-frame 4D flow dataset.

4D flow-based pressure estimation

Pressure comparison performed between 4DF-FEPPE and a CFD simulation results enabled to validate and benchmark the proposed workflow against CFD-derived data taken as ground truth. Overall, 4DF-FEPPE proved to be able to capture pressure distributions with high accuracy, mismatching CFD-based space-averaged pressures by no more than 3 mmHg even when noise was added to the velocity fields. Furthermore, the methodology implemented in this work proved to be extremely efficient: keeping the computational time as short as possible is of critical importance in order to translate 4D flow-based pressure estimation in clinical diagnosis.

For what concerns the idealized model used to validate and benchmark 4DF-FEPPE, the addition of Gaussian noise resulted in velocity fields whose values were systematically higher than downsampled velocities. In this context, the application of DFW led to velocities that were lowered by 48% on average with respect to the noisy case. Therefore, the tendency of the noise addition process to increase velocity values, together with the lowered velocities resulting from the DFW application, led to DFW-processed pressure distributions that were in better agreement with CFD-derived values (Figures 25 and 26). Pressure fields calculated with the proposed algorithm showed distributions typically observed in CoA patients. In the reported patient-specific case, the use of the DFW filter allowed for efficient denoising of the raw 4D flow data while retaining the observed fluid structures. However, the resulting space-averaged velocity magnitude values were consistently lower than unprocessed data by up to 30%, which, near the coarctation, led to a decreased jet velocity magnitude, in turn associated with a Δp_{pp} lowered by 5 mmHg. The tendency of the DFW filter to lower velocity values was observed to similar extent in the synthetically generated dataset. Nevertheless, as previously discussed, artificial noise addition resulted in velocity fields whose values were significantly higher than the downsampled non-noisy case, whereas actual 4D flow noise does not have such an effect on velocity fields.

Numerical simulations

The two numerical simulations herein reported differed in 3-WK parameter values at the supra-aortic branches outlets. More specifically, while in Simulation-1 the same mean pressure (80 mmHg) was assumed at all outlets to tune the 3-WKs, in Simulation-2 the mean pressure for the 3-WKs at the branches was increased by an estimation of the peak-to-peak pressure drop observed from Simulation-1 results. Since no information about the patient's pressure was available, in Simulation-1 the same mean pressure for tuning all 3-WK was assumed. However, in the context of CoA this assumption could be regarded as unrealistic, and in order to evaluate the effect of this assumption on the coarctation pressure drop, Simulation-2 was carried out.

In both simulation setups, vessel wall mechanical behavior was assumed to be homogeneous, linear elastic and isotropic. The choice of using values from [12] was the result of a trial and error process; different combinations of elastic moduli and thicknesses were tested, but they all produced worse results compared to 4D flow data in terms of flow rate distributions and velocity magnitude contours.

In Simulation-1 assuming the same mean pressure for 3-WK tuning led to good agreement between flow rates from 4D flow data and simulation results in the supra-aortic branches, with a maximum difference in mean flow rate of 0.26 L/min in the LSA, corresponding to 21% of the 4D flow flow rate. In Simulation-2 the 18 mmHg increase in mean pressure used to tune 3-WK at the supra-aortic vessels led to a higher flow rate through the DAo with respect to Simulation-1, while very similar qualitative results were obtain in terms of velocity contours and streamlines.

Overall, both simulations produced results that were in good agreement with raw 4D flow velocity data, and despite the 18 mmHg increase in mean pressure at the branches outlets of Simulation-2, pressure drops across the coarctation differed slightly between the two simulations.

Validation of 4DF-FEPPE results

In the patient-specific case at issue, a Δp_m of 22.43 mmHg and a Δp_{pp} of 16.85 mmHg were obtained with Simulation-1, while a Δp_m of 23.89 mmHg and a Δp_{pp} of 18.56 mmHg were obtained with Simulation-2. 4DF-FEPPE-derived pressure drops obtained with raw 4D flow data as input tended to slightly underestimate maximum and peak-to-peak values by 1 mmHg and 2.8 mmHg respectively compared to Simulation-2 results. Compared to Simulation-1 results, 4DF-FEPPE-derived maximum and peak-to-peak pressure drops were 1.34 mmHg lower and 0.75 mmHg higher respectively. Application of the DFW filter on the 4D flow velocity fields led to significantly worse results in terms of pressure drops compared to simulations results. In particular, DFW-processed velocity fields led to maximum and peak-to-peak pressure drops that were lower than both simulation results by more than 5 mmHg. Thus, despite achieving efficient denoising of the raw 4D flow data, the use of the DFW filter was ineffective in improving trans-coarctation pressure drops. For what concerns the synthetic dataset previously discussed, the addition of artificial noise led to overall higher velocities that were smoothed and lowered by the DFW filter, thus producing better results. The increase in velocity values due to noise addition was not accurate in replicating the actual noise affecting 4D flow velocity fields.

The setup of the experimental hydraulic test bench allowed to further validate 4DF-FEPPE results and confirm its accuracy. In fact, despite Δp measurements performed with pressure transducers differed from 4DF-FEPPE results by 0.37 to 4.5 mmHg, *in vitro* measurements were taken in a rigid model with a steady flow rate. This simplification leads to uncertainties on the measured trans-coarctation pressure drop. On one hand, rigid walls should theoretically lead to higher pressure difference, as stiffer vessels experiencing higher pressure drops are a well-known phenomenon in vascular applications [9, 19]. On the other hand, imposing a steady flow rate implies neglecting transient effects which contribute to the total pressure drop [114].

Conclusions

In conclusion, the proposed workflow showed how an image processing approach based

on 4D flow MRI combined with *in silico* and *in vitro* methodologies allows to produce accurate non-invasive assessment of CoA severity and hemodynamics. The developed tool enables even unexperienced users to obtain, in a few minutes, 4D vascular pressure distributions from 4D flow images of any district of interest. This algorithm was designed with the purpose of aiding clinicians to obtain early non-invasive pressure difference estimation for patients with CoA, a disease in which the pressure drop across the narrowing is a major diagnostic factor.

Chapter 1

Clinical background and main objectives

In this chapter, aortic coarctation pathophysiology, diagnostic methodologies and treatment approaches are briefly described to provide a general understanding of this disease. The second part of the chapter is dedicated to 4D flow magnetic resonance imaging with an emphasis on some of its applications in the field of hemodynamic measurements. Finally, several recent numerical studies on aortic coarctation will be briefly presented.

1.1 Aortic coarctation

1.1.1 Anatomy and pathophysiology

In recent years, cardiovascular diseases have been the leading cause of death in the Western world [20]. Among these, congenital heart defects (CHDs) are estimated to affect about 1'000'000 people in the United States alone [20]. CHDs are the most common type of birth defects and their incidence varies, depending on the study, from 0.4% to 5% of all live births causing 45% of deaths for infants aged less than 1 year [21]. Aortic coarctation (CoA) accounts for up to 8% of all CHDs [22, 23] and affects approximately 0.1% of all newborns [24], with a male to female predominance ratio of 2:1 [25]. This disease is characterized by a narrowing of the aorta, which, in most cases, is situated just downstream of where the supra-aortic vessels branch off to convey blood to the brain and upper limbs [26].

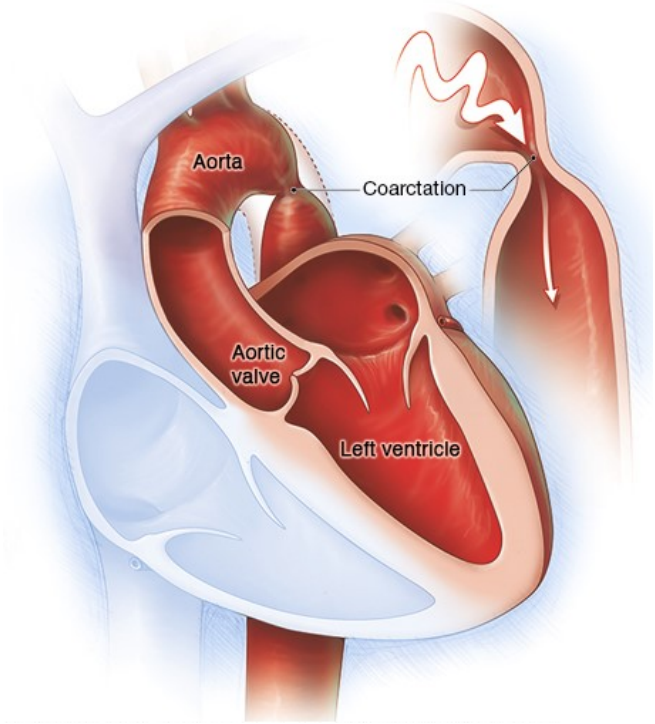

Figure 1.1: Representation of an aortic coarctation (CoA) anatomy [27].

The causes of a CoA onset are still uncertain [28]. A reduced flow through the aorta during pregnancy, resulting from intracardiac anomalies, and an extension of the ductal tissue into the aortic wall are among the main hypotheses [29]. CoA is often found together with other CHDs such as bicuspid aortic valve, ventricular septum anomalies, aortic stenosis, ventricular septal defect, patent ductus arteriosus or mitral valve abnormalities [30]. Additionally, CoA is common in girls with Turner's syndrome [31]. Traditionally, there are two forms of CoA: an infant form and an adult form. The former develops *in utero* when the aorta of the fetus does not form correctly; it accounts for 70% of cases and is usually referred to as pre-ductal CoA, since it is located upstream of the ductus arteriosus. The ductus arteriosus is a blood vessel connecting the pulmonary artery to the descending aorta which allows, in the fetus, venous blood from the right ventricle to circumvent the non-functioning lungs. At birth, the ductus arteriosus closes and becomes the ligamentum arteriosum (Figure 1.2). In infantile CoA, the ductus arteriosus is still patent, and downstream of the narrowing, deoxygenated blood can reach the descending aorta and downstream organs. Without intervention, infants may not survive past the neonatal period. In the adult form, usually referred to as post-ductal CoA, the ligamentum arteriosum replaces the patent ductus arteriosus [29] (Figure 1.2). In this case, increased upstream pressure leads to higher cerebral pressure and blood flow, associated with a higher risk of aneurysm formation [29]. Lowered downstream pressure may result in a reduction of perfusion to the kidneys, which respond by increasing water retention, ultimately leading to hypertension [32]. Nowadays, however, this distinction is regarded as too simplistic since great variability is observed in the coarctation location in neonates [33].

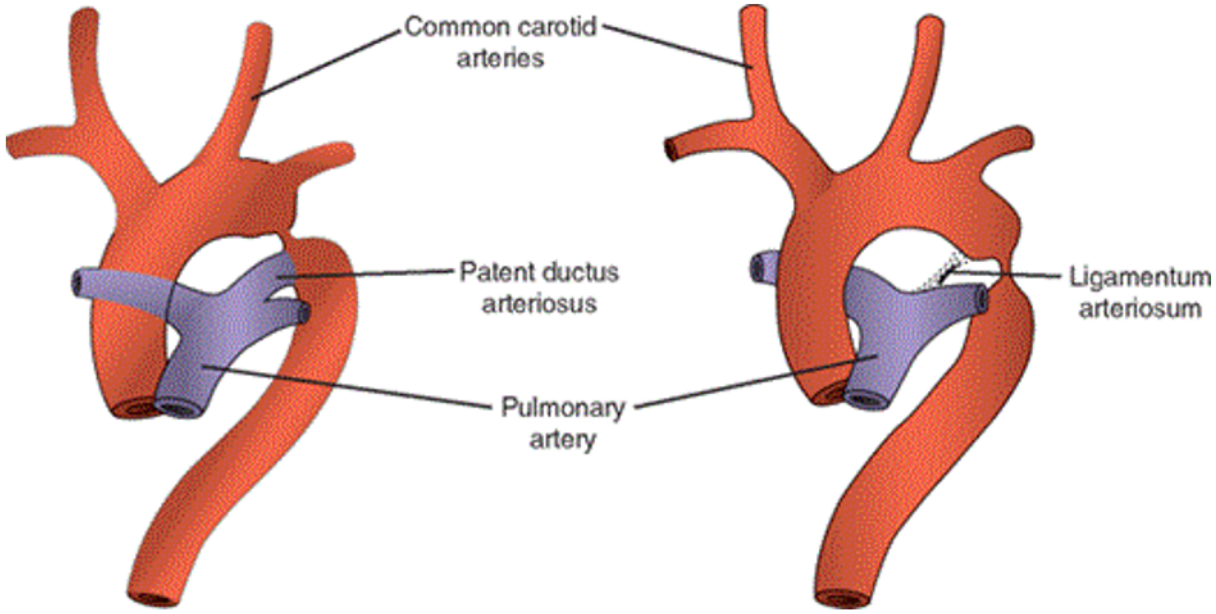

Figure 1.2: Representation of pre-ductal (left) and post-ductal (right) CoA, with ductus arteriosus and ligamentum arteriosum respectively [34].

In 98% of all cases CoA is characterized by an isolated narrowing, rather than by an elongated narrowed tract [35]. The narrowed aortic wall represents an abnormal impedance to flow, thus forcing the left ventricle to generate a higher pressure to provide sufficient blood flow through the aorta. Consequently, pathologic features include cardiac hypertrophy, degenerative changes in the proximal aorta and increased blood pressure in the upper part of the body [1]. In extremely severe cases, the pressure drop across the coarctation zone may prevent the supply of oxygenated blood to the lower body. This poor blood flow leads to various impairments, such as leg weakness, underdevelopment of the lower limbs and pain during exercise [36]. As these symptoms usually manifest during the first few weeks of life, symptomatic newborns should undergo urgent intervention, since the age at CoA repair is an important predictor of long-term cardiovascular complications [2, 3, 37].

1.1.2 Diagnosis

Albeit antenatal diagnosis of CoA has a critical importance for early treatment preplanning, this disease remains one of the most difficult cardiac defects to diagnose before birth [38]. Postnatal evaluation of CoA and consequent intervention recommendations are based upon the following indications [4]:

- a peak-to-peak pressure gradient across the coarctation greater than 20 mmHg. This characteristic is the most distinguishing diagnostic factor to determine the functional severity of the coarctation [5];

- a peak-to-peak coarctation gradient lower than 20 mmHg in the presence of anatomic imaging evidence of significant coarctation.

The diagnosis can be confirmed using different types of techniques, from the more traditional sphygmomanometry to the more sophisticated imaging modalities (e.g. magnetic resonance, echocardiography, etc.) [30, 39]. Cardiac catheterization is considered the gold standard to invasively assess pressure differences across a coarctation, and to evaluate the accuracy of different less invasive methods [40]. This technique consists in the insertion of a catheter in a heart chamber or vessel, and it is often used for interventional purposes. Pressure transducers can be connected to the catheter to measure blood pressure within the vessel of choice. In adults and children, such technique is commonly executed together with a therapeutic intervention or if CoA is associated with other cardiac disorders such as coronary artery disease [41]. While a direct measurement of the pressure drop using an intravascular pressure catheter is considered the most accurate method, such technique is often advised against unless other non-invasive methods are not available or there appear to be discrepancies between the measured value and the presenting symptoms [42]. Even if very rarely, serious complications may arise from cardiac catheterization. These include infection and bleeding at the catheter site, damage to blood vessels, stroke or heart attack caused by blood coagulation.

As a direct measurement of the pressure drop across the coarctation site requires invasive

procedures, easily accessible velocity information obtained from Doppler echocardiography is often used to quantify this parameter. Using echocardiography one can, within certain limits, produce assessment of the direction of blood flow and the velocity of blood at any arbitrary point using the Doppler effect. With this imaging modality, the pressure difference across a CoA can be estimated from the peak velocity magnitude acquired along the direction of an ultrasound beam through a simplified Bernoulli formulation [43]. However, the accuracy of this approach is limited by operator dependence and by mathematical assumptions which rely on neglecting transient effects, viscous losses on the flow and the effect of pressure recovery distal to the coarctation [44]. This last assumption in particular, often leads to an overestimation of the true pressure drop [39, 45–47].
Despite its higher costs, magnetic resonance imaging (MRI) is a more accurate, non-invasive method compared to Doppler echocardiography to evaluate CoA. Apart from an assessment of stenosis morphology (site and area reduction), the advancement of time-resolved, three-directional and three-dimensional phase-contrast magnetic resonance imaging (widely known as 4D flow MRI) has enabled the quantification of various hemodynamic features and a deeper understanding of complex pathologies [48].

1.1.3 Overview of current treatments

Patients born with CoA require lifelong medical care, including invasive and non-invasive imaging, drug therapy, and, upon specific indications, invasive catheterization or surgical intervention to reduce blood pressure in the ascending aorta. Intervention techniques aim at relieving the constriction rather than alleviating hypertension with medications. CoA is currently treated by surgical correction or by minimal invasive procedures through balloon angioplasty or stent deployment [49].

Surgical techniques

Four types of surgical interventions are commonly used: resection with end-to-end anastomosis (Figure 1.3a), patch aortoplasty (Figure 1.3c), by-pass graft insertion (Figure 1.3b) and subclavian flap aortoplasty (Figure 1.3d) [49].

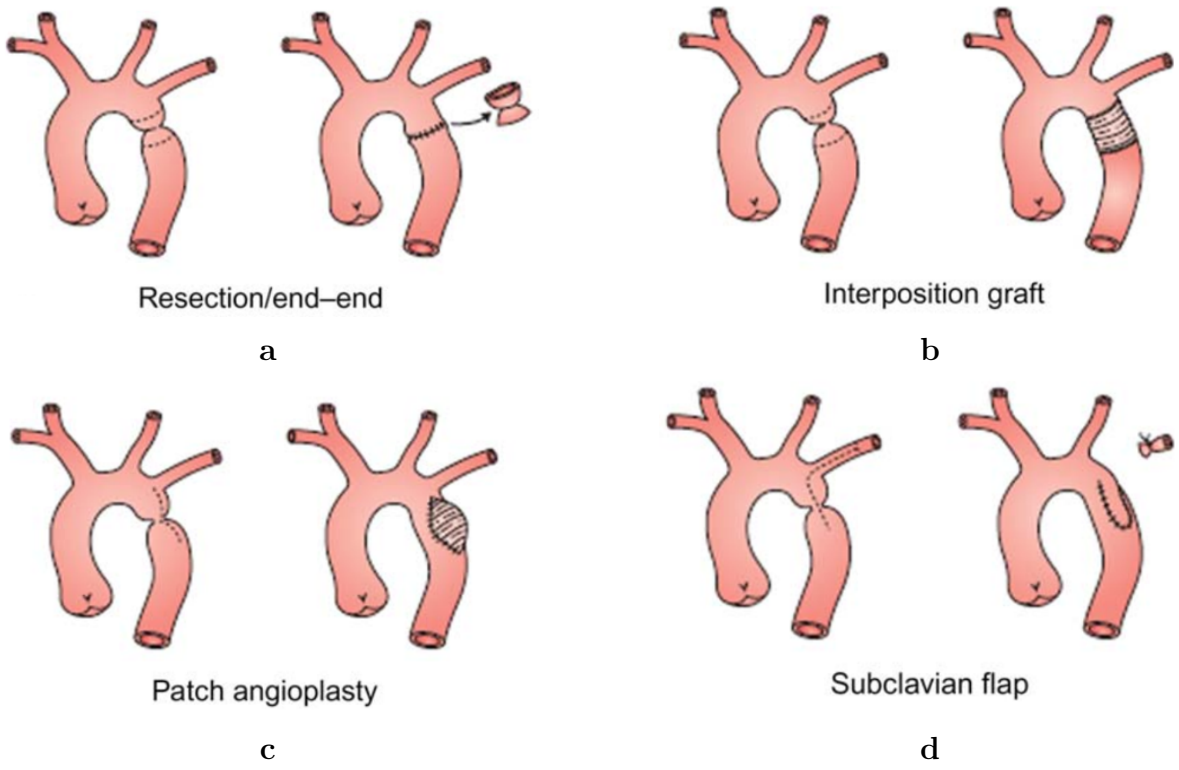

Figure 1.3: Schematic representations of the main surgical repair techniques for CoA [49]; end-end resection (a), graft interposition (b), patch angioplasty (c) and subclavian flap (d).

The repair strategy depends on the age of the patient, the individual anatomy, associated defects and the preference of the surgeon [50]. Resection with end-to-end anastomosis is usually performed on infants because of the small dimensions of the excised tissue. Aortas treated with this technique show a circular ring of scar tissue (Figure 1.3a). In patch aortoplasty, the aortic wall is cut and a patch of synthetic material is sutured to enlarge the narrowing (Figure 1.3c). This surgery, however, has been shown to promote aneurysm formation [51]. When the distance to be bridged is protracted, a bypass graft is inserted across the area of coarctation (Figure 1.3b). Finally, another surgical approach

consists in sacrificing the left subclavian artery to expand the aortic wall at the site of the coarctation (Figure 1.3d).

Minimally invasive techniques

Balloon angioplasty and stent implantation procedures have become a favorable alternative to surgical treatments because of the associated shorter recovery time and reduced costs. In balloon angioplasty an inflatable balloon is introduced in the aorta via a catheter; the balloon is then expanded to enlarge the narrowed tract, partially tearing the intima. Balloon angioplasty is effective in reducing the pressure drop early after treatment, but patients treated with this technique might experience recoarctation, thus requiring repeated treatments [49]. Stent implantation after balloon angioplasty has the advantage of preventing recurrent coarctations. In infants and small children, the use of stents is still problematic, since these metallic structures do not grow in dimensions with the patient's vessels. Despite successfully correcting the anatomy in the coarctation zone, there is some evidence indicating that subjects treated with stent implantation show a significant long-term morbidity, requiring long-term follow-up [52]. Such complications involve systemic hypertension and higher risk of dissection and aneurysm formation [52–54]. In particular, there is still contrasting evidence of hypertension persistence in patients successfully treated for CoA [55], and the adverse effects on hemodynamics of a noncompliant stent remain to be fully elucidated.

1.2 PC-MRI

1.2.1 Magnetic resonance imaging

MRI is a medical imaging technique that allows to obtain pictures of a specific district's internal anatomy. It uses magnetic fields and radio frequencies rather than ionizing radiations employed by other imaging techniques such as CT and X-rays [56]. The magnetic field intensity generated by an MRI machine is measured in Tesla (T), with most modern equipments being able to generate fields above 7T. However, the majority of MRI systems used in clinical practice produce magnetic fields ranging from 1.5T to 3T. MRI relies on the magnetic properties of hydrogen atoms (protons), which are abundant in soft tissues containing water. As a positively charged particle, a hydrogen proton spins about its axis producing a magnetic moment. Normally, when no external magnetic field is applied, protons magnetic moments are oriented randomly (Figure 1.4b). The main components of an MRI system are: a primary magnet, gradients magnets, radiofrequency (RF) coils and a computer system. The primary magnet generates a constant primary magnetic field (B_0) which causes the protons spins to align either parallel or antiparallel to it (Figure 1.4c), with more spins aligned in a parallel fashion (low energy state) rather than in an antiparallel one (high energy state). This arrangement creates a net magnetic vector (M_0) in the direction of B_0 called longitudinal magnetization (Figure 1.4c). The protons spins, however, are not static, but precess around the direction of B_0. The precession frequency is called Larmor frequency and depends on the strength of the magnetic field. The gradient magnets then generate secondary magnetic fields over the primary field. The arrangement of these magnets allows MRI to image directionally along different perpendicular directions. Gradient magnets spatially alter the intensity of the magnetic field felt by hydrogen atoms, therefore changing their precessing frequency in space. Such mechanism allows for 3D spatial encoding in MR images. The RF coils transmit a RF pulse which has a double effect: first, it causes some low energy protons to switch to a

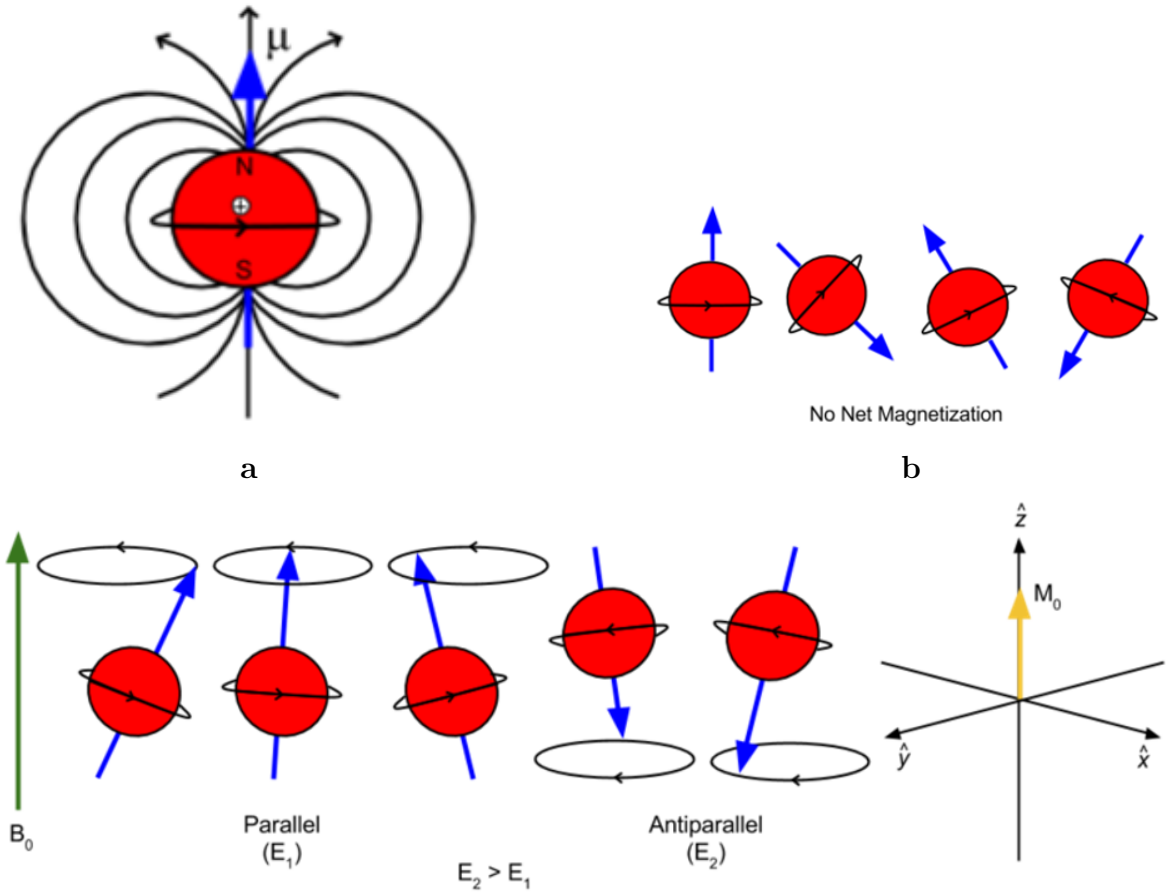

Figure 1.4: Schematic representation of protons magnetic properties without an applied magnetic field (a,b) and with an external field (c) [57].

high energy state, decreasing the net longitudinal magnetization; second, it causes protons to synchronize and to precess in phase. As a result, the net magnetization vector turns 90° from the primary field towards the transverse plane (transverse magnetization) (Figure 1.5).

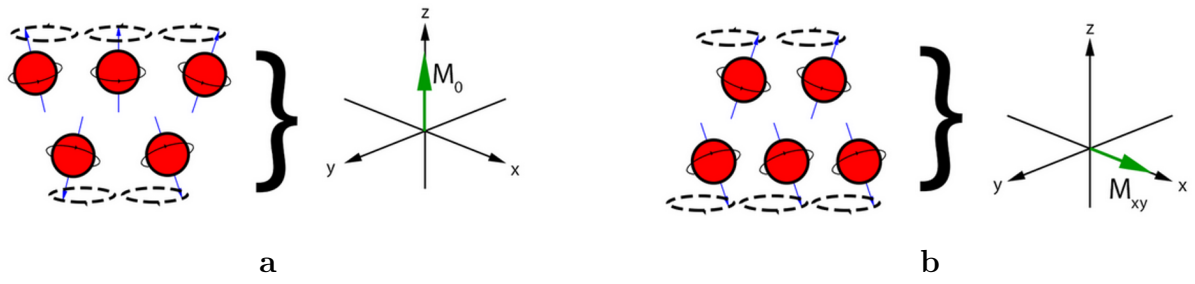

Figure 1.5: Representation of magnetization vectors depending on proton spins [57]

After the RF pulse, relaxation occurs and protons resume their normal state in the primary magnetic field. Some protons flip back from the high energy state to the low energy state, parallel to B_0, giving up their energy to the surrounding lattice. This is known as spin-lattice, or T1, relaxation and it results in an increase of the longitudinal magnetization. Together with this phenomenon, spin-spin, or T2, relaxation occurs, where protons that were in phase begin to dephase, resulting in a reduction of transverse magnetization. As time passes after the RF pulse, the net longitudinal magnetization increases and the net transverse magnetization decreases. The net magnetic vector, sum of the two, spirals around the longitudinal axis, changing its net magnetic moment. This phenomenon induces an electric signal that is received by the RF coils and is later analyzed and converted to a digital signal by the computer system. Finally, Fourier transforms are applied to the digital signal and images are constructed [56]. MRI datasets can then be stored in a standard format called DICOM. DICOM files can be freely exchanged and read by multiple users. Each DICOM file contains several tags, corresponding to different information about imaging and acquisition features, as well as some patient's data.

1.2.2 PC-MRI basic principles

In the last decades, MRI has been further developed to provide not only anatomical and morphological information, but also quantitative functional measurements about moving fluids [58]. Phase contrast MRI (PC-MRI) is a particular type of MRI that allows to obtain information about blood flow velocities. Initially, analogously to traditional MRI, a magnetic field gradient is applied, altering the protons precession frequency in such a way that protons subject to different magnetic field intensities precess with different frequencies. This phase shift can be calculated as a function of the gradient and of the proton position [59]:

$$\phi = \gamma \int_0^t B_0 + \boldsymbol{G_0}(\tau) \cdot \boldsymbol{r}(\tau) d\tau, \tag{1.1}$$

where G_0 is the magnetic field gradient, γ is the gyromagnetic ratio and r is the position of the spin. Then, another magnetic field gradient is applied. If the second gradient is opposite and equal in amplitude to the first (bipolar gradients), then, static protons will have an null net phase shift, while moving protons will accumulate a phase shift that is proportional to their velocity (Figure 1.6).

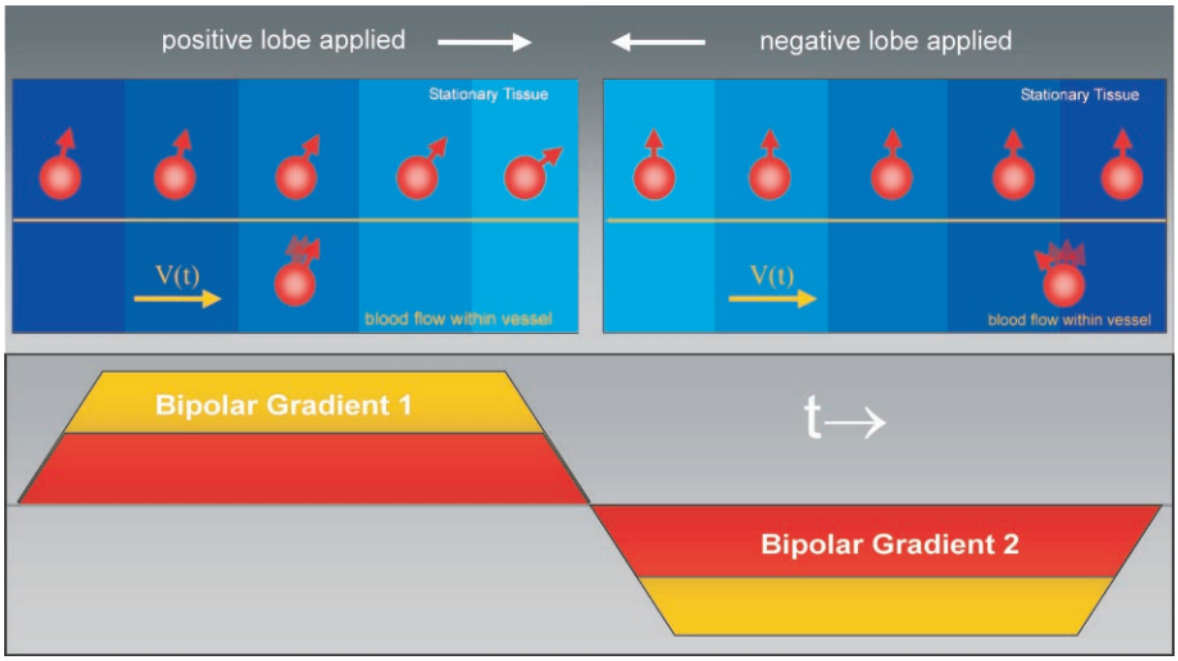

Figure 1.6: Principle of bipolar gradient phase-contrast sequences. Two acquisitions are performed, using opposite gradients. V=velocity and t=time [58].

In this way, the accumulated phase shift along the direction specified by the gradients can be calculated as:

$$\Delta\phi = v(\gamma\Delta M), \tag{1.2}$$

where v is the spin velocity ΔM is the gradient moment difference. This phase shift is then measured and converted to a velocity value:

$$v = \frac{VENC}{\pi}\Delta\phi, \tag{1.3}$$

where the *VENC* value determines the range of detectable velocities encoded by a phase contrast (PC) sequence. In PC-MRI the operator is required to set this parameter depending on the amplitudes of the gradients used. *VENC* is inversely related to the area

of the flow encoding gradients, hence, stronger gradient magnitudes encode smaller velocities [58]. If *VENC* is too low, and below the maximum velocity in the vessel of interest, aliasing occurs. In PC sequences, pixels with aliasing appear to have opposite velocity values with respect to the surrounding pixels. This makes aliasing relatively simple to detect and correct if the peak velocities are not too far from the *VENC* range. If *VENC* is too high, and above the the maximum velocity in the vessel of interest, the measurement sensitivity and the signal-to-noise ratio (SNR) decrease. Additionally, a larger range of detectable velocities will conceal the smallest flow features.

It is worth saying that every MRI acquisition yields information about both the signal magnitude and phase in each acquired voxel. Signal intensities are processed into an anatomic image, the magnitude image. In conventional MR sequences, the phase information is discarded, while in PC measurements, the phase information is used to calculate the velocity in each voxel.

When dealing with cardiac imaging, unless the heart and lungs were stopped, motion artifacts are inevitable. To overcome this issue, prospective or retrospective cardiac gating are employed. In prospective gating techniques MR data acquisition begins after the QRS complex of the electrocardiogram (ECG) (referred to as trigger) and it is paused at the end of the cardiac cycle, until the next trigger signal. This technique is used to compensate for physiologic variations in the duration of cardiac cycles. As a consequence, late diastolic flow will not be determined correctly. In retrospective gating RF pulses are generated continuously and MR data are not acquired in response to a particular trigger, but rather throughout the entire ECG, which is simultaneously recorded. Albeit these corrections are necessary to remove significant artifacts otherwise present in MR acquisitions, they also imply that MR scans are cardiac-averaged, namely, that the measured blood velocities are an average over multiple cardiac cycles. Motion artifacts due to respiratory movements can also be accounted for. In case of prospective gating, the subject under examination is asked to hold his breath, while in case of retrospective gating, the subject's diaphragm motion is recorded and successively accounted for.

4D flow MRI

When magnetic field encoding gradients are applied along three perpendicular directions throughout the cardiac cycle, volumetric, temporal and 3-directional data are obtained. Such imaging technique is known as 4D flow MRI, or simply 4D flow [60]. In 4D flow MRI, the same methodology of traditional PC-MRI is employed, with three different magnetic field gradient combinations, each encoding fluid velocities along a direction. In these acquisitions, the three *VENC* values can be set independently, if they are different, we talk about multi-venc acquisitions [61]. In order to capture blood velocities at different time points in the cardiac cycle, a cine-MRI technique is used. The set of recorded cardiac cycles are subdivided into time intervals whose duration depends on the subject's heart beat. To each interval, a frame in the 4D flow sequence is associated (Figure 1.7). Once the acquisition is over, each frame is the result of a combination of the respective time intervals within each cardiac cycle. Therefore, the final outcome represents an average heart cycle of the patient, and each frame contains information about anatomy and velocity at a specific time point.

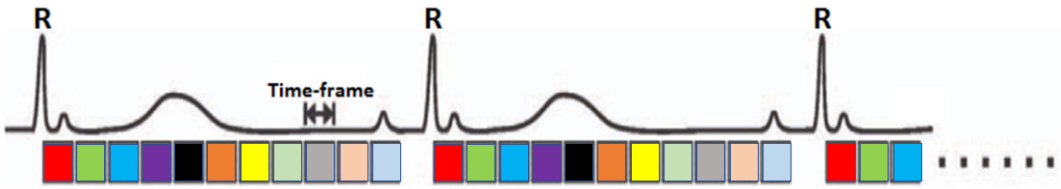

Figure 1.7: Representation of standard cine-MRI principle. Each time frame is the result of an average of its corresponding intervals in the different cycles (identified by the same color). Modified from [62].

Although PC-MRI and 4D flow can provide invaluable insight into the hemodynamics involved in many cardiovascular diseases, it still comes with numerous limitations. Due to the finite resolution, when a voxel is located at the boundary between static and moving tissues the phase shift measured by PC-MR results from an average of both stationary and flowing spins, leading to unreliable velocity measurements and generating partial volume effects [63]. In cases of detailed turbulent flow, inadequate temporal and spatial

resolutions fail to capture the fine flow structures that exist at a sub-voxel scale, and can, therefore, be sources of unreliability [58]. However, 4D flow measurements in large arteries have been thoroughly validated in various studies [48, 64, 65] demonstrating the feasibility of this imaging technique to quantify flow compared to literature data and conservation of mass. In order to improve blood flow measurements and visualization from 4D flow acquisitions, researchers have been focusing on 4D flow MRI noise reduction by exploiting physical conditions of blood flow in flow data denoising [11, 66, 67]. As blood is an incompressible fluid, hence divergence-free, 4D flow denoising filters often aim at eliminating the non-divergence-free component of the velocity field by projecting it onto a solenoidal vector field [67]. Nonetheless, strictly enforcing the divergence-free condition on blood flow velocities measured with the PC-MRI technique may lead to significant error propagation [11]. In [11], a robust divergence-free wavelet (DFW) denoising algorithm was developed. Such filter was shown to be efficient in denoising 4D flow MRI velocity fields through soft-thresholding of the non-divergence-free velocity field component.

1.2.3 4D flow MRI-based hemodynamic measurements

In recent years, with the improvements in PC-MRI acquisition techniques, researchers have shown a growing interest in investigating hemodynamic features using 4D flow [8]. As already established in several numerical studies [68–71], there is a strict correlation between hemodynamics and cardiovascular health. In this regard, 4D flow MRI allows to assess hemodynamics *in vivo*, providing several hemodynamic biomarkers that are believed to play a significant role in pathology onset and development [8]. However, this imaging technique could present produce images with background phase errors and noise which can negatively affect the quality of measurements [72]. Most researchers working with 4D flow data are aware of these errors and usually correct these using in-house software [8]. In order to minimize error propagation, phase errors and noise reduction is

especially important when deriving indirect hemodynamic measurements (e.g. pressure) from velocity data.

Velocity and flow rate

As previously described (Equation 1.3), blood flow velocities can be directly extracted from 4D flow images using the sequence *VENC*. Consequently, flow rate measurements can be performed by integrating velocities over the areas of interest. These measurements can then be used, for example, to assess the severity of valve stenosis and CoA [73], as a fluid flowing through restricted conduits naturally increases its velocity. Furthermore, 4D flow based flow rate and velocity measurements have been used to validate computational fluid dynamics (CFD) studies in the past [74, 75]. For clinical purposes, colored streamlines and contours can be visualized in the vessel domain and flow rates plotted in time to obtain information on how these quantities vary throughout the whole cardiac cycle.

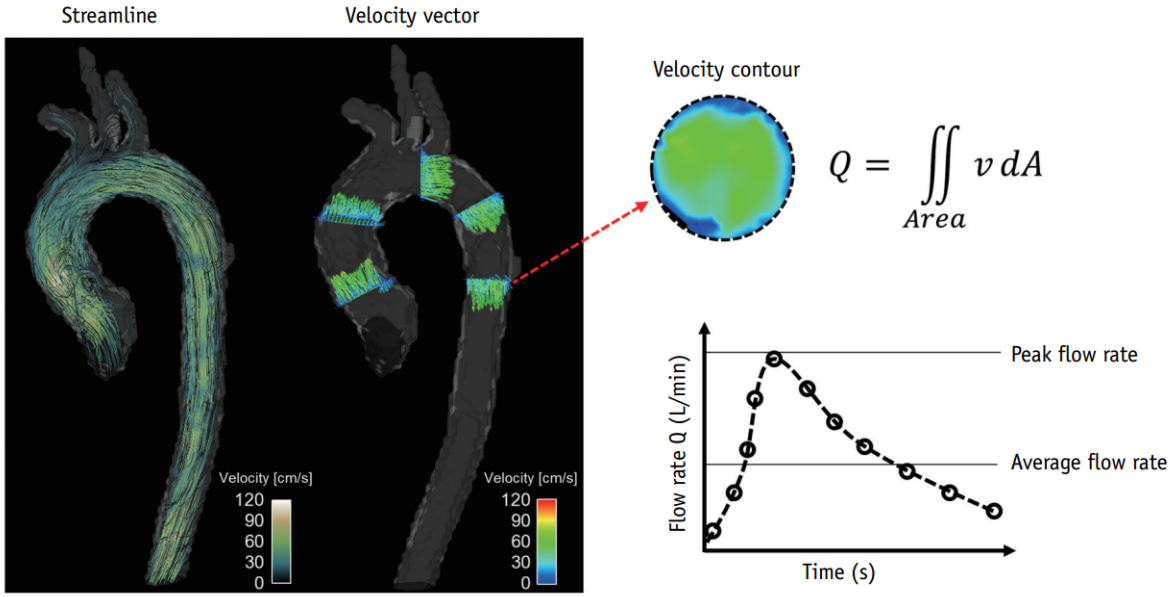

Figure 1.8: Example of velocity visualization and quantification of flow rate from 4D flow [8]

.

Wall shear stress

Wall shear stress (WSS) is a measure of the drag force felt by endothelial cells exerted by blood flow. Endothelial cellular response to altered WSS has been studied and correlated to a range of vascular diseases [69, 70, 76]. Studies focusing on the role played by WSS in atherosclerosis concluded that atherosclerotic plaque formation occurs in regions of low oscillatory WSS [70, 77, 78]. Hence, knowledge of *in vivo* WSS patterns can provide deeper insights into the pathophysiology involved in vascular diseases. Usually, WSS is calculated using CFD, which allows for a detailed spatial and temporal resolution, but requires engineering expertise and long computational times. Several recent numerical studies assessed the feasibility of calculating WSS *in vivo* from 4D flow MRI [79–81]. By definition, WSS can be computed as:

$$\boldsymbol{\tau} = \mu \frac{\partial \boldsymbol{v}}{\partial \boldsymbol{n}}\bigg|_{wall}, \tag{1.4}$$

where $\boldsymbol{v}$ is blood velocity, μ represents the dynamic viscosity and $\boldsymbol{n}$ indicates the direction perpendicular to the wall. When calculating WSS distributions from 4D flow, it is crucial to perform an accurate segmentation of the lumen in order to estimate the velocity gradient along the direction perpendicular to the wall [8]. In [82] the author compares WSS patterns calculated using CFD with the ones obtained from MRI. Although the two methods yielded different values of WSS, WSS patterns closely matched, suggesting that PC-MRI based WSS could be potentially used in the clinical routine. In another recent study, the feasibility of calculating peak WSS in the aorta from 4D flow data was assessed [10]. The authors, show that it is possible to correctly identify peak WSS differences in the aorta of healthy and bicuspid aortic valve-affected subjects. However, the limited spatial resolution of 4D flow dataset proved to be a major source of error in the estimation of WSS values.

Pressure

Blood flow pressure distributions are of critical importance in the assessment of many cardiovascular pathologies. Localized pressure drops indicate a loss of flow energy generated by the heart, and have been used to estimate stenosis severity in CoA [83–85]. Driven by the idea that the pressure gradient across the coarctation is the most important hemodynamic parameter for clinical management of CoA [5, 85], part of this work will focus on pressure difference calculation from 4D flow images. Several recent works have dealt with the estimation of pressure differences from 4D flow using different mathematical formulations [84, 86–89], and a number of numerical methods have been proposed to solve the Navier-Stokes equations for pressure from 4D flow MRI data.

The feasibility of an iterative solution method was assessed in [88], validated against numeric simulations [90] and compared to catheter measurements in human patients [91]. In [86], the authors performed a 3D pressure gradient mapping determined from PC-MRI in CoA patients. Briefly, pressure gradients were calculated assuming a viscous, incompressible fluid using the Navier-Stokes equation:

$$-\nabla p = \rho\left(\frac{\partial \boldsymbol{v}}{\partial t} + \boldsymbol{v}\cdot\nabla\boldsymbol{v} - g\right) - \mu\Delta\boldsymbol{v}, \tag{1.5}$$

which is normally coupled with the divergence free condition due to the incompressibility of the fluid:

$$\nabla\cdot\boldsymbol{v} = 0, \tag{1.6}$$

where $\boldsymbol{v}$ is velocity, p is pressure, g body acceleration, μ the dynamic viscosity and ρ is blood density. For a given voxel in the image volume, velocity values of the nearest temporal and spatial neighbors were used for calculation of a central difference scheme as an approximation for temporal and spatial first and second-order velocity derivatives. Taking the divergence of Navier-Stokes equation (Equation 1.5), the Poisson pressure

equation (PPE) is obtained:

$$-\Delta p = \nabla \cdot \left[\rho \left(\frac{\partial \boldsymbol{v}}{\partial t} + \boldsymbol{v} \cdot \nabla \boldsymbol{v} - g \right) - \mu \Delta \boldsymbol{v} \right], \tag{1.7}$$

where pressure is derived explicitly as a function of the acquired velocity field, allowing the estimation of convective effects in all spatial directions and the contribution of viscous dissipation (Figure 1.9). However, relative pressure computed from PC-MRI was compared only to echo-based pressure estimation, which are obtained through a simplified Bernoulli formulation; no systematic comparison with CFD or experimental results was performed. Nonetheless, this approach may lead to pressure underestimation [84] and to large errors for some vessel geometries [89].

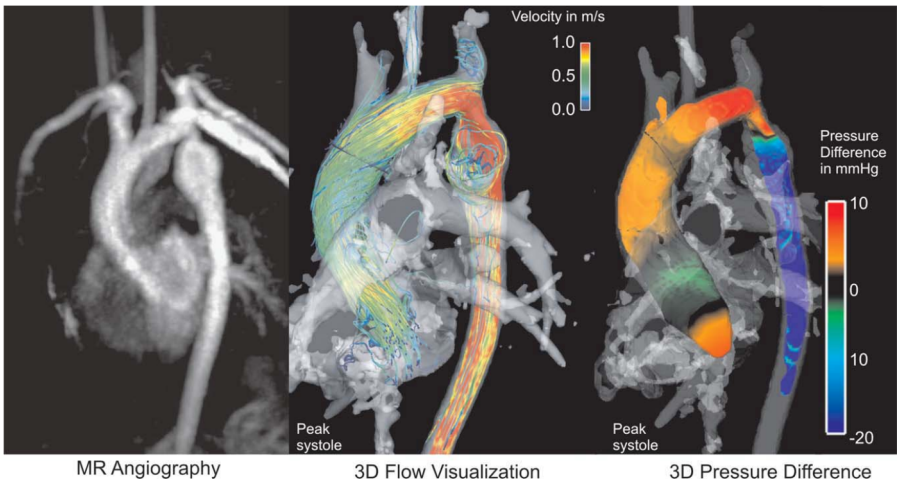

Figure 1.9: Visualization of aortic geometry by MRA, blood flow, and 3D pressure differences in a patient with CoA calculated with an iterative approach. Taken from [8].

In a second recent study, a method for computing and visualizing pressure differences derived from 4D Flow MRI was developed [85]. Pressure difference maps obtained from untreated and repaired CoA patients were then compared to healthy volunteers. The authors adopted an approach based on Navier-Stokes equation similar to the one previously described, albeit a greater emphasis is laid on the accuracy of the integration step. Although the authors were able to correlate an increase in pressure at the aortic isthmus to residual narrowing after intervention, this study lacks of validation against

other pressure measurements.

Another strategy consists in using a finite element–based method to solve the PPE. This method has been adopted by various researchers [84, 87, 92], and, compared to iterative approaches, was shown to be less susceptible to pressure underestimation and less computationally expensive. Additionally, this approach has been successfully applied to estimate pressure differences in CoA [84]. In this recent landmark study the authors investigated the agreement between 4D flow MRI based pressure fields and cardiac catheterization which is the clinical gold standard. A finite element-based solution for the Poisson pressure equation (FE-PPE) was pursued to compute 4D intravascular blood pressure differences (Figure 1.10). The authors report a good agreement between peak systolic pressure gradients measured by catheterization and 4D flow MRI, with only a slight underestimation by the MR-based method. The proposed finite element-based approach would provide a good basis for a comparison between spatiotemporal pressure fields and other hemodynamic features, such as WSS or wall compliance. Such information would provide the opportunity for an advanced analysis of pathophysiological processes associated with CoA, like arterial hypertension and correlated morbidity. Nevertheless, this kind of investigation has never been conducted. Moreover, treated patients were not evaluated, whereas it would be useful to adopt the described technique to assess pressure differences after virtual coarctation repair.

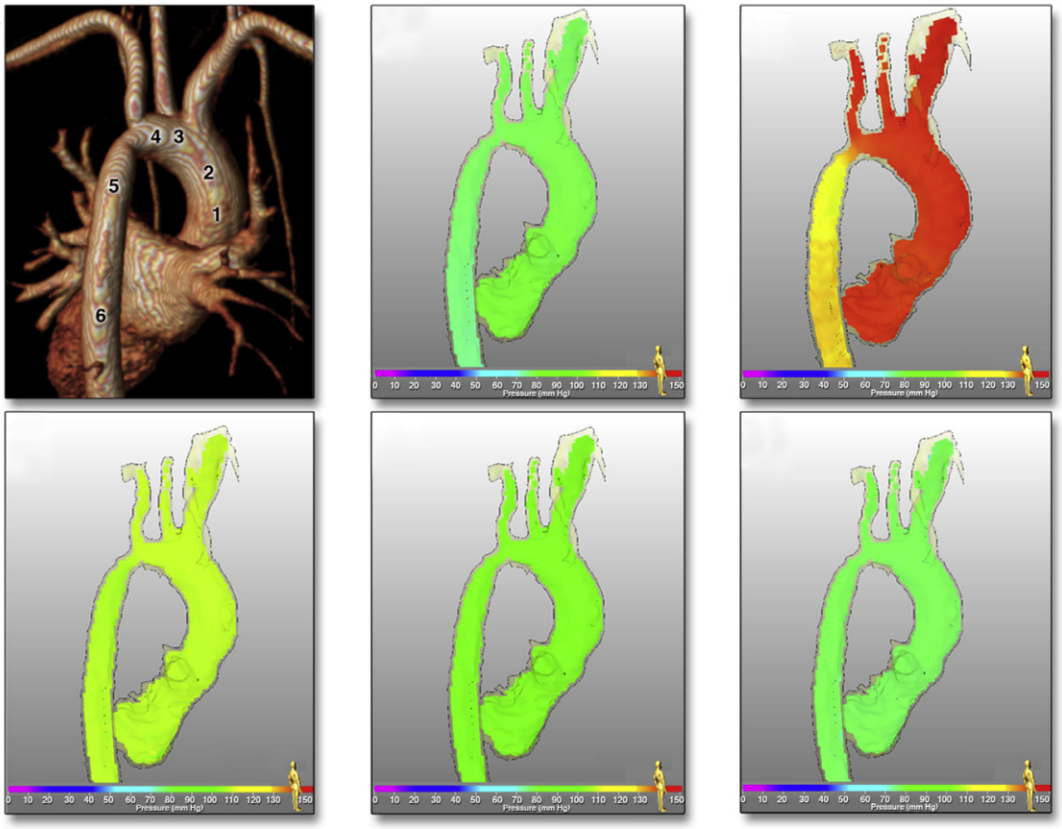

Figure 1.10: Cardiac MRA of the aorta with PC-MRI-derived color-coded pressure fields at different points in the cardiac cycle. Taken from [84].

In [93] pressure differences were calculated based on the work-energy relative principle (WERP), which, with a few simplifying assumptions, yields the equation:

$$\Delta p = -\frac{1}{\Lambda}\left(\frac{\partial}{\partial t}K_e + A_e + V_e\right) \tag{1.8}$$

where the pressure difference is given by the contribution of kinetic energy (K_e), advected energy (A_e) and viscous dissipation rate (V_e), while Λ is a term accounting for the flux through surfaces. The method was validated against results from CFD simulations in a patient-specific model of CoA which accounted for arterial compliance using a coupled-momentum method for fluid-structure interaction (CMM-FSI) [9]. However, the image data were synthesized from the simulations through a spatiotemporal downsampling, rather than being acquired *in vivo*. This method was also applied on real clinical imaging data of healthy volunteers. Despite the thorough analysis of the WERP method and of its performance with respect to other proposed techniques (Figure 1.11), this study lacks

of a systematic comparison with *in vivo* PC-MRI data of CoA patients. In this way, a complete clinical validation cannot be achieved. Furthermore, this approach does not provide 3D pressure distributions, but rather pressure differences along the centerline of a vessel of interest.

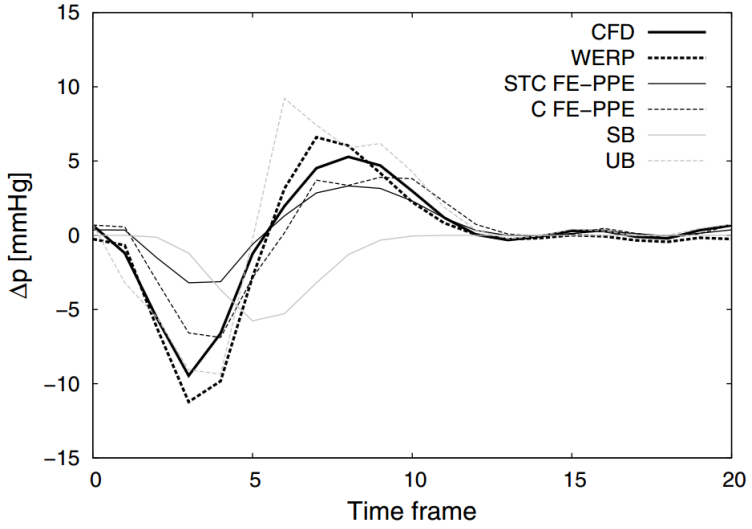

Figure 1.11: Comparison of pressure differences over the cardiac cycle computed with different methods: CFD (solid black line), WERP (dashed black line), static tissue + core mesh (STC) FE-PPE (solid dark grey line), core mesh only (C) FE-PPE (dashed dark grey line), simplified Bernoulli (SB) (solid light grey line) and unsteady Bernoulli (UB) (dashed light grey line). Taken from [93].

A different numerical approach, based on a multigrid solver for the PPE, was presented in [89]. Through recursive smoothing, coarsening and refining of the solution, this solver was shown to be able to capture pressure distributions in phantoms and in an aorta in *in vivo*. As reported by the authors, this numerical strategy has the advantage of being extremely efficient and less sensitive to pressure underestimation compared to iterative solutions.

1.3 Overview of recent numerical studies on aortic coarctation

The hypothesis that morbidity among patients with CoA can be related to altered hemodynamics and vascular biomechanics was suggested decades ago [68]. Recently, researchers have thoroughly characterized changes of hemodynamic parameters such as pulse blood pressure, vorticity and wall shear stress due to the presence of a CoA [80, 94]. Decreased WSS values and increased oscillatory stress index (OSI), together with augmented vorticity, are among the most common hemodynamic features which could play a role in CoA related morbidity, such as hypertension and post-stenotic dilatation [95, 96]. CFD and fluid-structure interaction (FSI) models have been extensively used to assess detailed local flow patterns and to analyze pressure gradients across coarctations in patient specific geometries. In [83] the authors studied the pressure drop across the coarctation segment at rest and during pharmacological stress. As a validation, the results of their CFD models were compared to catheter-based measurements. Although an accurate correspondence with the invasive pressure drop was obtained, one of the prescribed boundary conditions was a pressure profile extracted from catheterization. This weakens the clinical relevance of the model, since requiring invasive measurements adds little value to CFD studies. In another study, blood flow was simulated in both untreated and repaired CoA to assess a possible correlation of hemodynamic parameters with aortic arch morphology [97]. The authors concluded that the altered WSS distribution with a single peak, present in certain arch morphologies, might be related to the vascular dysfunctions observed.

In [98], it was shown that aortic wall compliance has a significant impact on the hemodynamics involved in a CoA. In fact, wall compliance allows for the ascending aorta to dilate during systolic peak, storing energy and thus increasing diastolic run-off in the descending aorta. LaDisa et al. [95] conducted a sophisticated numerical study on a sampling of CoA patients. Simulations were carried out incorporating vessel displacements and

lumped parameter models to account for downstream vascular resistance and compliance. With respect to healthy cases, patients with CoA exhibited greater deformations upstream of the coarctation and a larger portion of the vessel wall subject to abnormal time averaged WSS (TAWSS) and OSI, but a significant improvement was found after treatment.

Kim et al. [12] developed a multidomain method, in which particular emphasis is laid on the coupling of reduced-order zero-dimensional models with 3D FSI simulations. The authors adopt a finite element solver for blood flow and vessel wall elastodynamics, the same used in this thesis. The domain's outlet boundary conditions are represented by 3-element Winkessel models (3-WK), whose parameters were set according to flow distributions measured using 4D flow MRI and literature data. As inlet boundary condition, a lumped parameter model of the heart was designed. Their model includes a time-varying elastance to reproduce the ventricular pressure-volume behavior. Both rest and exercise conditions were simulated in untreated and "virtually repaired" coarctations. The main focus of this study was to assess the feasibility of the multidomain method to investigate the interactions between the heart and the systemic circulation. However, it showed how the methods adopted by the authors, very similar to the ones which will be herein described, are valid to simulate blood flow in CoA.

An exhaustive FSI study on CoA was conducted by Taelman in [6]. In particular, the hemodynamic impact of pressure wave reflections in a model of stent-repaired CoA was investigated. The author concludes that an increase in stent length and stiffness causes higher pressure build-up proximal to the stent. However, pressure wave reflections generated at the stent extremities tend to cancel each other out, leaving blood flow rate and pressure almost unaffected. Moreover, this work proved that a FSI approach is of fundamental importance in assessing CoA hemodynamics accurately. In fact, aortic compliance significantly damps out blood flow pulsatility, reducing peak velocities in the narrowing and, consequently, the associated pressure drop. Finally, Coogan et al. [99] investigated the hemodynamic impact of stenting in a repaired CoA, modeling the stent as a stiff segment with a circular cross-section. In particular, the effect of the stiff segment on cardiac

workload and blood pressure was assessed. The authors compared stenting to surgery, concluding that the former does not induce any significant adverse hemodynamic effect. Despite CoA has attracted growing attention during the last years and has been extensively studied through numerical simulations, it is necessary to further elucidate the role played by hemodynamics and wall biomechanics in both untreated and repaired coarctations. With continuous advancements in computational modeling, new studies could either strengthen or contradict our current understanding of CoA. Additionally, new non-invasive methods, compatible with daily clinical practice, need to be developed to reliably evaluate coarctation severity.

1.4 Main objectives

The main objective of the present work is to assess the feasibility and reliability of pressure estimation based on 4D flow MRI. 4D flow-based pressure distributions will be validated against both *in silico* numerical simulations and *in vitro* experimental tests. Improving early non-invasive assessment of coarctation severity is essential in treatment preplanning: being able to reliably provide pressure distributions based on medical images would represent a step forward for CoA clinical management.

Chapter 2

Materials and methods

In the first part of this chapter, the workflow developed to calculate pressure differences from 4D flow is described. The finite element framework for the solution of the Poisson pressure equation is illustrated. In the second part of this chapter, the patient-specific numerical simulations that were carried out are presented. Finally, the experimental test bench used to further validate in vivo pressure estimations will be described.

2.1 4D flow MRI-based pressure difference estimation

The methodologies described in this chapter were applied to a 4D flow dataset of a fiftyseven-year-old male patient with a CoA, which consisted of an 85% area reduction. 4D flow MRI and MRA acquisitions were provided by the Multimodality Cardiac Imaging Section, IRCCS Policlinico San Donato, San Donato Milanese, Milan, Italy. The algorithm developed in this thesis work will be referred to as 4DF-FEPPE.

2.1.1 Image visualization and segmentation

Using in-house MATLAB code, PC-MRI datasets were imported and visualized. Briefly, the employed tool uses the MATLAB function *dicomread* to create a 5-dimensional matrix containing the three velocity components for each row, column, slice and frame of the acquired volume (Figure 2.1).

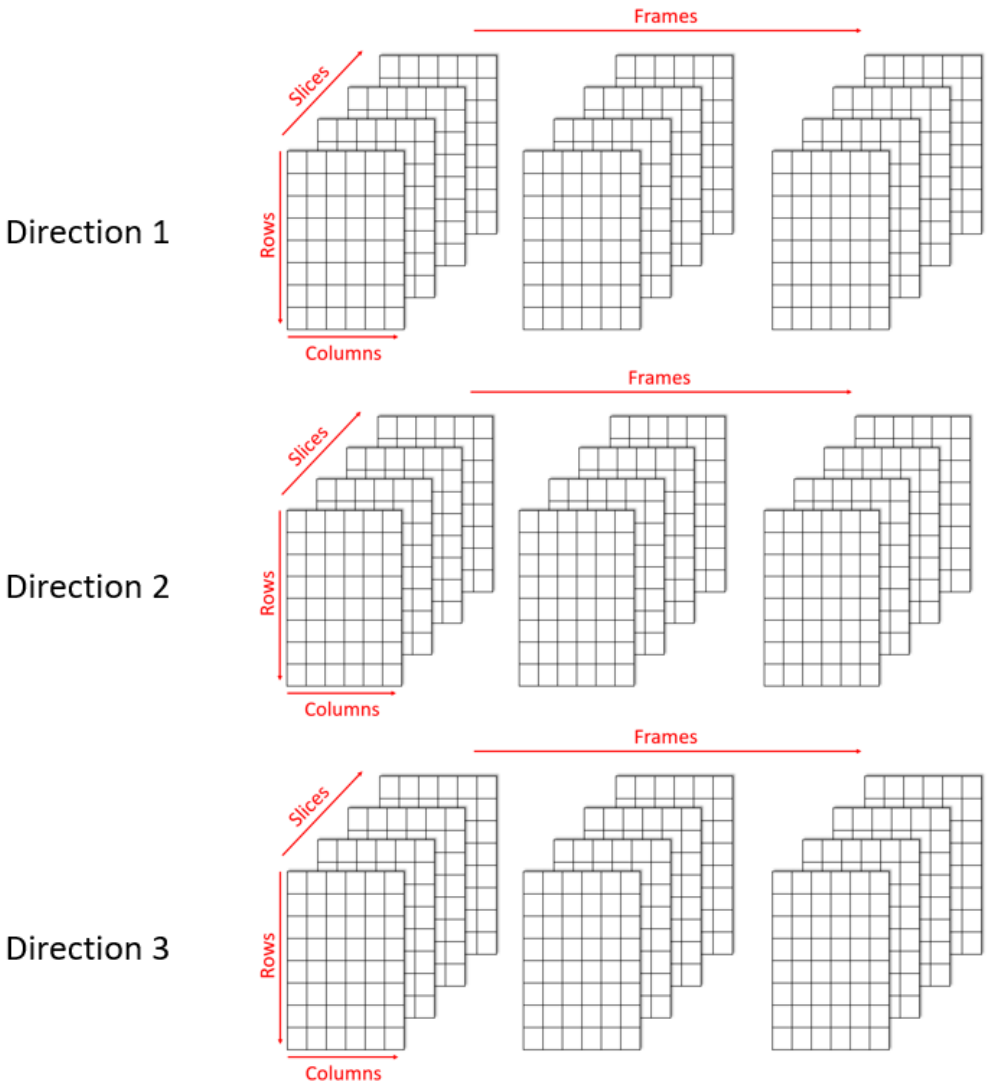

Figure 2.1: Schematic representation of the 5D velocity matrix created in MATLAB to deal with 4D flow data.

In order to observe anatomical structures more clearly, phase contrast magnetic resonance angiographic (PCMRA) images were derived from the magnitude images and velocity components as [100]:

$$PCMRA = \sqrt{\frac{1}{N}\sum_{t=1}^{N} M^2(t) \cdot \Big((v_x^2(t) + v_y^2(t) + v_z^2(t)\Big)}, \tag{2.1}$$

where N is the total number of frames, M represents the magnitude images and v the velocity images. Once all variables were properly generated by the code, PC-MRA images were visualized (Figure 2.2) and, from these, a static 3D region of interest (ROI) encom-

passing the coarctation was extracted by manually tracing vessel contours in each slice (Figure 2.3). The ROI was stored as a binary matrix, whose dimensions corresponded to the image volume dimensions. For each voxel selected in the segmentation process, the corresponding element in the ROI matrix was set equal to 1.

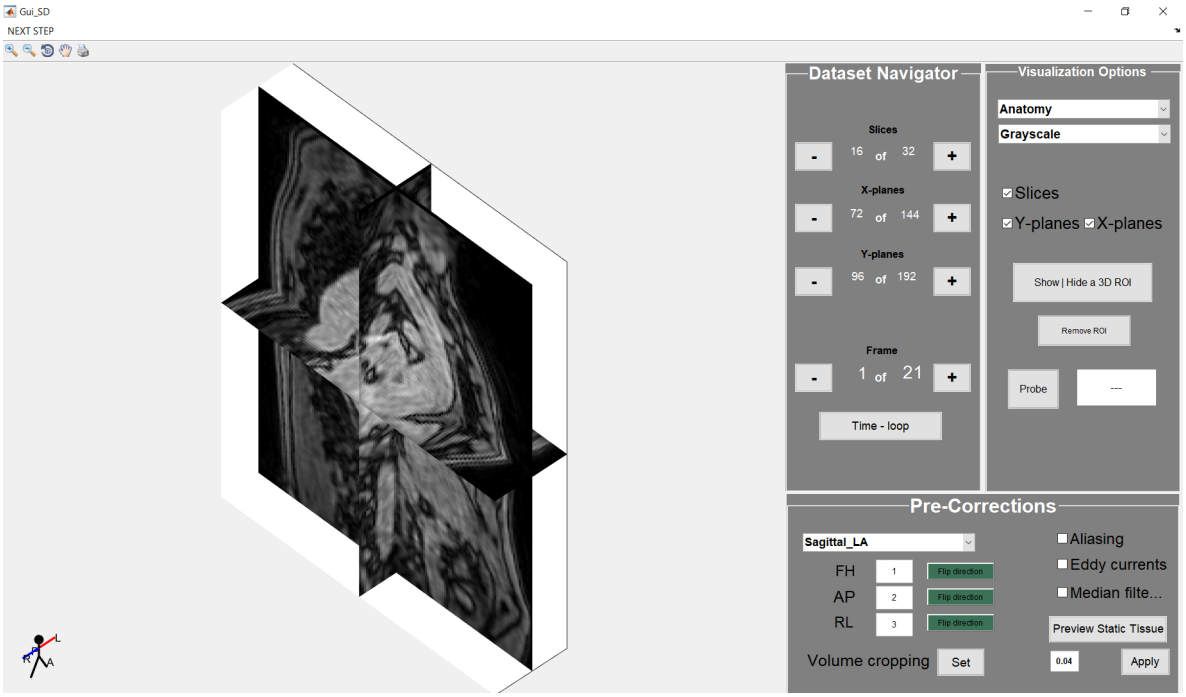

Figure 2.2: Visualization of 4D flow images through the in-house MATLAB code.

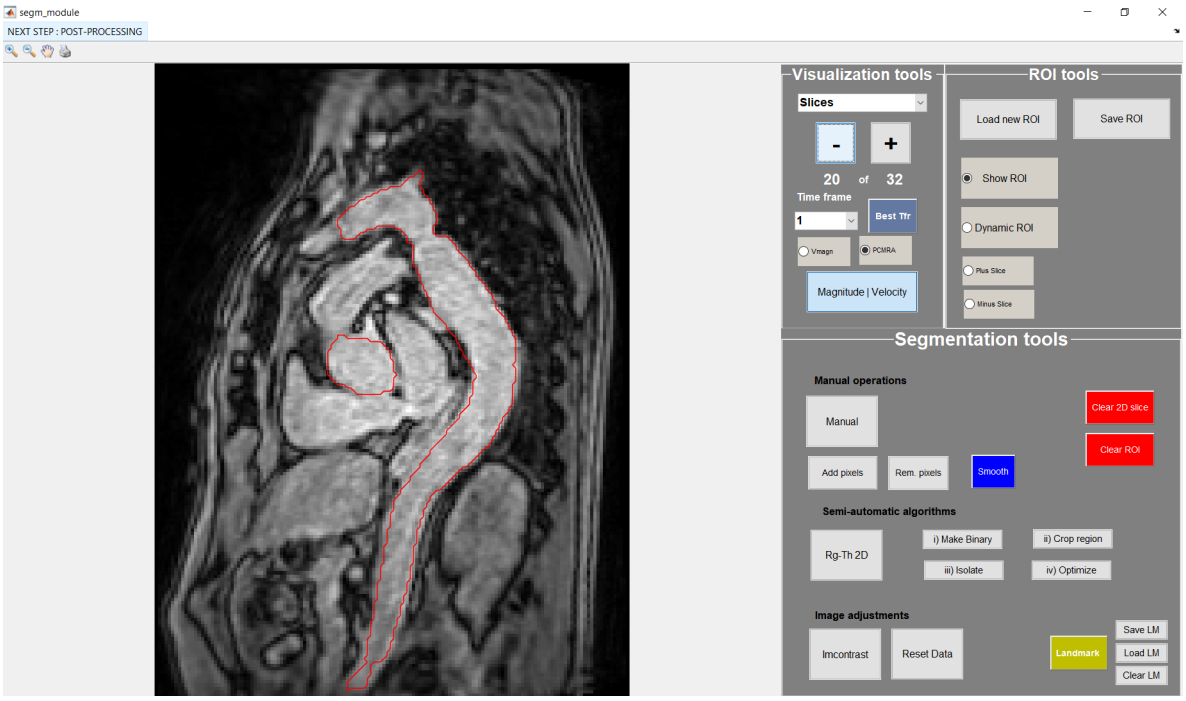

Figure 2.3: Screenshot of one slice of the 4D flow image volume segmented with the manual segmentation tool.

2.1.2 Anti-aliasing correction

The analyzed datasets showed aliasing in a number of voxels close to the coarctation (Figure 2.4a). This artifact was manually removed in each affected image through previously written in-house MATLAB code. Briefly, this tool allowed to visualize an image and select the pixels of interest, changing their associated velocity value to *VENC* or making them equal to other selected pixel (Figure 2.4b).

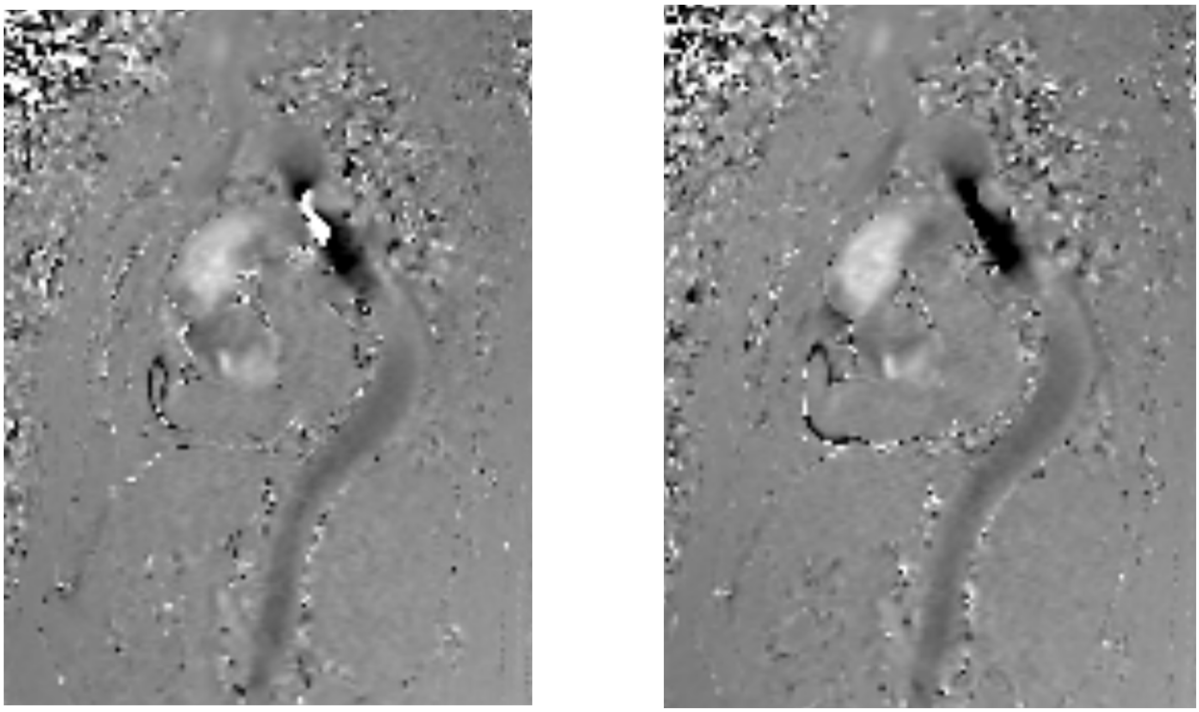

a **b**

Figure 2.4: Aliasing appearing as pixels with velocity value opposite to surroundings (a) and corrected (b).

2.1.3 Finite element solution of the Poisson pressure equation

Governing equations

The workflow adopted in the present study was in part based on the approach proposed by Krittian et al. [87]. In this work, the authors show that the PPE can be derived directly from the Navier–Stokes equations, which, on an arbitrary Eulerian reference frame can be formulated as:

$$-\nabla p = \rho\left(\frac{\partial \boldsymbol{v}}{\partial t} + \boldsymbol{v}\cdot\nabla\boldsymbol{v} - g\right) - \mu\Delta\boldsymbol{v}, \tag{2.2}$$

coupled with the divergence free condition due to the incompressibility of the fluid:

$$\nabla\cdot\boldsymbol{v} = 0, \tag{2.3}$$

where $\boldsymbol{v}$ represents the velocity field, p pressure, g external forces, μ the dynamic viscosity and ρ blood density. Hence, such pressure calculation method is based directly on the continuum mechanics principles of mass and momentum conservation. Taking the divergence of Navier-Stokes equation, the PPE is obtained:

$$-\Delta p = \nabla\cdot\left[\rho\left(\frac{\partial \boldsymbol{v}}{\partial t} + \boldsymbol{v}\cdot\nabla\boldsymbol{v} - g\right) - \mu\Delta\boldsymbol{v}\right]. \tag{2.4}$$

In a more compact form:

$$\Delta p = \nabla\cdot\boldsymbol{b}. \tag{2.5}$$

It is worth noticing that the right hand side of the equation depends exclusively of the acquired velocity field. As a partial differential equation, the corresponding pressure field can then be solved using finite elements, avoiding, with respect to finite differences, the use of unknown gradient boundary conditions. Multiplying Equation 2.5 by a test function q and integrating in the domain Ω, its weak form can be obtained; find $p \in$

$H^1(\Omega)$ such that:

$$\int_\Omega (\nabla \cdot \nabla p) q d\Omega = \int_\Omega (\nabla \cdot \boldsymbol{b}) q d\Omega, \qquad \forall q \in H^1(\Omega), \tag{2.6}$$

where $H^1(\Omega)$ is the Sobolev space of square-integrable functions with first derivatives in Ω. Integrating by parts both sides of Equation 2.6, leads to the surface integral:

$$\int_\Omega ((\nabla p - \boldsymbol{b}) \cdot \boldsymbol{n}) q d\Omega = 0, \tag{2.7}$$

leaving the volume integrals:

$$\int_\Omega \nabla p \cdot \nabla q d\Omega = \int_\Omega \boldsymbol{b} \cdot \nabla q d\Omega, \qquad \forall q \in H^1(\Omega). \tag{2.8}$$

Adopting a Galerkin finite element approximation, Equation 2.8 can be written as a linear system:

$$\mathbf{Kp} = \sum_{l=1}^{3} \mathbf{L}^{(x_l)} \mathbf{b}^{(x_l)}, \qquad l = 1, 2, 3. \tag{2.9}$$

$\mathbf{K}$ is the stiffness matrix and it is defined as:

$$\mathbf{K} = \underset{e=1}{\overset{n_{el}}{\mathrm{A}}} \left[\int_{\Omega_e} \nabla N_i \cdot \nabla N_j \right], \tag{2.10}$$

while $\mathbf{L}^{(x_l)}$ is a non-symmetric matrix:

$$\mathbf{L}^{(x_l)} = \underset{e=1}{\overset{n_{el}}{\mathrm{A}}} \left[\int_{\Omega_e} N_i \frac{\partial N_j}{\partial x_l} \right], \qquad l = 1, 2, 3, \tag{2.11}$$

where N_i are the finite element shape functions, n_{el} is the total number of elements, Ω_e represents the element domain and A is the assembly operator.

Finally, for all time steps a zero pressure was imposed at the lowest point in the descending aorta as boundary condition. All pressure values within the domain are then pressure differences with respect to this point.

Mesh generation

A preliminary mesh made of 8-node linear hexahedral elements was built within the whole image volume such that all vertices coincided with voxel centers (Figure 2.5). Consequently, element edge lengths were the same for all hexahedra and corresponded to the image dataset pixel spacings. The extracted ROI was then applied to the preliminary mesh as a mask in order to filter out the elements outside the selected domain while keeping the elements inside (Figure 2.6).

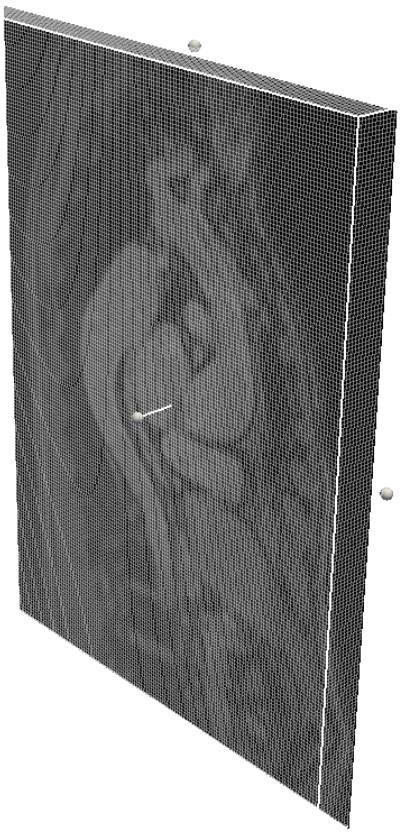

Figure 2.5: Preliminary hexahedral mesh over the whole image domain.

Figure 2.6: Masked mesh on the image domain visualized as a white wireframe.

Subsequently, a co-registration was performed using an additional segmented model (obtained through the procedure described in Section 2.2): the *.stl* file representing the geometry was imported in MATLAB as a point cloud, which was registered to the 4D flow-based mesh using the function *pcregrigid*. Additionally, to avoid error propagation near the walls, the *.stl* file volume was first shrunk using the mesh analysis software Meshmixer (Autodesk, San Rafael, CA, USA) and its volume was reduced by approximately 30% (Figure 2.7).

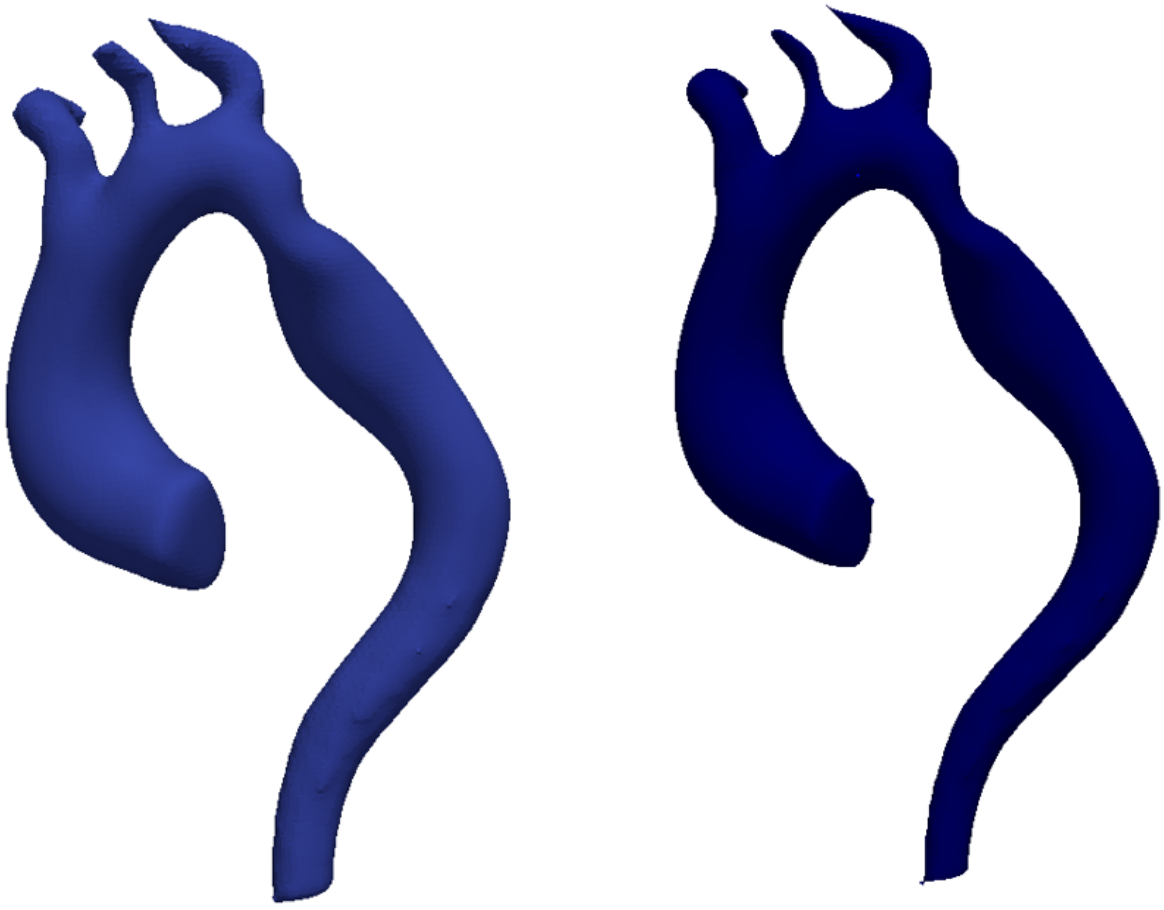

a **b**

Figure 2.7: Visualization of the original *.stl* volume (a) and its shrunk version (b), used for computing pressure differences from 4D flow.

Finite element framework

All mesh elements were hexahedra, each with 8 nodes (Figure 2.8), whose dimensions corresponded to the acquired voxel spacings. These elements are also referred to as "brick" elements in the finite element literature. With an isoparametric formulation, each element's shape functions are Lagrangian polynomials defined as:

$$N_i = \frac{1}{8}(1+\xi_i\xi)(1+\eta_i\eta)(1+\mu_i\mu), \qquad i = 1, 2, ...8, \tag{2.12}$$

where ξ_i, η_i and μ_i are the natural coordinates of the *i-th* node (Figure 2.8).

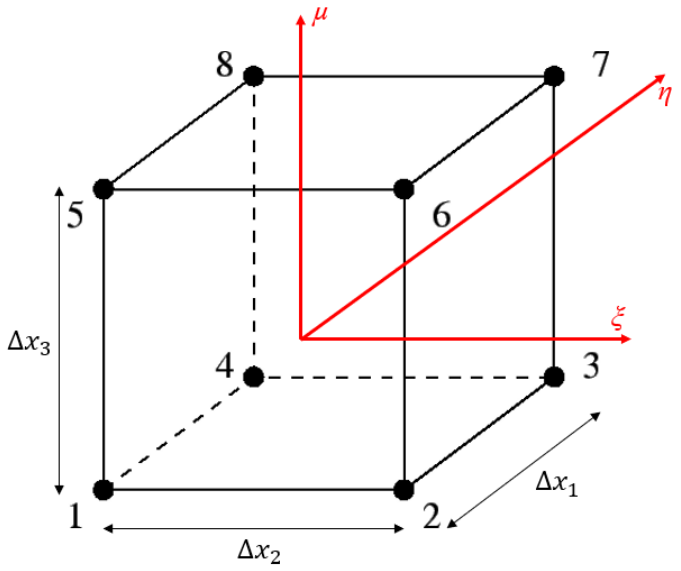

Figure 2.8: Representation of the 8-node linear hexahedron with its natural coordinates.

In order to be able to define the algebraic matrices in Equation 2.9, one must calculate the partial derivatives of each hexahedron's shape functions with respect to Cartesian coordinates. Using the chain rule, for the *i-th* node:

$$\frac{\partial N_i}{\partial x_l} = \frac{\partial N_i}{\partial \xi}\frac{\partial \xi}{\partial x_l} + \frac{\partial N_i}{\partial \eta}\frac{\partial \eta}{\partial x_l} + \frac{\partial N_i}{\partial \mu}\frac{\partial \mu}{\partial x_l}, \qquad l = 1, 2, 3. \tag{2.13}$$

Rewriting Equation 2.13 in matrix form:

$$\begin{bmatrix} \frac{\partial N_i}{\partial x_1} \\ \frac{\partial N_i}{\partial x_2} \\ \frac{\partial N_i}{\partial x_3} \end{bmatrix} = \begin{bmatrix} \frac{\partial \xi}{\partial x_1} & \frac{\partial \eta}{\partial x_1} & \frac{\partial \mu}{\partial x_1} \\ \frac{\partial \xi}{\partial x_2} & \frac{\partial \eta}{\partial x_2} & \frac{\partial \mu}{\partial x_2} \\ \frac{\partial \xi}{\partial x_3} & \frac{\partial \eta}{\partial x_3} & \frac{\partial \mu}{\partial x_3} \end{bmatrix} \begin{bmatrix} \frac{\partial N_i}{\partial \xi} \\ \frac{\partial N_i}{\partial \eta} \\ \frac{\partial N_i}{\partial \mu} \end{bmatrix} = \mathbf{J}^{-1} \begin{bmatrix} \frac{\partial N_i}{\partial \xi} \\ \frac{\partial N_i}{\partial \eta} \\ \frac{\partial N_i}{\partial \mu} \end{bmatrix}, \tag{2.14}$$

where **J** is the Jacobian matrix defined as:

$$\mathbf{J} = \begin{bmatrix} \frac{\partial x_1}{\partial \xi} & \frac{\partial x_2}{\partial \xi} & \frac{\partial x_3}{\partial \xi} \\ \frac{\partial x_1}{\partial \eta} & \frac{\partial x_2}{\partial \eta} & \frac{\partial x_3}{\partial \eta} \\ \frac{\partial x_1}{\partial \mu} & \frac{\partial x_2}{\partial \mu} & \frac{\partial x_3}{\partial \mu} \end{bmatrix}. \tag{2.15}$$

Then, to evaluate the integrals in Equations 2.10 and 2.11, Gauss integration was implemented. In case of 8-node hexahedral elements (Figure 2.8), the number of integration

points for each direction p must be such that $p \geq 2$. Then, in computing the aforementioned integrals (Equations 2.10 and 2.11), $p = 2$ was chosen. With this choice, Gauss points natural coordinates (α) and weights (ω) are shown in Table 2.1:

$\alpha = \xi, \eta, \mu$	ω
$\sqrt{1/3}$	1
$-\sqrt{1/3}$	1

Table 2.1: Points and weights for 2-point Gauss integration.

For each element, rewriting Equations 2.12 and 2.13 in matrix form, the matrices $\mathbf{N}$ and $\mathbf{B}$ were defined as:

$$\mathbf{N} = \begin{bmatrix} N_1 & N_2 & N_3 & N_4 & N_5 & N_6 & N_7 & N_8 \end{bmatrix}, \tag{2.16}$$

$$\mathbf{B} = \begin{bmatrix} \frac{\partial \mathbf{N}}{\partial \xi} \\ \frac{\partial \mathbf{N}}{\partial \eta} \\ \frac{\partial \mathbf{N}}{\partial \mu} \end{bmatrix} = \begin{bmatrix} \frac{\partial N_1}{\partial \xi} & \frac{\partial N_2}{\partial \xi} & \frac{\partial N_3}{\partial \xi} & \frac{\partial N_4}{\partial \xi} & \frac{\partial N_5}{\partial \xi} & \frac{\partial N_6}{\partial \xi} & \frac{\partial N_7}{\partial \xi} & \frac{\partial N_8}{\partial \xi} \\ \frac{\partial N_1}{\partial \eta} & \frac{\partial N_2}{\partial \eta} & \frac{\partial N_3}{\partial \eta} & \frac{\partial N_4}{\partial \eta} & \frac{\partial N_5}{\partial \eta} & \frac{\partial N_6}{\partial \eta} & \frac{\partial N_7}{\partial \eta} & \frac{\partial N_8}{\partial \eta} \\ \frac{\partial N_1}{\partial \mu} & \frac{\partial N_2}{\partial \mu} & \frac{\partial N_3}{\partial \mu} & \frac{\partial N_4}{\partial \mu} & \frac{\partial N_5}{\partial \mu} & \frac{\partial N_6}{\partial \mu} & \frac{\partial N_7}{\partial \mu} & \frac{\partial N_8}{\partial \mu} \end{bmatrix}, \tag{2.17}$$

then, element matrices (Equations 2.10, 2.11) were calculated as:

$$\mathbf{K}^{(e)} = \sum_{i=1}^{p} \sum_{j=1}^{p} \sum_{k=1}^{p} \omega_{ijk} \mathbf{B}_{ijk}^{T} \mathbf{B}_{ijk} J_{ijk}, \tag{2.18}$$

$$\mathbf{L}^{(e)(x_1)} = \sum_{i=1}^{p} \sum_{j=1}^{p} \sum_{k=1}^{p} \omega_{ijk} \left(\frac{\partial \mathbf{N}}{\partial \xi} \right)_{ijk}^{T} \mathbf{N}_{ijk} J_{ijk}, \tag{2.19}$$

$$\mathbf{L}^{(e)(x_2)} = \sum_{i=1}^{p} \sum_{j=1}^{p} \sum_{k=1}^{p} \omega_{ijk} \left(\frac{\partial \mathbf{N}}{\partial \eta} \right)_{ijk}^{T} \mathbf{N}_{ijk} J_{ijk}, \tag{2.20}$$

$$\mathbf{L}^{(e)(x_3)} = \sum_{i=1}^{p} \sum_{j=1}^{p} \sum_{k=1}^{p} \omega_{ijk} \left(\frac{\partial \mathbf{N}}{\partial \mu} \right)_{ijk}^{T} \mathbf{N}_{ijk} J_{ijk}, \tag{2.21}$$

where the subscripts ijk imply: $(\cdot)_{ijk} = (\cdot)_i (\cdot)_j (\cdot)_k$ and $J = det(\mathbf{J})$.

Finally, global matrices were assembled as sparse and the linear system (Equation 2.9) was solved. Mesh nodes and elements with their associated velocity and pressure fields

were then written as *.vtk* files that could be read by the visualization software Paraview (Kitware, Clifton Park, NY, USA), which was used for results post-processing.

Numerical approximation of the pressure gradient

In order to solve the PPE (Equation 2.4), the right-hand side of equation 2.2 must be defined. For each time frame of the phase-contrast cardiac sequence, velocity first and second order spatial derivatives were calculated using various combinations of finite difference schemes. In particular, to attain the highest possible accuracy, first order derivatives were approximated by 4^{th} order schemes (Equations 2.22, 2.23, 2.24) in the internal points of the domain, while 3^{rd} order schemes (Equations 2.25, 2.26) were used on the boundaries.

$$y'(x) + O(h^4) = \frac{-y(x+2h) + 8y(x+h) - 8y(x-h) + y(x-2h)}{12h}, \tag{2.22}$$

$$y'(x) + O(h^4) = \frac{-3y(x-h) - 10y(x) + 18y(x+h) - 6y(x+2h) + y(x+3h)}{12h}, \tag{2.23}$$

$$y'(x) + O(h^4) = \frac{3y(x+h) + 10y(x) - 18y(x-h) + 6y(x-2h) - y(x-3h)}{12h}, \tag{2.24}$$

$$y'(x) + O(h^3) = \frac{-11y(x) + 18y(x+h) - 9y(x+2h) + 2y(x+3h)}{6h}, \tag{2.25}$$

$$y'(x) + O(h^3) = \frac{11y(x) - 18y(x-h) + 9y(x-2h) - 2y(x-3h)}{6h}. \tag{2.26}$$

$$y'(x) + O(h^2) = \frac{y(x+h) - y(x-h)}{2h} \tag{2.27}$$

$$y'(x) + O(h^2) = \frac{-3y(x) + 4y(x+h) - y(x+2h)}{2h} \tag{2.28}$$

$$y'(x) + O(h^2) = \frac{3y(x) - 4y(x-h) + y(x-2h)}{2h} \tag{2.29}$$

Similarly, second order derivatives were approximated using $4th$ order (Equations 2.30) and 3^{rd} order (Equations 2.31, 2.32) schemes where applicable, and 2^{nd} order schemes

(Equations 2.33, 2.34, 2.35) on the boundaries.

$$y''(x) + O(h^4) = \frac{-y(x+2h) + 16y(x+h) - 30y(x) + 16y(x-h) - y(x-2h)}{12h^2}, \quad (2.30)$$

$$y''(x) + O(h^3) = \frac{11y(x-h) - 20y(x) + 6y(x+h) + 4y(x+2h) - y(x+3h)}{12h^2}, \quad (2.31)$$

$$y''(x) + O(h^3) = \frac{11y(x+h) - 20y(x) + 6y(x-h) + 4y(x-2h) - y(x-3h)}{12h^2}, \quad (2.32)$$

$$y''(x) + O(h^2) = \frac{y(x+h) - 2y(x) + y(x-h)}{h^2}, \quad (2.33)$$

$$y''(x) + O(h^2) = \frac{2y(x) - 5y(x+h) + 4y(x+2h) - y(x+3h)}{h^2}, \quad (2.34)$$

$$y''(x) + O(h^2) = \frac{2y(x) - 5y(x-h) + 4y(x-2h) - y(x-3h)}{h^2}. \quad (2.35)$$

The decrease in order of accuracy near the volume boundaries is forced by the dependency on neighboring nodes of higher order finite difference schemes. Time derivatives were calculated using 2^{nd} order schemes (Equations 2.27, 2.28, 2.29).

2.1.4 Evaluation of the effect of a divergence-free wavelet filter

In order to reduce noise-like phase errors that are present in 4D flow acquisitions, the effect of the DFW filter developed by Ong et al. [11] was investigated. A MATLAB implementation of such filter was freely downloaded from: `http://www.eecs.berkeley.edu/~mlustig/Software.html`. Briefly, the three velocity components measured with 4D flow are processed through forward wavelet transforms, which allow to separate the velocity field in a divergence-free component and a non-divergence-free component. Then, a soft divergence-free condition is enforced by shrinking the two components coefficients through a threshold, without strictly requiring a divergence-free velocity field (Figure 2.9). Several strategies can be used for appropriate threshold selection; in this thesis, however,

only an automatic criterion for threshold selection was adopted, which was embedded in the MATLAB implementation. Then, the divergence-free and non-divergence-free components are combined back together, and the three divergence-free velocities are obtained through an inverse wavelet transform (Figure 2.9).

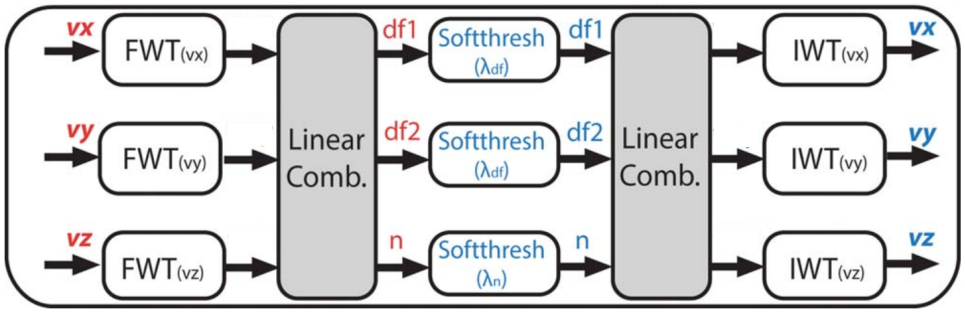

Figure 2.9: Diagram of DFW denoising. Separate wavelet transforms are applied on each velocity component and the coefficients are linearly combined. (FWT: forward wavelet transform, IWT: inverse wavelet transform, df: divergence-free, n: nondivergence-free. Modified from [11].

Overall, the DFW filter allows to achieve robust 4D flow denoising, resulting in a velocity field that is closer to the divergence-free condition. A more in-depth description of the DFW filter can be found in [11].

In order to quantify denoising performance, the normalized root mean squared error (NRMSE) in velocity magnitude was calculated as [11]:

$$NRMSE = \frac{1}{max_i(\mid v_{i,ref} \mid)} \sqrt{\frac{1}{N} \sum_{i=0}^{N} (\mid v_{i,ref} - v_{i,dfw} \mid)}, \tag{2.36}$$

where $v_{i,ref}$ and $v_{i,dfw}$ are the reference and denoised velocity magnitudes respectively, at the i^{th} voxel in the domain, with N being the total number of voxels.

The effect of the DFW filter on the synthetically generated noisy velocity fields can be visualized in Figure 2.12.

2.1.5 Validation against a synthetic dataset

In order to validate the FE-PPE through the previously described approach, a transient CFD simulation was carried out using Fluent (Ansys Inc., Canonsburg, PA, USA). An idealized 3D model of a healthy aorta (Figure 2.10) was meshed using ICEM (Ansys Inc., Canonsburg, PA, USA).

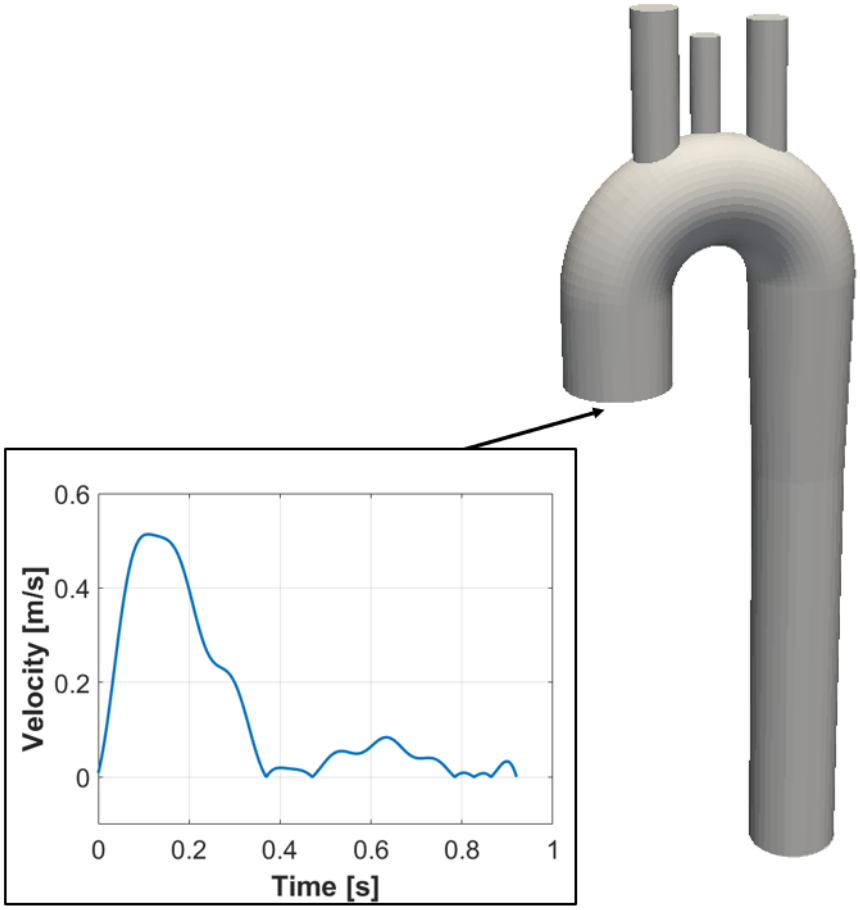

Figure 2.10: Idealized 3D model of healthy aorta used for a CFD simulation whose results were exported to generated a synthetic dataset.

The unstructured mesh comprised of a mix of tetrahedral and hexahedral elements, for a total of 143599 elements. A time-dependent velocity was imposed at the aorta inlet (Figure 2.10), while supra-aortic branches and aorta outlets were set as zero-pressure outlets. A no-slip condition was assumed at the wall, and blood was modeled as an incompressible Newtonian fluid ($\mu = 3.5$ cP, $\rho = 1060$ kg/m^3). Artificial 4D flow datasets were

obtained following the methodology described in [101] and [10], using in-house software. Velocities and element Cartesian coordinates were exported from the simulation results, then, velocity fields were downsampled to mimic a voxel grid with an isotropic spatial resolution of 2 mm (Figure 2.11b). Since the CFD-based mesh enjoys a much higher resolution, more than one point of the CFD mesh fall within each voxel of the downsampled domain. Therefore, the velocity components associated with each voxel were calculated as a weighted average of the CFD-derived velocities within the voxel itself. The weights associated to the points falling within each voxel were computed with a Gaussian function of their distance to the voxel center. Then, Gaussian noise with a *VENC* related variance was added to the downsampled velocity fields to emulate 4D MRI noise (Figure 2.11c). In particular, noise exceeding the actual maximum velocity by 5% was added. Furthermore, CFD simulations allow for a much higher temporal resolution than cine-MRI acquisition. Therefore, Fluent-based velocity fields corresponding to six systolic time points were exported with an interval of 0.045 s between each other. Downsampled velocities and noisy downsampled velocities were then used as input for the solution of the FE-PPE following the workflow previously described. The effect of both downsampling and noise addition on the computed pressure distributions was evaluated by comparing the FE-PPE solution to the simulation results. In this analysis, pressure differences were calculated with respect to the lowest point of the descending aorta, where pressure was set to zero at all time steps. Finally, velocity fields with the addition of Gaussian noise were processed using the DFW filter (described in Subsection 2.1.4). In this regard, application of the DFW on the noisy velocity field was performed iteratively until good qualitative agreement with downsampled velocities was observed and until the $NRMSE$ (Equation 2.36), calculated using downsampled velocities as reference, was reduced by at least 50% with respect to the $NRMSE$ calculated between downsampled and noisy velocities. Therefore, the DFW filter was applied for 10 iterations. Then, the resulting velocity fields were used as input for 4DF-FEPPE.

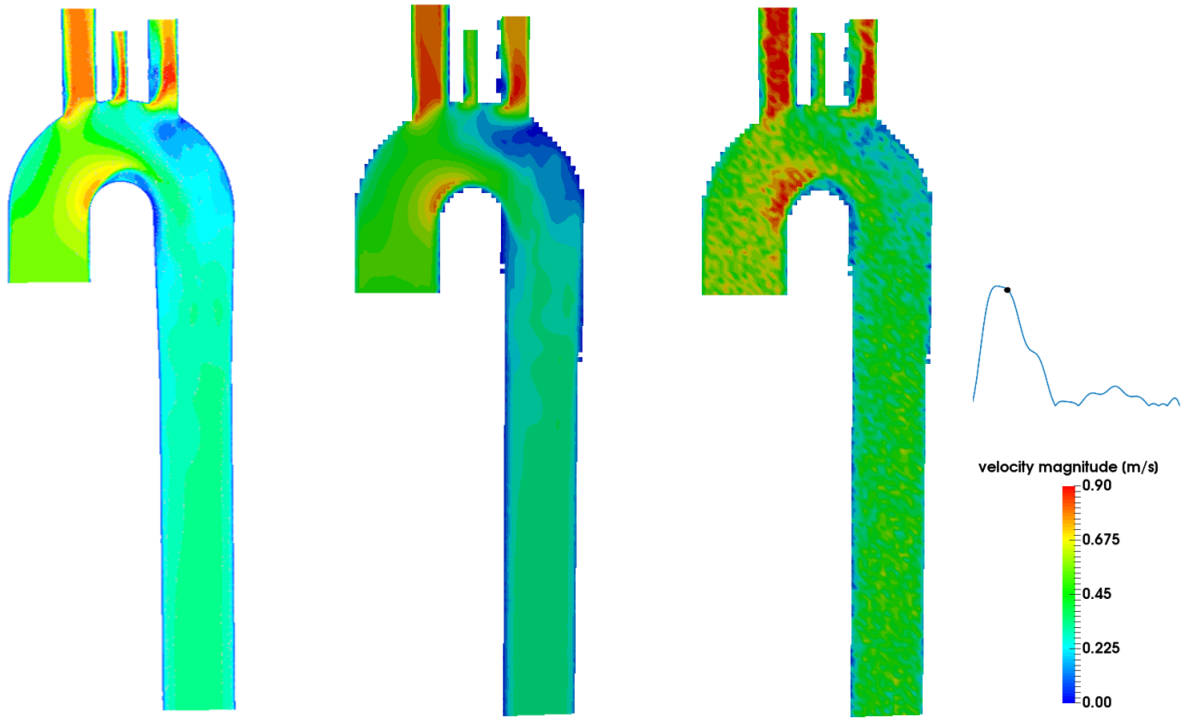

Figure 2.11: Effect of downsampling (b) and noise addition (c) on the original velocity field obtained from Fluent (a).

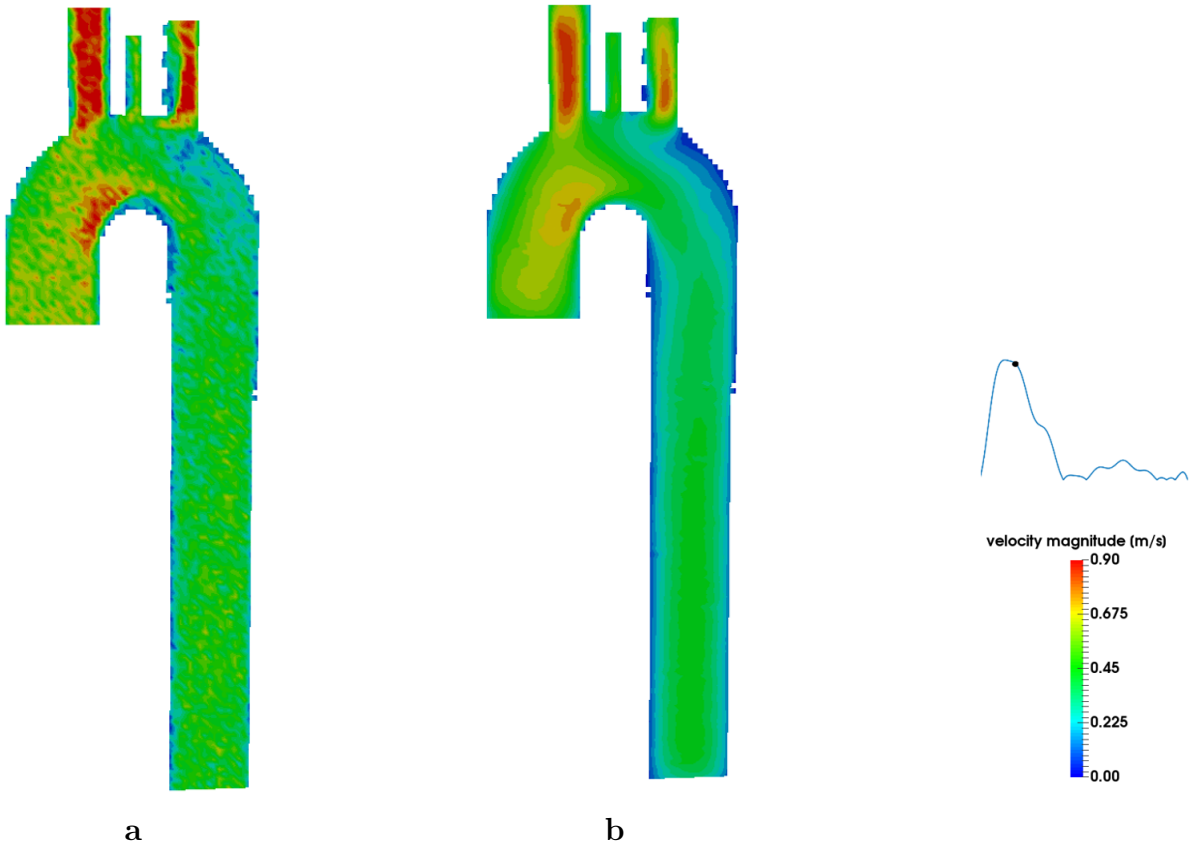

Figure 2.12: Effect of DFW filter on a synthetically generated noisy velocity field; before (a) and after (b) filtering.

2.1.6 Comparison with a previously developed algorithm

Pressure fields were also calculated using in house MATLAB code previously developed by Prof. Sergii V. Siryk and used in [102]. This approach (referred to as Siryk-FEPPE) differs from the one implemented in this work, mainly, in the finite element framework setup. In fact, instead of building a hexahedral voxel-based mesh (Section 2.1.3), Siryk-FEPPE takes advantage of the Partial Differential Equation MATLAB toolbox to generate a tetrahedral mesh and to setup the finite element framework automatically. Another difference between the 4DF-FEPPE and Siryk-FEPPE methodologies lies in the way numerical derivatives are calculated near the volume boundaries. In 4DF-FEPPE, lower order finite difference schemes are used for the image volume boundaries, regions in which, usually, vessels of interest do not lie. In this way, if the ROI lies well within the image volume, all derivatives are approximated by 4^{th} order schemes. Instead, in Siryk-FEPPE the points where lower order finite difference schemes are used lie on the boundary of the ROI.

2.2 Numerical simulations

The numerical simulations described in this chapter were carried out using the open-source software CRIMSON (**C**ardiovascula**r** **I**ntegrated **M**odelling and **S**imulatio**n**). The CRIMSON environment is equipped with a user-friendly and intuitive graphic user interface (GUI) and allows to run 3D finite element simulations of blood flow and vessel wall elastodynamics.

These simulations accounted for both hemodynamics and linearized wall mechanics, and differed in the type of outlet boundary conditions. In all simulations, 3 element Winkessel (3-WK) models were assigned to all outlets (Figure 2.13). In tuning 3-WK parameters, a

mean pressure value was required, however, no patient-specific data was available. Therefore, in order to evaluate the effect of this value on the trans-coarctation pressure drop, two simulations are herein reported. In Simulation-1 a mean pressure of 80 mmHg was used to tune 3-WK for all outlets, whereas in Simulation-2 a mean pressure of 80 mmHg was used to tune the 3-WK at the DAo, while a mean pressure of 98 mmHg was used for the 3-WK at the supra-aortic branches outlets. This analysis was performed in order to evaluate the sensitivity of the trans-coarctation pressure drop to the mean pressure used to tune 3-WK at the outlets.

Simulations details will be further described in Sections 2.2.3 and 2.2.4. A representation of the simulation boundary condition setup can be visualized in Figure 2.13.

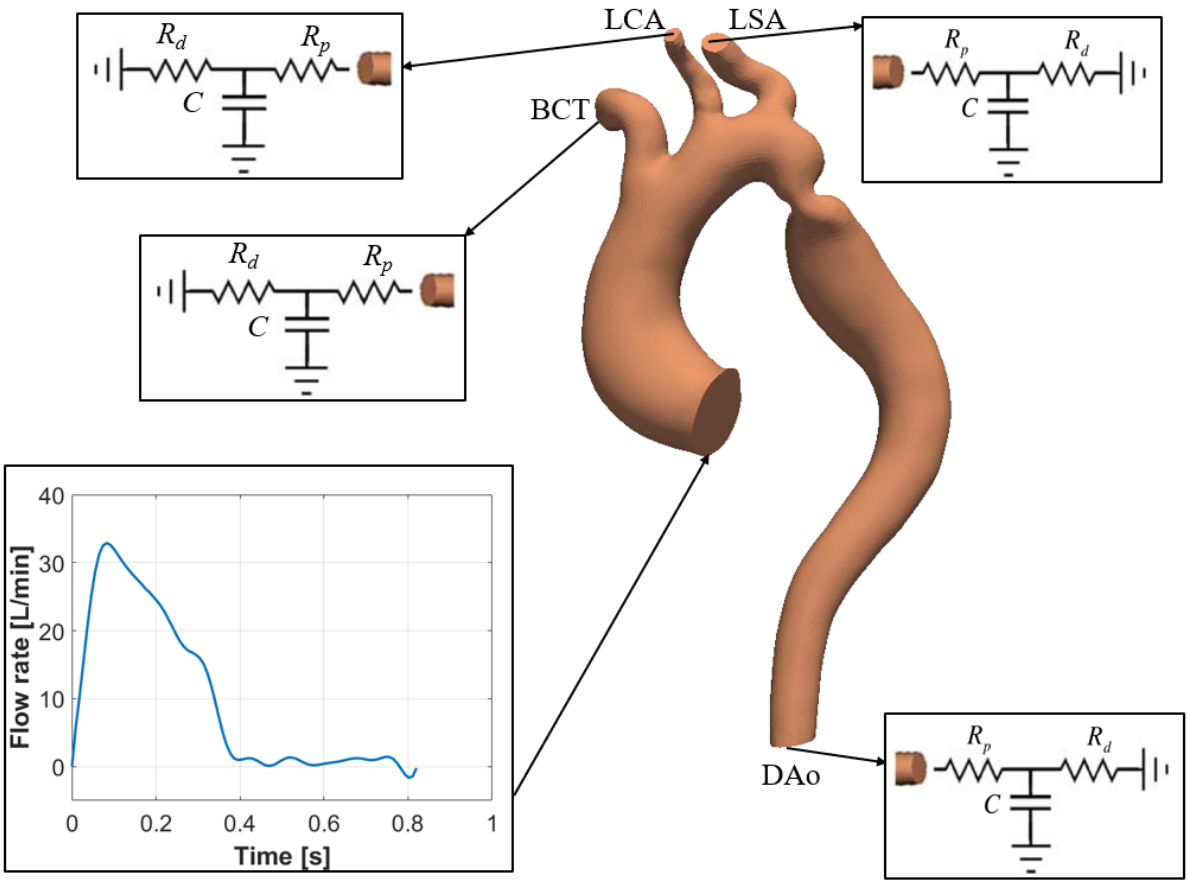

Figure 2.13: Description of the model boundary conditions used in the numerical simulations; the patient-specific transient flow rate was imposed at the inlet, while 3-WK were set as outlet boundary conditions for the brachiocephalic trunk (BCT), left carotid artery (LCA), left subclavian artery (LSA) and descending aorta (DAo).

2.2.1 Segmentation

A 3D geometry encompassing the aorta and the three supra-aortic vessels was segmented using the open-source software ITK-SNAP [103]. Through a combination of manual and semi-automatic tools, regions of interest were labeled and a 3D model was created (Figure 2.14). Segmentation was performed on magnetic resonance angiographic (MRA) images obtained with the use of a contrast agent.

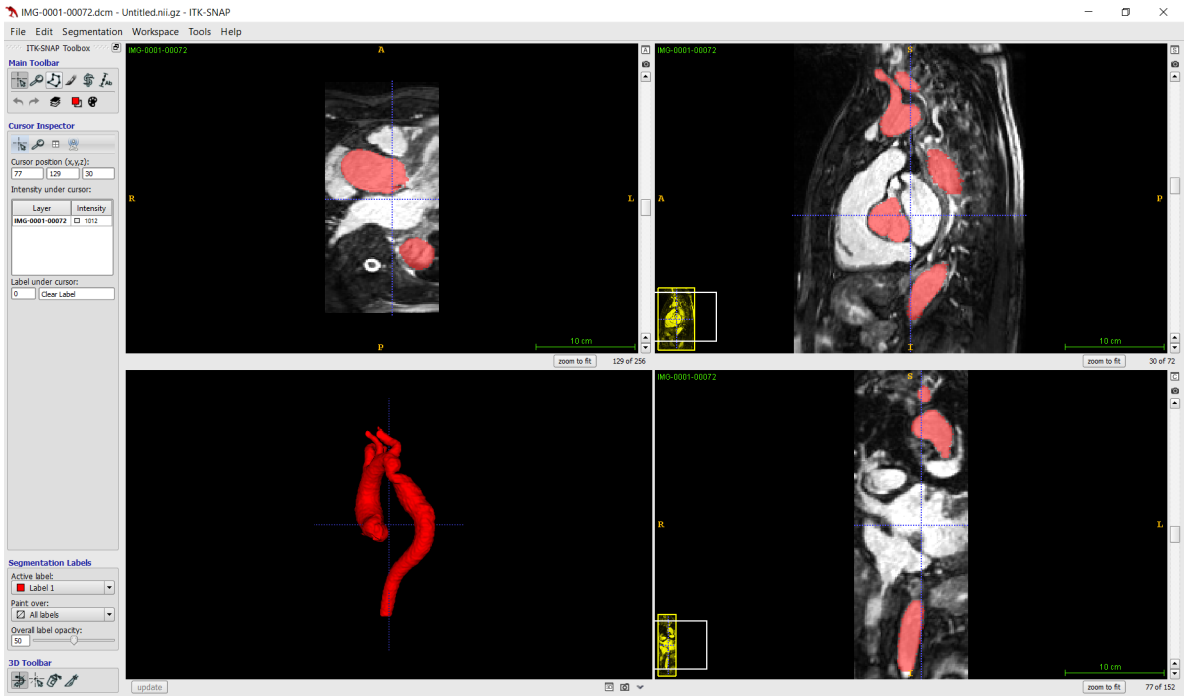

Figure 2.14: Screenshot of ITK-SNAP segmentation workspace; regions of interest are labeled in red and a representation of the 3D surface is visualized (bottom left panel).

The 3D surface was then exported (Figure 2.15a) as a *.vtk* file, converted to *.stl* in Paraview and further processed using Autodesk Meshmixer. In particular, both manual and automatic smoothing tools were employed, and the surface was clipped at the extremities (Figure 2.15b). Finally, the *.stl* surface was imported in CRIMSON to be meshed.

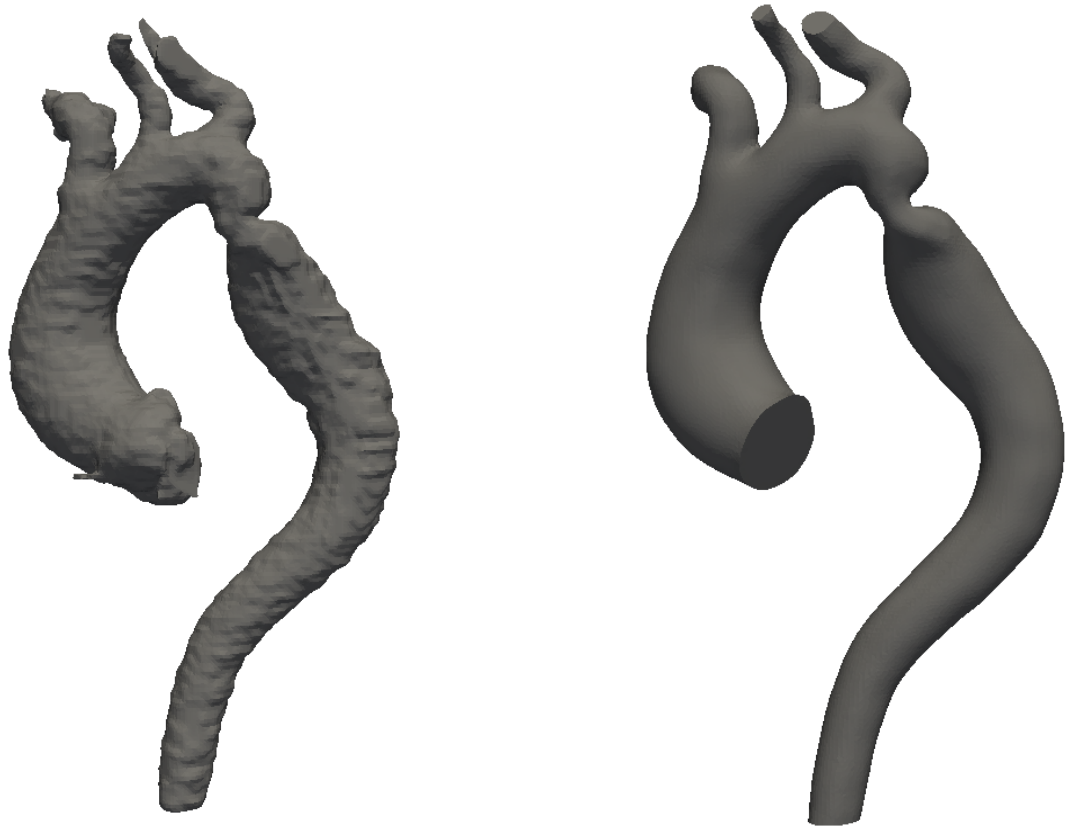

a b

Figure 2.15: Segmented 3D model before (a) and after (b) smoothing in Meshmixer.

2.2.2 Meshing

The geometry was meshed using CRIMSON embedded meshing tools. A sensitivity analysis was performed by running steady flow simulations using meshes consisting of ∼1.4, ∼2.4, ∼4 and ∼7.7 million elements. A steady flow rate corresponding to systolic peak was imposed at the inlet, while zero pressure was set for all outlets. For the four meshes, velocity magnitude contours within the coarctation are shown in Figure 2.16. Similar velocity patterns were captured by all three meshes, but different maximum values of velocity magnitude within the narrowing were computed with the four grids. To choose the best suited mesh, the maximum velocity magnitude value on a cross-section within the coarctation was chosen as parameter of grid convergence (Figure 2.16). Then, the Grid Convergence Index (GCI) [13] was calculated for the fine-to-medium and medium-

to-coarse grid refinements according to [14]. The GCI is a measure of how much the variable of interest (trans-coarctation maximum velocity magnitude) is different from the asymptotic numerical value; it indicates how much the calculated variable of interest would change with a further grid refinement.

Let the subscripts 1,2,3 indicate the fine, medium and coarse meshes respectively:

$$r \approx \left(\frac{N_1}{N_2}\right)^{1/3} \approx \left(\frac{N_2}{N_3}\right)^{1/3}, \tag{2.37}$$

$$p = \frac{\log\left(\frac{f_3 - f_2}{f2 - f1}\right)}{\log(r)}, \tag{2.38}$$

$$E_1 = \frac{\frac{f_2 - f_1}{f_1}}{r^p - 1}, \qquad E_2 = \frac{\frac{f_3 - f_2}{f_2}}{r^p - 1}, \tag{2.39}$$

$$GCI_{1,2} = F_s * |E_1|, \qquad GCI_{2,3} = F_s * |E_2|, \tag{2.40}$$

where N is the number of elements, f is the parameter of interest and F_s is the "factor of safety" equal to 1.25 [14]. In particular, $f_1 = 1.871$ m/s, $f_2 = 1.849$ m/s and $f_3 = 1.8209$ m/s were found. The mesh sensitivity analysis revealed that the solution computed by the fine was relatively insensitive to further mesh refinement (Figure 2.16), and the grid chosen herein was the fine one, corresponding to a grid $GCI_{1,2}$ of approximately 3.4%, which is in agreement with GCIs reported in recent studies [14, 104]. Additionally, to ensure that grids were in the asymptotic range of convergence the ratio: $k = \frac{GCI_{2,3}}{r^p \cdot GCI_{1,2}}$ was calculated, and the relation $k \approx 1$ was satisfied [13].

The chosen mesh consisted of a tetrahedra (Figure 2.17). Maximum element size was set as 0.9 mm and an exponential growth ratio between adjacent layers close to the boundary was chosen, with a minimum element thickness of 0.2 mm and a total thickness of 2 mm.

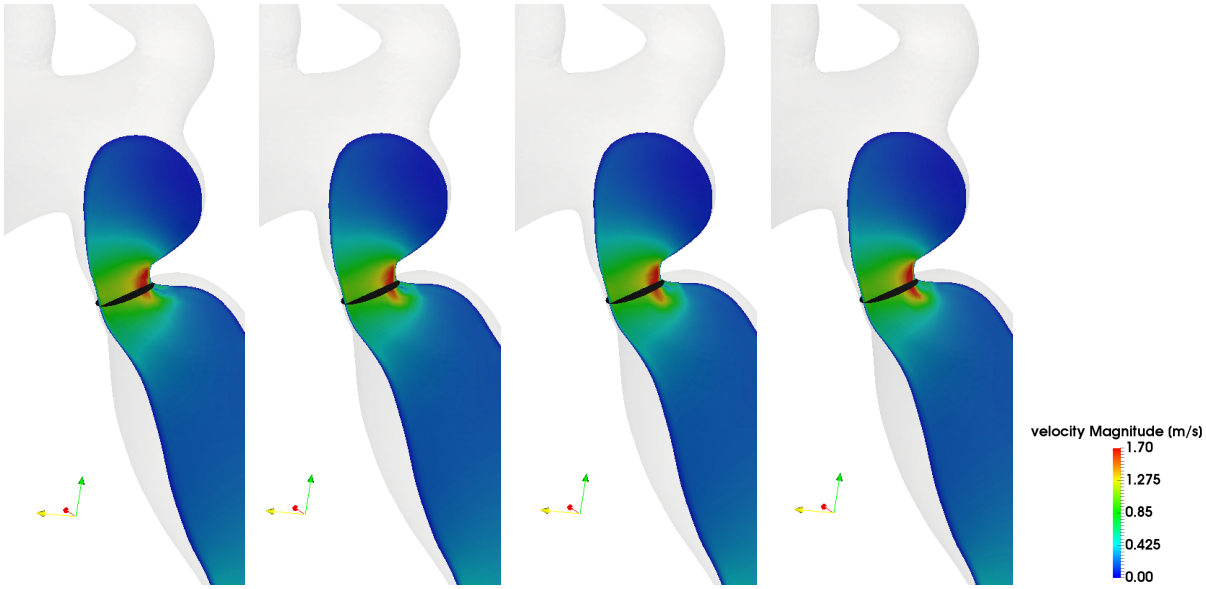

Figure 2.16: Velocity magnitude within the coarctation visualized in four meshes for sensitivity analysis: ∼1.4m element mesh (a), ∼2.4m element mesh (b), ∼4m element mesh (c) and ∼7.7m element mesh (d). Maximum velocity magnitude computed on the black cross-section was used as parameter of interest.

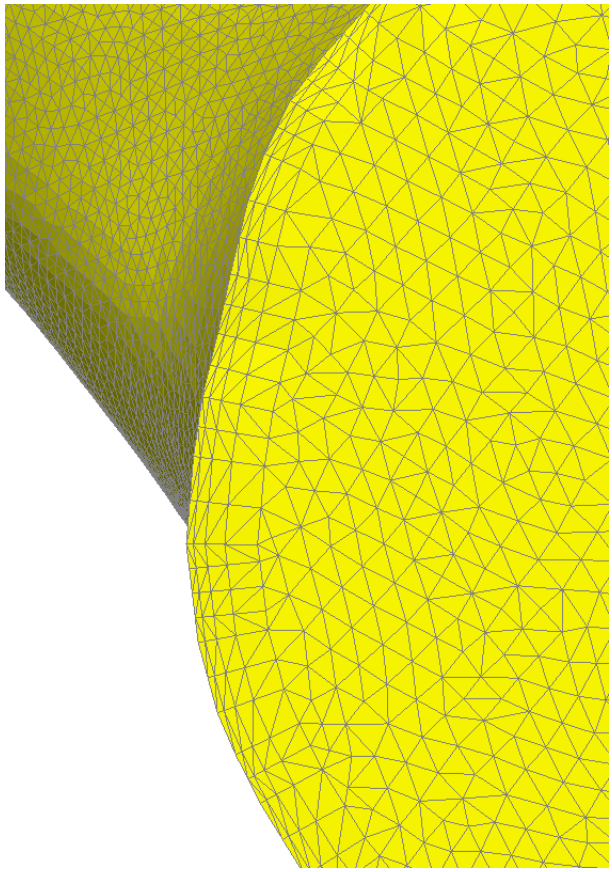

Figure 2.17: Visualization of mesh details in a zoomed in screenshot of the aortic inlet.

2.2.3 Boundary conditions: Simulation-1

Taking advantage of the procedure described at the end of Section 2.1.3, 4D flow velocity data were visualized in Paraview and a time-varying flow rate curve was extracted and used to prescribe the inlet boundary condition for the model. To account for the effect of distal vasculature and obtain physiological flow rate and pressure curves, at each outlet, 3-WK models were set as boundary conditions (Figure 2.13). The values reported in Table 2.2, were calculated following the approach described in [15]. Briefly, for each outlet an average pressure over the cardiac cycle $\overline{P} = 80$ mmHg was assumed; then the total resistance R_t was calculated as $R_t = \overline{P}/\overline{Q}$, with $\overline{Q}$ being the average flow rate obtained from 4D flow. Hence, the proximal resistance R_p was calculated as $R_p = \rho c/A$, where ρ is blood density, c is pulse wave velocity and A is the vessel cross-sectional area obtained from MRA images. The value of c was calculated using the relation $c = a_2/(2r)^{b_2}$, with $a_2 = 13.3$, $b_2 = 0.3$ and r being the vessel radius in mm [16]. Next, the distal resistance R_d was calculated as $R_d = R_t - R_p$. Previous to this step, flow rate curves relative to the supra-aortic branches and descending aorta were extracted from 4D flow data. Due to the limited spatial resolution of 4D flow images, flow rates in the three branches were calculated as the difference between flow rates through planes intersecting the aortic arch immediately upstream and downstream of each vessel [105]. For each outlet, the total compliance C was calculated as $C = \tau/R_t$ as described in [17], with $\tau = 1.79$, which corresponds to the exponential decay of diastolic pressure in normotensive patients [18]. This simulation was run for 2 cardiac cycles with a convergence residual of 10^{-5} and a time step of 2 ms. Blood was modeled as a Newtonian fluid with viscosity $\mu = 4$ cP and density $\rho = 1060$ kg/m^3.

Outlet	R_p	C	R_d
BCT	0.0294	12.1872	0.1281
LCA	0.0872	1.2950	1.3955
LSA	0.0418	3.7653	0.4682
DAo	0.0203	10.0218	0.1583

Table 2.2: Windkessel parameter values used in Simulation-1: proximal resistance R_p, compliance C and distal resistance R_d for the brachiocephalic trunk (BCT), left carotid artery (LCA), left sublavian artery (LSA) and descending aorta (DAo). Resistances are expressed in g/(mm^4·s), while compliances are expressed in mm^4·s^2/g.

2.2.4 Boundary conditions: Simulation 2

In order to evaluate the effect of the value of $\overline{P}$ at the outlets on trans-coarctation pressure drop, in Simulation-2 $\overline{P}$ = 80 mmHg was used for the the descending aorta outlet (DAo), while $\overline{P}$ = 98 mmHg was used for the three supra-aortic branches. This value corresponded to the $\overline{P}$ used for the DAo plus the peak-to-peak pressure drop across the coarctation obtained from Simulation 1 increased by 1 mmHg. The 3-WK parameters used in this simulation were calculated as described in Section 2.2.3, and their vales are reported in Table 2.3. The inlet boundary conditions was kept equal to the one used in Simulation 1. In Simulation-1 no significant difference in pressure waveforms was observed between first and second cardiac cycles. Therefore, Simulation-2 was run for 1 cardiac cycle with a convergence residual of 10^{-3} and a time step of 2 ms. Blood was modeled as a Newtonian fluid with viscosity $\mu = 4$ cP and density $\rho = 1060$ kg/m^3.

Outlet	R_p	C	R_d
BCT	0.0294	9.2751	0.1635
LCA	0.0872	0.9855	1.7291
LSA	0.0418	2.8656	0.5829
DAo	0.0203	10.0218	0.1583

Table 2.3: Windkessel parameter values used in Simulation-2: proximal resistance R_p, compliance C and distal resistance R_d for the brachiocephalic trunk (BCT), left carotid artery (LCA), left sublavian artery (LSA) and descending aorta (DAo). Resistances are expressed in g/(mm^4·s), while compliances are expressed in mm^4·s^2/g.

2.2.5 Wall mechanical properties

In both simulations, vessel wall elastic behavior was modeled as isotropic, with a constant Young's modulus of 878000 Pa, Poisson ratio $\nu = 0.5$ and constant thickness of 1 mm [12]. According to Moens-Korteweg equation [106], these parameters correspond to a pulse wave velocity (PWV) of approximately 5.25 m/s, which is in agreement with previous studies on CoA stiffness [107, 108], and with the values of c used to tune 3-WK (Sections 2.2.3 and 2.2.4).

2.2.6 Governing equations

All simulations were carried out assuming deformable vessel walls. In CRIMSON, fluid and solid governing equations are solved using a recently described formulation called coupled momentum method for fluid-solid interaction (CMM-FSI). This formulation modifies a conventional finite element solution for the Navier–Stokes equations in a rigid domain so that wall elasticity is taken into account [9]. In the fluid domain, the governing equations are represented by the incompressible Navier-Stokes equations, while the vessel wall displacement is described by the elastodynamics equations. The assumption that, in large arteries, vessel wall constitutive behavior can be modeled as linear elastic within the physiological range of pressure, has been experimentally validated [109].

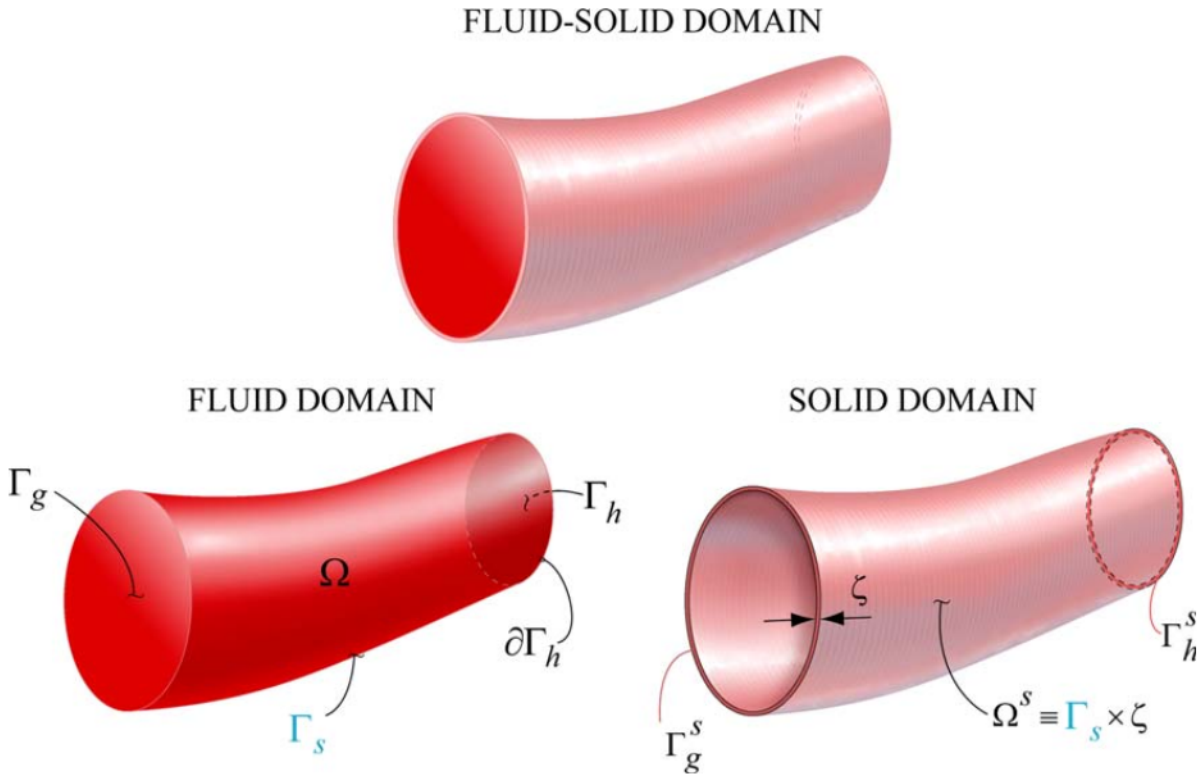

Figure 2.18: Schematic representation of the fluid and solid domains and their boundaries [9].

The full detailed description of the CMM-FSI method is presented in [9]; in order to provide a general understanding of the mathematical formulation of the method, only the some of the main equations are herein reported. Given $\boldsymbol{f} : \Omega \times (0,T) \to \mathbb{R}^3, \boldsymbol{g} : \Gamma_g \times (0,T) \to \mathbb{R}^3,\ \boldsymbol{h} : \Gamma_h \times (0,T) \to \mathbb{R}^3,\ \boldsymbol{v}^0 : \Omega \to \mathbb{R}^3$; find $\boldsymbol{v}(\boldsymbol{x},t)$ and $p(\boldsymbol{x},t)\ \forall \boldsymbol{x} \in \Omega,\ \forall t \in [0,T]$ such that:

$$\nabla \cdot \boldsymbol{v} \qquad \text{for } (\boldsymbol{x},t) \in \Omega \times (0,T), \tag{2.41}$$

$$\rho \boldsymbol{v}_t + \rho \boldsymbol{v} \cdot \nabla \boldsymbol{v} = -\nabla p + \nabla_{\underset{\sim}{\mathcal{T}}} + \boldsymbol{f} \qquad \text{for } (\boldsymbol{x},t) \in \Omega \times (0,T), \tag{2.42}$$

with a Dirichlet boundary condition:

$$\boldsymbol{v} = \boldsymbol{g} \qquad \text{for } (\boldsymbol{x},t) \in \Gamma_g \times (0,T), \tag{2.43}$$

and Neumann boundary conditions:

$$\boldsymbol{t_n} = \sigma \boldsymbol{n} = [-p\underset{\sim}{I} + \underset{\sim}{\tau}]\boldsymbol{n} = \boldsymbol{h} \qquad \text{for } (\boldsymbol{x}, t) \in \Gamma_h \times (0, T), \tag{2.44}$$

$$\boldsymbol{t_n} = \boldsymbol{t}^f \qquad \text{for } (\boldsymbol{x}, t) \in \Gamma_s \times (0, T), \tag{2.45}$$

plus the initial condition:

$$\boldsymbol{v}(\boldsymbol{x}, 0) = \boldsymbol{v}^0(\boldsymbol{x}) \qquad \text{for } \boldsymbol{x} \in \Omega. \tag{2.46}$$

In these equations, apart from the notation already defined in Equation (2.2), $\boldsymbol{f}$ is the prescribed volume force, the term $\underset{\sim}{\tau}$ represents the viscous stress tensor, and $\boldsymbol{g}$ the prescribed velocity field. Particular emphasis should be laid on the term $\boldsymbol{t}^f$ defined on the fluid-solid interface Γ_s, which is, in fact, unknown. Next, the weak form of the fluid governing equations is introduced by Figueroa in [9]. Referring to Figure 2.18, for the 3D fluid domain Ω with boundary $\Gamma = \Gamma_g \cup \Gamma_h \cup \Gamma_s; \Gamma_g \cap \Gamma_h \cap \Gamma_s = \emptyset$, the following function spaces are defined:

$$\overrightarrow{\mathcal{S}}_h^k = \left\{ \boldsymbol{v} \middle| \boldsymbol{v}(\cdot, t) \in H^1(\Omega), t \in [0, T], \boldsymbol{v}\Big|_{\boldsymbol{x} \in \overline{\Omega}_e} \in P_k(\overline{\Omega}_e), \boldsymbol{v} = \hat{\boldsymbol{g}} \quad \text{on} \quad \Gamma_g \right\}, \tag{2.47}$$

$$\overrightarrow{\mathcal{W}}_h^k = \left\{ \boldsymbol{w} \middle| \boldsymbol{w}(\cdot, t) \in H^1(\Omega), t \in [0, T], \boldsymbol{w}\Big|_{\boldsymbol{x} \in \overline{\Omega}_e} \in P_k(\overline{\Omega}_e), \boldsymbol{v} = \boldsymbol{0} \quad \text{on} \quad \Gamma_g \right\}, \tag{2.48}$$

$$\overrightarrow{\mathcal{P}}_h^k = \left\{ p \middle| p(\cdot, t) \in H^1(\Omega), t \in [0, T], p\Big|_{\boldsymbol{x} \in \overline{\Omega}_e} \in P_k(\overline{\Omega}_e) \right\}, \tag{2.49}$$

where $\overline{\Omega}_e$ represents the closure of the finite element domain, $\hat{\boldsymbol{g}}$ the finite element approximation of the prescribed velocity field, $P_k(\overline{\Omega}_e)$ the space of continuous polynomials within each element and the subscripts h and k represent the discrete approximation indexes. Then, for the fluid domain, the Galerkin finite element formulation yields the

following weak form: find $\boldsymbol{v} \in \overrightarrow{\mathcal{S}}_h^k$ and $p \in \overrightarrow{\mathcal{P}}_h^k$ such that

$$\begin{aligned} B_G(\boldsymbol{w}, q; \boldsymbol{v}, p) = \int_\Omega \{\boldsymbol{w} \cdot (\rho \boldsymbol{v}_t + \rho \boldsymbol{v} \cdot \nabla \boldsymbol{v} - \boldsymbol{f}) + \nabla \boldsymbol{w} : (-p\underset{\sim}{I} + \underset{\sim}{\tau}) - \nabla q \cdot \boldsymbol{v}\} d\boldsymbol{x} + \\ + \int_{\Gamma_h} \{-\boldsymbol{w} \cdot \boldsymbol{h} + q v_n\} ds + \int_{\Gamma_s} \{-\boldsymbol{w} \cdot \boldsymbol{t}^f + q v_n\} ds + \\ + \int_{\Gamma_g} q v_n ds = 0, \quad \forall \boldsymbol{w} \in \overrightarrow{\mathcal{W}}_h^k \text{ and } \forall q \in \overrightarrow{\mathcal{P}}_h^k. \end{aligned} \tag{2.50}$$

An analogous procedure is followed for the solid governing equations. Given $\boldsymbol{b}^s : \Omega^s \times (0,T) \to \mathbb{R}^3$, $\boldsymbol{g} : \Gamma_g^s \times (0,T) \to \mathbb{R}^3$, $\boldsymbol{h}^s : \Gamma_h^s \times (0,T) \to \mathbb{R}^3$, $\boldsymbol{u}^0 : \Omega^s \to \mathbb{R}^3$, $\boldsymbol{u}_t^0 : \Omega^s \to \mathbb{R}^3$; find $\boldsymbol{u}(\boldsymbol{x}, t)$ $\forall \boldsymbol{x} \in \Omega^s, \forall t \in [0,T]$ such that:

$$\rho^s \boldsymbol{u}_{tt} = \nabla \cdot \underset{\sim}{\sigma}^s + \boldsymbol{b}^s \qquad \text{for } (\boldsymbol{x}, t) \in \Omega^s \times (0,T), \tag{2.51}$$

with boundary conditions:

$$\boldsymbol{u} = \boldsymbol{g} \qquad \text{for } (\boldsymbol{x}, t) \in \Gamma_g^s \times (0,T), \tag{2.52}$$

$$\boldsymbol{t_n} = \underset{\sim}{\sigma}^s \boldsymbol{n} = \boldsymbol{h}^s \qquad \text{for } (\boldsymbol{x}, t) \in \Gamma_h^s \times (0,T), \tag{2.53}$$

and initial conditions:

$$\boldsymbol{u}(\boldsymbol{x}, 0) = \boldsymbol{u}^0(\boldsymbol{x}) \qquad \text{for } \boldsymbol{x} \in \Omega^s, \tag{2.54}$$

$$\boldsymbol{u}_t(\boldsymbol{x}, 0) = \boldsymbol{u}_t^0(\boldsymbol{x}) \qquad \text{for } \boldsymbol{x} \in \Omega^s, \tag{2.55}$$

where $\boldsymbol{u}$ is the displacement field, $\boldsymbol{b}^s$ the prescribed body force, and $\underset{\sim}{\sigma}^s$ the stress tensor. In this case, the assumption of thin-walled structure allows to relate the traction term $\boldsymbol{t}^f$ appearing in equation 2.50 to a body force $\boldsymbol{b}^s$ acting on the solid domain:

$$\boldsymbol{b}^s = -\frac{\boldsymbol{t}^f}{\zeta}, \tag{2.56}$$

where ζ is the wall thickness. It is then possible to express the unknown integral on Γ_s (Equation 2.50) using the weak form for the solid governing equations, which is not herein explicitly reported for conciseness. Finally, the combined formulation leads to the

CMM-FSI weak form: find $\boldsymbol{v} \in \overrightarrow{\mathcal{S}}_h^k$ and $p \in \overrightarrow{\mathcal{P}}_h^k$ such that

$$\begin{aligned} B_G(\boldsymbol{w}, q; \boldsymbol{v}, p) = &\int_\Omega \{\boldsymbol{w} \cdot (\rho \boldsymbol{v}_t + \rho \boldsymbol{v} \cdot \nabla \boldsymbol{v} - \boldsymbol{f}) + \nabla \boldsymbol{w} : (-p\underset{\sim}{I} + \underset{\sim}{\tau}) - \nabla q \cdot \boldsymbol{v}\} d\boldsymbol{x} + \\ &+ \int_{\Gamma_h} \{-\boldsymbol{w} \cdot \boldsymbol{h} + q v_n\} ds + \int_{\Gamma_s} \{+q v_n\} ds + \\ &+ \zeta \int_{\Gamma_s} \{\boldsymbol{w} \cdot \rho^s \boldsymbol{v}_t + \nabla \boldsymbol{w} : \underset{\sim}{\sigma}^s(\boldsymbol{u})\} ds - \zeta \int_{\partial\Gamma_h} \boldsymbol{w} \cdot \boldsymbol{h}^s dl + \\ &+ \int_{\Gamma_g} q v_n ds = 0, \quad \forall \boldsymbol{w} \in \overrightarrow{\mathcal{W}}_h^k \text{ and } \forall q \in \overrightarrow{\mathcal{P}}_h^k. \end{aligned} \tag{2.57}$$

It should be specified that the actual weak formulation reported in [9] is a stabilized version of equation 2.57, which is not herein reported for the sake of simplicity.

With this formulation, vessel wall motion effects of blood flow are accounted for in the weak form governing the fluid behavior, thus resulting in only one weak form comprehensive of both fluid and solid problems. To sum up, the CMM-FSI method starts with rigid wall formulation for blood flow and removes the no-slip condition with the contribution of vessel wall elastodynamics. Furthermore, the degrees of freedom of the membrane-like solid wall are strongly coupled with the fluid boundary, namely they coincide. This feature, together with a linearized kinematics approach, results in a fixed mesh at the fluid-solid interface, whose nodes can have nonzero velocities. All these features make the CMM-FSI method much less computationally demanding than other FSI formulations such as Arbitrary Lagrangian Eulerian (ALE) formulation, and at the same time, a suitable approach to investigate wave propagation phenomena and linearized vessel wall dynamics.

2.3 *In vitro* analysis

In order to further validate 4D flow-derived pressure estimations, an *in vitro* test bench was set up. The segmented 3D *.stl* surface (Figure 2.15b) was modified using Meshmixer and then printed in 3D. More specifically, the three supra-aortic vessels were removed

and five ports were created along the aorta. Referring to the coarctation diamater as D_{CoA}, the first port was located at a distance D_{CoA} proximal to the coarctation; ports 2 and 3 were placed just downstream of the coarctation, while the fourth port was located at $2 * D_{CoA}$ from port 3 and port 5 at D_{CoA} from port 4 (Figure 2.19). Additionally, inlet and outlet were extruded by 1 cm and 7 mm respectively to allow for proper fastening of tubes. A Polyjet Eden 260 V 3D printer (Stratasys, Inc, Eden Prairie, Minn) was used to generate the 2 mm-thick rigid polylactic acid (PLA) 3D model shown in Figure 2.20. The aortic inlet was connected to a centrifugal pump (SYN10 series, Bonfiglioli Vectron, Carpiano, Italy), while the aortic outlet flowed into an atmospheric pressure reservoir. Pressure drops along the aorta were measured with piezoelectric pressure transducers (PC140 series, Honeywell INC, Morristown, NJ), while an ultrasound flow-meter (HT110R, Transonic System INC, Ithaca, NY) was employed to measure flow. The peak flow rate value through the DAo was extracted from 4D flow data and was equal to 8.56 L/min. In order to account for uncertainties of the 4D flow measurement, three different tests were performed, imposing the measured flow rate value, its 90% and its 110%. The platform configuration is shown in Figure 2.21, while flow rate probe and pressure transducers are shown in Figure 2.22.

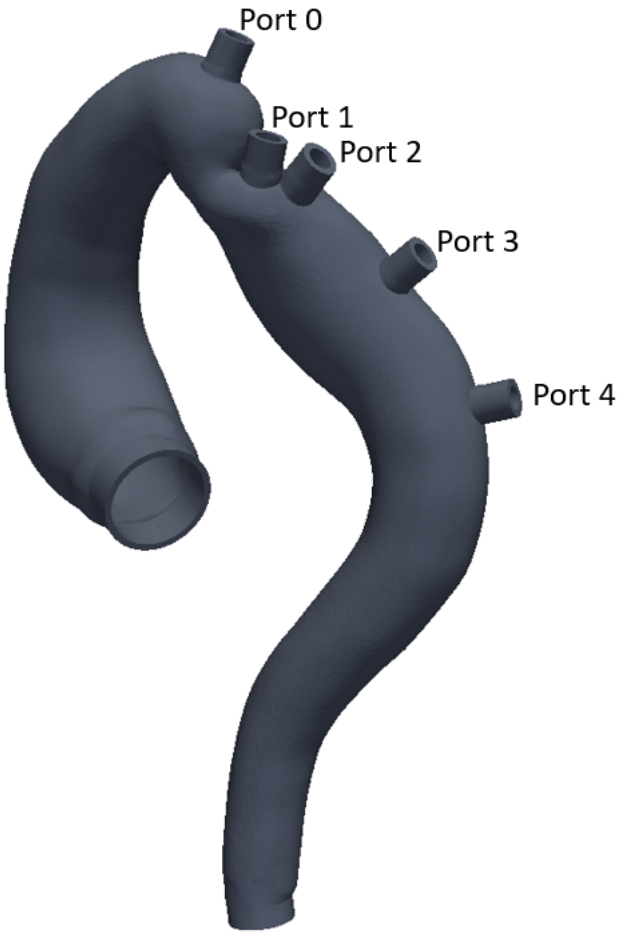

Figure 2.19: Modified 3D model with ports.

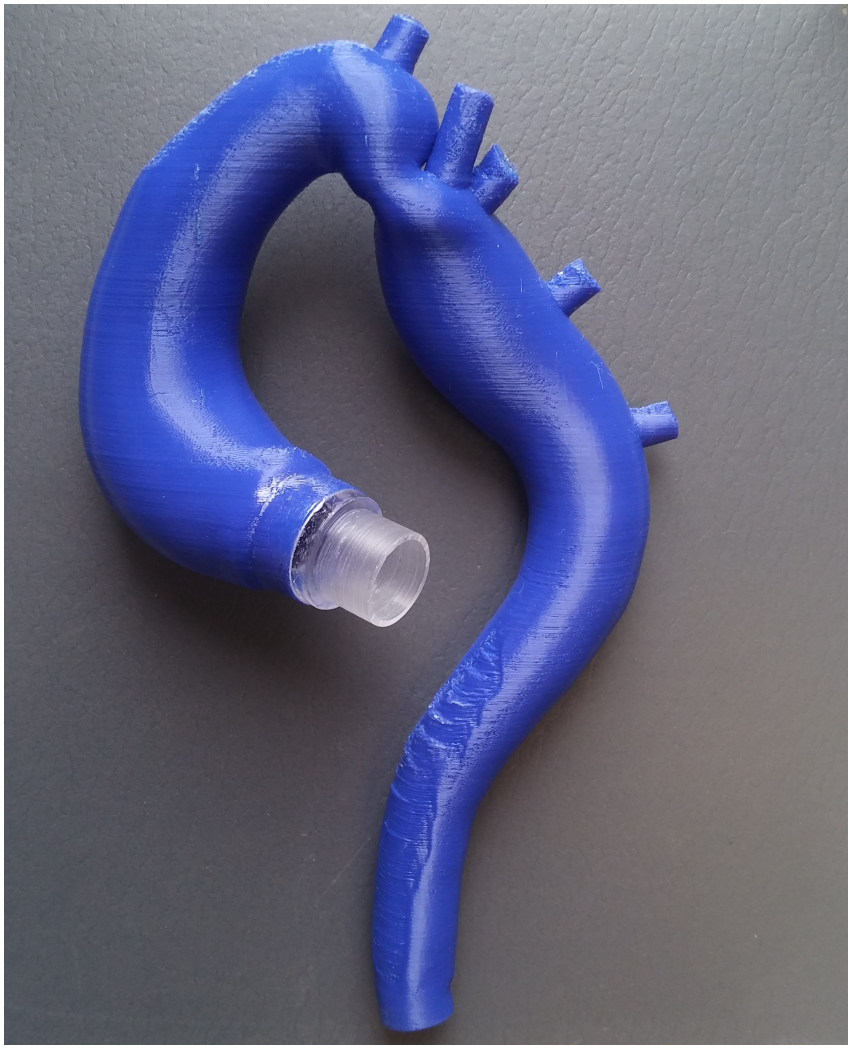

Figure 2.20: 3D printed of the aorta with connection ports.

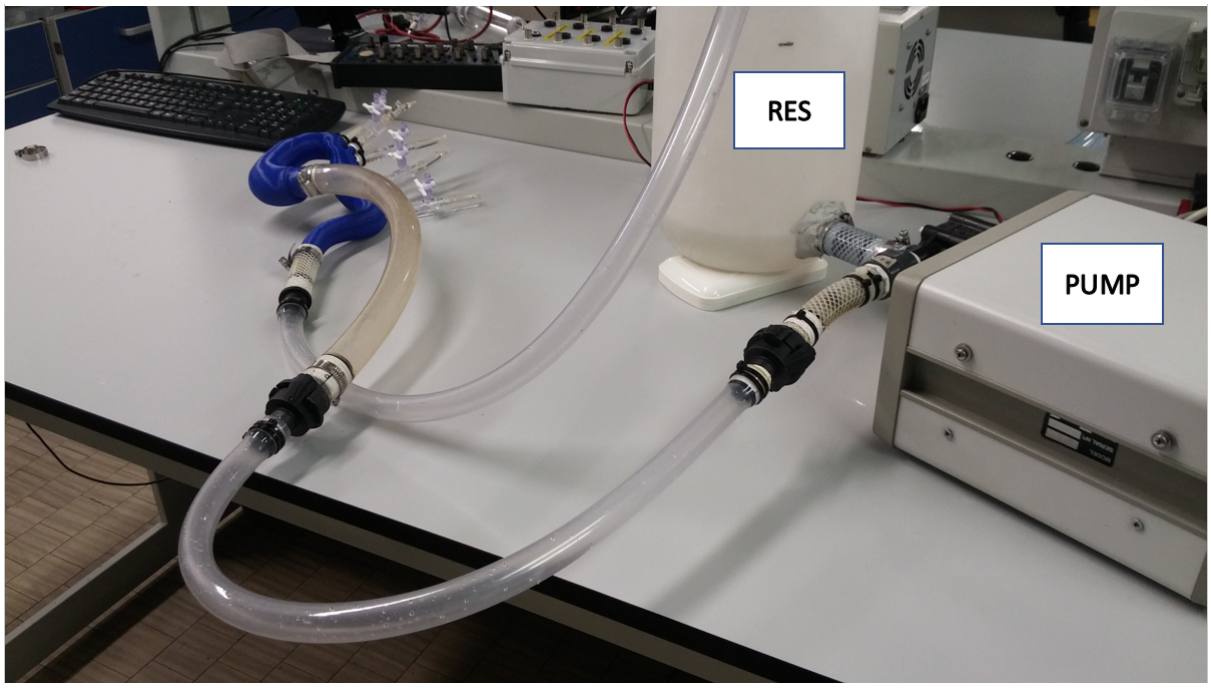

Figure 2.21: Platform configuration with the atmospheric pressure reservoir (RES) and centrifugal pump (PUMP).

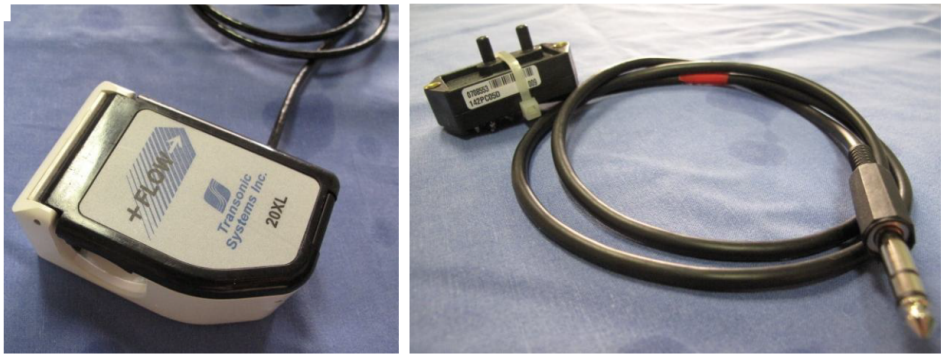

Figure 2.22: Probe for flow measure (left) and pressure transducer (right)

Chapter 3

Results

In this chapter, the results obtained with the developed algorithm for pressure estimation will be illustrated. First, results from a CFD simulation will be used to validate and benchmark 4DF-FEPPE results in an idealized aortic geometry. Then, the efficiency and accuracy of 4DF-FEPPE will be compared to a similar preexisting piece of code (Siryk-FEPPE). Successively, 3D pressure maps calculated with 4DF-FEPPE from a 4D flow dataset of a CoA patient will be shown. In the second part of this chapter, the results of the simulations that were carried out will be shown and validated against raw 4D flow data in terms of flow rate distributions and velocity contours. Finally, pressure distributions obtained from 4D flow with 4DF-FEPPE will be compared to the simulation results and to experimental measurements to validate the developed algorithm.

3.1 4D flow MRI-based pressure difference estimation

In this section the results of the developed algorithm described in Section 2.1 (4DF-FEPPE) will be presented. First, the validation against a synthetic dataset (Subsection 2.1.5) will be reported; then, pressure results in a patient-specific case of CoA will be described.

3.1.1 Validation against a synthetic dataset

The effect of the downsampling procedure described in Subsection 2.1.5 are shown in Figure 2.11. In order to evaluate the effects of velocity downsampling and noise addition, 4DF-FEPPE was tested using two types of velocity fields as input. First, pressure distributions were calculated using the downsampled velocity values exported from the simulation results with no added noise; results are shown in Figure 3.1 as a comparison with pressure fields calculated by Fluent. Color maps at different systolic time points (Figure 3.1), showed good agreement with pressure fields calculated through 4DF-FEPPE and with the ones obtained with Fluent. Maximum, minimum and mean pressure values are reported in Table 3.1. Comparing average pressure values, the larger error was of 197 Pa and it was observed at Time 1, which corresponded to early systole. A greater difference between the two pressure distributions was observed in the supra-aortic branches rather than in the aortic arch, especially right before and after systolic peak (Figure 3.1b, c, f and g). In these regions 4DF-FEPPE results overestimated pressure differences with respect to CFD.

The effect of Gaussian noise addition on pressure estimation was evaluated by using noisy downsampled velocity fields as input for 4DF-FEPPE (P_n) (Figure 2.11c). In this case, albeit pressures values calculated with 4DF-FEPPE were within similar ranges compared

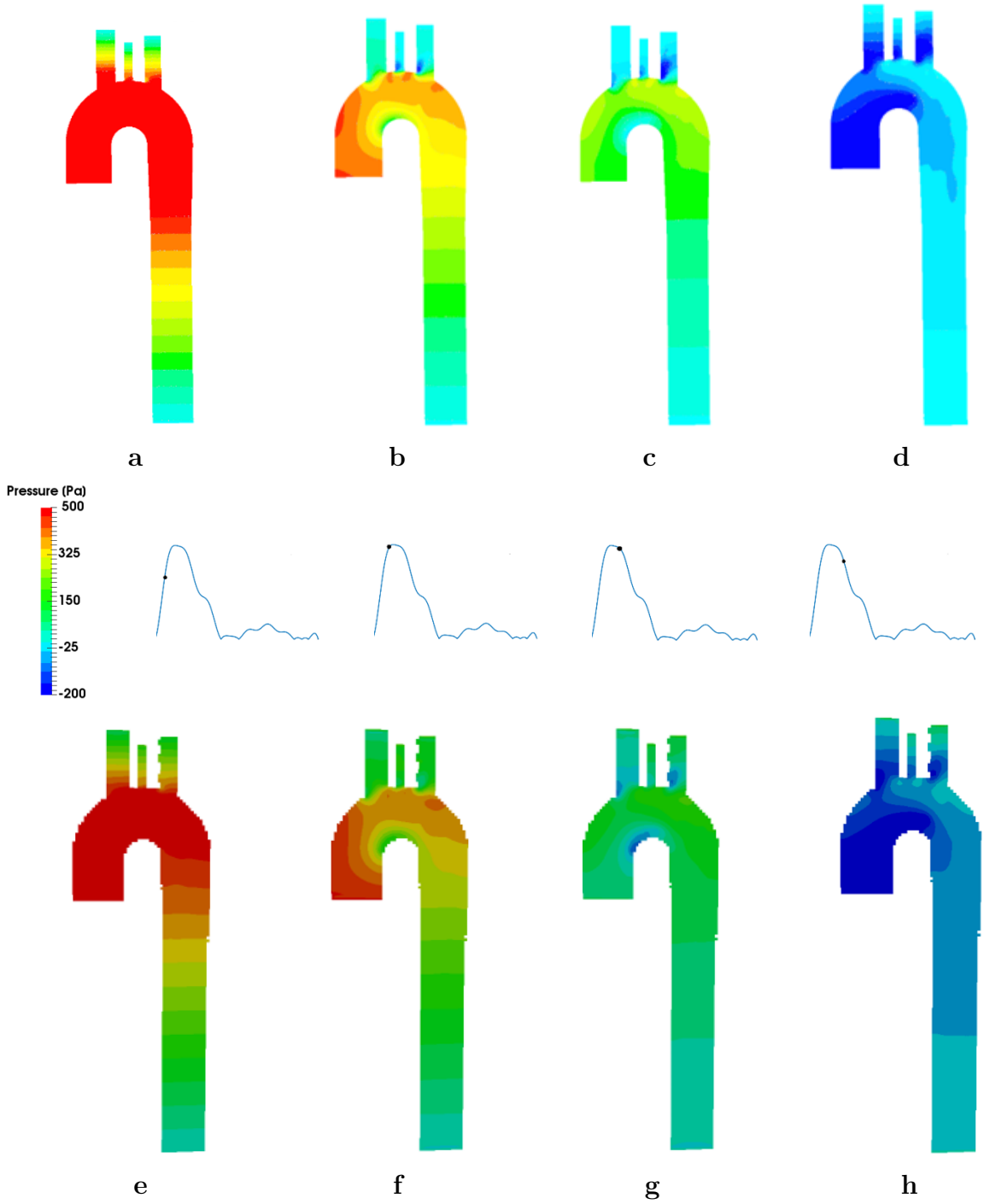

Figure 3.1: Pressure comparison between Fluent results (a-d) (P_{CFD}) and FE-PPE solution (e-h) using downsampled velocities as input (P_{ds}).

to CFD resluts, pressure contours did not resemble the CFD solution as well as in the previous case. In particular, a tendency to overestimate pressure was observed, especially right before and after systolic peak (Figure 3.2b, c, d, f, g and h), in both the aortic arch and supra-aortic branches. Maximum, minimum and average pressure values are reported in Table 3.1, where the maximum difference in average pressure was observed again at Time 1. Mean pressure values with standard deviation are shown in Figure 3.6.

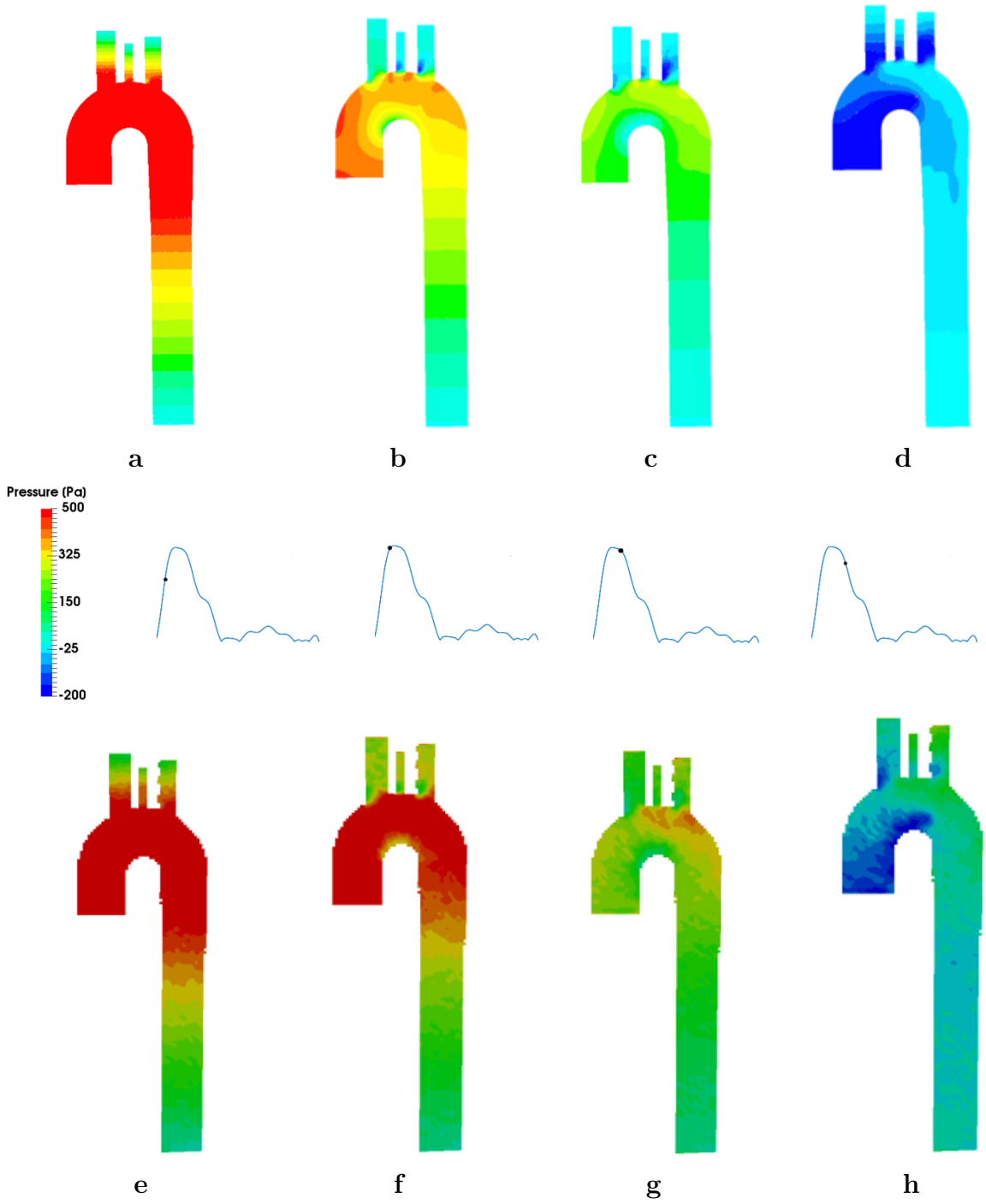

Figure 3.2: Pressure comparison between Fluent results (a-d) and 4DF-FEPPE solution (e-h) using downsampled velocities with added Gaussian noise as input.

Finally, pressure fields calculated using noisy velocity fields preprocessed with a DFW filter (Subsection 2.1.4) are reported in Figure 3.3 and Table 3.1, where the time points taken into account are shown with respect to the cardiac cycle in Figure 3.5.

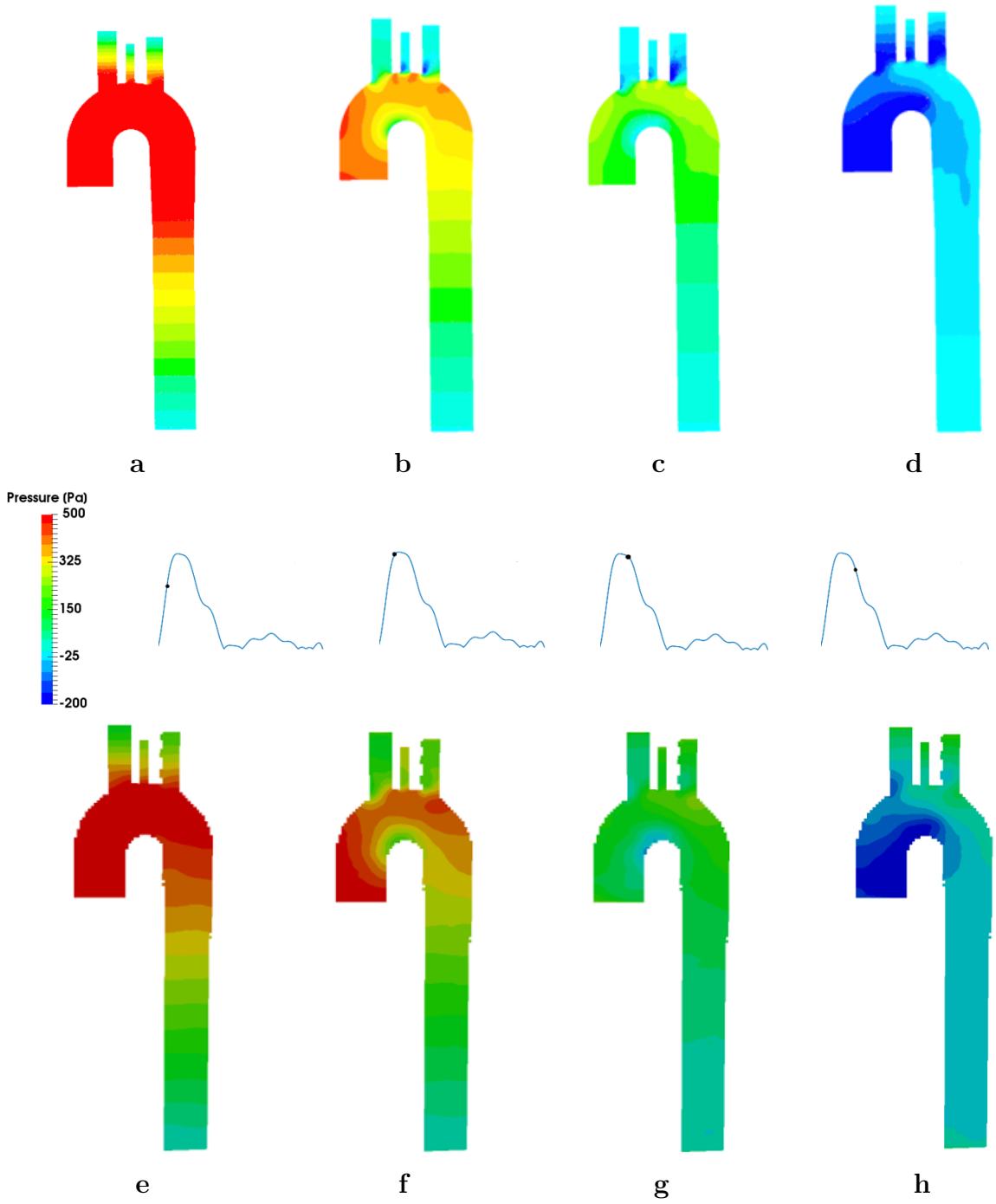

Figure 3.3: Pressure comparison between Fluent results (a-d) and 4DF-FEPPE results (e-h) using downsampled velocities with added Gaussian noise preprocessed with a DFW filter as input.

In this case, pressure distributions calculated by the developed algorithm resemble the CFD-based results (Figure 3.3). In particular, an improvement with respect to the unprocessed noisy input can be observed immediately before and after systolic peak.

Overall, the best comparison with the CFD data was achieved by 4DF-FEPPE when only

donwsampled velocity fields were used as input. Worse results are obtained when using velocities with the addition of Gaussian noise, but preprocessing the noisy input with a DFW filter allows to attain pressure distributions that better resemble CFD results (Figure 3.4).

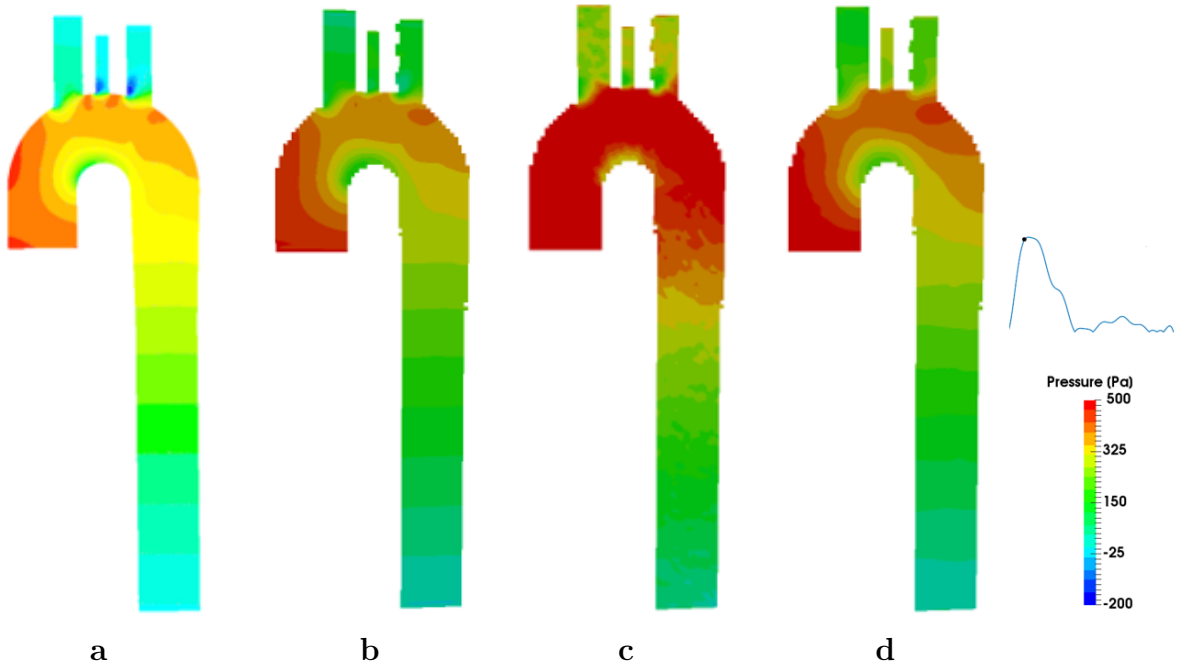

Figure 3.4: Pressure comparison between Fluent results (a) and FE-PPE solution using as input: downsampled velocities (b), downsampled velocities with added Gaussian noise (c) and downsampled velocities with noise preprocessed with a DFW filter (d).

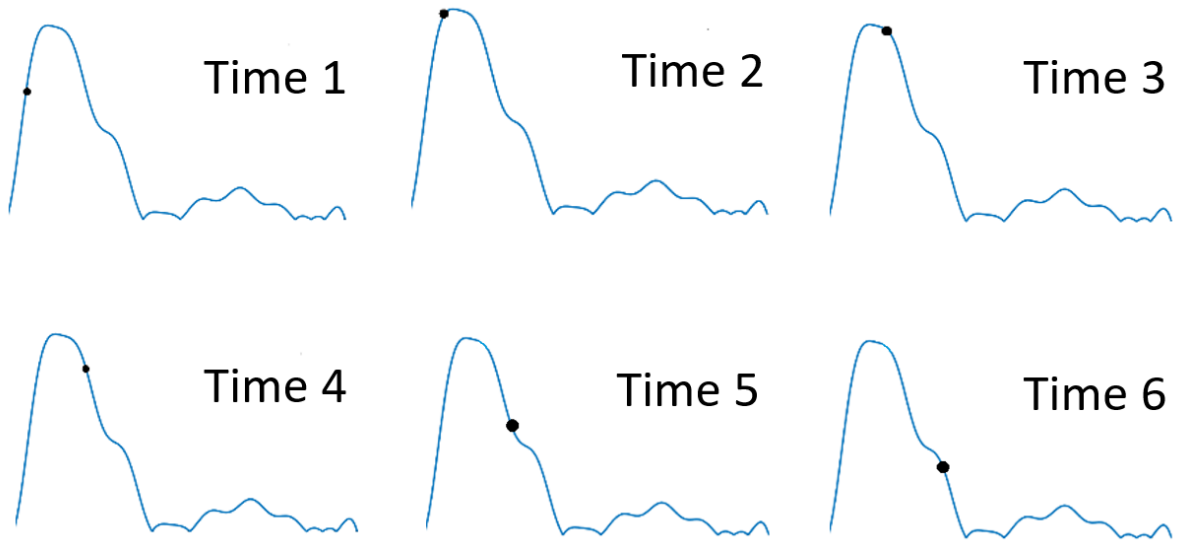

Figure 3.5: Time points extracted from the CFD simulation named Time 1 to Time 6 identified within the cardiac cycle by the black dot on the blue flow rate waveform.

		P_{CFD}	P_{ds}	P_n	P_{dfw}
Time 1	min.	-15	-50.6	-152	-68
	avg.	243	440	521	380
	max.	639	1152	1334	1072
Time 2	min.	0	-4.5	-158	-2.2
	avg.	543	394	497	376
	max.	1350	908	1230	924
Time 3	min.	-318	-4.2	-83	-7.3
	avg.	235	243	385	256
	max.	479	474	1020	588
Time 4	min.	-375	-117	-89	-74
	avg.	106	69	239	89
	max.	304	202	662	255
Time 5	min.	-372	-318	-323	-261
	avg.	-104	-76	41	55
	max.	4.3	100	415	191
Time 6	min.	-494	-721	-751	-697
	avg.	-198	-295	-209	-291
	max.	0	5.8	187	51

Table 3.1: Pressure difference values calculated with Fluent (P_{CFD}) and with 4DF-FEPPE using downsampled velocities (P_{ds}), downsampled velocities with Gaussian noise (P_n) and downsampled velocities with Gaussian noise preprocessed with a DWF filter (P_{dfw}). All values are reported in Pa.

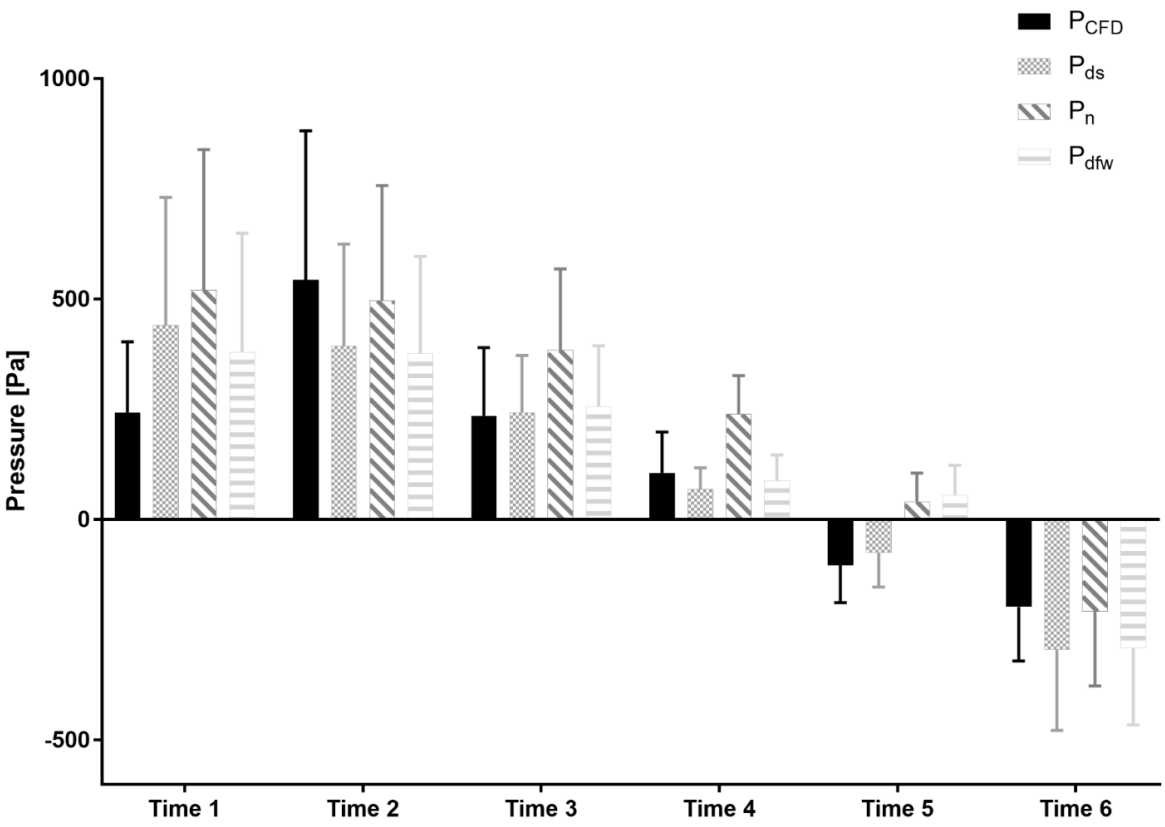

Figure 3.6: Mean pressure values with standard deviation obtained with the CFD simulation (P_{CFD}) and mean pressure differences with respect to the lowest point in the descending aorta with standard deviation obtained with 4DF-FEPPE using downsampled velocities (P_{ds}), downsampled velocities with Gaussian noise (P_n) and downsampled velocities with Gaussian noise preprocessed with a DWF filter (P_{dfw}).

However, the addition of Gaussian noise resulted in an overestimation of velocities with respect to the downsampled case (Figure 3.7). More specifically, space-averaged noisy velocity magnitudes were higher than downsampled values by 199% for Time 1, and by less than 60% for all other time points (Figure 3.7). On the other hand, application of the DFW tended to decrease noisy velocities for all time points, and while an overestimation of 60% was observed at Time 1, space-averaged velocity magnitudes were higher than downsampled values by less than 15% for all other time points (Figure 3.7). Additionally, a greater pressure mismatch was observed in the supra-aortic branches, where the limited spatial resolution imposed by the downsampling process led to a pressure overestimation of 4DF-FEPPE.

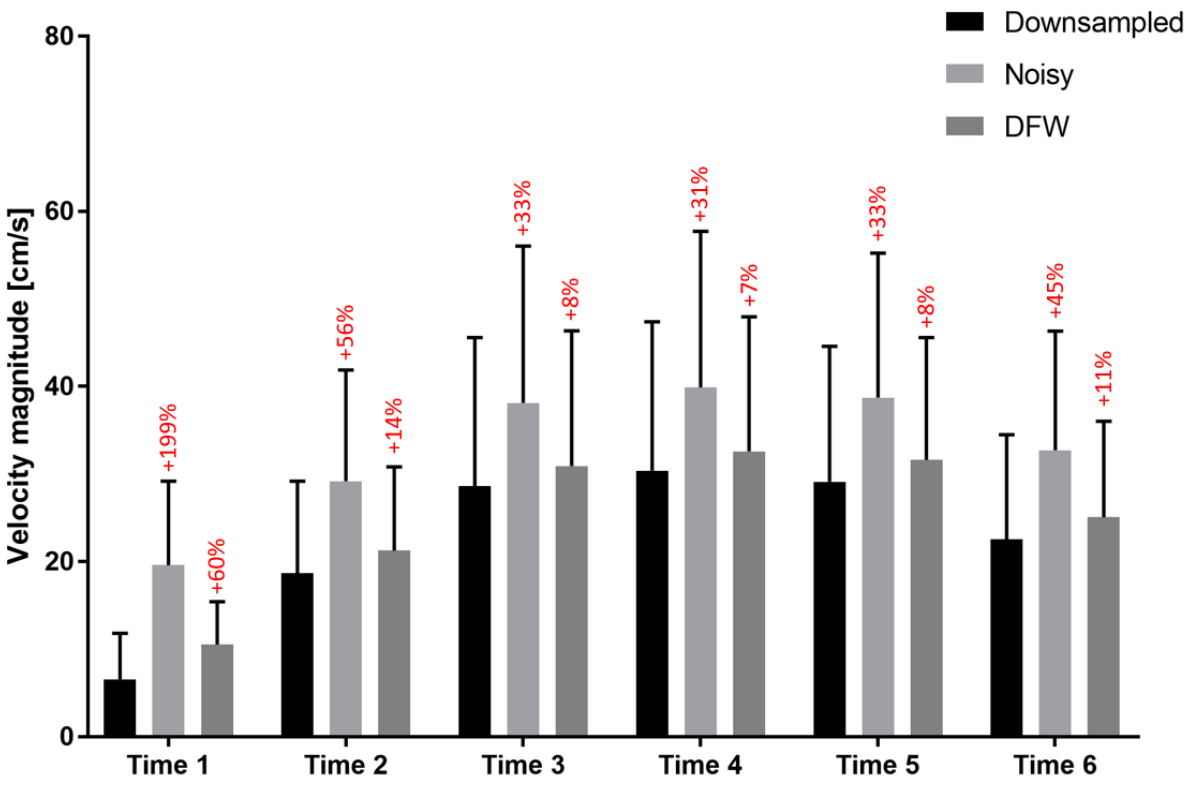

Figure 3.7: Space-averaged and standard deviation values of velocity magnitudes in cm/s for the downsampled case, noisy case, and DFW-processed case.

3.1.2 Comparison with the previously developed code

Pressure difference results calculated from the synthetic dataset using the approach introduced in Subsection 2.1.6 were compared to the results of 4DF-FEPPE. As no significant difference in the results of the two algorithms was observed with the downsampled velocities as input, these results are not herein reported. Using downsampled velocities with Gaussian noise as input, differences between the solutions obtained with the two approaches were more noticeable (Figure 3.8). After systolic peak (Figure 3.8e and f) the average pressure value in the domain calculated using Syrik-FEPPE (previously developed code) was 152 Pa and using hexahedral elements (4DF-FEPPE) an average pressure of 239 Pa was obtained, whereas CFD-derived average pressure was 106 Pa. At all time

points, except for Time 6, the algorithm previously developed by Prof. Siryk led to average values that were slightly closer to the values exported from Fluent. A more extensive quantitative comparison is reported in Table 3.2 and Figure 3.9, where mean pressures with standard deviations derived with the two algorithms are shown.

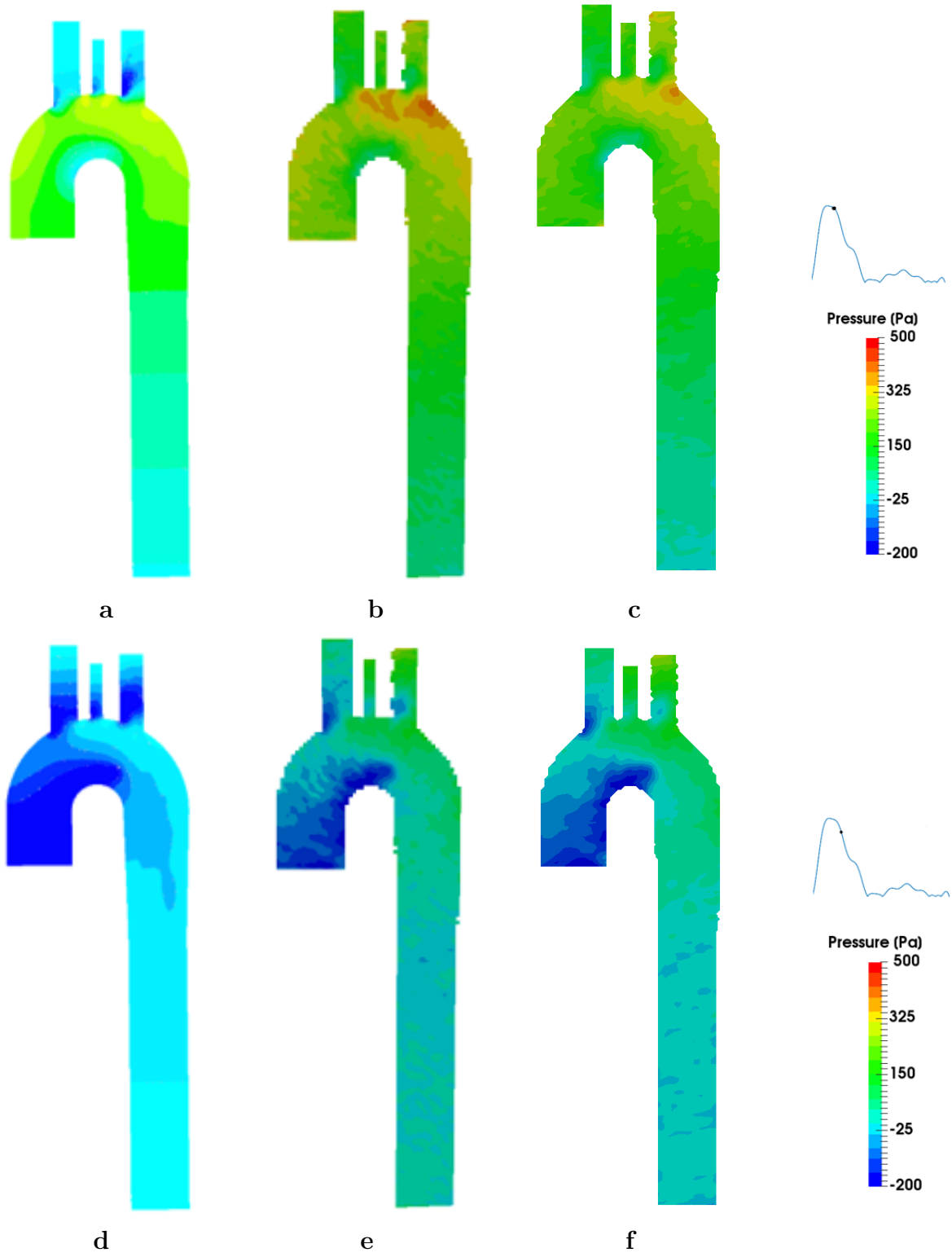

Figure 3.8: Pressure comparison between Fluent results (a, b) and 4DF-FEPPE results with noisy downsampled velocities as input using 4DF-FEPPE (b, e) and Siryk-FEPPE (c, f).

		P_{CFD} [Pa]	P_n [Pa]	P_{Siryk} [Pa]
Time 1	min.	-15	-152	-129
	avg.	243	521	488
	max.	639	1334	1280
Time 2	min.	0	-158	-77
	avg.	543	497	499
	max.	1350	1230	1203
Time 3	min.	-318	-83	-76
	avg.	235	385	367
	max.	479	1020	923
Time 4	min.	-375	-89	-122
	avg.	106	239	152
	max.	304	662	454
Time 5	min.	-372	-323	-251
	avg.	-104	41	-14
	max.	4.3	415	293
Time 6	min.	-494	-751	-679
	avg.	-198	-209	-229
	max.	0	187	166

Table 3.2: Pressure values calculated with Fluent (P_{CFD}), with 4DF-FEPPE (P_n) and with Siryk-FEPPE (P_{Siryk}) using noisy velocity fields as input.

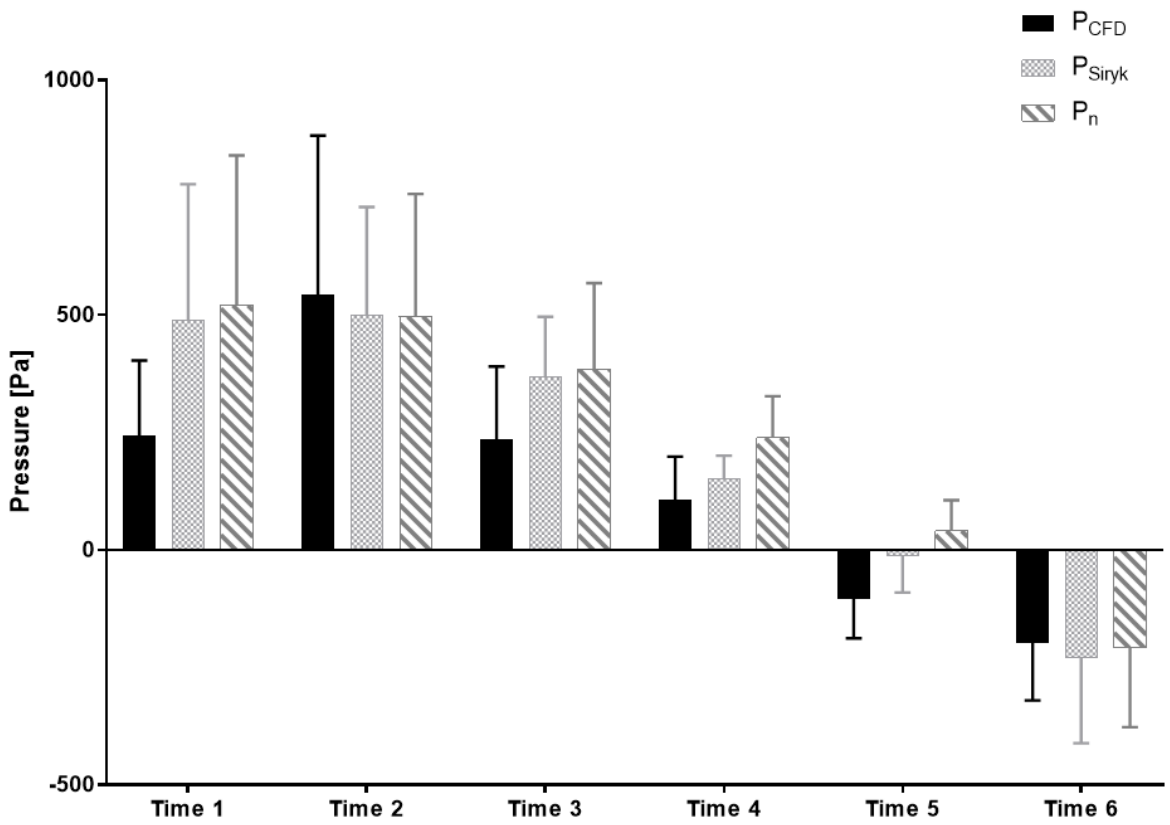

Figure 3.9: Mean pressure values with standard deviation obtained with the CFD simulation (P_{CFD}) and mean pressure differences with respect to the lowest point in the descending aorta with standard deviation, obtained by using downsampled velocities with Gaussian noise through 4DF-FEPPE (P_n) and through Siryk-FEPPPE (P_{Siryk}).

Computational times required by the two methods for a six-frame dataset were 20 minutes for Siryk-FEPPE and 2 minutes for 4DF-FEPPE. The previously developed code showed a tenfold increase in the required computational time with respect to the newly developed one. All computations were run on a laptop with 4-core Intel i7-7700HQ CPUs at 2.80 GHz, 16 GB of system RAM and an Intel(R) HD Graphics 630 GPU.

3.1.3 Patient-specific aortic coarctations

The workflow described in Section 2.1 was followed to calculate 3D pressure difference maps corresponding to the 4D flow time frames of a CoA patient. Pressure difference contours at different time points in the cardiac cycle can be visualized in Figure 3.10 along

with velocity contours extracted from 4D flow data. In this calculation, all pressure results were calculated as pressure differences with respect to the lowest point in the descending aorta, where pressure wass set to zero at all time points (Figure 3.11). A net pressure difference was clearly visible between the region upstream of the coarctation and downstream, with the former consistently showing higher pressure values.

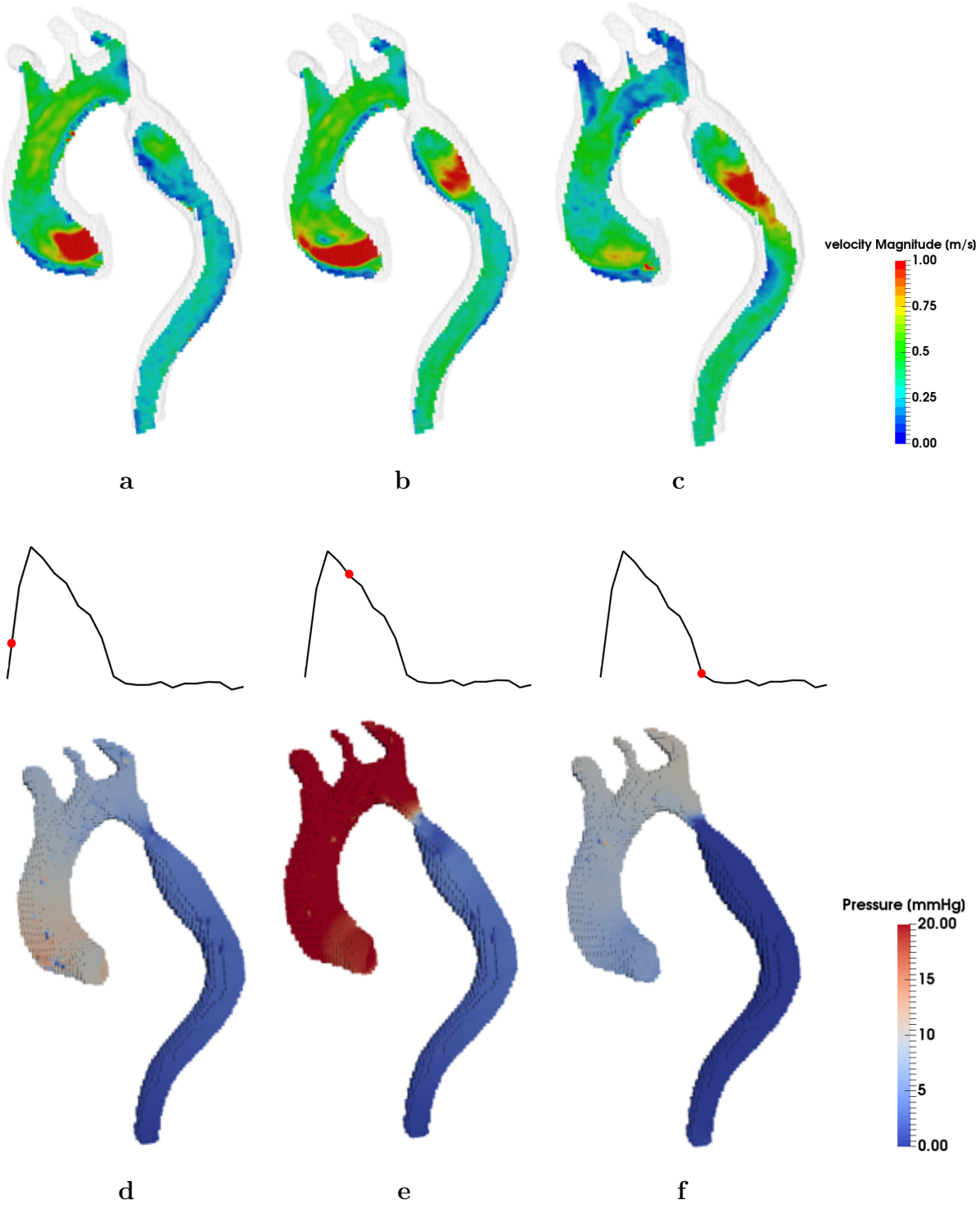

Figure 3.10: Velocity contours extracted from 4D flow MR images (a-c) and pressure difference maps calculated using 4DF-FEPPE (d-f).

Cross-section averaged pressure differences over time are shown in Figure 3.11. Typical pressure waveforms could be observed in the ascending aorta, while pressure just downstream of the coarctation reached a maximum of 4 mmHg. Considering the pressure

difference values between the plane upstream of the coarctation and the one downstream, a peak-to-peak pressure drop (Δp_{pp}) of 17.6 mmHg was evaluated (Figure 3.12), while the maximum instantaneous pressure difference (Δp_m) was 21.09 mmHg.

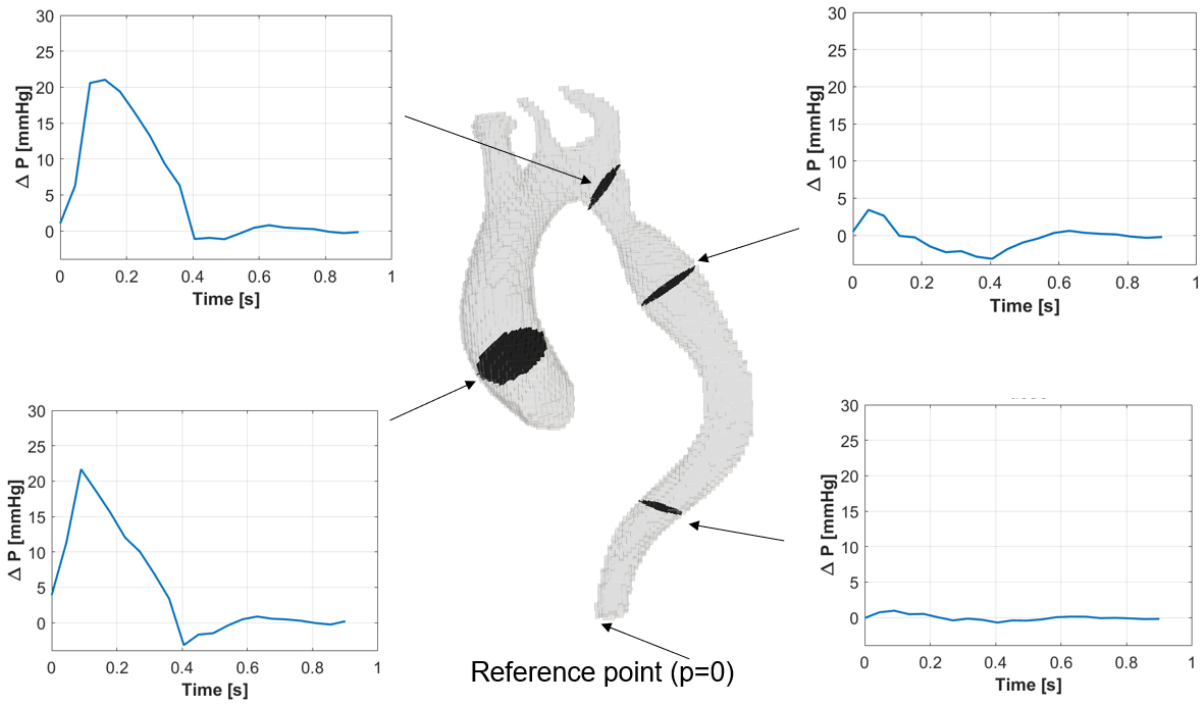

Figure 3.11: Cross-section averaged pressure differences over time on sections at in the ascending aorta (bottom left), proximal (top left) and distal (top right) to the coarctation, and in the descending aorta (bottom right)

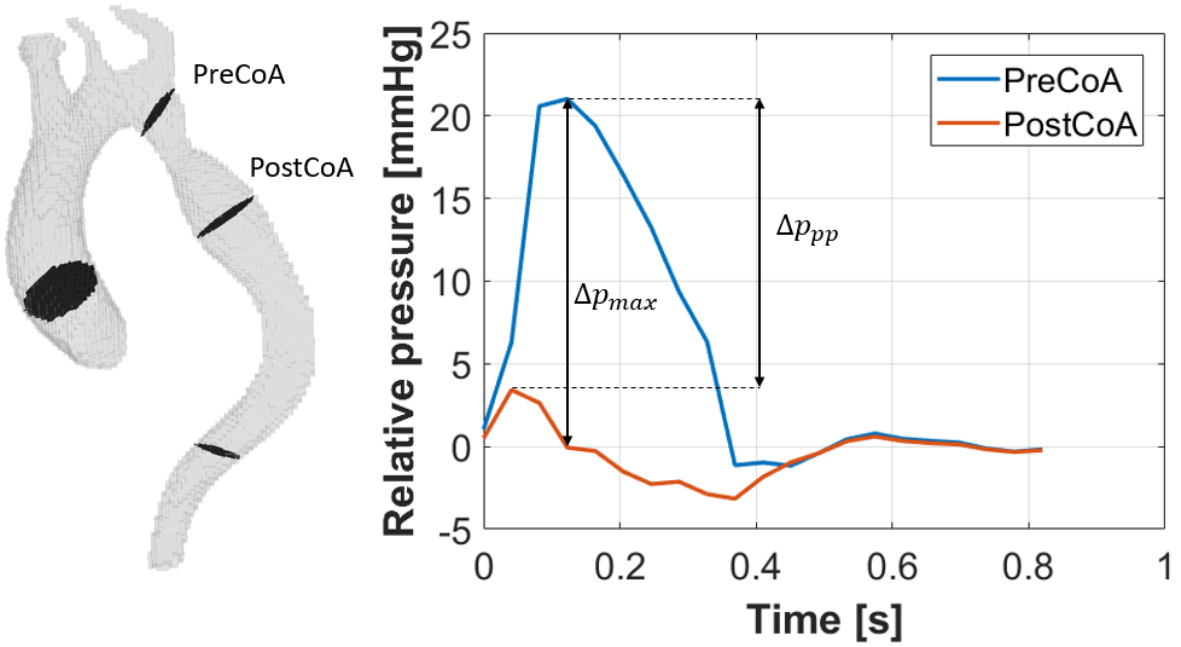

Figure 3.12: Cross-section averaged pressure differences over time on planes proximal (PreCoA) and distal (PostCoA) to the coarctation.

The effect of the DFW filter described in Subsection 2.1.4 was evaluated on this case of CoA. As explained in Subsection 2.1.5, the DFW filter was applied for 10 iterations using an automatic algorithm for threshold selection (Section 2.1.4). Velocity magnitude contours on two transversal planes can be visualized in Figure 3.13. Fluid structures were preserved after processing and efficient denoising was achieved. However, application of the DFW filter resulted in a reduction of velocities, similarly to what was observed for the synthetic dataset (Section 3.1.1). Space-averaged velocity magnitudes for all time frames in the 4D flow sequence are reported in Table 3.3, where the percentage error was calculated as:

$$error = \frac{\overline{v}_{dfw} - \overline{v}_{raw}}{\overline{v}_{raw}} \cdot 100, \tag{3.1}$$

with $\overline{v}_{dfw}$ and $\overline{v}_{raw}$ being the processed and unprocessed average velocity values. A systematic velocity reduction by the DFW can be observed, with the largest percent difference of -30.6% attained at T21. Consequently, the trans-coarctation Δp_{pp} was reduced to 12.9 mmHg after DFW application (Figure 3.14).

	$\overline{v}_{raw}$	$\overline{v}_{dfw}$	$error$
T1	10.892	7.790	-28.5%
T2	26.577	23.121	-13%
T3	43.891	39.16	-10.8%
T4	53.172	47.23	-11.2%
T5	56.63	49.819	-12%
T6	56.691	49.223	-13.2%
T7	51.333	43.808	-14.7%
T8	44.645	37.654	-15.7%
T9	36.777	30.41	-17.3%
T10	28.705	23.089	-19.6%
T11	22.523	17.604	-21.8%
T12	18.965	14.52	-23.4%
T13	16.39	12.205	-25.5%
T14	15.306	11.465	-25.1%
T15	14.155	10.542	-25.5%
T16	13.521	10.005	-26%
T17	12.681	9.2458	-27.1%
T18	12.228	8.7827	-28.2%
T19	11.726	8.3002	-29.2%
T20	11.359	7.9657	-29.8%
T21	10.796	7.4874	-30.6%

Table 3.3: Space-averaged velocity magnitudes in cm/s for all time frames in the 4D flow sequence (T1-T21). Unprocessed raw 4D flow data ($\overline{v}_{raw}$) and DFW-filtered results ($\overline{v}_{dfw}$) are reported with their relative percentage error.

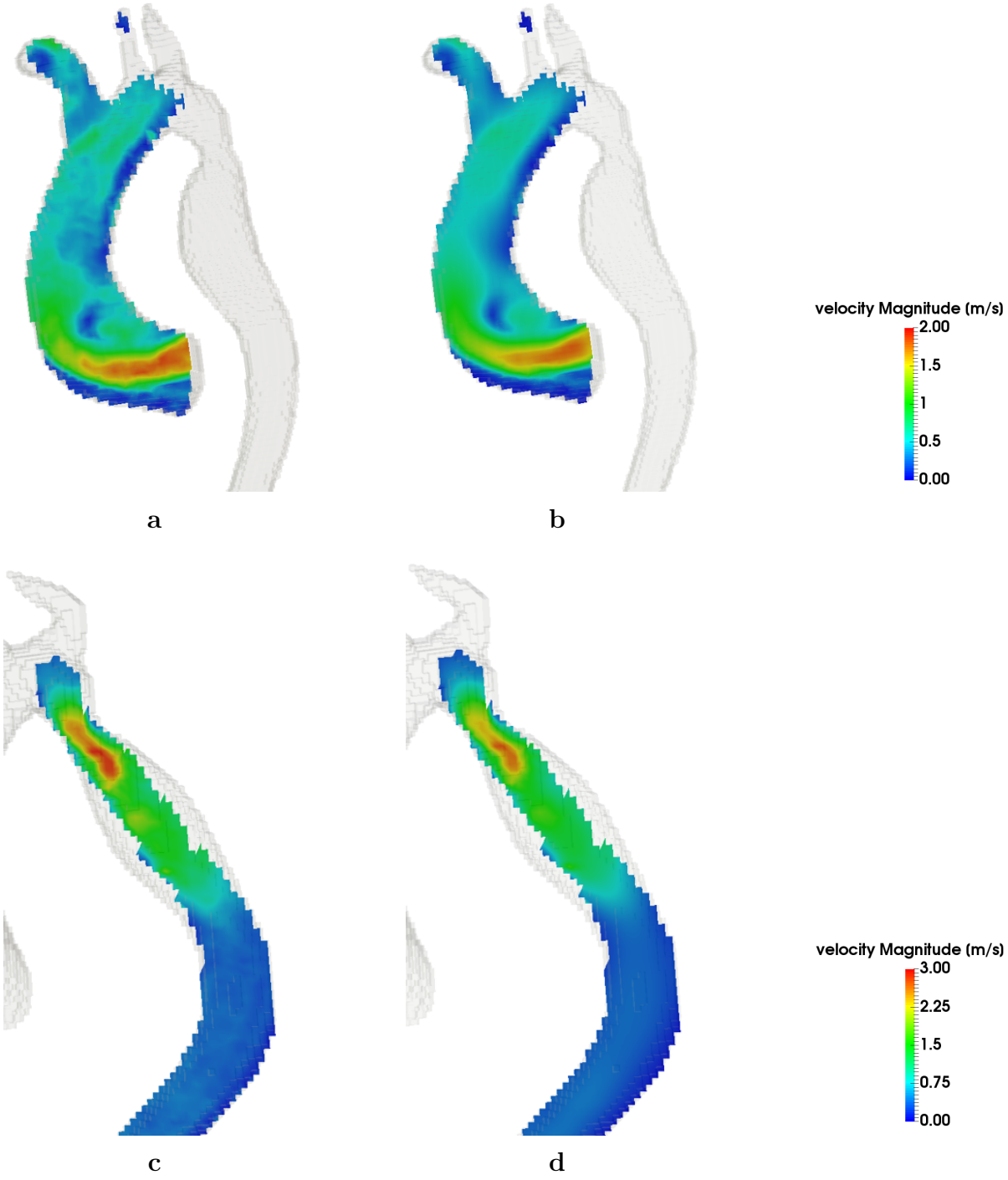

Figure 3.13: Effect of the DFW filter on velocity magnitude contours on two longitudinal planes.

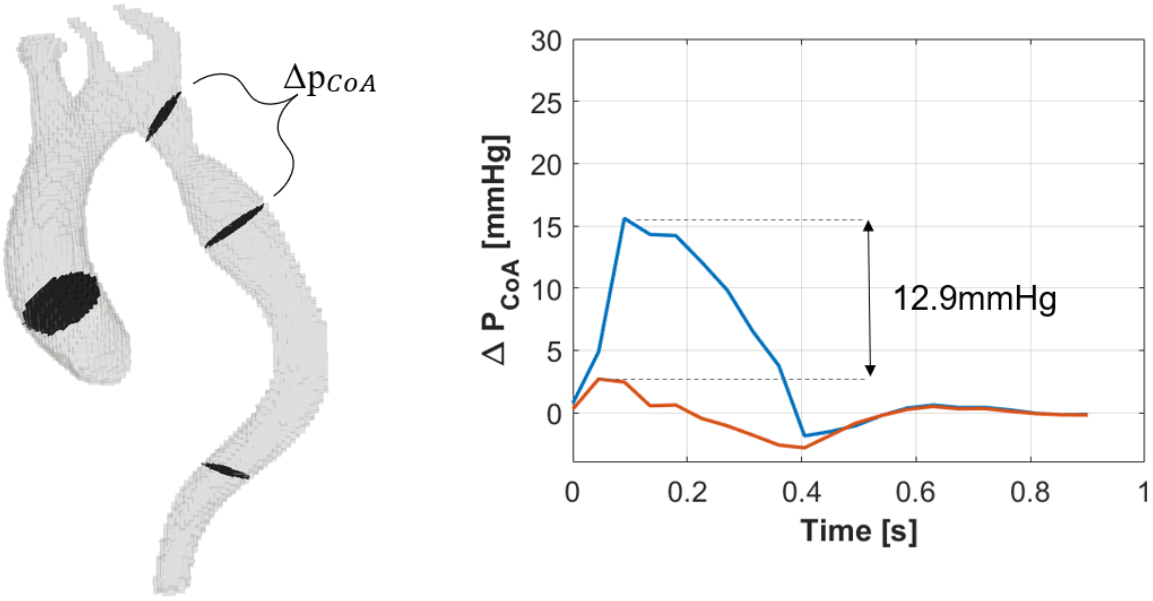

Figure 3.14: Pressure differences over time across the coarctation after the application of the DFW filter on planes proximal (blue) and distal (red) to the coarctation.

In addition, pressure fields calculated adopting 4DF-FEPPE, could also be used to gain insight into how pressure varies in regions of high vorticity: Figure 3.15 shows how the high velocity jet coming out of the aortic valve during systole creates a vortex-like structure with a lower pressure region at its center.

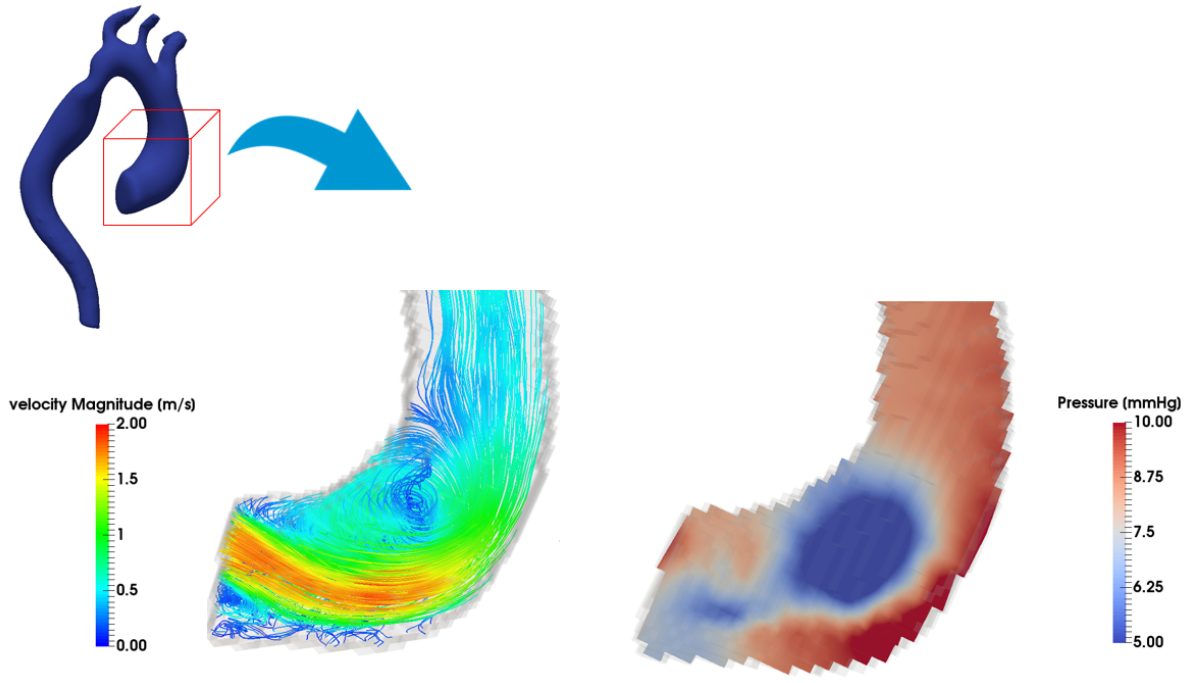

Figure 3.15: Streamlines representation near the aortic valve at systolic peak (left) and corresponding pressure distribution (right) calculated from 4D flow.

For this analysis, once the ROI was segmented from PCMRA images, pressure calculation (i.e. creation of the finite element mesh and PPE solution) took approximately 3 minutes and 30 seconds for a 21-frame 4D flow sequence without co-registration. Application of the DFW filter added an extra 5 minutes and 45 seconds per filtering iteration, for a total increase in computational time of approximately 1 hour.

3.2 Numerical simulations

The results obtained from the two numerical simulations described in the Chapter 2 were compared to 4D flow MRI data for validation. First, for the three supra-aortic branches and descending aorta, flow rates over time were compared (Figures 3.17 and 3.26) (Tables 3.4 and 3.5). Then, a more qualitative comparison was performed by observing velocity magnitude contours and streamlines distal to the coarctation. In order to check for turbulent flow, for both simulations, Reynolds (Re) and Womersley (α) numbers were

calculated on a plane just distal to the coarctation neck, where the highest velocities were observed. The two dimensionless numbers were calculated as:

$$Re = \frac{v_m D \rho}{\mu}, \tag{3.2}$$

$$\alpha = \frac{D}{2}\left(\frac{\omega\rho}{\mu}\right)^{1/2}, \tag{3.3}$$

where v_m is the maximum velocity on the selected plane, D its diameter, ω is heart frequency in beats/s, ρ is blood density and μ blood viscosity. The maximum Re value obtained was 18316, while $\alpha = 7.55$ was found. The critical Reynolds number ($\hat{Re}$) was calculated according to the relation $\hat{Re} = 250\alpha$ [110]. This analysis showed that turbulent flow develops just downstream of the coarctation during systolic peak.

For both simulations, a qualitative validation with 4D flow was performed by comparing velocity contours on specific planes in the domain. The cross-sectional planes where velocity magnitude was visualized are shown in Figure 3.16.

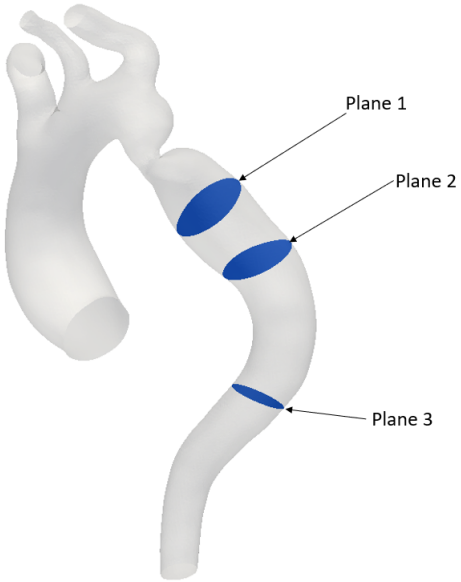

Figure 3.16: Cross-sectional planes along the descending aorta where velocity contours were visualized.

3.2.1 Simulation-1 results

Figure 3.17 shows flow rates over time for the three supra-aortic vessels and descending aorta for both 4D flow (blue line) and Simulation-1. Average values are in Table 3.4. The largest difference between average flow rates was obtained at the LSA outlet and it corresponded to a 0.26 L/min. Overall, flow rate curves obtained with Simulation-1 resembled the waveforms extracted from 4D flow MRI. In the LSA and BCT both the upslope and the downslope well matched 4D flow data, whereas in the DAo outlet, the simulation results showed an underestimation of the peak flow rate and a longer temporal decay (Figure 3.17). In particular, the difference between peak flow rates through the DAo was 1.43 L/min.

The mean inlet flow rate obtained from 4D flow was 9.33 L/min, implying that 56% of the total flow rate is channeled into the BCT.

The 85% lumen reduction represented by the coarctation, together with a cross-sectional area of 2.0744 cm^2, could cause this abnormal flow distribution with respect to a healthy case [111].

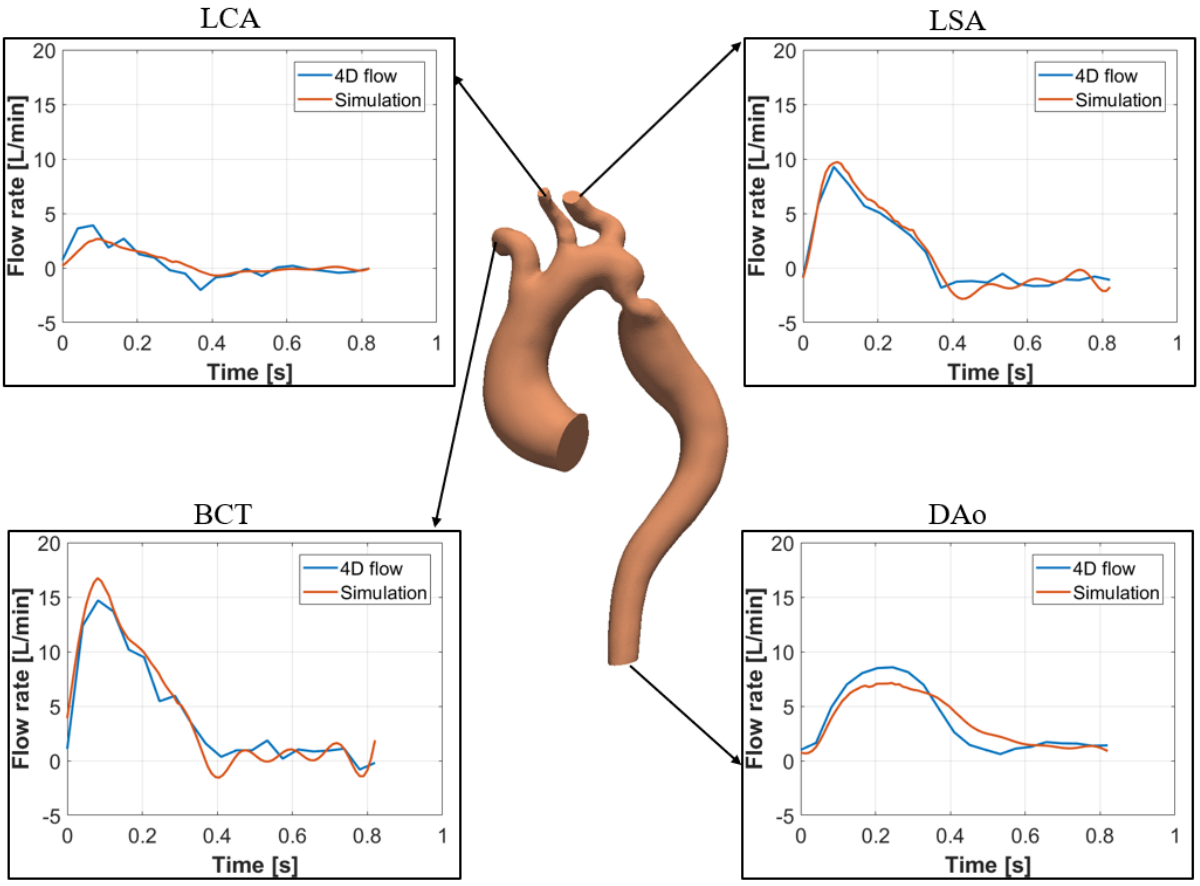

Figure 3.17: Flow rates over time compared between 4D flow data and Simulation-1 results.

Outlet	$\overline{Q}_{4Dflow}$	$\overline{Q}_{Simulation-1}$
BCT	4.06	4.22
LCA	0.43	0.48
LSA	1.26	1.52
DAo	3.58	3.55

Table 3.4: Time averaged flow rates comparison between 4D flow data and Simulation-1 for the brachiocephalic trunk (BCT), left carotid artery (LCA), left subclavian artery (LSA) and descending aorta (DAo). All values are expressed in L/min.

Further qualitative validation was provided by visualizing streamlines and velocity contours on planes transversal and longitudinal to the descending aorta (Figures 3.18 - 3.22). On Plane 1 (Figure 3.18), the velocity profile peak appeared to be more flattened near the wall compared to 4D flow data, and it was still present at T9, in disagreement with 4D flow. However, velocity value ranges were observed to be very similar in the two cases. On Plane 2 (Figure 3.19), the velocity profile peak obtained from Simulation-1

was shifted toward the center of the lumen with respect to 4D flow-based contours. In particular, at T5 the two contours were in disagreement, while at T7 and T9 good agreement was observed in terms of high velocity profile shape and location. On Plane 3 (Figure 3.20), at T5 and T7 4D flow-derived contours showed high velocity peaks that were not captured by Simulation-2, whereas at T9 a very good agreement was found in terms of velocity profile. Comparing streamlines and velocity contours on a plane longitudinal to the descending aorta, the high velocity jet created by the narrowing was observed. In both 4D flow-derived velocity fields and Simulation-1 results, peak velocity values and distributions were similar. However, the flow jet observed in Simulation-1 results lasted longer in time and covered a larger volume of the descending aorta compared to what was observed from 4D flow; this can be observed in Figure 3.21 at times T6 and T8. Since an idealized velocity profile was imposed at the inlet, Simulation-1 velocity streamlines in the ascending aorta were in disagreement with 4D flow data (Figure 3.21).

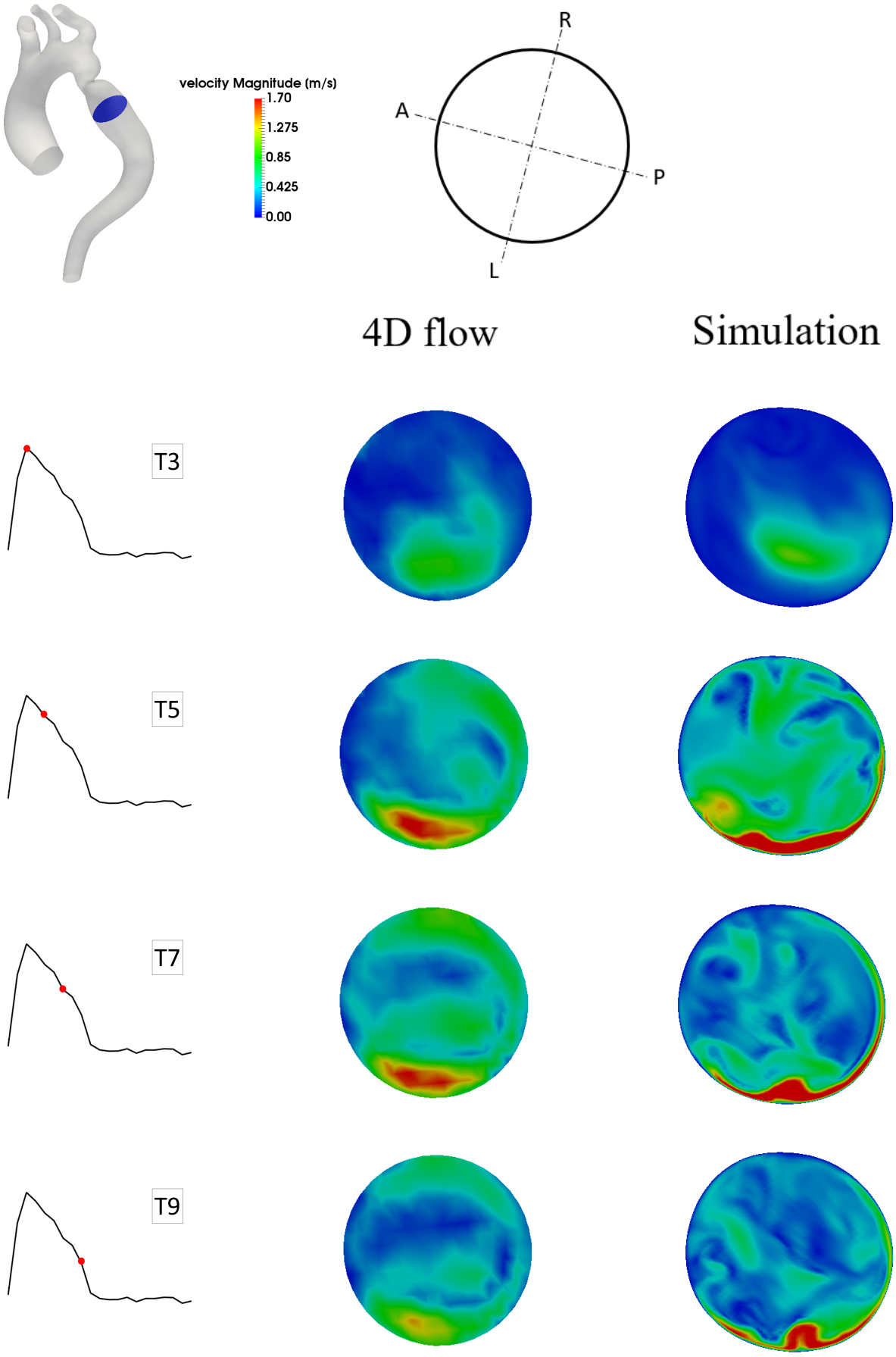

Figure 3.18: Velocity magnitude comparison between 4D flow and Simulation-1 on Plane 1.

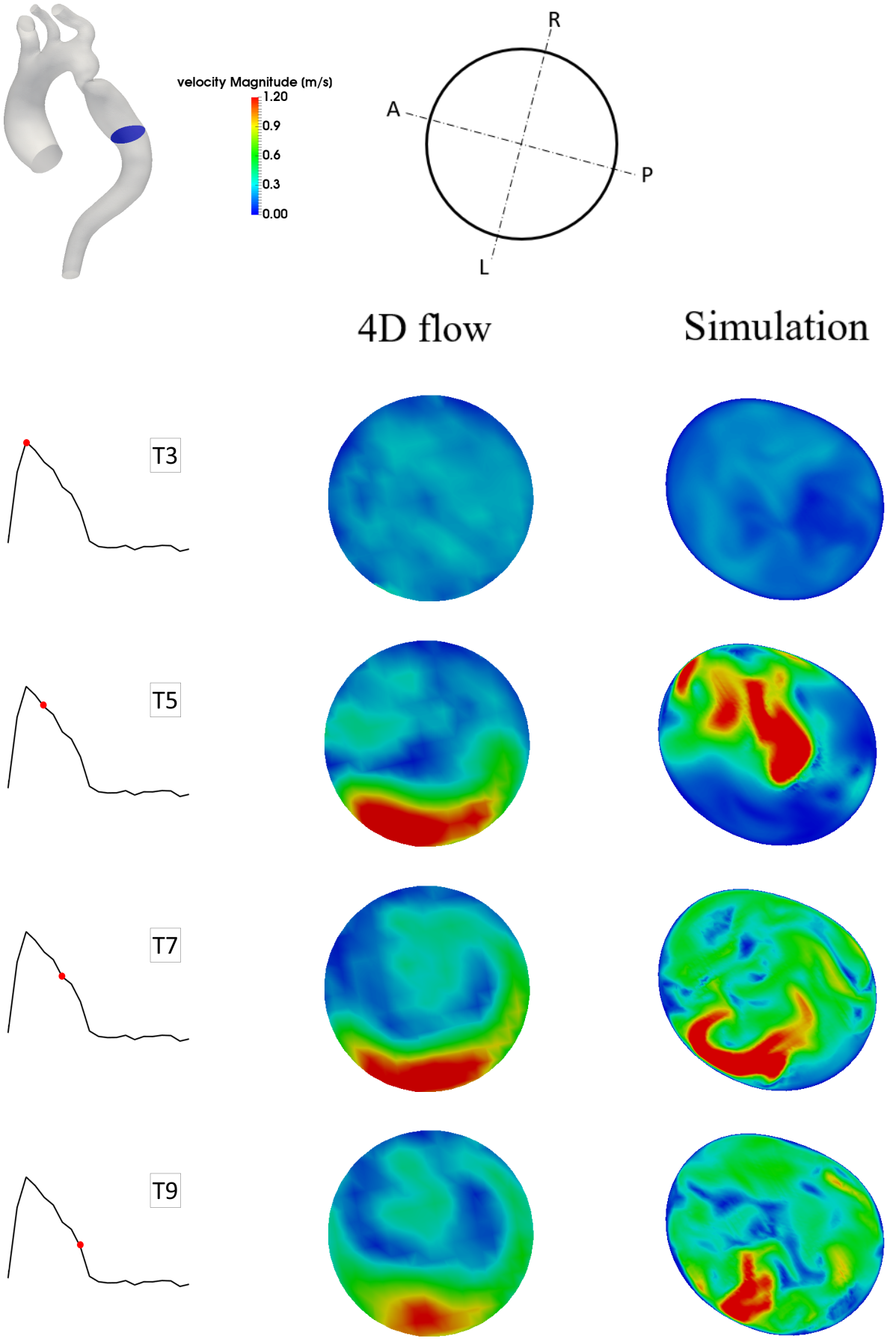

Figure 3.19: Velocity magnitude comparison between 4D flow and Simulation-1 on Plane 2.

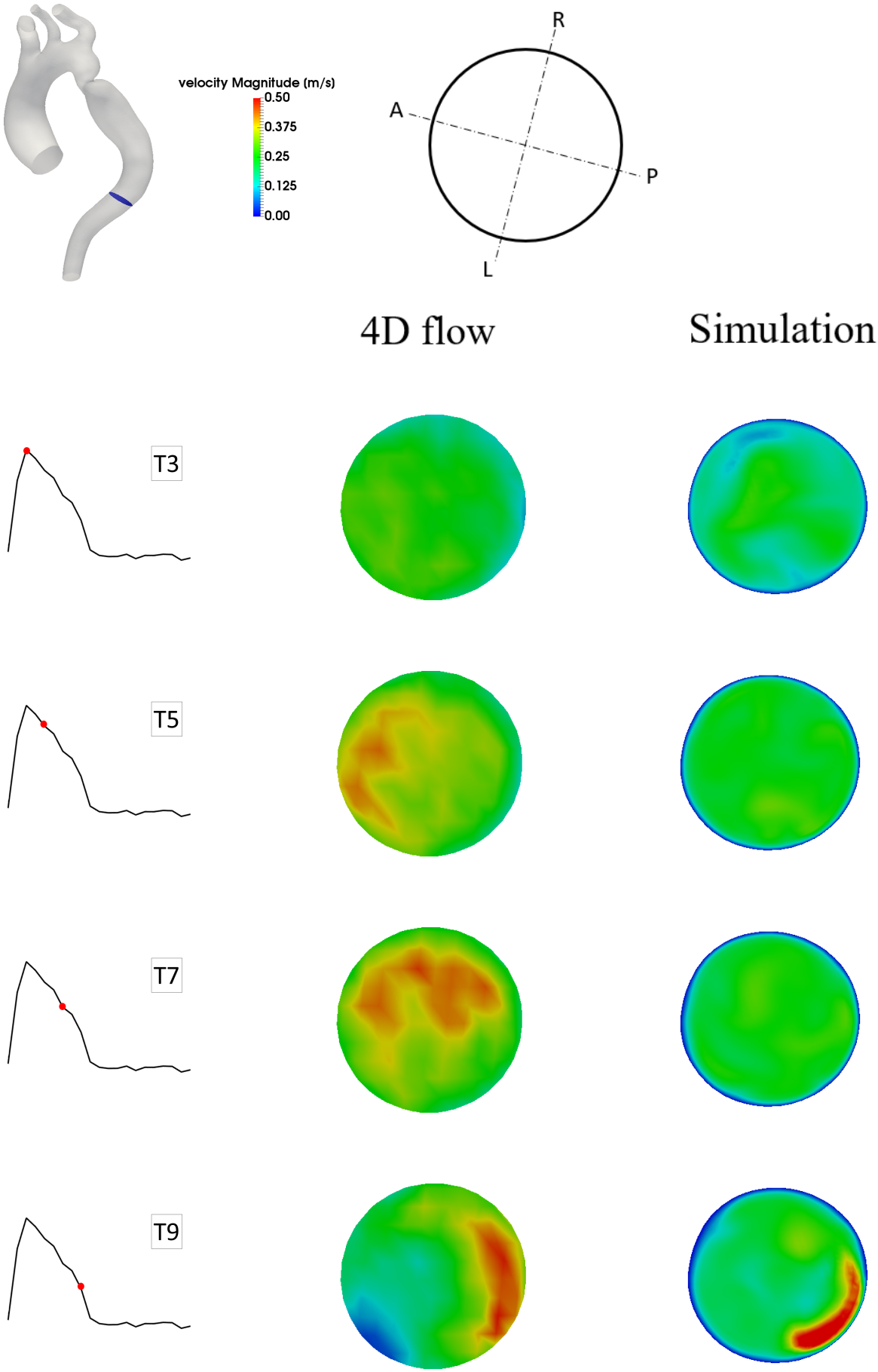

Figure 3.20: Velocity magnitude comparison between 4D flow and Simulation-1 on Plane 3.

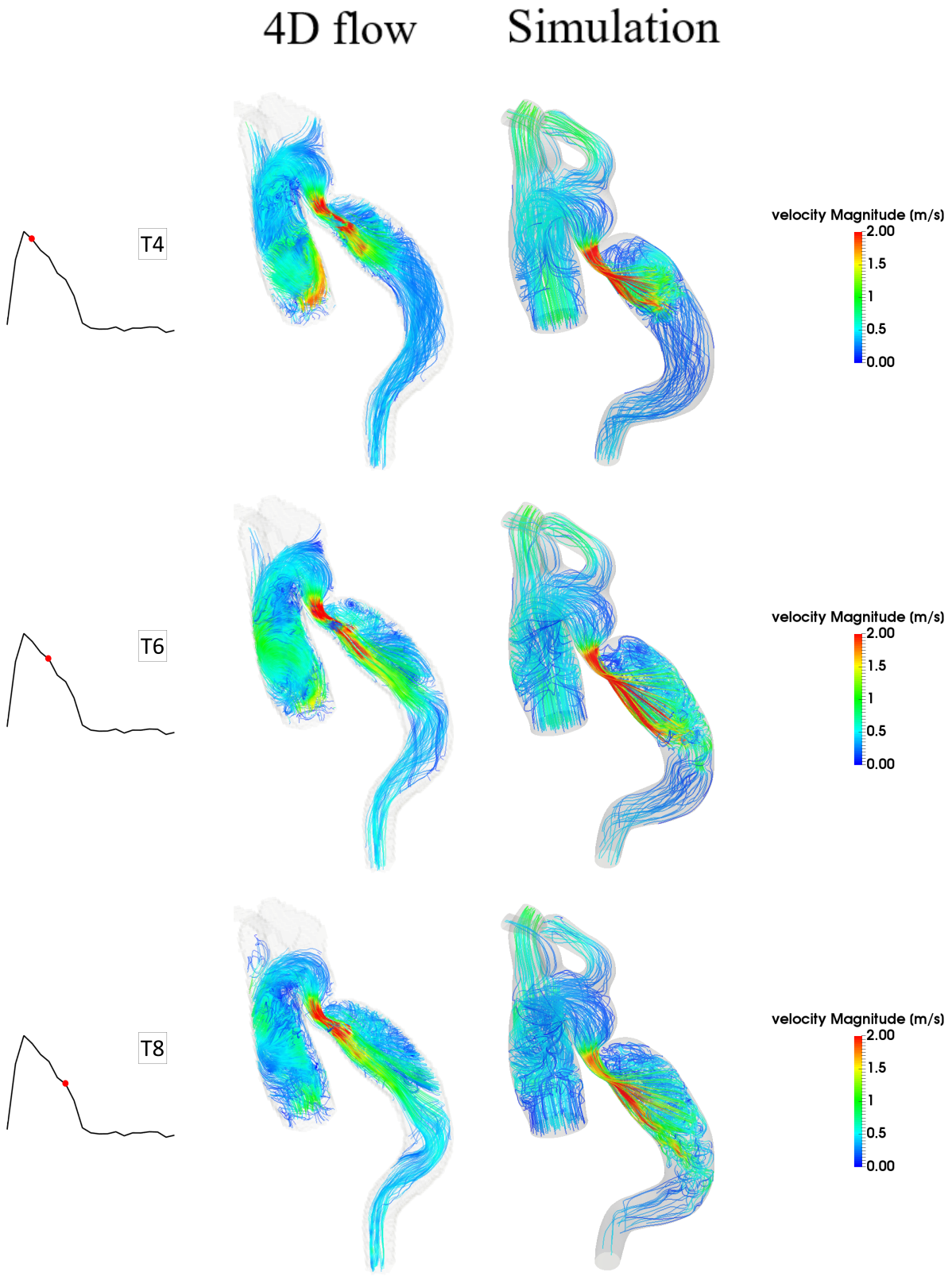

Figure 3.21: Comparison between velocity streamlines obtained from 4D flow (left) and from Simulation-1 (right).

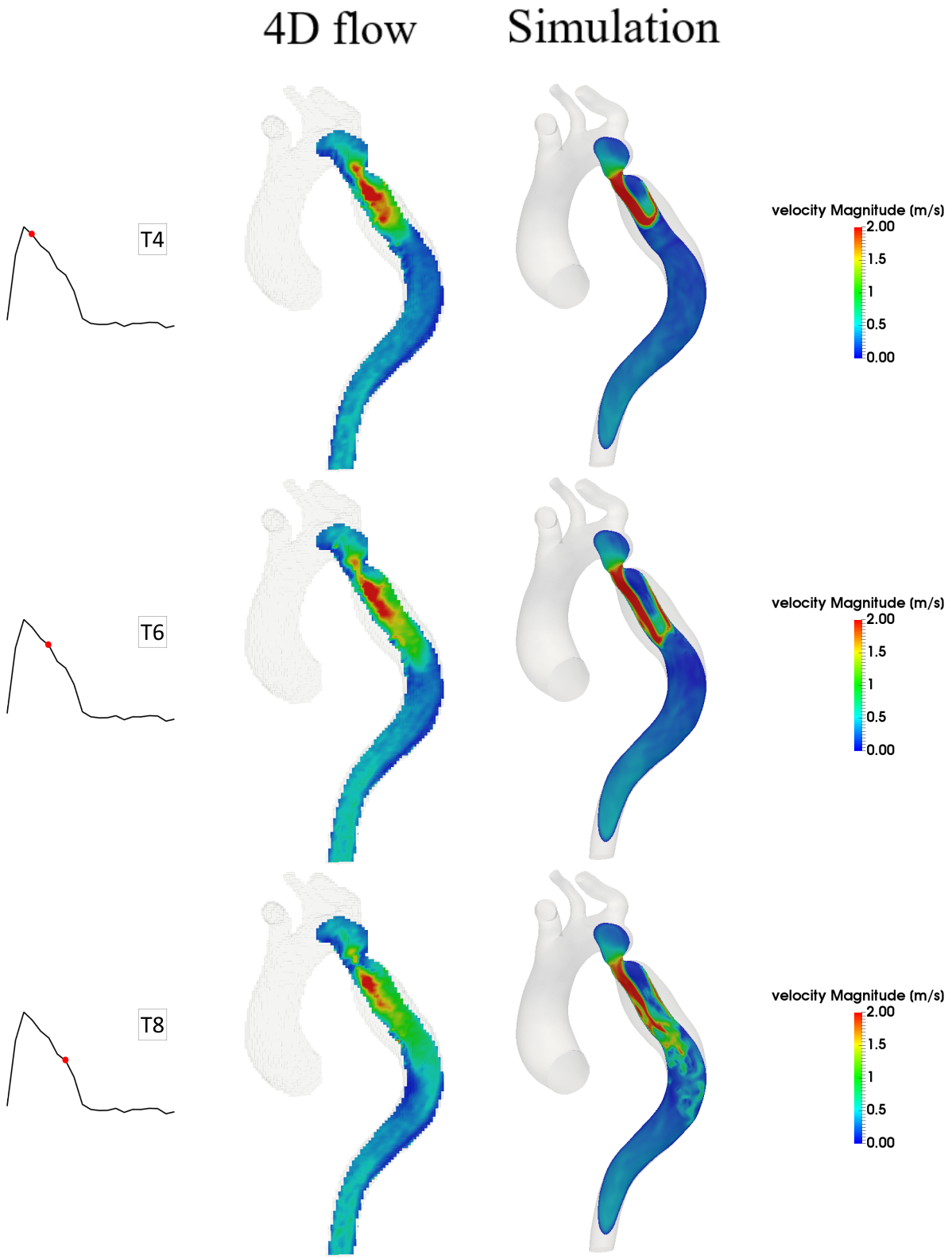

Figure 3.22: Velocity magnitude visualized as contours on a longitudinal plane: comparison between 4D flow (left) and Simulation-1 (right).

The pressure difference across the coarctation extracted from the simulation results was compared to the 4D flow-derived result obtained with 4DF-FEPPE (Section 2.1). The trans-coarctation pressure drops calculated from 4D flow and from Simulation-1 are reported in Figure 3.23. Additionally, in order to reproduce the same output obtained from 4D flow data analysis, the pressure at the DAo was used as reference pressure to obtain pressure difference curves at the PreCoA and PostCoA planes (Figure 3.24). Pressure difference curves obtained with this simulation (Figure 3.24) were in good agreement with the oned obtained with 4DF-FEPPE (Figure 3.12). While the 4D flow based approach led to a peak-to-peak pressure drop of 17.6 mmHg and a maximum difference of 21.09 mmHg, in Simulation-1 a peak-to-peak value of 16.85 mmHg was found and a maximum instantaneous difference of 22.43 mmHg was calculated. The relative error, calculated as $error = \left|\frac{\Delta p_{simulation} - \Delta p_{4Dflow}}{\Delta p_{simulation}}\right|$, is plotted together with pressure drop curves (Figure 3.23). At a time point corresponding to the peak values, a relative error of 3.6% was found.

Pressure difference contours at three different time points in the cardiac cycle obtained with Simulation-1 were compared to 4DF-FEPPE results (Figure 3.25). While 4DF-FEPPE results are shown as pressure differences with respect to pressure in the lowest point of the descending aorta (where pressure equals zero for all time points), Simulation-1 results are shown as pressure differences with respect to cross-section-averaged pressure at the DAo. 4D flow-derived pressure distributions were in very good agreement with Simulations-1 results.

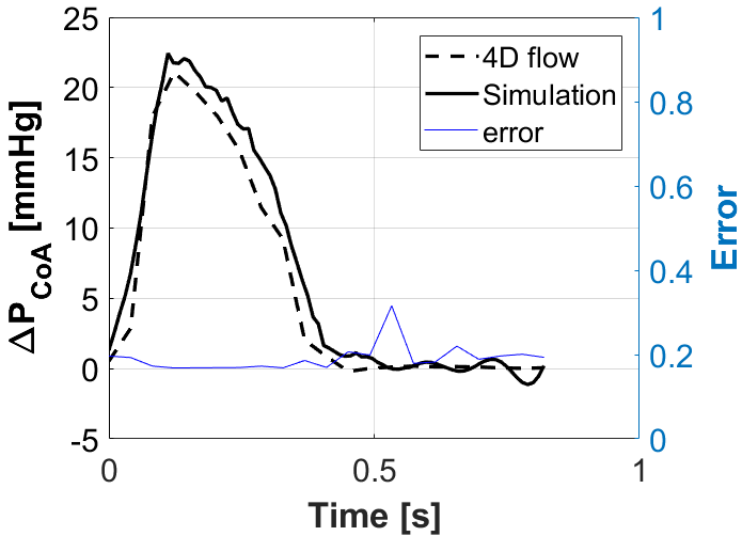

Figure 3.23: Plane averaged pressure difference across the coarctation: 4D flow-based curve calculated with 4DF-FEPPE vs. Simulation-1 results. Relative error is plotted as a dashed line.

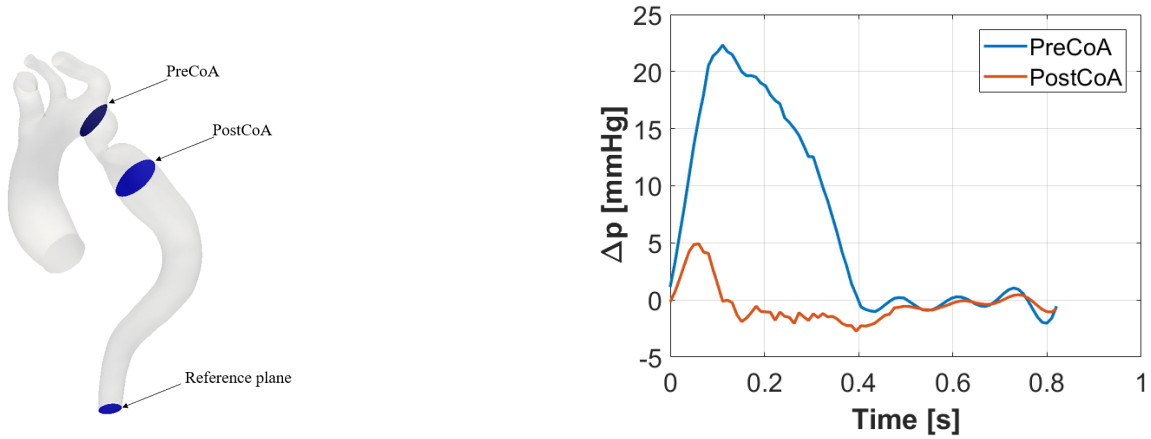

Figure 3.24: Pressure difference waveforms between planes proximal (PreCoA) and distal (PostCoA) to the coarctation and a reference plane at the DAo calculated from Simulation-1.

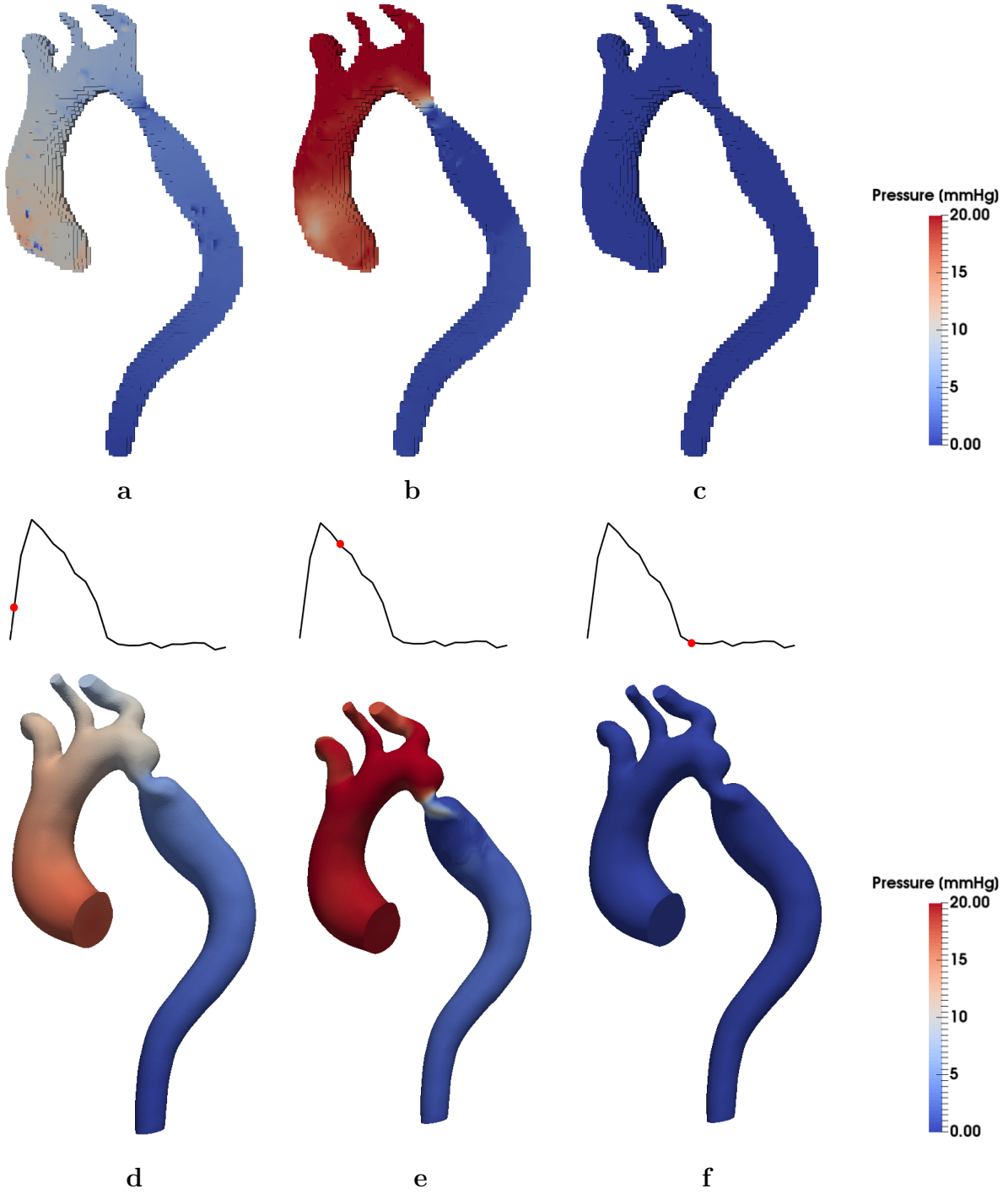

Figure 3.25: Pressure difference contours calculated with 4DF-FEPPE (a-c) and with Simulation-1 (d-f). Pressure differences are calculated with respect to the lowest point in the descending aorta for 4DF-FEPPE results (a-c), and with respect to cross-section-averaged pressure in the descending aorta outlet (DAo) for Simulation-1 results (d-f).

3.2.2 Simulation-2 results

Flow rates over time obtained with Simulation-2 for the three supra-aortic vessels and descensing aorta are shown in Figure 3.26. Average values are reported in Table 3.5. Flow rates curves were in good agreement with 4D flow data and very similar to the results of Simulation-1; in this case as well the DAo flow rate waveform showed an underestimation of the peak value and a longer temporal decay with respect to 4D flow information. In particular, the difference between peak flow rates through the DAo was 0.83 L/min.

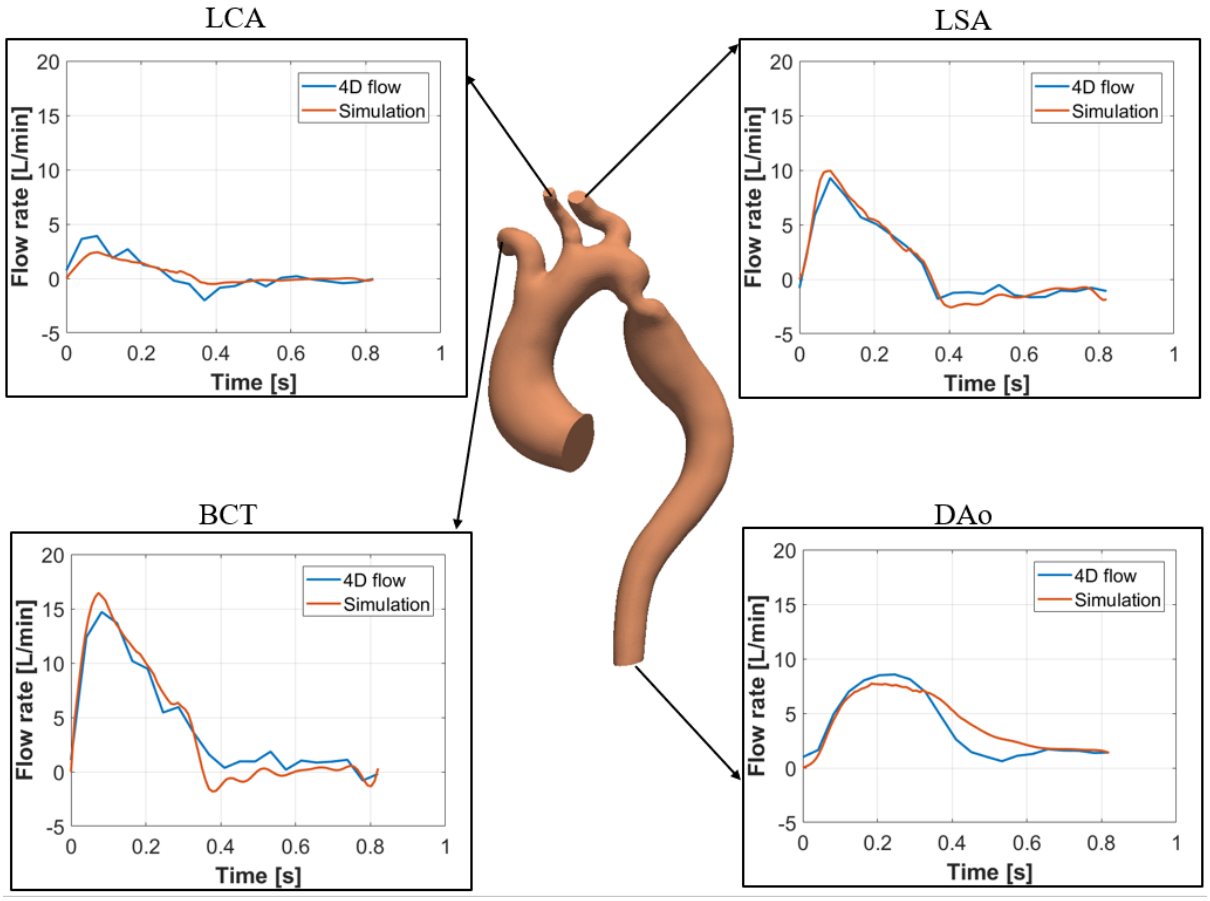

Figure 3.26: Flow rates over time compared between 4D flow data and Simulation-2 results.

Outlet	$\overline{Q}_{4Dflow}$	$\overline{Q}_{Simulation-2}$
BCT	4.06	3.93
LCA	0.43	0.44
LSA	1.26	1.35
DAo	3.58	4.05

Table 3.5: Time averaged flow rates comparison between 4D flow data and Simulation-2 for the brachiocephalic trunk (BCT), left carotid artery (LCA), left subclavian artery (LSA) and descending aorta (DAo). All values arae expressed in L/min.

Further qualitative validation was provided by visualizing streamlines (Figure 3.30) and velocity contours on planes transversal and longitudinal to the descending aorta (Figures 3.27- 3.31). Similar to Simulation-1 results, on Plane 1 (Figure 3.27), the velocity profile peak appeared to be more flattened near the wall compared to 4D flow data, and very similar to Simulation-1 results. However, velocity value ranges were observed to be very similar in the two cases. On Plane 2 (Figure 3.28), the velocity profile peak obtained with Simulation-2 was shifted toward the center of the lumen with respect to 4D flow-based contours. In particular, at T5 the two contours were in disagreement, while at T7 and T9 good agreement was observed in terms of high velocity profile shape and location. On Plane 3 (Figure 3.29), at T5 and T7 4D flow-derived contours showed higher velocity peaks than Simulation-2 results, while at T9 a better agreement was observed in terms of velocity profile, with a slight overestimation of Simulation-2 results with respect to 4D flow. Comparing streamlines and velocity contours on a plane longitudinal to the descending aorta, a high velocity jet created by the narrowing was observed. In both 4D flow-derived velocity fields and Simulation-2 results, peak velocity values and distributions were similar. However, the flow jet observed in Simulation-2 results lasted longer in time and covered a larger volume of the descending aorta compared to what was observed from 4D flow; this can be observed in Figure 3.30 at times T6 and T8. Very good agreement was observed between Simulation-2 and Simulation-1 results in terms of velocity streamlines and contours, with no significant difference between the two.

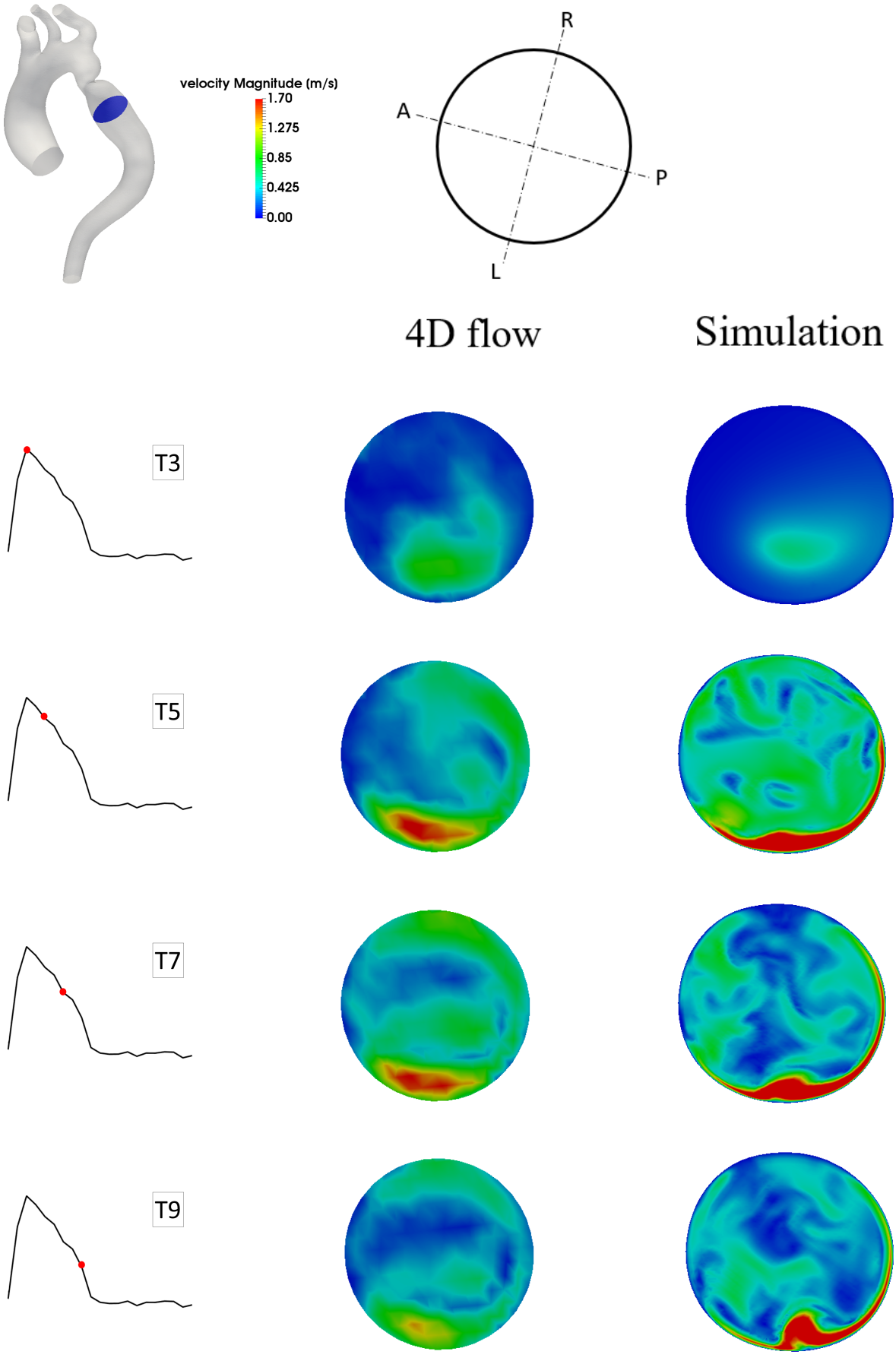

Figure 3.27: Velocity magnitude comparison between 4D flow and Simulation-2 on Plane 1.

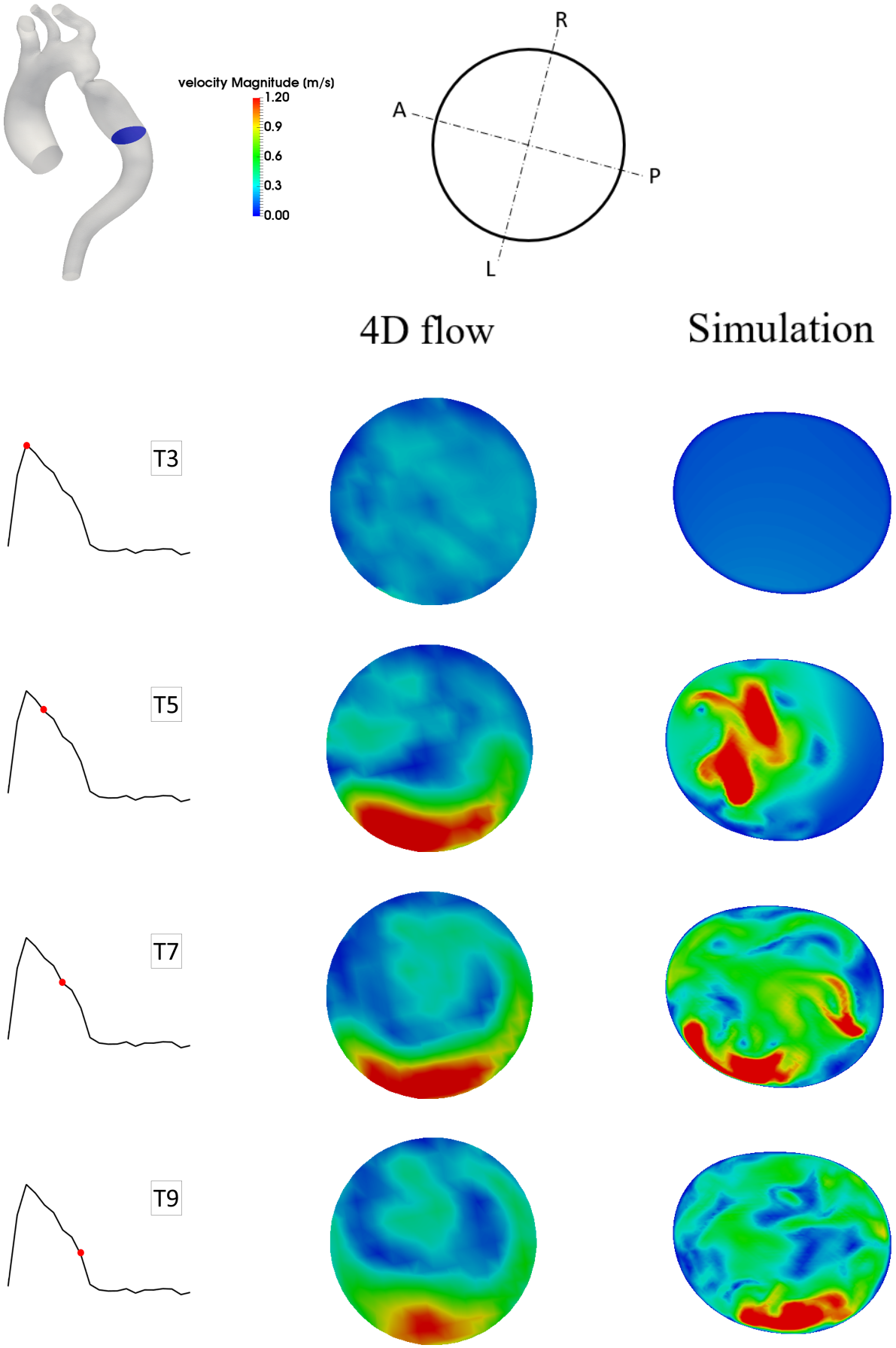

Figure 3.28: Velocity magnitude comparison between 4D flow and Simulation-2 on Plane 2.

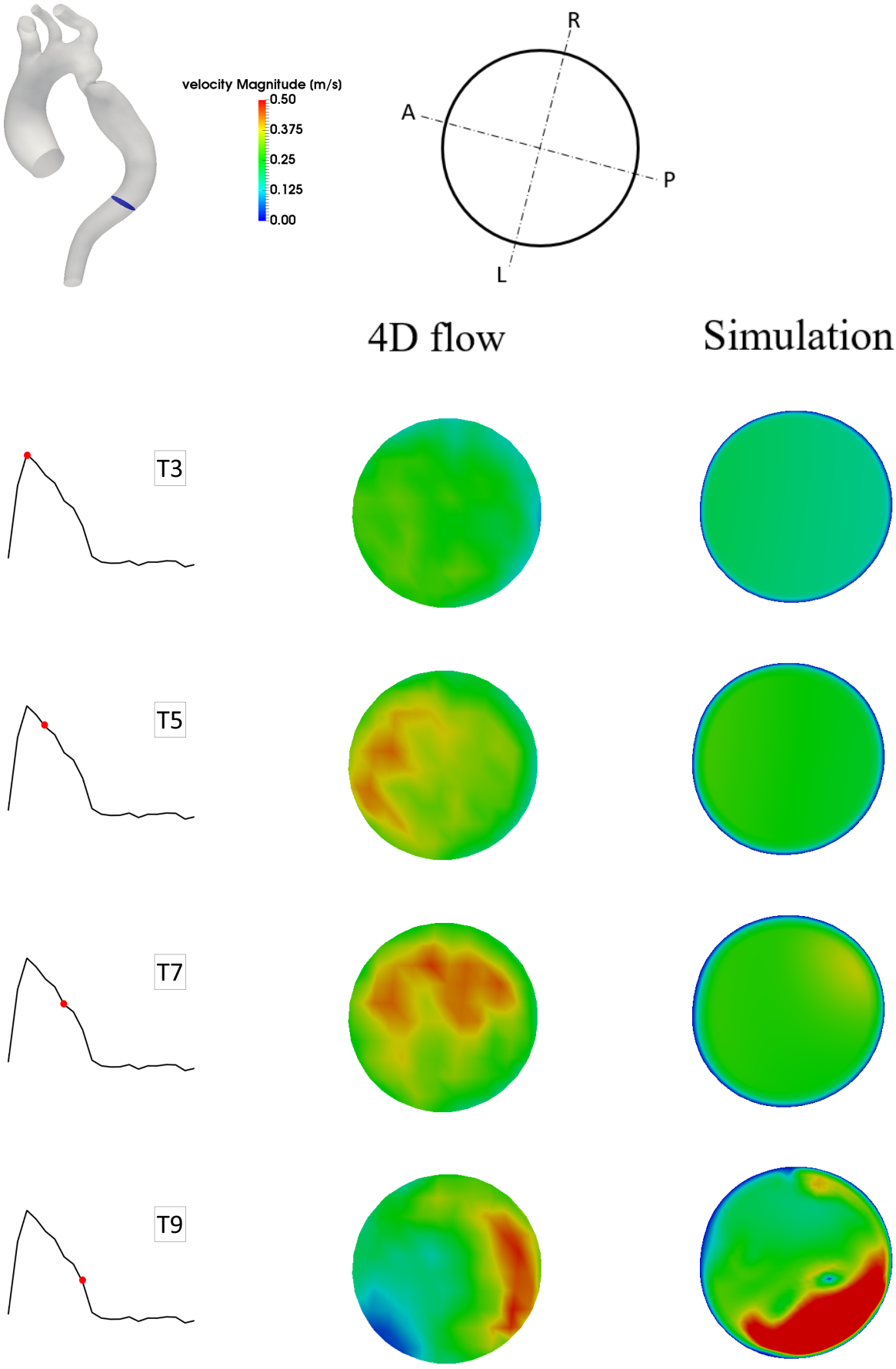

Figure 3.29: Velocity magnitude comparison between 4D flow and Simulation-2 on Plane 3.

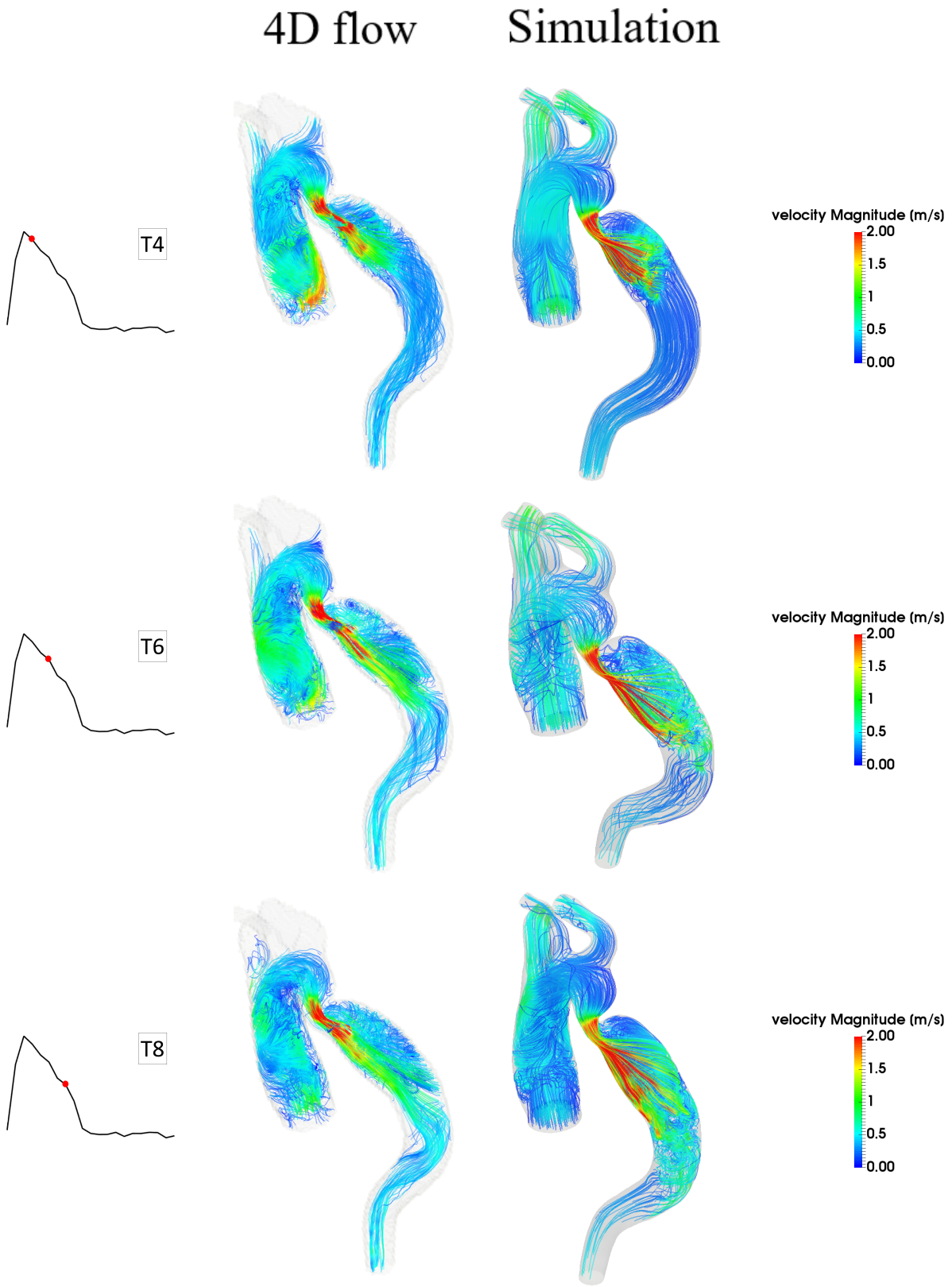

Figure 3.30: Comparison between velocity streamlines obtained from 4D flow (left) and from Simulation-2 (right).

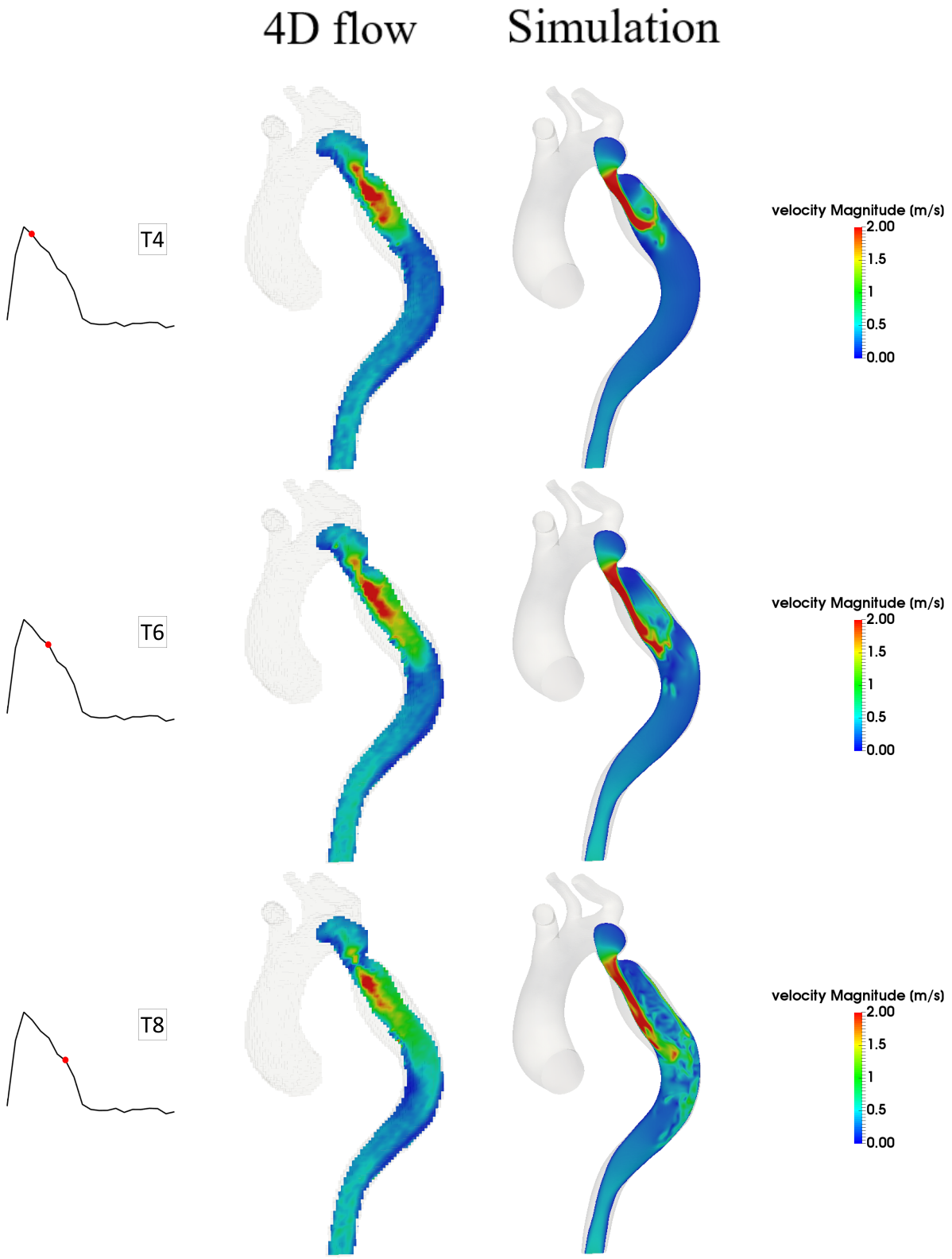

Figure 3.31: Velocity magnitude visualized as contours on a longitudinal plane: comparison between 4D flow and Simulation-2.

Trans-coarctation pressure difference was extracted from the simulation results and it was compared to 4D flow-derived results obtained with the approach developed in this work (Section 2.1). The pressure drops calculated from 4D flow and from the Simulation-2 are reported in Figure 3.32. Additionally, as for Simulation-1, the pressure waveform calculated in Simulation-2 at the descending aorta outlet was subtracted from pressures calculated on the PreCoA and PostCoA planes (Figure 3.33). The resulting pressure difference curves obtained with Simulation-2 were in good agreement with 4DF-FEPPE results (Figure 3.12) as well as Simulation-1 results, with only a slight underestimation of 4DF-FEPPE and Simulation-1 with respect to Simulation-2 results. While the 4D flow based approach led to a peak-to-peak pressure drop of 17.6 mmHg and a maximum difference of 21.09 mmHg, in Simulation-2 a peak-to-peak value of 18.56 mmHg was found and a maximum instantaneous difference of 23.89 mmHg was calculated. The relative error, calculated as $error = \left|\frac{\Delta p_{simulation} - \Delta p_{4Dflow}}{\Delta p_{simulation}}\right|$, is plotted together with pressure drop curves (Figure 3.32). At a time point corresponding to the peak values, a relative error of 12% was found.

Further qualitative comparison was provided by pressure difference contours in Figure 3.34. Similarly to the comparison with Simulation-1, 4D flow-derived pressure distributions were in very good agreement with Simulations-2 results. Pressure differences calculated with respect to the DAo are shown in Figure 3.34

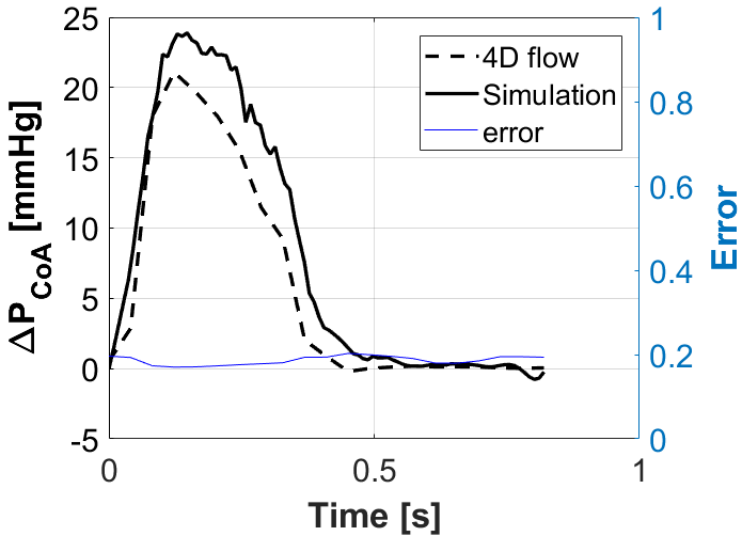

Figure 3.32: Plane averaged pressure difference across the coarctation: 4D flow-based curve vs. Simulation-2. Relative error is shown as dashed line.

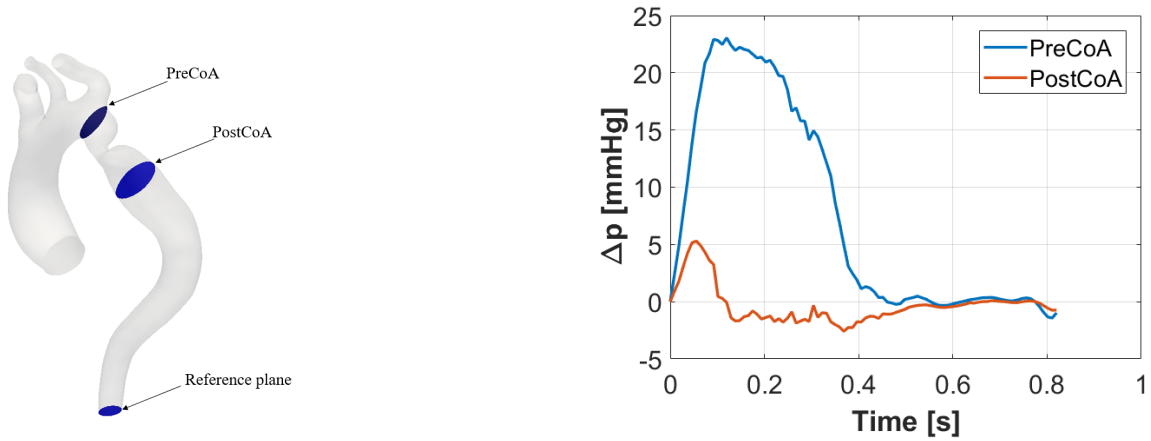

Figure 3.33: Pressure difference waveforms between planes proximal (PreCoA) and distal (Post-CoA) to the coarctation and a reference plane at the DAo calculated from Simulation-2.

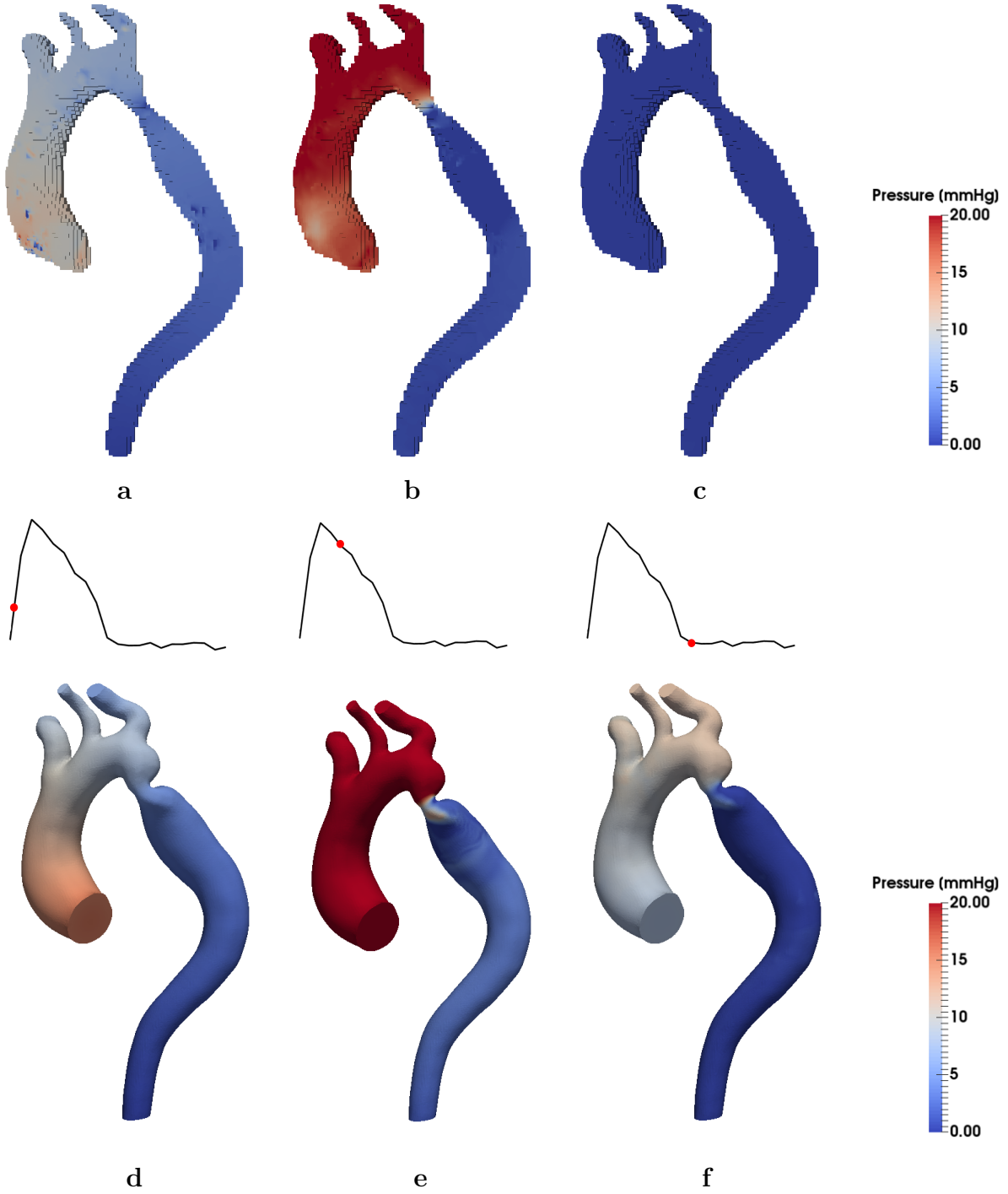

Figure 3.34: Pressure difference contours calculated with 4DF-FEPPE (a-c) and with Simulation-2 (d-f). Pressure differences are calculated with respect to the lowest point in the descending aorta for 4DF-FEPPE results (a-c), and with respect to cross-section-averaged pressure in the descending aorta outlet (DAo) for Simulation-2 results (d-f).

Even though trans-coarctation pressure drops obtained from the two simulations were in agreement, pressure values in the entire aorta differed by approximately 20 mmHg. The

higher pressure values obtained with Simulation-2 caused a larger wall displacement in the ascending aorta during systole (Figure 3.35).

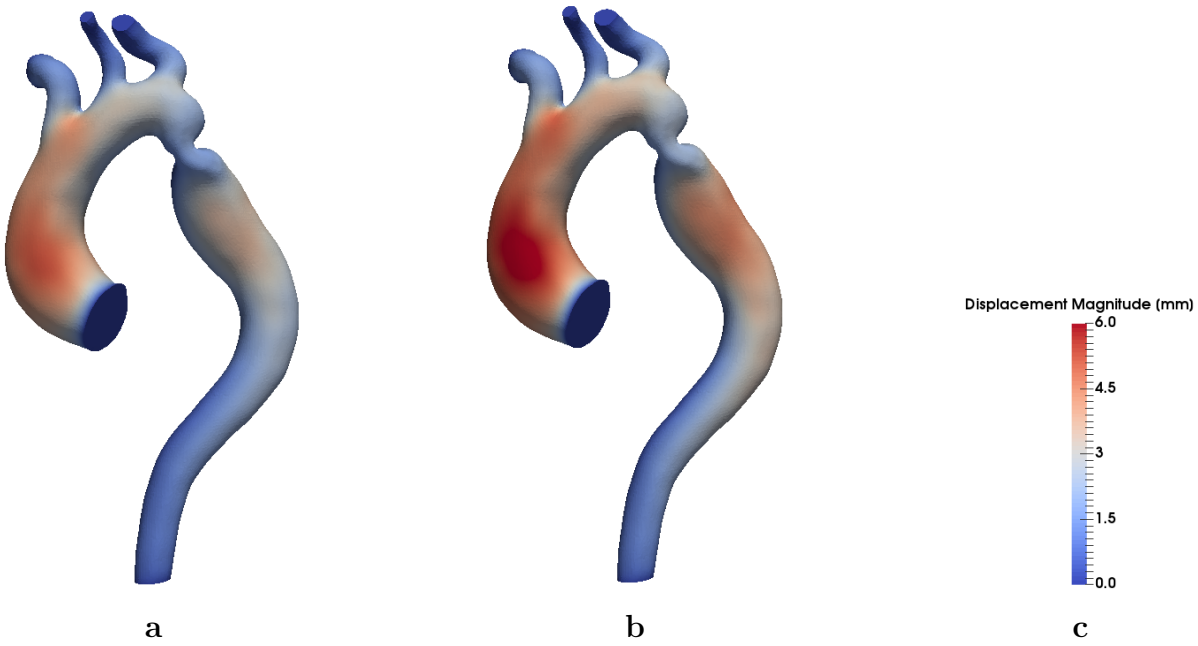

Figure 3.35: Wall displacement magnitude color maps at systolic peak for Simulation-1 (a) and Simulation-2 (b).

3.2.3 Computational times

Times required by Simulation-1 and -2 are reported in Table 3.6 as a comparison with 4DF-FEPPE. Despite being calculated in only a fraction of the simulation time, the FEPPE solution based on 4D flow produced very similar maximum (Δp_m) and peak-to-peak (Δp_{pp}) pressure drops.

	Simulation-1	Simulation-2	4DF-FEPPE
Total time	∼2 days	∼1 day	<5 minutes
Δp_m [mmHg]	22.43	23.89	21.09
Δp_{pp} [mmHg]	16.85	18.56	17.6

Table 3.6: Computational times required by Simulations 1 and 2 and 4DF-FEPPE, with their relative maximum and peak-to-peak pressure drops. Simulation-1 was run with a convergence residual of 10^{-5}, while a residual of 10^{-3} was used in Simulation-2.

3.3 *In vitro* analysis

In order to compare pressure measurements performed with the *in vitro* workbench, cross-section-averaged pressures were calculated, from 4DF-FEPPE and both simulations results, on planes corresponding to pressure transducer port locations (Figure 3.36). The three different tested flow rates were: $Q_{low} = 0.9Q$, Q and $Q_{high} = 1.1Q$, where $Q = 8.56$ L/min is the DAo peak flow rate value extracted from 4D flow. Pressure transducers measurements obtained at different locations along the aorta (Figure 2.19) are reported in Table 3.7 together with maximum instantaneous pressure drops obtained from 4DF-FEPPE and both Simulations 1 and 2. All Δp values in Table 3.7 were calculated as differences with respect to pressure at Port 1 in the *in vitro* case, and with respect to section PRE in the *in silico* case. Δp_1, Δp_2, Δp_3 and Δp_4 calculated with 4DF-FEPPE were greater than test bench measurements using Q by 1 mmHg, 0.37 mmHg, 4.5 mmHg and 2.8 mmHg respectively; while Simulation-1 produced results that overestimated *in vitro* measurements by 1 to 4.3 mmHg and Simulation-2 pressure differences were higher than measurements by up to 6.4 mmHg.

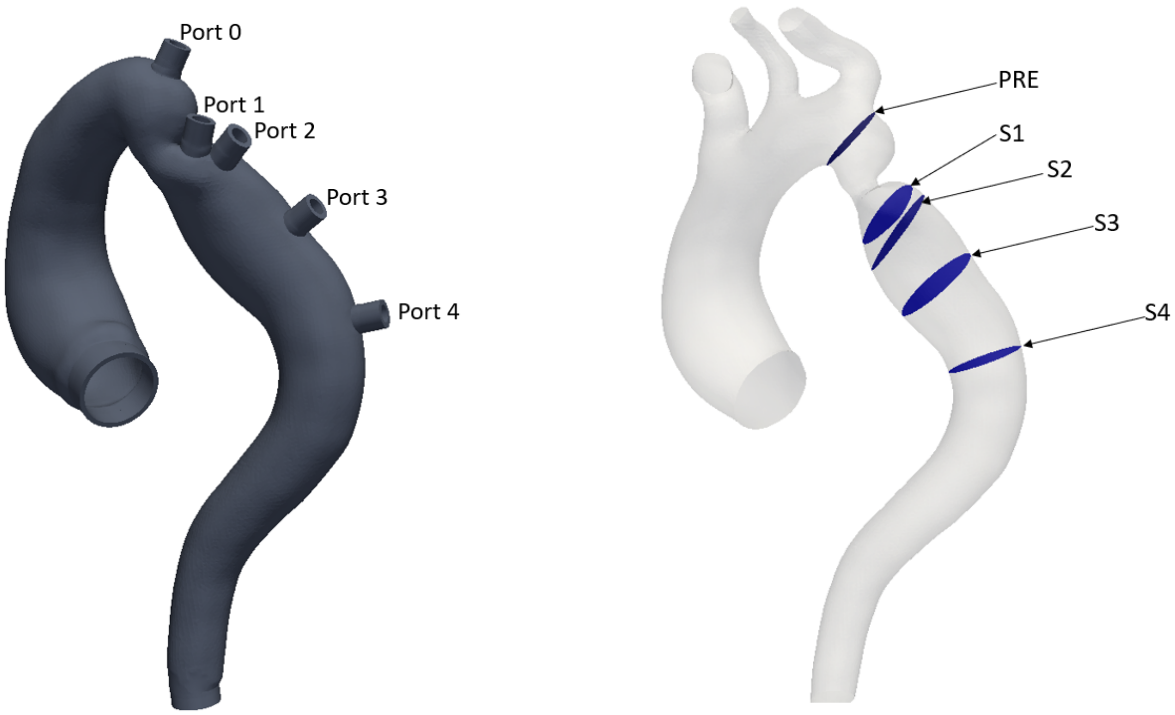

a **b**

Figure 3.36: 3D model used in the *in vitro* setup with ports for pressure transducers (a) and corresponding cross-sections in the computational domain (b) (referred to as S1-S4).

	Δp_1 [mmHg]	Δp_2 [mmHg]	Δp_3 [mmHg]	Δp_4 [mmHg]
in vitro (Q_{low})	14.6	13.7	13.6	14.5
in vitro (Q)	19.4	20.73	16.6	16.8
in vitro (Q_{high})	23.6	23.2	23.5	21.6
Simulation-1	21.5	21.8	20.9	19.7
Simulation-2	22.7	23.1	23	21
4DF-FEPPE	20.4	21.1	21.1	19.6

Table 3.7: Pressure differences measured *in vitro* and calculated with Simulations 1 and 2 and 4DF-FEPPE. All Δp values are pressure differences between a certain Port (or section) identified by the subscript and Port 1 (or section PRE).

Chapter 4

Discussion and conclusions

In this last chapter, the results obtained with the proposed thesis work will be discussed. The most important and innovative aspects will be highlighted and general conclusions will be drawn. Then, the limitations and difficulties encountered throughout the development of this work will be summarized. Finally some of the possible future developments will be briefly outlined.

4.1 Discussion

In the proposed work, the feasibility and reliability of 4D flow-based pressure difference estimation was assessed. For this purpose, the 4DF-FEPPE algorithm was developed and its results were compared to numerical simulations validated through a quantitative and qualitative correlation with raw 4D flow data. Further validation was provided by comparing 4D flow-derived pressure drops along the descending aorta with *in vitro* measurements taken on an *ad hoc* designed experimental model. In the following sections the rationale behind the proposed methodologies, together with the results obtained will be discussed. In particular, the main considerations will focus on the most important aspects of the pressure estimation algorithm, and on the two different numerical simulations, with their assumptions and results.

4D flow-based pressure estimation

Throughout the development of the workflow presented in this study, several steps revealed to be particularly important. First and foremost, the co-registration of the 4D flow images with a geometry segmented from MRA significantly improved flow visualization and pressure calculation. Specifically, the volume reduction performed on the 3D surface before co-registration enabled to filter out partial volume effects near the vessel boundary, thus leading to smoother pressure distributions. In fact, preliminary analyses showed that even if very few elements lying outside the lumen are included in the ROI, this would have a strong impact on pressure in the whole domain. Similarly, correcting all pixels affected by aliasing was of fundamental importance (Section 2.1.2). If these pixels had not been corrected for, the high velocity within the coarctation would have been lowered, thus resulting in a smaller pressure drop.

8-node hexahedral elements seemed the most natural choice for building a mesh over the image voxel structure; given the regular voxel spacing, these elements were also relatively

easy to be manually implemented. Although higher order elements, such as 20-node biquadratic or 32-node tricubic hexahedra, would be able to capture larger pressure gradients, their implementation would require an upsampling of velocity fields measured with 4D flow and would result in higher computational costs. Furthermore, velocity derivatives would depend on the upsampling strategy, which, in some cases, could lead to error amplification. In developing this algorithm, an image upsampling method was explored to increase the number of elements in the domain. This strategy led to an increase in computational time but no significant improvement of accuracy.

Pressure color maps comparison performed between 4DF-FEPPE results and a CFD simulation enabled to validate and benchmark the proposed workflow against CFD-derived data taken as ground truth. This process allowed to gain a deeper insight into the results obtained with the proposed methodology. The solution of the FE-PPE led to a larger pressure mismatch in the supra-aortic vessels with respect to CFD results than in the aorta. The possible causes of such pressure mismatch are two. First, the imposition of only one reference point in the descending aorta. In fact, CFD results were obtained imposing zero pressure boundary conditions at the DAo as well as at the supra-aortic branches extremities. Second, the coarse spatial resolution imposed by the downsampling process to mimic MRI limited the number of elements in the smaller vessels which inevitably led to larger errors. Even though imposing zero pressure at the upper extremities of the domain would have led to a more accurate solution in the branches, in a real case situation, this boundary condition would require knowledge of the absolute pressure at the branches, not available in most cases. Furthermore, this comparison showed how the temporal component of the velocity field plays an important role in determining pressure. In fact, larger errors were observed at the first time frame taken into account, for which velocity temporal derivatives are limited by a 1^{st} order finite difference scheme. Overall, the solution of the FE-PPE proved to be able to capture pressure distributions with high accuracy, mismatching CFD-based calculation by no more than 3 mmHg. Furthermore, the methodology implemented in this work proved to be significantly more efficient than the preexisting code. Keeping the computational time as short as possible is of critical

importance in order to translate 4D flow-based pressure estimation in clinical diagnosis. For what concerns the idealized model used to validate and benchmark 4DF-FEPPE, the addition of Gaussian noise resulted in velocity fields whose values were systematically higher than downsampled velocities (Figure 3.7), with a maximum increase in space-averaged velocity magnitude of 199%. In this context, the application of DFW led to velocities that were lowered by 48% on average with respect to the noisy case (Figure 3.7). Therefore, the tendency of the noise addition process to increase velocity values, together with the lowered velocities resulting from the DFW application, led to DFW-processed pressure distributions that were in better agreement with CFD-derived values (Figure 3.4, 3.6 and Table 3.1).

Pressure fields calculated with the proposed algorithm showed distributions typically observed in CoA patients, which are characterized, during systole, by a net difference between regions proximal and distal to the narrowing. 4D flow-based pressure distributions over time were validated against the results of the two simulations included in this work. It should be noted that the assumptions made to assign outlet boundary conditions did not significantly influence the results obtained with the proposed pressure algorithm. In this way, one could consider the closely matching pressure drop across the coarctation to be more reliable. In this patient-specific case, the use of the DFW filter allowed for efficient denoising of the raw 4D flow data while retaining the observed fluid structures. However, the resulting space-averaged velocity magnitude values were consistently lower than unprocessed data by up to 30% (Table 3.3), which, near the coarctation, led to a decreased jet velocity magnitude, in turn associated with a 5 mmHg lower Δp_{pp}. The tendency of the DFW filter to lower velocity values was observed to a similar extent in the synthetically generated dataset. Nevertheless, as previously discussed, artificial noise addition resulted in velocity fields that were significantly higher than the downsampled non-noisy case, whereas actual 4D flow noise does not have such an effect on velocity fields.

Numerical simulations

Two numerical simulations were reported in this work; Simulations 1 and 2 differed in 3-WK parameter values set at the supra-aortic branches outlets. More specifically, while in Simulation-1 the same mean pressure (80 mmHg) was assumed at all outlets to tune the 3-WKs, in Simulation-2 the mean pressure for the 3-WKs at the branches was increased by an estimation of the peak-to-peak pressure drop observed from Simulation-1 results. Since no information about the patient's pressure was available, in Simulation-1 the same mean pressure for tuning all 3-WK was assumed. However, in CoA this assumption could be regarded as unrealistic, and in order to evaluate the effect of this assumption on the coarctation pressure drop, Simulation-2 was carried out.

In both simulation setups, vessel wall mechanical behavior was assumed to be homogeneous, linear elastic and isotropic, whereas there is evidence suggesting that aortic properties can significantly vary spatially between regions proximal and distal to the coarctation. The choice of using values from [12] was the result of a trial and error process; different combinations of elastic moduli and thicknesses were tested, but they all produced worse results compared to 4D flow data in terms of flow rate distributions and velocity magnitude contours.

For all simulations, a parabolic inlet velocity profile was assumed. While in the ascending aorta this simplification led to velocity profiles that did not resemble 4D flow data, in the descending aorta a strong similarity was observed. Furthermore, recent evidence seem to suggest that hemodynamics parameters such as TAWSS and velocity distributions in the descending aorta are less sensitive to inlet velocity profiles [112].

In Simulation-1 assuming the same mean pressure for 3-WK tuning proved to be acceptable. In particular, very good agreement was found between flow rates from 4D flow data and simulation results in the supra-aortic branches, with a maximum difference in mean flow rate of 0.26 L/min in the LSA, corresponding to 21% of the 4D flow flow rate. In the descending aorta, Simulation-1 results showed an underestimation of the flow rate peak and higher diastolic flow rate. The worse matching of flow rate curves at the DAo could

be due to an underestimation of the pressure decay time constant τ or to an underestimation of the true ascending aorta stiffness. In fact, a higher τ would lead to a slower pressure decay, meaning that a higher pressure would persist during late systole, which in turn would lead to a lower flow rate. On the other hand, a less compliant aorta proximal to the coarctation would allow for less blood to be stored by the ascending aorta during early systole, thus decreasing the diastolic run-off. The lower flow rate peak during late systole obtained from Simulation-1 is directly related to the velocity magnitude contours visualized on the cross-sectional plane furthest from the coarctation. In fact, on this plane, higher velocities are observed from 4D flow during late systole. Additionally, an underestimation of the value of $\overline{P}$ used to tune 3-WK at the DAo could cause the higher flow rates observed in the simulations through this outlet.

In Simulation-2 the 18 mmHg increase in mean pressure used to tune 3-WK at the supra-aortic vessels led to a higher flow rate in the DAo with respect to Simulation-1. In particular, the difference between 4D flow and Simulation-2 peak flow rates was 0.83 L/min, whereas comparing 4D flow and Simulation-1 a value of 1.43 L/min was found. Through the DAo, Simulation-2 results showed a significantly higher diastolic flow rate compared to both 4D flow data and Simulation-1 results. In fact, the higher mean pressure used to set up boundary conditions for the three branches, led to an increase of 0.5 L/min in Simulation-2 mean flow rate with respect to Simulation-1.

Overall, both simulations produced results that were in good agreement with raw 4D flow velocity data, and despite the 18 mmHg increase in mean pressure at the branches outlets of Simulation-2, pressure drops across the coarctation differed slightly between the two simulations.

Validation of 4DF-FEPPE results

A Δp_m of 22.43 mmHg and a Δp_{pp} of 16.85 mmHg were obtained with Simulation-1, while a Δp_m of 23.89 mmHg and a Δp_{pp} of 18.56 mmHg were obtained with Simulation-2. Since a closer match of flow rate peaks through the DAo was obtained between Simulation-2

results and raw 4D flow data, Simulation-2 maximum pressure drop could be considered as more reliable. Therefore, 4DF-FEPPE-derived pressure drops obtained with raw 4D flow data as input tended to slightly underestimate maximum and peak-to-peak values by 1 mmHg and 2.8 mmHg respectively compared to Simulation-2 results. Compared to Simulation-1 results, 4DF-FEPPE-derived maximum and peak-to-peak pressure drops were 1.34 mmHg lower and 0.75 mmHg higher respectively. Application of the DFW filter on the 4D flow velocity fields led to significantly worse results in terms of pressure drops compared to simulations results. In particular, DFW-processed velocity fields led to maximum and peak-to-peak pressure drops that were lower than both simulation results by more than 5 mmHg. Thus, despite achieving efficient denoising of the raw 4D flow data, the use of the DFW filter was ineffective in improving trans-coarctation pressure drops. For what concerns the synthetic dataset (Section 2.1.5), the addition of artificial noise led to overall higher velocities (Figure 3.13) that were smoothed and lowered by the DFW filter, thus producing better results (Section 3.1.1). The increase in velocity values due to noise addition was not accurate in replicating the actual noise affecting 4D flow velocity fields. Nonetheless, it should be noted that the DFW filter was only used with an automatic threshold selection for simplicity; manually identifying a better suited threshold could have led to better results, but would have required additional time and was not within the purpose of this work.

Further qualitative pressure comparison was provided by pressure color maps visualization at different time points in the cardiac cycle; assuming a higher mean pressure for 3-WK tuning significantly affected absolute pressure values in the entire domain. In fact, while Simulation-1 pressure results were scaled from 60 to 100 mmHg in order to match 4D flow-derived pressures, Simulation-2 results were scaled from 80 to 120 mmHg. Such difference between the two simulations was directly realted to the different flow rate distribution caused by the different mean pressures imposed at the outlets. Specifically, the increased resistance values in the supra-aortic branches of Simulation-2 caused a higher flow rate to the DAo, thus through the coarctation. Nonetheless, pressure differences between ascending and descending aorta were not significantly affected by the different mean

pressures used to set outlet boundary conditions. This analysis allowed to gain a deeper understanding of the discrepancy observed in Simulation-2 diastolic flow rate through the DAo with respect to Simulation-1 and 4D flow. In fact, the higher absolute pressure values within the ascending aorta obtained with Simulation-2 caused a larger displacement of the arterial wall, which in turn resulted in a higher diastolic run-off.

Finally, blood rheology could play a role in the estimated trans-coarctation pressure drop. However, the assumption of Newtonian viscosity has been shown to be reasonable for bulk flow analysis, affecting the blood flow metric by less than 10% [113].

The setup of the experimental hydraulic test bench allowed to further validate 4DF-FEPPE results and confirm its accuracy. In fact, despite Δp measurements performed with pressure transducers differed from 4DF-FEPPE results by 0.37 to 4.5 mmHg, *in vitro* measurements were taken in a rigid model with a steady flow rate. This simplification leads to uncertainties on the trans-coarctation pressure drop. On one hand, rigid walls should theoretically lead to higher pressure difference, as stiffer vessels experiencing higher pressure drops are a well-known phenomenon in vascular applications [9, 19]. On the other hand, imposing a steady flow rate implies neglecting transient effects which contribute to the total pressure drop [114].

Limitations and future work

Although the developed pressure algorithm proved to be extremely efficient, its limitations are related to the shortcomings of 4D flow itself. This imaging technique, in fact, enjoys limited spatial and, perhaps most importantly, temporal resolutions. While direct hemodynamic measurements such as flow rates are less sensitive to these limitations, pressure estimation, which requires velocity derivatives to be computed, is much more significantly influenced by these sources of errors. These limitations in temporal and spatial resolutions resulted in a tendency of the algorithm to slightly underestimate the maximum pressure drop with respect to simulations. Additionally, the 4D flow-based flow rate measurement relative to the DAo was significantly lower than physiological values

reported in the literature [111]. Despite having an impact on adaptation in terms of flow rate distributions, the CoA at issue could not cause such a low flow rate to the lower part of the body. In fact, some collateral vessels branching distal to the coarctation are present, but could not be properly visualized and accounted for in the 4D flow images.

A limitation of this work consists in having implemented only one numerical method to solve the PPE. Future efforts should focus on investigating multi-grid based solvers to compare pressure results with finite element-based solutions.

Arterial vessel wall properties were assumed to be isotropic, linear elastic and homogeneous. This choice was forced by the difficulties encountered in estimating PWV from 4D flow in the aorta. Future efforts should focus on alternative techniques to evaluate wall mechanical properties from MRI.

In running all simulations, a laminar solver was used, even if Reynolds number analysis suggested that some turbulent flow is present downstream of the coarctation. On one hand, adopting a turbulence model could provide additional quantification of the pressure drop due turbulent energy dissipation. On the other hand, the mesh used to solve the two simulations was able to capture the flow features observed from 4D flow and the pressure difference across the coarctation matched the one computed from 4D flow, indicating that only a fraction of the total pressure drop could be attributed to turbulence. Additionally, modeling both vessel wall deformation and turbulent flow is a challenging task which would imply a cosiderable increase in computational effort.

Another limitation of the numerical simulation herein reported is represented by the segmentation process. In fact, the segmented 3D geometry extracted from MRA images was acquired from an average configuration throughout the cardiac cycle, whereas knowing the load acting on the arterial wall one could obtain a more accurate diastolic configuration.

Finally, a limitation of this work consists in having analyzed only one patient. In this thesis a MATLAB code to calculate pressure from 4D flow MRI was developed and validated against both synthetic and patient-specific; future studies could take advantage

of the present work and include more patients in order to evaluate the effect of different geometries on CoA hemodynamics.

4.2 Conclusions

In conclusion, the proposed workflow showed how an image processing approach based on 4D flow MR images combined with *in silico* and *in vitro* methodologies allows to produce accurate non-invasive assessment of CoA severity and hemodynamics. The developed tool enables even unexperienced users to obtain, in a few minutes, vascular pressure distributions from 4D flow images of any district of interest. This algorithm was designed with the purpose of aiding clinicians to obtain early non-invasive pressure estimation for patients with CoA, a disease in which the pressure drop across the narrowing is a major diagnostic factor.

Bibliography

[1] J. Lantz, T. Ebbers, J. Engvall, and M. Karlsson. Numerical and experimental assessment of turbulent kinetic energy in an aortic coarctation. *Journal of biomechanics* 46.11 (2013), pp. 1851–1858.

[2] R. M. Brouwer, M. E. Erasmus, T. Ebels, and A. Eijgelaar. Influence of age on survival, late hypertension, and recoarctation in elective aortic coarctation repair. *The Journal of thoracic and cardiovascular surgery* 108.3 (1994), pp. 525–531.

[3] A. Bocelli et al. Prevalence and long-term predictors of left ventricular hypertrophy, late hypertension, and hypertensive response to exercise after successful aortic coarctation repair. *Pediatric cardiology* 34.3 (2013), pp. 620–629.

[4] C. A. Warnes et al. ACC/AHA 2008 guidelines for the management of adults with congenital heart disease: a report of the American college of cardiology/American heart association task force on practice guidelines (writing committee to develop guidelines on the management of adults with congenital heart disease) developed in collaboration with the american society of echocardiography, heart rhythm society, international society for adult congenital heart disease, society for cardiovascular angiography and interventions, and society of thoracic surgeons. *Journal of the American College of Cardiology* 52.23 (2008), e143–e263.

[5] E. Rosenthal. *Stent implantation for aortic coarctation: the treatment of choice in adults?* 2001.

[6] L. Taelman. "Fluid-structure interaction simulation of (repaired) aortic coarctation". PhD thesis. Ghent University, 2014.

[7] L. Goubergrits et al. MRI-based computational fluid dynamics for diagnosis and treatment prediction: Clinical validation study in patients with coarctation of aorta. *Journal of Magnetic Resonance Imaging* 41.4 (2015), pp. 909–916.

[8] H. Ha et al. Hemodynamic Measurement using four-dimensional phase-contrast MRI: quantification of hemodynamic parameters and clinical applications. *Korean journal of radiology* 17.4 (2016), pp. 445–462.

[9] C. A. Figueroa, I. E. Vignon-Clementel, K. E. Jansen, T. J. Hughes, and C. A. Taylor. A coupled momentum method for modeling blood flow in three-dimensional deformable arteries. *Computer methods in applied mechanics and engineering* 195.41 (2006), pp. 5685–5706.

[10] F. Piatti et al. Towards the improved quantification of in vivo abnormal wall shear stresses in BAV-affected patients from 4D-flow imaging: Benchmarking and application to real data. *Journal of biomechanics* 50 (2017), pp. 93–101.

[11] F. Ong et al. Robust 4D flow denoising using divergence-free wavelet transform. *Magnetic resonance in medicine* 73.2 (2015), pp. 828–842.

[12] H. J. Kim et al. On coupling a lumped parameter heart model and a three-dimensional finite element aorta model. *Annals of biomedical engineering* 37.11 (2009), pp. 2153–2169.

[13] P. J. Roache. *Verification and validation in computational science and engineering.* Vol. 895. Hermosa Albuquerque, NM, 1998.

[14] B. A. Craven, E. G. Paterson, G. S. Settles, and M. J. Lawson. Development and verification of a high-fidelity computational fluid dynamics model of canine nasal airflow. *Journal of biomechanical engineering* 131.9 (2009), p. 091002.

[15] S. Pirola et al. On the choice of outlet boundary conditions for patient-specific analysis of aortic flow using computational fluid dynamics. *Journal of Biomechanics* 60 (2017), pp. 15–21.

[16] P. Reymond, F. Merenda, F. Perren, D. Rufenacht, and N. Stergiopulos. Validation of a one-dimensional model of the systemic arterial tree. *American Journal of Physiology-Heart and Circulatory Physiology* 297.1 (2009), H208–H222.

[17] N. Xiao, J. D. Humphrey, and C. A. Figueroa. Multi-scale computational model of three-dimensional hemodynamics within a deformable full-body arterial network. *Journal of computational physics* 244 (2013), pp. 22–40.

[18] A. C. Simon, M. Safar, J. Levenson, G. London, B. Levy, and N. Chau. An evaluation of large arteries compliance in man. *American Journal of Physiology-Heart and Circulatory Physiology* 237.5 (1979), H550–H554.

[19] C. Vlachopoulos, M. O'Rourke, and W. W. Nichols. *McDonald's blood flow in arteries: theoretical, experimental and clinical principles*. CRC press, 2011.

[20] L. National Heart, B. Institute, et al. Morbidity & Mortality: Chart Book on Cardiovascular, Lung and Blood Diseases. *http://www. nhlbi. nih. gov/resources/docs/chtbook/htm* (1998).

[21] J. I. Hoffman and S. Kaplan. The incidence of congenital heart disease. *Journal of the American college of cardiology* 39.12 (2002), pp. 1890–1900.

[22] P. S. Rao. "Coarctation of the aorta." *Seminars in nephrology*. Vol. 15. 2. 1995, pp. 87–105.

[23] C. Ferencz et al. Congenital heart disease: prevalence at livebirth: the Baltimore-Washington Infant Study. *American journal of epidemiology* 121.1 (1985), pp. 31–36.

[24] D. Bergsma. *Birth defects compendium*. Springer, 2016.

[25] K. L. McBride, L. Marengo, M. Canfield, P. Langlois, D. Fixler, and J. W. Belmont. Epidemiology of noncomplex left ventricular outflow tract obstruction malformations (aortic valve stenosis, coarctation of the aorta, hypoplastic left heart syndrome) in Texas, 1999–2001. *Birth Defects Research Part A: Clinical and Molecular Teratology* 73.8 (2005), pp. 555–561.

[26] G. M. Hutchins. Coarctation of the aorta explained as a branch-point of the ductus arteriosus. *The American journal of pathology* 63.2 (1971), p. 203.

[27] Mayo Clinic Staff. *Coarctation of the aorta*. 2017. URL: http://www.mayoclinic.org/diseases-conditions/coarctation-of-the-aorta/home/ovc-20325103 (visited on 09/30/2010).

[28] A. M. Rudolph, M. A. Heymann, and U. Spitznas. Hemodynamic considerations in the development of narrowing of the aorta. *The American journal of cardiology* 30.5 (1972), pp. 514–525.

[29] B. Agarwala et al. Clinical manifestations and diagnosis of coarctation of the aorta. *Uptodate. com* (2011).

[30] D. C. Wendell et al. Including aortic valve morphology in computational fluid dynamics simulations: initial findings and application to aortic coarctation. *Medical engineering & physics* 35.6 (2013), pp. 723–735.

[31] C. Gøtzsche, B Krag-Olsen, J Nielsen, K. Sørensen, and B. O. Kristensen. Prevalence of cardiovascular malformations and association with karyotypes in Turner's syndrome. *Archives of disease in childhood* 71.5 (1994), pp. 433–436.

[32] R. Klabunde. *Cardiovascular physiology concepts*. Lippincott Williams & Wilkins, 2011.

[33] R. Massey and D. F. Shore. Surgery for complex coarctation of the aorta. *International journal of cardiology* 97 (2004), pp. 67–73.

[34] URL: https://healtheappointments.com/chapter-13-cardiovascular-system-essays/4/.

[35] R. Brian, R. Nicki, and H. Stuart. *Davidson's Principles and Practice of Medicine, CHURCHILL, LIVINGSTONE*. 2010.

[36] J. E. Vargas. *Biochemistry, Genetics, and Embryology*. Vol. 297. Lippincott Williams & Wilkins, 2004.

[37] J. W. Vriend and B. J. Mulder. Late complications in patients after repair of aortic coarctation: implications for management. *International journal of cardiology* 101.3 (2005), pp. 399–406.

[38] A. Buyens et al. Difficult prenatal diagnosis: fetal coarctation. *Facts, views & vision in ObGyn* 4.4 (2012), p. 230.

[39] D. E. Teien, H. Wendel, J Björnebrink, and L. Ekelund. Evaluation of anatomical obstruction by Doppler echocardiography and magnetic resonance imaging in patients with coarctation of the aorta. *Heart* 69.4 (1993), pp. 352–355.

[40] P. Nihoyannopoulos, S. Karas, R. N. Sapsford, K. Hallidie-Smith, and R. Foale. Accuracy of two-dimensional echocardiography in the diagnosis of aortic arch obstruction. *Journal of the American College of Cardiology* 10.5 (1987), pp. 1072–1077.

[41] J. Marek et al. Seven-year experience of noninvasive preoperative diagnostics in children with congenital heart defects: comprehensive analysis of 2,788 consecutive patients. *Cardiology* 86.6 (1995), pp. 488–495.

[42] H. Baumgartner et al. Echocardiographic assessment of valve stenosis: EAE/ASE recommendations for clinical practice. *European Journal of Echocardiography* (2008).

[43] L. Hatle, A. Brubakk, A. Tromsdal, and B. Angelsen. Noninvasive assessment of pressure drop in mitral stenosis by Doppler ultrasound. *Heart* 40.2 (1978), pp. 131–140.

[44] J. Holen, R. Aaslid, K. Landmark, and S. Simonsen. Determination of Pressure Gradient in Mitral Stenosis with a Non-invasive Ultrasound Doppler Technique. *Journal of Internal Medicine* 199.1-6 (1976), pp. 455–460.

[45] S. De Mey, P. Segers, I. Coomans, H. Verhaaren, and P. Verdonck. Limitations of Doppler echocardiography for the post-operative evaluation of aortic coarctation. *Journal of biomechanics* 34.7 (2001), pp. 951–960.

[46] L. Itu et al. Non-invasive hemodynamic assessment of aortic coarctation: validation with in vivo measurements. *Annals of biomedical engineering* 41.4 (2013), pp. 669–681.

[47] A. W. Aldousany, T. G. DiSessa, B. S. Alpert, S. E. Birnbaum, and E. S. Willey. Significance of the Doppler-derived gradient across a residual aortic coarctation. *Pediatric cardiology* 11.1 (1990), pp. 8–14.

[48] P. Dyverfeldt et al. 4D flow cardiovascular magnetic resonance consensus statement. *Journal of Cardiovascular Magnetic Resonance* 17.1 (2015), p. 72.

[49] H. Suradi and Z. M. Hijazi. Current management of coarctation of the aorta. *Global Cardiology Science and Practice* (2015), p. 44.

[50] J. L. Gibbs. *Treatment options for coarctation of the aorta*. 2000.

[51] H. Aebert, J. Laas, P. Bednarski, U. Koch, M. Prokop, and H. Borst. High incidence of aneurysm formation following patch plasty repair of coarctation. *European journal of cardio-thoracic surgery* 7.4 (1993), pp. 200–205.

[52] R. Holzer et al. Stenting of aortic coarctation: Acute, intermediate, and long-term results of a prospective multi-institutional registry—Congenital cardiovascular interventional study consortium (CCISC). *Catheterization and Cardiovascular Interventions* 76.4 (2010), pp. 553–563.

[53] A. Hager, S. Kanz, H. Kaemmerer, C. Schreiber, and J. Hess. Coarctation Long-term Assessment (COALA): significance of arterial hypertension in a cohort of 404 patients up to 27 years after surgical repair of isolated coarctation of the aorta, even in the absence of restenosis and prosthetic material. *The Journal of Thoracic and Cardiovascular Surgery* 134.3 (2007), pp. 738–745.

[54] M. Mullen. *Coarctation of the aorta in adults: do we need surgeons?* 2003.

[55] E. De Caro, I. Spadoni, R. Crepaz, M. Saitta, G. Trocchio, and G. Pongiglione. Stenting of aortic coarctation and exercise-induced hypertension in the young. *Catheterization and Cardiovascular Interventions* 75.2 (2010), pp. 256–261.

[56] D. B. Plewes and W. Kucharczyk. Physics of MRI: a primer. *Journal of magnetic resonance imaging* 35.5 (2012), pp. 1038–1054.

[57] URL: `http://199.116.233.101/index.php/Physics_of_MRI`.

[58] J. Lotz, C. Meier, A. Leppert, and M. Galanski. Cardiovascular flow measurement with phase-contrast MR imaging: basic facts and implementation. *Radiographics* 22.3 (2002), pp. 651–671.

[59] C. J. Elkins and M. T. Alley. Magnetic resonance velocimetry: applications of magnetic resonance imaging in the measurement of fluid motion. *Experiments in Fluids* 43.6 (2007), pp. 823–858.

[60] M. Markl, A. Frydrychowicz, S. Kozerke, M. Hope, and O. Wieben. 4D flow MRI. *Journal of Magnetic Resonance Imaging* 36.5 (2012), pp. 1015–1036.

[61] H. Ha et al. Multi-VENC acquisition of four-dimensional phase-contrast MRI to improve precision of velocity field measurement. *Magnetic resonance in medicine* 75.5 (2016), pp. 1909–1919.

[62] Z. Stankovic, B. D. Allen, J. Garcia, K. B. Jarvis, and M. Markl. 4D flow imaging with MRI. *Cardiovascular diagnosis and therapy* 4.2 (2014), p. 173.

[63] C. Tang, D. D. Blatter, and D. L. Parker. Accuracy of phase-contrast flow measurements in the presence of partial-volume effects. *Journal of Magnetic Resonance Imaging* 3.2 (1993), pp. 377–385.

[64] A. Roldán-Alzate et al. In vivo validation of 4D flow MRI for assessing the hemodynamics of portal hypertension. *Journal of magnetic resonance imaging* 37.5 (2013), pp. 1100–1108.

[65] S. Nordmeyer et al. Flow-sensitive four-dimensional cine magnetic resonance imaging for offline blood flow quantification in multiple vessels: a validation study. *Journal of Magnetic Resonance Imaging* 32.3 (2010), pp. 677–683.

[66] D. Schiavazzi, F. Coletti, G. Iaccarino, and J. K. Eaton. A matching pursuit approach to solenoidal filtering of three-dimensional velocity measurements. *Journal of Computational Physics* 263 (2014), pp. 206–221.

[67] I. Azijli and R. P. Dwight. Solenoidal filtering of volumetric velocity measurements using Gaussian process regression. *Experiments in Fluids* 56.11 (2015), p. 198.

[68] M. F. O'rourke and T. B. Cartmill. Influence of aortic coarctation on pulsatile hemodynamics in the proximal aorta. *Circulation* 44.2 (1971), pp. 281–292.

[69] A. B. Fisher, S. Chien, A. I. Barakat, and R. M. Nerem. Endothelial cellular response to altered shear stress. *American Journal of Physiology-Lung Cellular and Molecular Physiology* 281.3 (2001), pp. L529–L533.

[70] D. N. Ku, D. P. Giddens, C. K. Zarins, and S. Glagov. Pulsatile flow and atherosclerosis in the human carotid bifurcation. Positive correlation between plaque location and low oscillating shear stress. *Arteriosclerosis, thrombosis, and vascular biology* 5.3 (1985), pp. 293–302.

[71] M. M. Bissell et al. Aortic dilation in bicuspid aortic valve disease: flow pattern is a major contributor and differs with valve fusion type. *Circulation: Cardiovascular Imaging* (2013), CIRCIMAGING–113.

[72] P. G. Walker, G. B. Cranney, M. B. Scheidegger, G. Waseleski, G. M. Pohost, and A. P. Yoganathan. Semiautomated method for noise reduction and background phase error correction in MR phase velocity data. *Journal of Magnetic Resonance Imaging* 3.3 (1993), pp. 521–530.

[73] J. Garcia et al. Assessment of altered three-dimensional blood characteristics in aortic disease by velocity distribution analysis. *Magnetic resonance in medicine* 74.3 (2015), pp. 817–825.

[74] G. Biglino et al. Using 4D cardiovascular magnetic resonance imaging to validate computational fluid dynamics: a case study. *Frontiers in pediatrics* 3 (2015).

[75] S. Miyazaki et al. Validation of numerical simulation methods in aortic arch using 4D Flow MRI. *Heart and Vessels* (2017), pp. 1–13.

[76] C. K. Zarins, D. P. Giddens, B. Bharadvaj, V. S. Sottiurai, R. F. Mabon, and S. Glagov. Carotid bifurcation atherosclerosis. Quantitative correlation of plaque

localization with flow velocity profiles and wall shear stress. *Circulation research* 53.4 (1983), pp. 502–514.

[77] C. Cheng et al. Atherosclerotic lesion size and vulnerability are determined by patterns of fluid shear stress. *Circulation* 113.23 (2006), pp. 2744–2753.

[78] P. A. VanderLaan, C. A. Reardon, and G. S. Getz. Site specificity of atherosclerosis. *Arteriosclerosis, thrombosis, and vascular biology* 24.1 (2004), pp. 12–22.

[79] P. Ooij et al. Wall shear stress estimated with phase contrast MRI in an in vitro and in vivo intracranial aneurysm. *Journal of magnetic resonance imaging* 38.4 (2013), pp. 876–884.

[80] A. Frydrychowicz et al. Three-dimensional analysis of segmental wall shear stress in the aorta by flow-sensitive four-dimensional-MRI. *Journal of Magnetic Resonance Imaging* 30.1 (2009), pp. 77–84.

[81] A. F. Stalder, M. Russe, A Frydrychowicz, J Bock, J Hennig, and M Markl. Quantitative 2D and 3D phase contrast MRI: optimized analysis of blood flow and vessel wall parameters. *Magnetic resonance in medicine* 60.5 (2008), pp. 1218–1231.

[82] M. Cibiş. *Haemodynamics of Large Vessels by Phase Contrast MRI*. 2016.

[83] I. Valverde et al. Predicting hemodynamics in native and residual coarctation: preliminary results of a Rigid-Wall Computational-Fluid-Dynamics model (RW-CFD) validated against clinically invasive pressure measures at rest and during pharmacological stress. *Journal of Cardiovascular Magnetic Resonance* 13.1 (2011), P49.

[84] E. Riesenkampff et al. Pressure fields by flow-sensitive, 4D, velocity-encoded CMR in patients with aortic coarctation. *JACC: Cardiovascular Imaging* 7.9 (2014), pp. 920–926.

[85] F. Rengier et al. Noninvasive pressure difference mapping derived from 4D flow MRI in patients with unrepaired and repaired aortic coarctation. *Cardiovascular diagnosis and therapy* 4.2 (2014), p. 97.

[86] J. Bock et al. In vivo noninvasive 4D pressure difference mapping in the human aorta: phantom comparison and application in healthy volunteers and patients. *Magnetic resonance in medicine* 66.4 (2011), pp. 1079–1088.

[87] S. B. Krittian et al. A finite-element approach to the direct computation of relative cardiovascular pressure from time-resolved MR velocity data. *Medical image analysis* 16.5 (2012), pp. 1029–1037.

[88] J. M. Tyszka, D. H. Laidlaw, J. W. Asa, and J. M. Silverman. Three-dimensional, time-resolved (4D) relative pressure mapping using magnetic resonance imaging. *Journal of Magnetic Resonance Imaging* 12.2 (2000), pp. 321–329.

[89] T. Ebbers and G. Farnebäck. Improving computation of cardiovascular relative pressure fields from velocity MRI. *Journal of Magnetic Resonance Imaging* 30.1 (2009), pp. 54–61.

[90] A. Nasiraei-Moghaddam, G. Behrens, N. Fatouraee, R. Agarwal, E. T. Choi, and A. A. Amini. Factors affecting the accuracy of pressure measurements in vascular stenoses from phase-contrast MRI. *Magnetic resonance in medicine* 52.2 (2004), pp. 300–309.

[91] J. Bock, A. Frydrychowicz, K. Johnson, O. Wieben, J. Hennig, and M. Markl. "Optimized data analysis for the assessment of aortic pressure difference maps". 2009.

[92] S. Meier, A. Hennemuth, O. Friman, J. Bock, M. Markl, and T. Preusser. "Non-invasive 4D blood flow and pressure quantification in central blood vessels via PC-MRI". *Computing in Cardiology, 2010*. IEEE. 2010, pp. 903–906.

[93] F. Donati, C. A. Figueroa, N. P. Smith, P. Lamata, and D. A. Nordsletten. Non-invasive pressure difference estimation from PC-MRI using the work-energy equation. *Medical image analysis* 26.1 (2015), pp. 159–172.

[94] J. S. Coogan, J. D. Humphrey, and C. A. Figueroa. Computational simulations of hemodynamic changes within thoracic, coronary, and cerebral arteries following early wall remodeling in response to distal aortic coarctation. *Biome-*

chanics and Modeling in Mechanobiology 12.1 (2013), pp. 79–93. ISSN: 1617-7940. DOI: 10.1007/s10237-012-0383-x. URL: https://doi.org/10.1007/s10237-012-0383-x.

[95] J. F. LaDisa et al. Computational simulations for aortic coarctation: representative results from a sampling of patients. *Journal of biomechanical engineering* 133.9 (2011), p. 091008.

[96] J. von Spiczak, G. Crelier, D. Giese, S. Kozerke, D. Maintz, and A. C. Bunck. Quantitative analysis of vortical blood flow in the thoracic aorta using 4D phase contrast MRI. *PLoS One* 10.9 (2015), e0139025.

[97] L. J. Olivieri, D. A. de Zélicourt, C. M. Haggerty, K. Ratnayaka, R. R. Cross, and A. P. Yoganathan. Hemodynamic modeling of surgically repaired coarctation of the aorta. *Cardiovascular engineering and technology* 2.4 (2011), pp. 288–295.

[98] C. G. DeGroff, W. Orlando, and R. Shandas. Insights into the effect of aortic compliance on Doppler diastolic flow patterns seen in coarctation of the aorta: a numeric study. *Journal of the American Society of Echocardiography* 16.2 (2003), pp. 162–169.

[99] J. S. Coogan, F. P. Chan, C. A. Taylor, and J. A. Feinstein. Computational fluid dynamic simulations of aortic coarctation comparing the effects of surgical-and stent-based treatments on aortic compliance and ventricular workload. *Catheterization and Cardiovascular Interventions* 77.5 (2011), pp. 680–691.

[100] A. Hennemuth et al. "Fast interactive exploration of 4D MRI flow data". *Medical Imaging 2011: Visualization, Image-Guided Procedures, and Modeling*. Vol. 7964. International Society for Optics and Photonics. 2011, 79640E.

[101] U. Morbiducci et al. Synthetic dataset generation for the analysis and the evaluation of image-based hemodynamics of the human aorta. *Medical & biological engineering & computing* 50.2 (2012), pp. 145–154.

[102] F. Piatti et al. Experimental quantification of the fluid dynamics in blood-processing devices through 4D-flow imaging: A pilot study on a real oxygenator/heat-exchanger module. *Journal of biomechanics* 68 (2018), pp. 14–23.

[103] P. A. Yushkevich et al. User-Guided 3D Active Contour Segmentation of Anatomical Structures: Significantly Improved Efficiency and Reliability. *Neuroimage* 31.3 (2006), pp. 1116–1128.

[104] E. Tedaldi, C. Montanari, K. I. Aycock, F. Sturla, A. Redaelli, and K. B. Manning. An experimental and computational study of the inferior vena cava hemodynamics under respiratory-induced collapse of the infrarenal IVC. *Medical Engineering and Physics* (2018).

[105] D. Gallo et al. On the use of in vivo measured flow rates as boundary conditions for image-based hemodynamic models of the human aorta: implications for indicators of abnormal flow. *Annals of biomedical engineering* 40.3 (2012), pp. 729–741.

[106] J. L. Cavalcante, J. A. Lima, A. Redheuil, and M. H. Al-Mallah. Aortic stiffness: current understanding and future directions. *Journal of the American College of Cardiology* 57.14 (2011), pp. 1511–1522.

[107] P. Ou et al. Angular (Gothic) aortic arch leads to enhanced systolic wave reflection, central aortic stiffness, and increased left ventricular mass late after aortic coarctation repair: evaluation with magnetic resonance flow mapping. *The Journal of thoracic and cardiovascular surgery* 135.1 (2008), pp. 62–68.

[108] P. Ou et al. Increased central aortic stiffness and left ventricular mass in normotensive young subjects after successful coarctation repair. *American heart journal* 155.1 (2008), pp. 187–193.

[109] J. Zhou and Y. Fung. The degree of nonlinearity and anisotropy of blood vessel elasticity. *Proceedings of the National Academy of Sciences* 94.26 (1997), pp. 14255–14260.

[110] C. Kousera, N. Wood, W. Seed, R. Torii, D. O'regan, and X. Xu. A numerical study of aortic flow stability and comparison with in vivo flow measurements. *Journal of Biomechanical Engineering* 135.1 (2013), p. 011003.

[111] L. P. Wittberg, S. van Wyk, L. Fuchs, E. Gutmark, P. Backeljauw, and I. Gutmark-Little. Effects of aortic irregularities on blood flow. *Biomechanics and modeling in mechanobiology* 15.2 (2016), pp. 345–360.

[112] S. Pirola et al. Computational study of aortic hemodynamics for patients with an abnormal aortic valve: The importance of secondary flow at the ascending aorta inlet. *APL Bionengineering* (2018).

[113] U. Morbiducci et al. On the importance of blood rheology for bulk flow in hemodynamic models of the carotid bifurcation. *Journal of biomechanics* 44.13 (2011), pp. 2427–2438.

[114] P. Lamata et al. Aortic relative pressure components derived from four-dimensional flow cardiovascular magnetic resonance. *Magnetic resonance in medicine* 72.4 (2014), pp. 1162–1169.